A study of muon neutrino disappearance in the MINOS detectors and the NuMI beam

By

Jiajie Ling

Bachelor of Science
Shanghai Jiaotong University 2000
Master of Science
Shanghai Jiaotong University 2003

Submitted in Partial Fulfillment of the Requirements

for the Degree of Doctor of Philosphy in

Physics

College of Arts and Sciences

University of South Carolina

2010

Accepted by:

Sanjib R. Mishra, Major Professor

Carl Rosenfeld, Committee Member

Roberto Petti, Committee Member

Donna A. Chen, Committee Member

James Buggy, Interim Dean of the Graduate School

Dedication

This work is dedicated to my parents and my family.

Acknowledgments

This dissertation would not have been possible without the guidance and the help of many people who in one way or another contributed and extended their valuable assistance in this study.

First and foremost, my utmost gratitude to my advisor professor Sanjib R. Mishra for his supervision, advice, and guidance for every stage of this research. Above all and the most needed, he provided me unflinching encouragement and support in various ways. His passion in physics inspire and enrich my growth as a student, a researcher and a scientist want to be. I will never forget professor Mishra has been my inspiration as I hurdle all the obstacles in the completion this research work.

During my last two years I had the fortune to work with Tingjun Yang. He is willing to answer all my unintelligent questions, as well as his advice and suggestions to this research. The close friendship and invaluable help are unforgettable. I am grateful in every possible way and hope to keep up our collaboration in the future.

Many thanks go in particular to Donna Naples and Debdatta Bhattacharya. I am much indebted to them for the valuable advice in discussion and critical comments about it.

I gratefully thank Robert Plunkett for all the help he provided during my stay at the Fermilab.

It is a pleasure to pay tribute also to the MINOS ν_e appearance analysis group. It has been a nice experience working for this wonderful analysis. Special thanks to Ptricia Vahle, Greg Pawloski, Ryan Patterson, Lisa Whitehead, Steven Cavanaugh, Jõao Coelho and Xiaobo Huang.

Thanks to Niki Saoulidou, Masaki Ishitsuka, Bob Armstrong and Zarko Pavlovich for their valuable discussions in this research.

Thanks to Nathaniel Tagg, Elisabeth Falk, Jeff Hartnell and Leon Mualem for helping me familiar with the calibration work.

I have also benefited by advice from Robert Hatcher who always kindly grants me his precious time for answering my unintelligent questions.

Thanks to Carl Rosenfeld for reading my thesis and giving valuable comments and suggestions.

I would like to thank Aziz Rahaman for generating all the files I needed for this analysis and helping me acquainted with the Fermilab.

Thanks to my collages, Jae Jun Kim, Qun Wu, Andrew Godley, Xinchun Tian, Hongxuan Liu, Xurong Chen, Woochun Park, Haiyun Lu, Zhiwen Zhao and Baowei Liu. And thanks to my Fermilab friends, Xinjie Qiu, Wenji Wu and Weimin Wu.

Last but not the least, the loving support and encouragement of my parents and my family has been totally invaluable over the years and without whom I would not be where I am today. Many thanks to them.

Abstract

There is now substantial evidence that the proper description of neutrino involves two representations related by the 3×3 PMNS matrix characterized by either distinct mass or flavor. The parameters of this mixing matrix, three angles and a phase, as well as the mass differences between the three mass eigenstates must be determined experimentally. The Main Injector Neutrino Oscillation Search experiment is designed to study the flavor composition of a beam of muon neutrinos as it travels between the Near Detector at Fermi National Accelerator Laboratory at 1 km from the target, and the Far Detector in the Soudan iron mine in Minnesota at 735 km from the target. From the comparison of reconstructed neutrino energy spectra at the near and far location, precise measurements of neutrino oscillation parameters from muon neutrino disappearance and electron neutrino appearance are expected. It is very important to know the neutrino flux coming from the source in order to achieve the main goal of the MINOS experiment: precise measurements of the atmospheric mass splitting $|\Delta m^2_{23}|$, $\sin^2 \theta_{23}$. The goal of my thesis is to accurately predict the neutrino flux for the MINOS experiment and measure the neutrino mixing angle and atmospheric mass splitting.

Contents

List of Tables

List of Figures

Chapter 1

Introduction

Neutrinos play a crucial role in fundamental particle physics and have a huge impact in astrophysics and cosmology. The Standard Model of electroweak interaction was constructed on the premise that the failure to observe right-handed neutrinos implies that neutrinos are massless, and there is no mixing between the leptons. The strong evidence for non-zero neutrino mass clearly indicates the existence of physics beyond the minimal Standard Model. The smallness of neutrino masses together with the amounts of lepton flavor violation found in neutrino oscillation experiments provide insights into possible modifications of the current Standard Model of electroweak interactions, and open a new window towards the Grand Unification of energy scale.

1.1. A Brief History of Neutrinos

The idea of neutrino was first proposed by Wolfgang Pauli in an open letter to a December 1930 physics conference at Tubingen. In order to explain the continuous beta decay spectra [Pauli, 1978], Pauli postulated the existence of a new particle, neutrino. Pauli required his hypothetical particle to be neutral and has spin 1/2, to ensure conservation of electric charge and angular momentum. Learning of Pauli's idea, Fermi [1934] formally developed a comprehensive theory of beta decay.

Neutrino is an elementary particle that usually travels close to the speed of light, is electrically neutral, and is able to pass through ordinary matter almost undisturbed. According to Bethe and Peierls, the weak interaction would allow a neutrino to pass through 50 billion miles of water without interacting [Bethe and Peierls, 1934]. Neutrino detection seems impossible. In the early 1950s, however, Reines addressed this

problem and searched for a way of measuring inverse beta decay

$$\overline{\nu}_e + p \rightarrow n + e^+ \tag{1.1}$$

To detect such a rare, low cross-section reaction required both a large target and an enormous flux. In 1956, Reines and Cowan settled on using the Savannah River nuclear reactor in South Carolina, which minimized background effects, and a large water target [Cowan et al., 1956]. Although reactors provide a large flux of anti-neutrinos from beta decays, their signal rate is only a couple per hour. On the other hand, they developed an ingenious method for identifying the outgoing positron. In target matter, positrons promptly slow down and annihilate with electrons, producing two 0.5 MeV gamma rays, which are detected by two large scintillation detectors. In a few microseconds the neutron is slowed down sufficiently in the water and finally captured by the cadmium chloride. Measurement of the slowdown time completed by the final identification. A small but clear signal of less than two events per hour was observed, their results provided unambiguous confirmation of the electron neutrino existence. This experiment was the first reactor-neutrino experiment.

In 1956, T.D.Lee and C.N.Yang suggested the parity violation in the weak interaction in order to explain the famous θ-τ puzzle [Lee and Yang, 1956]; K^+, the one called θ, decay into two pions, whereas K^+, the one called τ, decay into three pions. The puzzle was that θ and τ have the same mass, spin, and charge. A number of tests to observe parity violation were suggested by Lee and Yang. Subsequently, parity violation was observed in the β-decay of polarized ^{60}Co, $\pi^+ \rightarrow \mu^+ + \nu_\mu$ and $\mu^+ \rightarrow e^+ + \nu_e + \overline{\nu}_\mu$ [Wu et al., 1957].

The structure of the $V-A$ theory, formulated in 1958 by Feynman and Gell-Mann [1958], Sudarshan and Marshak [1958] and Sakurai [1958] can easily be realized in the lepton sector by using the two-component theory of a massless neutrino, proposed in 1957 by Landau [1957], Lee and Yang [1957] and Salam [1957]. In this theory,

neutrinos are left-handed and antineutrinos are right-handed, leading automatically to the $V - A$ coupling.

In 1958, Goldhaber, Grodzins, and Sunyar at Brookhaven National Laboratory (BNL) measured the polarization of a neutrino in the electron capture $e^- + {}^{152}Eu \rightarrow {}^{152} Sm^* + \nu_e$, with the subsequent decay ${}^{152}Sm^* \rightarrow {}^{152} Sm + \gamma$. They found the measured polarization of photon implies that the polarization of the ν_e was indeed in a direction opposite to its motion (left-handed) [Goldhaber et al., 1958], within experimental uncertainties. This result is in agreement with the V-A nature of the weak interaction predicted by Feynman and Gell-Mann [1958].

In 1962, L.M.Lederman, M.Schwartz, J.Steinberger *et at.* succeeded at BNL in establishing the existence of the second neutrino ν_μ [Danby et al., 1962]. This experiment marked the first serious accelerator neutrino experiment. In 1975, a new lepton, tau, was discovered by a group led by M.Perl at the Standard Linear Accelerator Center. Experiments performed shortly afterward provided strong evidence that there also exists a third species of neutrino, the tau neutrino, ν_τ. The tau neutrino was first detected in 2000 by the DONUT experiment [Kodama et al., 2001].

In 1980s the LEP experiments at CERN precisely measured the width of the Z resonance. This measurement was highly significant for neutrino physics as it provided very strong evidence there were only 3 light ($m_\nu < 45\,\mathrm{GeV}$), active neutrino flavors [Decamp et al., 1989].

A crucial milestone in the theory of weak interactions is the formulation of the Glashow-Weinberg-Salam Standard Model (SM) by Glashow [1961], Salam [1968], and Weinberg [1967] in 1967. The model is based on an $SU(2) \times U(1)$ gauge model proposed by S.L. Glashow in 1961, which predicted the existence of weak neutral currents and Z boson. The Standard Model incorporates the so-called Higgs mechanism into the Glashow model. The Higgs mechanism allows the original massless gauge bosons that appear in the local gauge group model to acquire longitudinal degrees of freedom, finally making them massive as demanded in nature.

In 1973, the Gargamelle experiment at CERN discovered the weak neutral current (NC) interaction

$$\overline{\nu}_\mu + e \rightarrow \overline{\nu}_\mu + e \tag{1.2}$$

mediated by the Z^0 boson. The same series of experiments also observed the corresponding neutrino-quark process by observing event induced by ν / $\overline{\nu}$ that produced hadrons, but no muon or electron [Hasert et al., 1973]:

$$\begin{aligned} \overline{\nu}_\mu + N &\rightarrow \overline{\nu}_\mu + X \\ \nu_\mu + N &\rightarrow \nu_\mu + X \end{aligned} \tag{1.3}$$

The observation of the neutral weak current and the discovery of the intermediate vector bosons W [Arnison et al., 1983] and Z [Bagnaia et al., 1983] at CERN in 1983, at $M_W = 82\,\mathrm{GeV/c^2}$ and $M_Z = 92\,\mathrm{GeV/c^2}$ (as predicted), further proved the success of this model.

No experiments that have been performed so far have detected conclusive deviations from the SM, except neutrino oscillation experiments, which have shown that neutrinos are massive and mixed. This discovery has made the SM an effective theory of the yet unknown theory beyond the SM. The understanding of how the neutrino would gain tiny masses and how they are mixed is an extremely challenging task that we have to face. The answer must be found in the theory beyond the SM. Thus, the neutrino is playing the role of a messenger of the new physics beyond the SM.

The rest of this chapter is devoted to the discussions of the properties of neutrino and the phenomenon "neutrino oscillation" whereby a neutrino created with a specific lepton flavor (electron, muon or tau) can later be measured to have a different flavor. A detailed neutrino oscillation experiments are discussed further later in this chapter.

1.2. The Standard Model

The Standard Model (SM) describes the strong, electromagnetic, and weak interactions of elementary particles in the framework of quantum field theory. It is a gauge theory based on the local symmetry group $SU(3)_C \times SU(2)_L \times U(1)_Y$, where the subscripts C, L and Y denote color, left-handed chirality and weak hypercharge, respectively. The gauge group uniquely determines the interactions and the number of vector gauge bosons that correspond to the generators of the group. They are eight massless gluons, corresponding to the generators of $SU(3)_C$, that mediate strong interactions; Four gauge bosons, of which three are massive ($W^{\pm}$ and Z) and one is massless (γ), corresponding to the three generators of $SU(2)_L$ and one generator of $U(1)_Y$, responsible for electroweak interactions.

As in all gauge theories, the symmetry group of the SM fixes the interactions, i.e. the number and properties of the vector gauge bosons, with only three independent unknown parameters, the three coupling constants of the $SU(3)_C$ $SU(2)_L$ and $U(1)_Y$ groups, all of which must be determined from experiments. On the other hand, the number and properties of scalar bosons and fermions are left unconstrained, except for the fact that they must transform in a definite way under the symmetry group, i.e. they must belong to the representations of the symmetry group, and the fermion representations must lead to the cancellation of quantum anomalies.

A puzzling feature of Nature is the existence of three generations of fermions with identical properties, except for different masses.

The known elementary fermions are divided in two categories, quarks and leptons, according to the scheme:

$$\begin{pmatrix} u \\ d \end{pmatrix} \quad \begin{pmatrix} c \\ s \end{pmatrix} \quad \begin{pmatrix} t \\ b \end{pmatrix}$$

and

$$\begin{pmatrix} \nu_e \\ e \end{pmatrix} \begin{pmatrix} \nu_\mu \\ \mu \end{pmatrix} \begin{pmatrix} \nu_\tau \\ \tau \end{pmatrix}$$

They are distinguished by the fact that quarks participate in all the interactions, whereas leptons participate in all the interactions except strong interactions.

The fermion sector of the SM depends on 13 independent parameters: six quark masses, three charged lepton masses (neutrinos are assumed to be massless in the SM), three quark mixing angles and one phase. The values of all these parameters must be determined from experimental measurements.

The SM is phenomenologically very successfully and so far has been able to describe all the known phenomena, except for the indications in favor of neutrino oscillations that I will discuss in the following sections. In particular, the SM interactions of neutrinos have been verified experimentally with high accuracy and are universally used for the analysis of the data of neutrino experiments.

1.3. Neutrino Induced Reactions

Neutrinos, besides electrons, provide an opportunity to probe the internal structure of composite particle such as proton or neutrons. And neutrino-nucleon scattering also offer one of the most precise tests of the electroweak theory within the non-Abelian gauge group, $SU(2)_L \times U(1)_Y$.

There are two types of neutrino interactions through weak nuclear force: charged-current (CC) and neutral current (NC) weak interactions. In the CC interaction, an incident neutrino interacts with a target nucleon, exchange a W charged boson between the neutrino and a quark in the target nucleon. A charged lepton is emitted, conserving the flavor, and hadronic jets are produced. In the NC interaction, the incident neutrino will exchange a neutral Z boson with the quark.

In neutrino oscillation experiments or in the measurement of its cross section, the emerging lepton in a CC interaction is useful for ascertaining neutrino flux as

the lepton can label each neutrino interaction type because it is charged (thus easily detected). NC interactions are studied primarily to determine the properties of the neutral current force or for the sterile neutrino search. Constraining the NC type interaction is important since it is the main background to the CC type events.

Typically neutrino interactions are divided into three different kinematic regions depending on its hadronic final states: quasi-elastic (QEL), single pion or resonance (RES) and deep inelastic scattering (DIS). QEL interactions dominate at low energy (less than a few GeV) region. In the case of the muon neutrino, it can be written as

$$\nu_\mu + n \rightarrow \mu^- + p \tag{1.4}$$

RES events refer to an interaction where a short term resonant state of the excited target nucleon is created then almost immediately decays. Resonance states are composed of isospin 1/2 N^* and 3/2 Δ excitation states, which generally decay into a nucleon and a pion, as shown in Table 1.1. DIS events are "high energy" processes in terms of the momentum transferred from lepton to hadron vertex with respect to the mass scale of nucleon, $|q|^2 >> m^2$ and produces hadronic jets (thus the name "inelastic"). On average the energy of the incident neutrino is higher than that of QEL and RES and thus causes a rupture of target nucleon.

Since the cross section of QEL and RES interaction are not proportionally increasing as a function of the energy of the incident neutrino, these two together are referred to as non-scaling process, where DIS process is referred to a scaling process.

TABLE 1.1. CC and NC ν_μ-N interaction modes in different energy regime

	CC	NC
QEL	$\nu_\mu + n \rightarrow \mu^- + p$	$\nu_m u + p \rightarrow \nu_\mu + p$
RES	$\nu_\mu + p \rightarrow \mu^- + p + \pi^+$	$\nu_\mu + p \rightarrow \nu_\mu + p + \pi^0$
	$\nu_\mu + n \rightarrow \mu^- + p + \pi^0$	$\nu_\mu + p \rightarrow \nu_\mu + n + \pi^+$
	$\nu_\mu + n \rightarrow \mu^- + n + \pi^+$	$\nu_\mu + n \rightarrow \nu_\mu + n + \pi^0$
		$\nu_\mu + n \rightarrow \nu_\mu + p + \pi^-$
DIS	$\nu_\mu + N \rightarrow \mu^- + X$	$\nu_\mu + N \rightarrow \nu_\mu + X$

1.4. Neutrinos Oscillation Physics

If neutrinos have masses, there will exist a set of mass eigenstates $|\nu_i\rangle (i = 1, 2, 3)$ [Amsler et al., 2008]. The mass eigenstates diagonalise the free Hamiltonian and so describe the evolution of neutrinos in time and space. Interactions with matter, however, are described by the flavor eigenstates, $|\nu_\alpha\rangle (\alpha = e, \mu, \tau)$, which couple to the weak force. The possibility of neutrino mixing means that the flavor and mass eigenstates need not be identical. In general, the flavor eigenstates can be written as a linear superposition of the mass eigenstates:

$$|\nu_\alpha\rangle = \sum_{i=1}^{3} U^*_{\alpha i} |\nu_i\rangle \tag{1.5}$$

where U is the unitary lepton mixing matrix, named the PMNS matrix in recognition of contributions to the physics of mixing and oscillations made by Pontecorvo and Maki, Nakagawa and Sakata.

In a vacuum, the mass eigenstates each propagate as a free particle, so a state $|\nu_i\rangle$ with position four-vector $\mathbf{x}$ and four-momentum $\mathbf{p}_i$ evolves as:

$$|\nu_i(\mathbf{x})\rangle = e^{-i\mathbf{p}_i \cdot \mathbf{x}} |\nu_i\rangle \tag{1.6}$$

A neutrino produced in a flavor eigenstate $|\nu_\alpha\rangle$ will therefore evolve as:

$$|\nu_\alpha(\mathbf{x})\rangle = \sum_{i=1}^{3} e^{-i\mathbf{p}_i \cdot \mathbf{x}} U_{\alpha i} |\nu_i\rangle \tag{1.7}$$

Using the unitarity of the PMNS matrix to invert Equation 1.5 then allows the evolution of the flavor eigenstate to be expressed as:

$$|\nu_\alpha(\mathbf{x})\rangle = \sum_{\beta} \left[\sum_{i} e^{-i\mathbf{p}_i \cdot \mathbf{x}} U_{\alpha i} U^*_{\beta i} \right] |\nu_\beta\rangle \tag{1.8}$$

Assuming that the mass eigenstate components all have the same energy E, and that this energy is much greater than the neutrino masses, the momentum of the $|\nu_i\rangle$

component can be approximated as:

$$p_i = \sqrt{E^2 - m_i^2} \simeq E - m_i^2/2E \tag{1.9}$$

Working in natural units and assuming highly relativistic neutrinos (for which $t \simeq L$), the phase at a distance L from the point of production can then be written as:

$$\mathbf{p} \cdot \mathbf{x} = Et - p_i L \simeq \frac{m_i^2 L}{2E} \tag{1.10}$$

A more rigorous approach, which avoids the assumption of a common energy for the mass eigenstates, has been demonstrated to produce this same result. Substituting for the phase in Equation 1.8 then gives:

$$|\nu_\alpha(\mathbf{x})\rangle = \sum_\beta \left[\sum_i e^{-im_i^2 L/2E} U_{\alpha i} U_{\beta i}^* \right] |\nu_\beta\rangle \tag{1.11}$$

Equation 1.11 demonstrates that, if the neutrino masses are different, the phases of the mass eigenstates will evolve at different rates. If the PMNS matrix has non-zero off-diagonal terms, a neutrino produced in one flavor eigenstate will therefore develop components of other flavor eigenstates and so may be detected as a different flavor.

The probability that a neutrino produced at the origin in flavor eigenstate $|\nu_\alpha\rangle$ is observed at $\mathbf{x}$ in flavor eigenstate $|\nu_\beta\rangle$ is given by:

$$P(\nu_\alpha \to \nu_\beta) = |\langle \nu_\beta | \nu_\alpha(\mathbf{x}) \rangle|^2 \tag{1.12}$$

Using Equation 1.11, this can be evaluated as:

$$\begin{aligned} P(\nu_\alpha \to \nu_\beta) = \delta_{\alpha\beta} \quad &- \quad 4 \sum_{i>j} Re(U_{\alpha i}^* U_{\beta i} U_{\alpha j} U_{\beta j}^*) \sin^2 \left(\frac{\Delta m_{ij}^2 L}{4E} \right) \\ &+ \quad 2 \sum_{i>j} Im(U_{\alpha i}^* U_{\beta i} U_{\alpha j} U_{\beta j}^*) \sin \left(\frac{\Delta m_{ij}^2 L}{2E} \right) \end{aligned} \tag{1.13}$$

where $\delta_{\alpha\beta}$ is the Kronecker's delta and $\Delta m_{ij}^2 = m_i^2 - m_j^2$ is the splitting between the squared masses of the i^{th} and j^{th} mass eigenstates. The transition probability in

Equation 1.13 is periodic with distance from the point of neutrino production. If the mass eigenstates have different masses, then if the flavor and mass eigenstates are not aligned, then neutrinos will oscillate between flavors as they propagate.

Assuming that CPT invariance holds,

$$P(\overline{\nu}_\alpha \to \overline{\nu}_\beta) = P(\nu_\beta \to \nu_\alpha) \tag{1.14}$$

But, from Equation 1.13 we see that

$$P(\nu_\beta \to \nu_\alpha; U) = P(\nu_\alpha \to \nu_\beta; U^*) \tag{1.15}$$

Thus, when CPT holds,

$$P(\overline{\nu}_\alpha \to \overline{\nu}_\beta; U) = P(\nu_\alpha \to \nu_\beta; U^*) \tag{1.16}$$

That is, the probability for oscillation of an antineutrino is the same as that for a neutrino, except that the mixing matrix U is replaced by its complex conjugate. Thus, if U is not real, the neutrino and antineutrino oscillation probabilities can differ by having opposite values of the last term in Equation 1.13. When CPT holds, any difference between these probabilities indicates a violation of CP invariance.

Neutrino oscillation experiments attempt to measure changes in the flavor composition of neutrino sources over long distances. If oscillations occur, the signature is a flavor composition that differs from the Standard Model prediction and which displays periodic variations with L/E. The period of the oscillations specifies the mass splittings, whilst the amplitude of the oscillations specifies the mixing angles.

To interpret the data from neutrino oscillation experiments, it is useful to use a specific representation of the PMNS matrix. The standard representation is obtained by expressing U as a product of three rotation matrices based on the mixing angles

between the mass eigenstates (θ_{12},θ_{23} and θ_{13}) and a complex phase factor ($e^{i\delta}$):

$$\begin{aligned} U &= \begin{pmatrix} 1 & 0 & 0 \\ 0 & c_{23} & s_{23} \\ 0 & -s_{23} & c_{23} \end{pmatrix} \begin{pmatrix} c_{13} & 0 & s_{13}e^{-i\delta} \\ 0 & 1 & 0 \\ -s_{13}e^{i\delta} & 0 & c_{13} \end{pmatrix} \begin{pmatrix} c_{12} & s_{12} & 0 \\ -s_{12} & c_{12} & 0 \\ 0 & 0 & 1 \end{pmatrix} \begin{pmatrix} e^{i\alpha_1/2} & 0 & 0 \\ 0 & e^{i\alpha_2/2} & 0 \\ 0 & 0 & 1 \end{pmatrix} \\ &= \begin{pmatrix} c_{12}c_{13} & s_{12}c_{13} & s_{13}e^{-i\delta} \\ -s_{12}c_{23} - c_{12}s_{23}s_{13}e^{-i\delta} & c_{12}c_{23} - s_{12}s_{23}s_{13}e^{i\delta} & s_{23}c_{13} \\ s_{12}s_{23} - c_{12}c_{23}s_{13}e^{i\delta} & -c_{12}s_{23} - s_{12}c_{23}s_{13}e^{i\delta} & c_{23}c_{13} \end{pmatrix} \begin{pmatrix} e^{i\alpha_1/2} & 0 & 0 \\ 0 & e^{i\alpha_2/2} & 0 \\ 0 & 0 & 1 \end{pmatrix} \end{aligned} \quad (1.17)$$

Here, $c_{ij} \equiv \cos\theta_{ij}$ and $s_{ij} \equiv \sin\theta_{ij}$, where θ_{12}, θ_{13}, and θ_{23} are the three mixing angles, and δ, α_1 and α_2 are the three CP-violating phases. The phase δ is referred to as a Dirac phase where the phases α_1 and α_2 are known as Majorana phases. This matrix is sometimes referred to as the Maki-Nakagawa-Sakata matrix, or as the Pontecorvo-Maki-Nakagawa-Sakata(PMNS) matrix, in recognition of the pioneering contributions of these physicists to the physics of mixing and oscillation [Maki et al., 1962, Pontecorvo, 1968].

An important special case is the case where only two different neutrinos are important. The two-neutrino approximation is a fairly accurate description of a number of experiments. Suppose that only two mass eigenstates, which we shall call ν_1 and ν_2, and two corresponding flavor states, which we shall call ν_α and ν_β are significant. The phase factors can be shown to have no effect on oscillations. The mixing matrix U takes the simple form

$$U = \begin{pmatrix} \cos\theta & \sin\theta \\ -\sin\theta & \cos\theta \end{pmatrix} \quad (1.18)$$

For $\beta \neq \alpha$, the neutrino oscillation probability is

$$P(\nu_\alpha \to \nu_\beta) = \sin^2 2\theta \sin^2(\Delta m^2 \frac{L}{4E}) \quad (1.19)$$

$\Delta m^2 \equiv m_1^2 - m_2^2$. In addition, the probability that the neutrino does not change flavor is, as usual, unity minus the probability that it does change flavor.

If neutrinos pass through enough matter between their source and a target detector, then their coherent forward scattering from particles in the matter can significantly modify their oscillation pattern. Flavor change in matter that grows out of an interplay between flavor-nonchanging neutrino-matter interactions and neutrino mass and mixing is known as the Mikheyev-Smirnov-Wolfenstein(MSW) effect [Wolfenstein, 1978, Mikheev and Smirnov, 1985, 1986].

Matter is composed of nucleons (or quarks) and electrons. The contribution of nucleons (or quarks) to the forward scattering amplitude is described by the neutral current (Z^0 exchange); it is identical for all neutrino flavors thus it has no effect on the neutrino oscillations. For electrons the situation is different; the electron neutrinos interact with electrons via both the neutral current and the charged-current (W^+ exchange). All other neutrino flavors interact only via the neutral current, so their interaction is different in magnitude than that of the electron neutrinos. Coherent forward scattering by electrons via W exchange gives rise to an extra interaction potential energy V possessed by electron neutrinos in matter. From the Standard Model, we find that

$$V = +\sqrt{2}G_F N_E \tag{1.20}$$

where G_F is the Fermi coupling constant and N_e is the number of electrons per unit volume. This interaction potential energy changes sign if we replace the ν_e in the beam by $\overline{\nu}_e$. This potential gives rise to an effective mixing and mass matrix. The MSW effect has a significant impact on the oscillations of solar neutrinos. Electron neutrinos produced in the core of the sun leave it's surface as almost pure mass eigenstate ν_2. This is an effect of neutrino adiabatic propagation through the high electron density in the sun. Also there will be an asymmetry between antineutrino oscillation and neutrino oscillation that is induced by matter effects. This asymmetry has nothing to do with genuine CP violation, and will have to be disentangled from the antineutrino-neutrino asymmetry that does come from genuine CP violation in order for us to be able to study the latter phenomenon. This antineutrino-neutrino

asymmetry coming from matter effects can be utilized to understand the neutrino mass hierarchy.

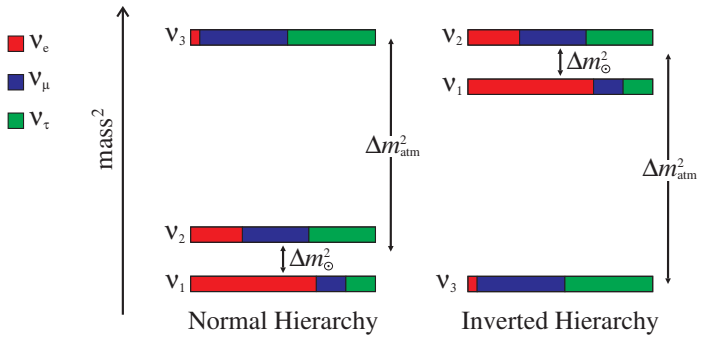

FIGURE 1.1. The Two possible mass hierarchies for the three known neutrino flavors.

Figure 1.1 shows graphically what we have learned so far about the neutrino masses from neutrino oscillation experiments. The overall mass scale is still unknown, but the lightest neutrino is constrained by tritium beta decay measurements to be less than about 2.2 eV. The solar neutrino experiment and the KamLAND reactor experiment measure the squared mass difference between the 1 and 2 mass eigenstates to be $(7.0 - 9.1) \times 10^{-5}\,\mathrm{eV}^2$. The atmospheric neutrino measurements and long baseline experiments constrain the squared mass difference between the 2 and 3 mass eigenstates to be $(1.9 - 2.98) \times 10^{-3}\,\mathrm{eV}^2$. Both are 3σ ranges. It is not determined, however, whether the mass of ν_3 is larger or smaller than ν_1 and ν_2 masses. These two scenarios are referred to as the normal hierarchy and inverted hierarchy respectively.

1.5. NEUTRINO OSCILLATION EXPERIMENTS

Neutrino oscillation experiments are divided into:

(1) **Appearance experiments.** These experiments measure transitions between different neutrino flavors. If the final flavor to be searched for in the detector is not present in the initial beam, the background can be very small. In this case, an experiment can be sensitive to rather small values of the mixing angle.

(2) **Disappearance experiments.** These experiments measure the survival probability of a neutrino flavor by counting the number of interactions in the detector and comparing it with the expected one. Since, even in the absence of oscillations, the number of detected events has statistical fluctuations, it is very difficult to reveal a small disappearance. Therefore, in this type of experiment, it is hard to measure small values of the mixing angle.

In the simplest case of two-neutrino mixing, an important characteristic of neutrino oscillations is that the transitions to different flavors cannot be measured if

$$\frac{\Delta m^2 L}{2E} \ll 1 \tag{1.21}$$

On the other hand, for

$$\frac{\Delta m^2 L}{2E} \gg 1 \tag{1.22}$$

only the average transition probability is observable, yielding information only on $\sin^2(2\theta)$.

Since the value of Δm^2 is fixed by nature, different experiments can be designed in order to be sensitive to different values of Δm^2, by choosing appropriate values of the ratio L/E. The so-called sensitivity to Δm^2 of an experiment is the value of Δm^2 for which

$$\frac{\Delta m^2 L}{2E} \sim 1 \tag{1.23}$$

Different types of neutrino oscillation experiments are traditionally classified depending on the average value of the ratio of L/E for an experiment, which determines its sensitivity to Δm^2.

1.5.1. Solar Neutrino Experiments – 12 Sector. Solar neutrinos have been providing a rather unique channel for physicists to precisely measure the mixing angle θ_{12} and the squared mass difference Δm^2_{12} between ν_2 and ν_1. There are two types of experiment that have probed this sector: solar neutrino measurements and long baseline anti-neutrino experiments.

The solar neutrino spectrum is essentially a sum of standard beta decay spectra from $p+p \rightarrow De^{+}\nu_e$, $^{8}B \rightarrow 2\alpha+e^{+}+\nu_e$, $^{13}N \rightarrow^{13} C+e^{+}+\nu_e$ and $^{15}O \rightarrow^{15} N+e^{+}+\nu_e$ and "lines" from the electron capture process $e+^{7}Be \rightarrow \nu_e+^{7}Li$ and $p+e+p \rightarrow D+\nu_e$ assuming that about 98% of solar energy is created through thermonuclear reaction of the *pp* chain and the remaining 2% by the CNO cycle. The relative contributions from those various channels depend on the chemical composition of the sun and its temperature and density variation, a model can be constructed to predict the neutrino fluxes.

For more than twenty years, the Homestake Solar Neutrino Experiment in the Homestake Gold Mine in South Dakota has been attempting to measure neutrino fluxes from space; in particular, this experiment has been gathering information on solar neutrino fluxes. The results of this experiment have been checked against predictions made by standard solar models and it has been discovered that only one-third of the expected solar neutrino flux has been detected [Cleveland et al., 1998]. This discrepancy is known as the "Solar Neutrino Problem". Several other experiments, including Kamiokande II [Hirata et al., 1989], Super-Kamiokande [Hosaka et al., 2006], GALLEX [Anselmann et al., 1992], SAGE [Abdurashitov et al., 1994], and GNO [Altmann et al., 2005], have noticed a definite neutrino shortfall. The measurements of solar neutrinos culminated in the Sudbury Neutrino Observatory (SNO) which used the deuterium in heavy water as a target for solar neutrinos. This enabled a measurement of both the electron neutrino flux through charged-current interactions and the flux of all active neutrino flavors through Neutral Current interactions. Figure 1.2 summarizes the set of measurements from SNO [Aharmim et al., 2005]. It plots the measured flux of electron neutrinos against the measured flux of muon and tau neutrinos. SNO finds that

$$\frac{\phi(\nu_e)}{\phi(\nu_e)+\phi(\nu_{\mu,\tau})} = 0.340 \pm 0.023\ (\text{stat})^{+0.029}_{-0.031}\ (\text{syst}). \tag{1.24}$$

The conclusion is that the electron flavor are oscillating into muon or tau neutrinos. The SNO measurement directly demonstrated neutrino oscillations in solar neutrinos. The results of the SNO experiment put the "Solar Neutrino Problem" to rest and, along with the KamLAND reactor neutrino experiment, enable precision measurement of the 12 Sector parameters.

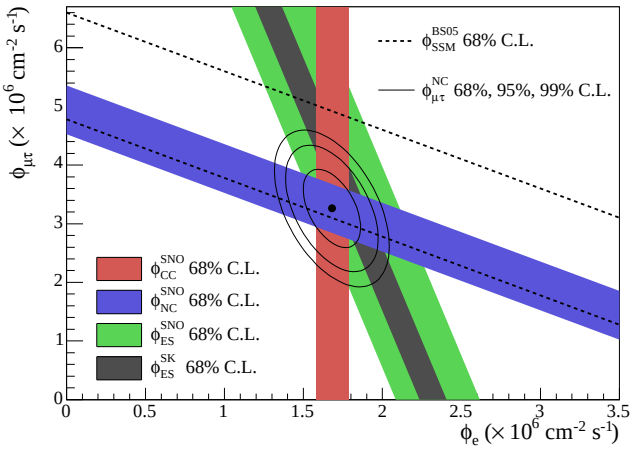

FIGURE 1.2. The SNO results expressed as a measurement of the flux $\mu+\tau$ neutrinos versus the flux of ν_e. The SNO measurements of CC, NC and ES neutrino interactions and the SK measurement of ES neutrino interactions are indicated by the filled bands, while the flux predicted by the SSM is indicated by the dotted lines. The $\pm 1\sigma$ uncertainties are represented by the intercepts on the axes [Aharmim et al., 2005].

Neutrinos are also created in the nuclear power plant through the nuclear fission process. Neutrinos created in the reactors has narrow energy spectrum and are rather "clean" in the sense that the contamination from other neutrino flavors is extremely small compare to that from other sources such as solar and atmospheric neutrinos. As I mentioned in Section 1.1, the discovery of the neutrino was made by a reactor experiment.

Fission reactors produce neutrinos at a rate of about 10^{20} $\overline{\nu}_e$ per second per nuclear core. Most neutrinos were created in the fission process of ^{235}U and ^{238}U. Contributions from ^{239}Pu and ^{241}PU increase as a typical nuclear cycle goes on.

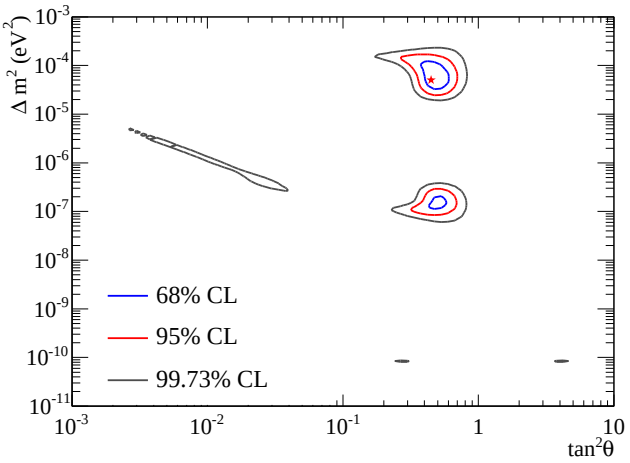

FIGURE 1.3. The Confidence limits for the oscillation parameters Δm^2_{12} and θ_{12} obtained from and analysis of results from the second phase of the SNO experiment. The best fit point is indicated by a star [Aharmim et al., 2005].

The KamLAND experiment is a reactor neutrino experiment which use a 1 kiloton liquid scintillator detector located in the Kamioka mine in central Japan. Most of the $\overline{\nu}_e$ flux incident at KamLAND comes from nuclear plants at distance of 80-350 km from the detector, making average baseline of about 180 km. By measuring reactor $\overline{\nu}_e$'s, this experiment provided a sensitive probe of the solar neutrino oscillations. The survival probability of electron neutrinos is

$$P(\overline{\nu}_e \to \overline{\nu}_e) \approx 1 - \sin^2 2\theta_{12} \sin^2(1.27\Delta m^2_{12} L/E) \tag{1.25}$$

The KamLAND collaboration has for the first time measured the disappearance of neutrino traveling to a detector from a power reactor. They observe a strong evidence for the disappearance of neutrinos during their flight over such distances, giving the first terrestrial confirmation of the solar neutrino anomaly and also establishing the oscillation hypothesis with man-produced neutrinos. Figure 1.5 shows the combined result of the KamLAND measurement and the solar neutrino experiments [Araki et al., 2005]. The combined analysis gives the 1σ range [Aharmim et al., 2005]:

$$\Delta m^2_{solar} = 8.0^{+0.4}_{-0.3} \times 10^{-5}\ \text{eV}^2, \quad \theta_{solar} = 33.9^{+1.6}_{-1.6}\ \text{degrees} \tag{1.26}$$

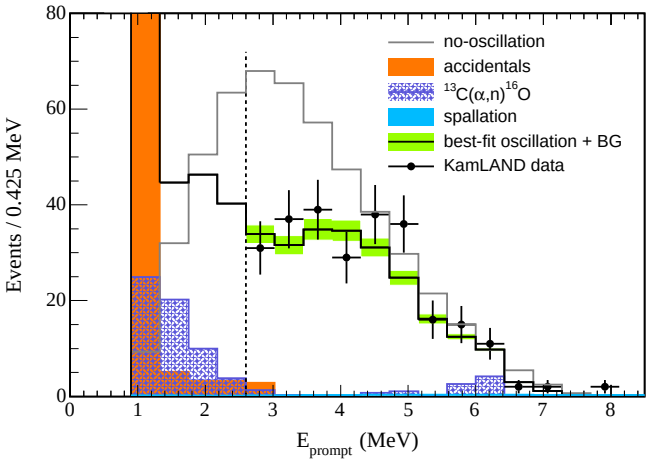

FIGURE 1.4. Energy spectrum of prompt e^+ from $\overline{\nu}_e$ interactions detected by KamLAND. There is a significant deficit in the measured spectrum relative to the no-oscillation expectation [Araki et al., 2005].

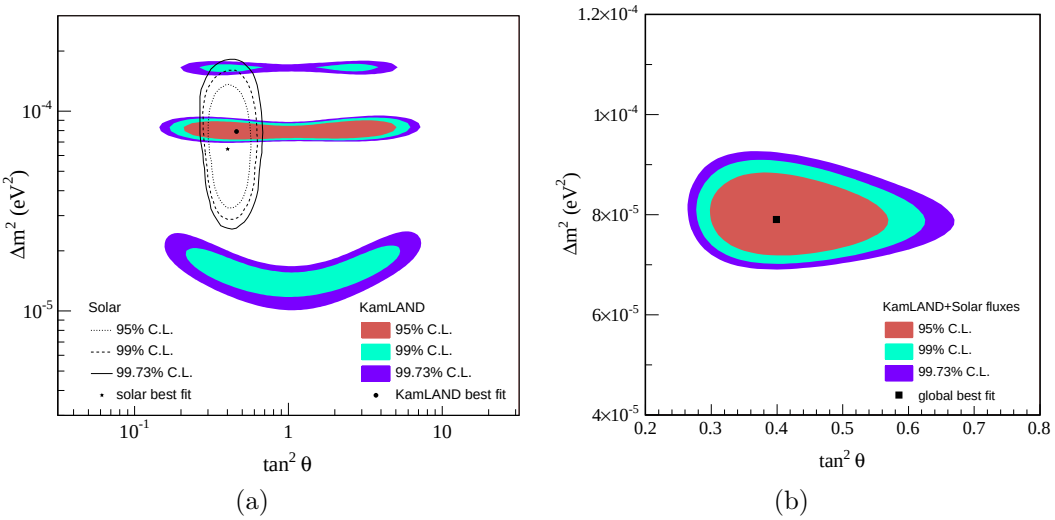

(a) (b)

FIGURE 1.5. (a) Neutrino oscillation parameter allowed region from KamLAND antineutrino data (shaded regions) and solar neutrino experiment (lines). (b) Result of a combined two-neutrino oscillation analysis of KamLAND and the observed solar neutrino fluxes under the assumption of CPT invariance [Araki et al., 2005].

1.5.2. Atmospheric Neutrino Experiments – 23 Sector. The 23 Sector of neutrino mixing matrix comprises the angle θ_{23} and the squared mass difference Δm^2_{32} between ν_3 and ν_2. There are two types of experiments that are sensitive to those oscillation parameters: experiments measuring the neutrinos produced when cosmic

rays hit the atmosphere and experiments located several hundred kilometers from an accelerator source of muon neutrinos.

Atmospheric neutrinos are produced in the collision of primary cosmic ray (typically protons) with nuclei in the upper atmosphere. This creates a shower of hadrons, mostly pions. The pions decay to a muon and a muon neutrino. The muons decay to an electron, another muon neutrino (actually anti muon neutrino), and an electron neutrino. Based on this simple kinematic chain, one predicts a flux ratio of 2:1 muon neutrinos to electron neutrinos.

In 1985, two experiments in deep mines, one in the United States called IMB and one in Japan called Kamiokande, observed a deficit in the number of muon neutrinos created in the atmosphere with respect to the number of electron neutrinos. This deficit became known as the "Atmospheric Neutrino Anomaly". Since then, several experiments measured the ratio of muon-like neutrino events to electron-like neutrino events, divided by their respective Monte Carlo simulation value

$$R' = \frac{(\nu_\mu/\nu_e)_{data}}{(\nu_\mu/\nu_e)_{MC}} \tag{1.27}$$

Their results are summarized in Figure 1.6. The Kamiokande, IMB and Super-Kamiokande experiments are based on the water Cerenkov technique, while FREJUS, NUSEX and SOUDAN are ionisation-based tracking detectors. The ratios are consistently below 1 except for FREJUS and NUSEX which had large error bars.

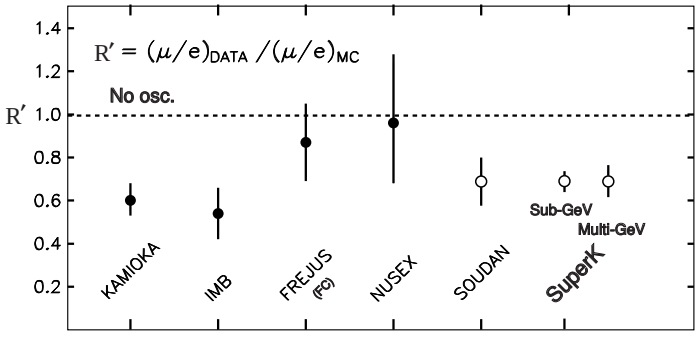

FIGURE 1.6. The atmospheric neutrino anomaly: The ratio of muon-like neutrino events to electron-like neutrino events, divided by their respective Monte Carlo simulation value [Mann, 1999].

In 1996, Super-Kamiokande (Super-K) was completed and began taking data. Super-K is a 50 kiloton ring-imaging water Cerenkov detector located at a depth of 2700 meters water equivalent in the Kamioka Mozumi mine in Japan. It supersedes its predecessors (IMB and Kamiokande) both in size and resolution and began detecting atmospheric neutrinos at much higher rates. In 1998, after analyzing more than 500 days of data, the experimentalists at Super-K announced that the atmospheric neutrino anomaly was not a statistical aberration and is consistent with two-flavor neutrino oscillations in 23 Sector [Fukuda et al., 1994]:

$$P(\nu_\mu \to \nu_\mu) \approx 1 - \sin^2 2\theta_{23} \sin^2(1.27\Delta m^2_{32} L/E_\nu) \tag{1.28}$$

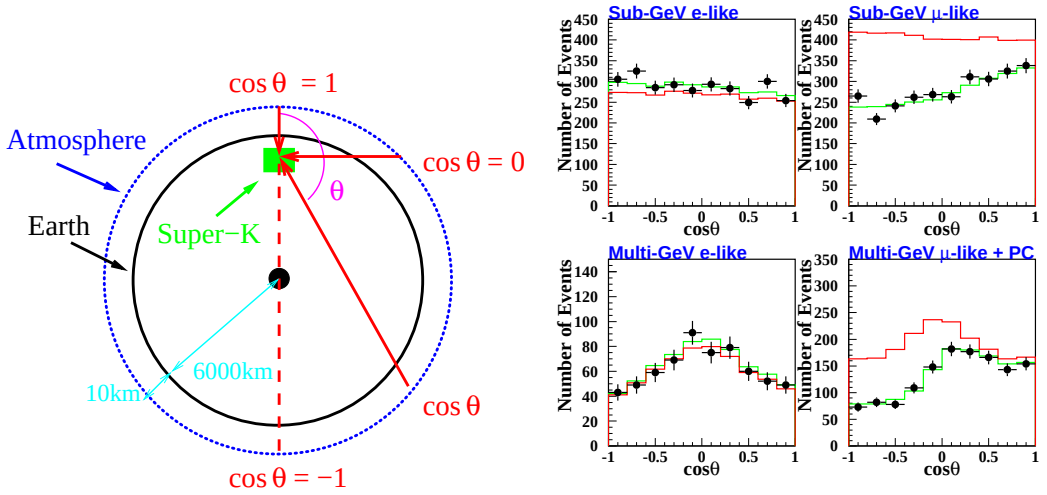

(a) A sketch plot shows atmospheric neutrino zenith angle [Howcroft]

(b) SuperK atmospheric neutrino zenith angle distributions of μ-like and e-like events for sub-GeV and multi-GeV data sets. [Scholberg, 1999]

FIGURE 1.7. SuperK atmospheric neutrino oscillation results.

Super-K measured the zenith angle distributions of μ-like and e-like events. Figure 1.7(a) shows the relation between zenith angle and the distance traveled by atmospheric neutrinos. Figure 1.7(b) shows the zenith angle distribution of μ-like and e-like events for sub-GeV and multi-GeV data sets. Upward-going particles have $\cos\Theta < 0$ and downward-going particles have $\cos\Theta > 0$. The conclusion is that the

deficit in muon neutrinos is mostly due to the upward traveling ones. Oscillations easily explain this: the muon neutrinos raining down on the mine do not have sufficient time to oscillate while those traveling through the Earth do. Detailed Super-K atmospheric neutrino data are very well described by the hypothesis that the oscillation is purely $\nu_\mu \to \nu_\tau$, and that is a quasi-two neutrino oscillation with a splitting Δm^2_{atm} and a mixing angle θ_{atm} that, at 90% CL, are in the ranges [Ashie et al., 2005]

$$\sin^2 2\theta_{atm} > 0.92 \text{ and } 1.5 \times 10^{-3} < \Delta m^2_{atm} < 3.4 \times 10^{-3}\,\text{eV}^2$$

In the three-flavor neutrino mixing, $\theta_{atm} \approx \theta_{23}$ and $\Delta m^2_{atm} \approx |\Delta m^2_{32}|$. For θ_{23} there is an ambiguity corresponding to $\theta_{23} \leftrightarrow \pi/2 - \theta_{23}$. Matter effects in future long-baseline experiments will resolve this. The often used parameter $\sin^2(2\theta_{23})$ is blind to the ambiguity.

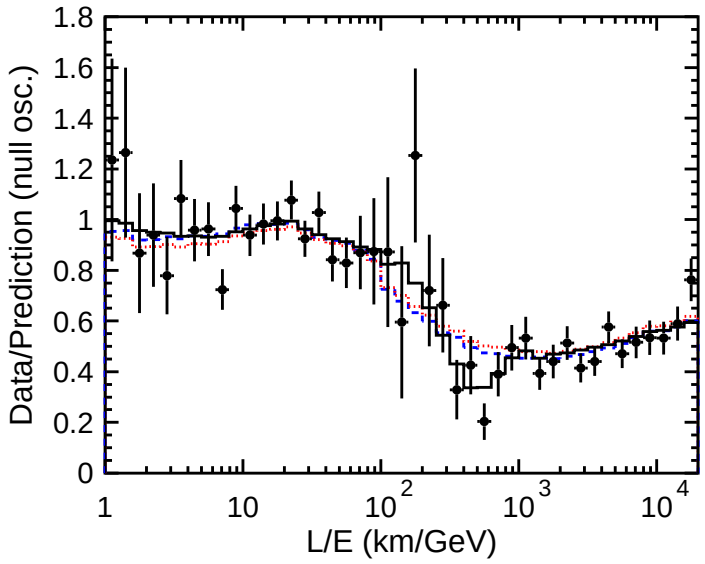

FIGURE 1.8. Ratio of the data to the MC events without neutrino oscillation (points) as a function of the reconstructed L/E together with the best-fit expectation for 2-flavor $\nu_\mu \to \nu_\tau$ oscillations (solid line). Also shown are the best-fit expectation for neutrino decay (dashed line) and neutrino decoherence (dotted line) [Ashie et al., 2004].

In 2004, the Super-K collaboration presented a new analysis of their data where they used a selected sample of events with good resolution in L/E [Ashie et al., 2004]. A dip in the L/E distribution was observed around $L/E = 500\,\text{km/GeV}$, as

shown in Figure 1.8. This provided the first direct evidence that the neutrino survival probability obeys the sinusoidal function as predicted by neutrino flavor oscillations. The 90% CL allowed parameter region was obtained as

$$\sin^2 2\theta_{atm} > 0.90 \text{ and } 1.9 \times 10^{-3} < \Delta m^2_{atm} < 3.0 \times 10^{-3}\,\text{eV}^2$$

This result is consistent with that of the oscillation analysis using zenith angle distributions.

The oscillation interpretation of the atmospheric neutrino data has received support from the KEK and Kamioka (K2K) long-baseline experiment. This experiment produces a beam of muon neutrinos with mean energy $\sim 1.3\,\text{GeV}$ at KEK accelerator laboratory. These neutrinos are aimed at the Super-K detector in Kamioka, 250 km away. The K2K experiment reported that after achieving 8.9×10^{19} proton-on-target (about four and a half years) the expected number of events occurring in the fiducial volume of Super-K detector is 151^{+12}_{-10} (syst.). However, only 107 events were observed [Aliu et al., 2005]. In addition, the spectrum of ν_μ events observed in Super-K detector was distorted relative to the no-oscillation spectrum. The anomalously small number of events and spectral distortion seen by K2K experiment are consistent with a neutrino oscillation interpretation, with parameters Δm^2_{atm} and θ_{atm} compatible with those that fit the atmospheric neutrino data.

MINOS is a long baseline neutrino experiment launched in 1995 to study the $\nu_\mu \to \nu_\tau$ oscillation. It mainly aims to improve the measurements of Δm^2_{23} performed by SuperK and K2K experiments. It uses a beam of neutrino particles produced by the NuMI beamline facility at Fermilab. The neutrino beam is directed towards Soudan Mine at Minnesota, a distance of 735 km away. The value of the oscillation parameters are $|\Delta m^2_{23}| = (2.43 \pm 0.13) \times 10^{-3}\,\text{eV}^2$ and $\sin^2(2\theta_{23}) > 0.95$ at the 68% C.L. [Adamson et al., 2008b], as shown in Figure 1.10.

1.5.3. The 13 Sector. The 13 Sector comprises the mixing angle θ_{13} and the phase δ which, if different from 0 or π, would induce CP violation into the scheme

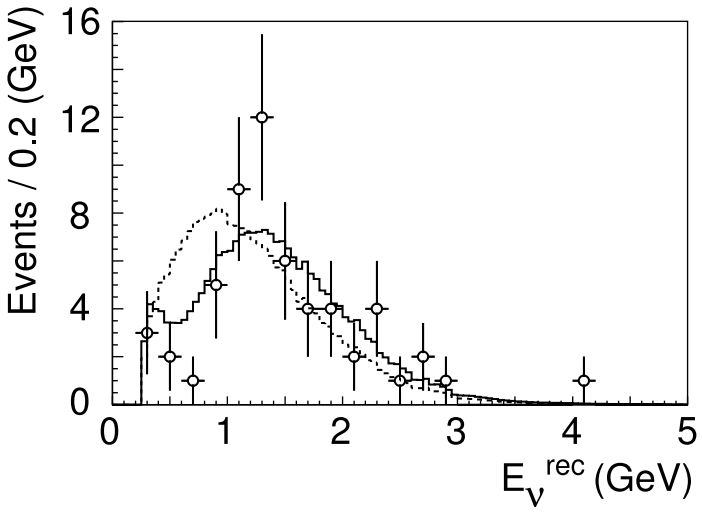

FIGURE 1.9. The reconstructed energy spectrum of ν_μ CC events measured by K2K. The data is represented by the points, the zero oscillation spectrum by the dotted line, and the best fit oscillations by the solid line [Aliu et al., 2005].

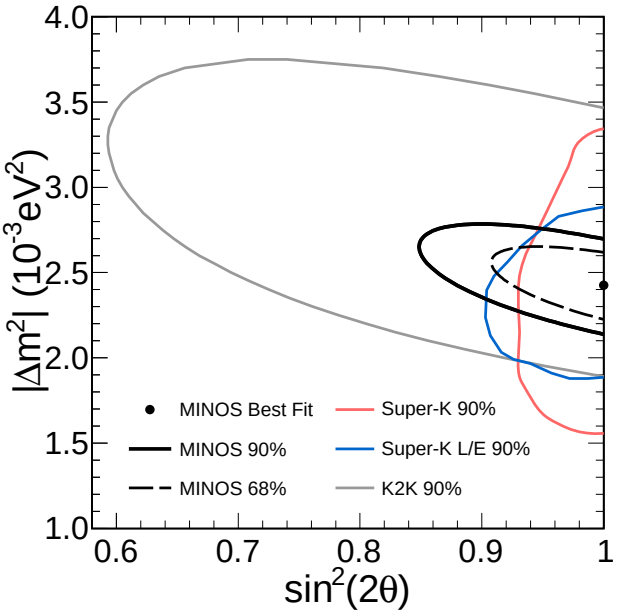

FIGURE 1.10. MINOS allowed region for $\nu_\mu \to \nu_\tau$ oscillation [Adamson et al., 2008b].

of neutrino oscillations. Note the squared mass difference Δm^2_{31} between ν_3 and ν_1 is not an independent parameter and $\Delta m^2_{31} = m^2_3 - m^2_1 = \Delta m^2_{32} + \Delta m^2_{21} \simeq \Delta m^2_{32}$ since $|\Delta m^2_{21}| \ll |\Delta m^2_{32}|$. Another issue that is often discussed in the context of the 13

Sector is the mass hierarchy which is the question of whether the masses are ordered with the almost degenerate double ν_1 and ν_2 higher or lower than the ν_3 mass. This is so far the least understood Sector. There are no constraints of any significance on δ and the mass hierarchy is unknown.

If we measure the disappearance of reactor anti-neutrinos at a baseline L of $\sim 1\,\mathrm{km}$ one can match the L/E to Δm^2_{31} and be sensitive to the parameters of the 13 Sector. The expression for the electron anti-neutrino survival probability is then

$$P(\overline{\nu}_e \to \overline{\nu}_e) \approx 1 - \sin^2 2\theta_{13} \sin^2(1.27\Delta m^2_{31} L/E_\nu) \tag{1.29}$$

The best reactor experiment measurement to date is the CHOOZ experiment that operated in France in the 1990's. The CHOOZ experiment detected electron anti-neutrino with a liquid scintillation calorimeter located 1.05 km from the reactor core. They found no evidence for neutrino oscillations in the $\overline{\nu}_e$ disappearance mode. If Δm^2 takes the current MINOS best fit point $2.4 \times 10^{-3}\,\mathrm{eV}^2$, the constraint on θ_{13} from CHOOZ is $\sin^2\theta_{13} \lesssim 0.15$ at 90% CL. Another measurement of the 13 Sector is the Palo Verde experiment operated in Arizona, USA [Boehm et al., 2001]. This experiment measured the anti-neutrino flux and spectrum at a distance of about 800 m from the three reactors of the Palo Verde Nuclear Generating Station using a segmented gadolinium-loaded scintillation detector. They excluded at 90% CL $\overline{\nu}_e \to \overline{\nu}_x$ oscillations. They posed a constraint on the parameter θ_{13}. Figure 1.11 shows the 90% CL exclusion region for the CHOOZ experiment and the Palo Verde experiment.

It has been reported that the solar and KamLAND data provide a non-trivial constraint on θ_{13} especially for lower value of Δm^2_{atm} [Maltoni et al., 2003, 2004, Goswami and Smirnov, 2005]. Figure 1.12 shows the current constraints on the 13 Sector mixing parameters from global data. The CHOOZ bound on $\sin^2\theta_{13}$ gets quickly weak when Δm^2_{atm} decreases. Such loosening in sensitivity is presented to

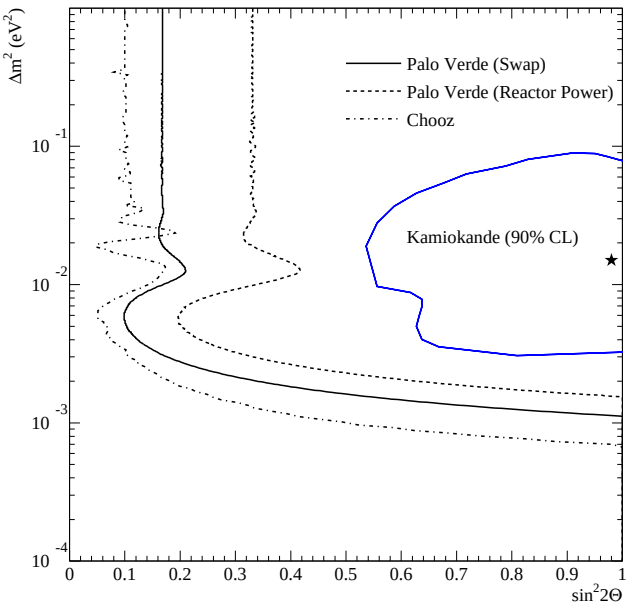

FIGURE 1.11. The 90% CL exclusion regions for the CHOOZ experiment and the Palo Verde experiment [Boehm et al., 2001].

some extent by solar neutrino and KamLAND data. The constraint on θ_{13} from global data is $\sin^2 2\theta_{13} \lesssim 0.11$ [Schwetz, 2008].

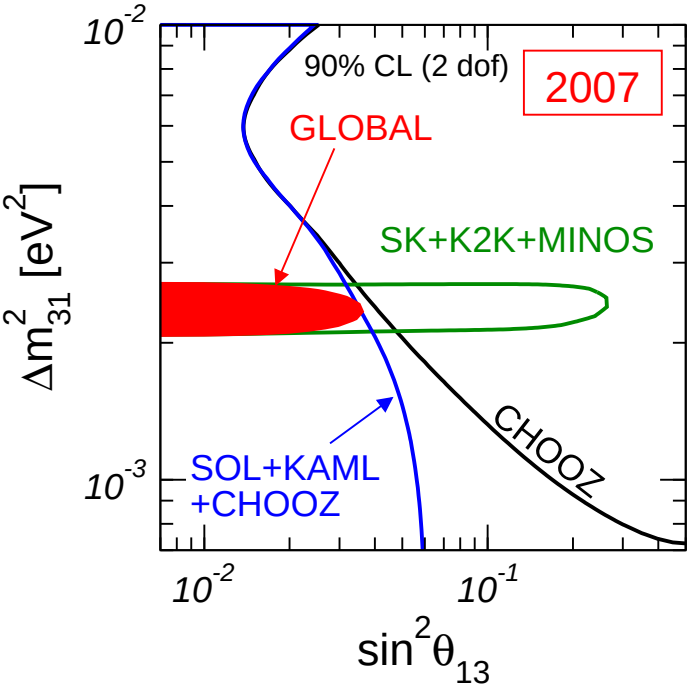

FIGURE 1.12. Current state of knowledge of the 13 Sector [Schwetz, 2008].

A new generation of reactor experiments is being constructed in the hope of improving on the CHOOZ measurement and further constraining the value of θ_{13}, either limiting it to be even closer to zero or measuring a non-zero value for it. These new experiments hope to be sensitive to a value of $\sin^2 2\theta_{13}$ as small as 0.01. To do this they are making several upgrades to the CHOOZ approach. Most importantly they are using multiple detectors to cancel systematics. These detectors will be larger, be located at very high flux reactors, and be exposed to the beam for longer. They will be underground to reduce the effect of cosmic ray muon and be thoroughly calibrated. The main contenders in this next round are Double CHOOZ [Ardellier et al., 2006], located at the same place as the original CHOOZ experiment, the Daya Bay experiment located in China [Guo et al., 2007], the Angra experiment located in Brazil [Anjos et al., 2006], and the RENO experiment located in South Korea [Joo, 2007].

Accelerator based neutrino experiments are important approaches to probe the 13 Sector by looking for the sub-dominant $\nu_\mu \to \nu_e$ oscillation at values of L/E matched to Δm^2_{31}. If we ignore the matter effect, solar terms, and CP violation phase, the oscillation probability is

$$P(\nu_\mu \to \nu_e) \approx \sin^2\theta_{23} \sin^2 2\theta_{13} \sin^2(1.27\Delta m^2_{31} L/E_\nu) \tag{1.30}$$

Unlike the $\overline{\nu}_e$ survival probability in Equation 1.25, the ν_e appearance probability in Equation 1.30 depends not only on the parameter θ_{13}, but also the parameter θ_{23}. Thus measuring θ_{13} by searching for $\nu_\mu \to \nu_e$ appearance relies on a good understanding of mixing angle θ_{23}. The MINOS experiment is designed to probe 23 Sector by measuring the disappearance of ν_μ events. MINOS also improves the current best limit on the neutrino mixing angle θ_{13} by searching for an electron neutrino appearance signal in the Far Detector from the ν_μ neutrino beam. MINOS recently released the latest measurement of θ_{13} based on 7×10^{20} protons on target (POT). Total 54 events are observed in the Far Detector, which is 0.7σ higher than the expected background of $49.1 \pm 7.0(\text{stat.}) \pm 2.7(\text{syst.})$. Interpreted as an upper limit on the probability

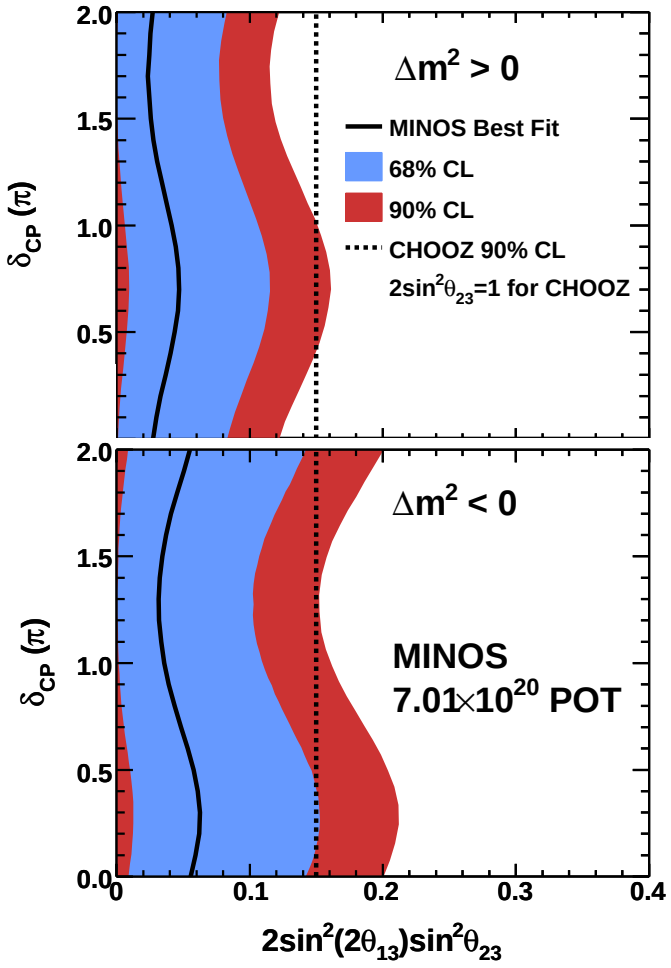

FIGURE 1.13. Values of $2\sin^2(2\theta_{13})\sin^2\theta_{23}$ and δ_{CP} that consistent with the MINOS observation for the normal hierarchy (top) and inverted hierarchy (bottom). Black lines show those values that best represent the data. Red (blue) regions show the 90% (68%) C.L. intervals. The CHOOZ limit is draw for $\Delta m^2_{32} = 2.43 \times 10^{-3}\,\mathrm{eV}^2$, and $\sin^2(2\theta_{23}) = 1.0$ [Adamson et al.]

of $\nu_\mu \to \nu_e$ oscillations, the MINOS data require $2\sin^2(2\theta_{13})\sin^2\theta_{23} < 0.12(0.20)$ at the 90% C.L. at $\delta_{CP} = 0$ for normal (inverted) hierarchy as in Figure 1.13.

A second generation of long baseline accelerator neutrino oscillation experiment has been proposed. They hope to extend the sensitivity for ν_e appearance roughly a factor of 10-20 beyond the CHOOZ limit. The matter effects induced by long baseline increase the potential to search for CP-violating phase δ and resolve mass hierarchy in the neutrino sector. These experiments will make use of an off-axis

beam. By placing the detector slightly off the neutrino beam axis (e.g. 15 mrad), the detector will see a narrow band beam peaking at low energy (e.g. 2 GeV). Because the backgrounds (intrinsic ν_e and neutral current events) in the ν_e appearance search are much broader in energy than the signal, a narrow beam will allow a much better signal to background ratio than for the MINOS measurement. Other highlights of these experiments include improved beam intensity, large detectors optimized for ν_e detection, and using two detectors to cancel systematics. There are two long baseline experiments under construction that will probe the 13 Sector, first by searching for a non-zero θ_{13} and if one is found then determine the mass hierarchy and searching for CP violation. The two experiments are NOνA [Ayres et al., 2004] and T2K [Itow et al., 2001]. NOνA will use the same beam line currently used by MINOS, with a new detector being built 810 km away in northern Minnesota. T2K use the existing Super-K detector and the beam are sent from the JPARC accelerator lab about 250 km away.

1.5.4. The LSND Result and MiniBooNE. The Liquid Scintillator Neutrino Detector (LSND) experiment [Aguilar et al., 2001] operated at Los Alamos National Lab in the 1990's and produced evidence for $\overline{\nu}_\mu \to \overline{\nu}_e$ oscillations at the $\Delta m^2 \sim 1\,\mathrm{eV}^2$ scale. This Δm^2 scale is incompatible with those of the solar and atmospheric oscillations, and so requires there be more than 3 neutrinos if all three are to be interpreted as evidence of neutrino oscillation. The Mini-Booster Neutrino Experiment (MiniBooNE) was built to test the oscillation interpretation of the LSND result. The detector is located 540 m from the target and comprises a spherical tank filled with 800 tons of pure mineral oil (CH_2). This experiment can distinguish electrons from other particles (in particular π^0's) and so test for $\nu_\mu \to \nu_e$ oscillations. In April 2007 the experiment released its first result [Aguilar-Arevalo et al., 2007]. The experiment found no evidence of neutrino oscillations in its analysis region above a neutrino energy of 475 MeV, though there was a excess of events found below this energy and this is currently under investigation. The exclusion plot that summarizes

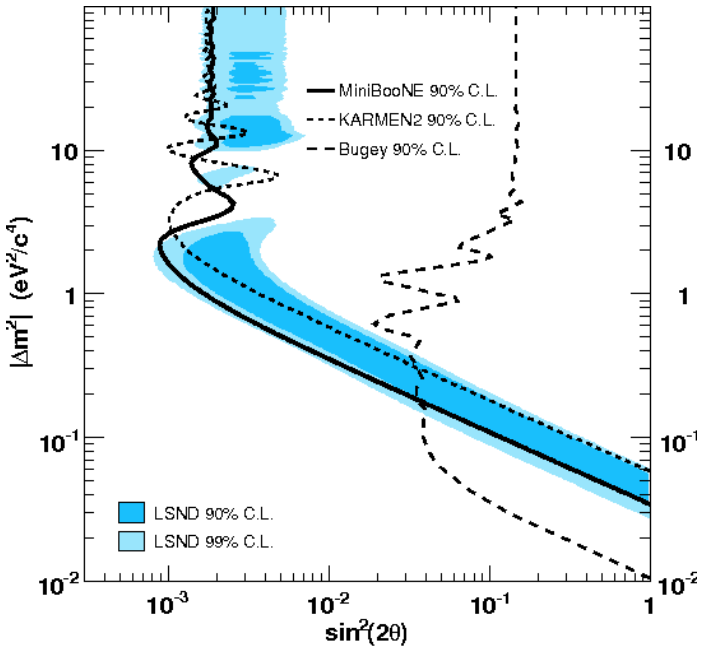

FIGURE 1.14. The region of oscillation parameter space excluded at 90% CL by the MiniBooNE result. Also shown are the regions allowed by the LSND result at 90% CL and 95% CL, and the 90% exclusion contours of the KARMEN2 [Armbruster et al., 2002] and Bugey [Declais et al., 1995] experiments [Aguilar et al., 2001].

results from this measurement is shown in Figure 1.14. The MiniBooNE and LSND results are only compatible at the 2% level if both are interpreted in the framework of two-flavor neutrino oscillations. MiniBooNE is currently taking data in anti-neutrino mode (where the horn focuses negative particles) and intends to make a measurement of $\overline{\nu}_e$ appearance to more fully check the LSND result.

1.6. Dirac and Majorana Neutrinos

Unlike quarks and charged leptons, neutrinos may be their own antiparticles. Whether they are depends on the nature of the physics that gives them mass[Amsler et al., 2008].

In order to incorporate the neutrino mass in the Standard Model (SM), it is straightforward to extend the SM to accommodate these masses in the same way that this model accommodates quark and charged lepton masses. When a neutrino ν

is assumed to be massless, the SM does not contain the chirally right-handed neutrino field ν_R, but only the left-handed field ν_L that couples to the W and Z bosons. To accommodate the ν mass in the same manner as quark masses are accommodated, we add ν_R to the model. Then we may construct the "Dirac mass term"

$$\mathcal{L}_D = -m_D \overline{\nu}_L \nu_R + h.c. \tag{1.31}$$

in which m_D is a constant. This term, which mimics the mass terms of quarks and charged leptons, conserves the lepton number L that distinguishes neutrinos and negatively-charged leptons on the one hand from antineutrinos and positively-charged leptons on the other. Since everything else in the SM also conserves L, we then have an L-conserving world. In such a world, each neutrino mass eigenstate ν_i differs from its antiparticle $\overline{\nu}_i$, the difference being that $L(\overline{\nu}_i) = -L(\nu_i)$. When $\overline{\nu}_i \neq \nu_i$, we refer to the $\nu_i - \overline{\nu}_i$ complex as a "Dirac neutrino".

Once ν_R has been added to our description of neutrinos, a "Majorana mass term",

$$\mathcal{L}_M = -m_R \overline{\nu_R^c} \nu_R + h.c. \tag{1.32}$$

can be constructed out of ν_R and its charge conjugate, ν_R^c. In this term, m_R is another constant. Since both ν_R and $\overline{\nu_R^c}$ absorb ν and create $\overline{\nu}$, $\mathcal{L}_M$ mixes ν and $\overline{\nu}$. Thus, a Majorana mass term does not conserve L. The $\nu - \overline{\nu}$ mixing induced by a Majorana mass term causes the neutrino mass eigenstates to be self-conjugate: $\overline{\nu_i} = \nu_i$. This is, for a given helicity h, $\overline{\nu_i}(h) = \nu_i(h)$. We then refer to ν_i as a "Majorana neutrino".

Suppose the right-handed neutrinos required by Dirac mass terms have been added to the SM. If we insist that this extended SM conserve L, then, of course, Majorana mass terms are forbidden. However, if we do not impose L conservation, but require only the general principles of gauge invariance and renormalizability, then Majorana mass terms are expected to be present. As a result, L is violated, and neutrinos are Majorana particles.

In the see-saw mechanism, which is the most popular explanation of why neutrinos – although massive – are nevertheless so light, both Dirac and Majorana mass are present. Hence, the neutrinos are Majorana particles. However, while half of them are the familiar light neutrinos, the other half are extremely heavy Majorana particles referred to as the N_i, with masses possibly as large as the GUT scale. The N_i may have played a crucial role in the baryogenesis in the early universe.

However experimentally proving that neutrinos are indeed Dirac or Majorana particles is a difficult task. Currently only neutrinoless double beta decay experiments have handles to confirm whether neutrinos are Majorana or not. In several nuclei with an even number of neutrons and an even number of protons the extra binding energy produced by the pairing leaves ordinary β decay energetically forbidden. In such nuclei double beta decay, where two electrons are emitted, is left as the only viable decay mode. Two neutrino double β ($2\nu\beta\beta$) decay has by now been observed in a number of nuclei, but neutrinoless double β ($0\nu\beta\beta$) decay has yet to be convincingly seen. If observed, $0\nu\beta\beta$ decay would imply that neutrinos are Majorana particles. It is expected that the process will be dominated by the diagram shown in Figure 1.15. In this diagram, one or another of the neutrino mass eigenstates ν_i is exchanged between two virtual W bosons to create the outgoing electrons. The $0\nu\beta\beta$ amplitude is then a coherent sum over the contributions of the different ν_i. The rate for the process is given by

$$\begin{aligned} \Gamma_{0\nu} &= G_{0\nu}|M_{0\nu}|^2 m_{\beta\beta}^2 \\ m_{\beta\beta} &= |\sum_i m_i U_{ei}^2| \end{aligned} \tag{1.33}$$

where $G_{0\nu}$ is a readily calculable phase space factor and $M_{0\nu}$ is the, not so readily calculable, matrix element for the process. U_{ei} and m_i are the mixing matrix elements and neutrino masses and $\nu_e = \sum_i U_{ei}\nu_i$. The signature for the $0\nu\beta\beta$ process is a peak in the measured energy of the pair of electrons at the Q value, where Q is

generally defined as (initial energy) - (mass of all particles in the final state except the neutrinos).

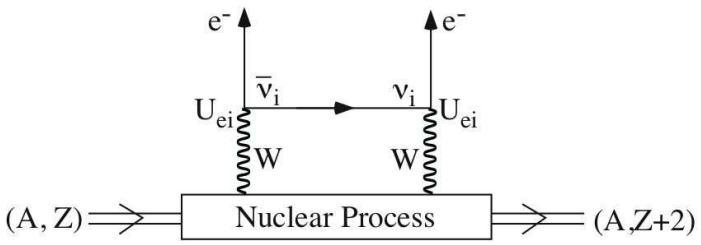

FIGURE 1.15. Neutrinoless double β decay.

1.7. Direct Measurements of Neutrino Mass

In 1930, Pauli mentioned the neutrino mass "should be of the same order of magnitude as the electron mass and in any event not larger than 0.01 proton masses". In 1933 Fermi and Perrin studied the effect of the neutrino mass in β-decays and concluded that the existing data are compatible with a massless neutrino. Further experiments showed that neutrinos could be massless and, in any case, the neutrino mass is much smaller than the electron mass. It was widely thought that neutrinos are massless, which led to the SM description of neutrinos are massless particles.

The results of neutrino oscillation experiments have recently proved that neutrinos are massive. Since these experiments give only information on the neutrino squared-mass differences, we currently know that there are at least two massive neutrinos, one with a mass larger than about $\sqrt{\Delta m^2_{21}} \simeq 9 \times 10^{-3}\,\text{eV}$ and another with a mass larger than about $\sqrt{\Delta m^2_{31}} \simeq 5 \times 10^{-2}\,\text{eV}$. Further information about the absolute values of neutrino masses must be investigated with other methods.

Take any known process involving neutrinos in the final state and calculate the rate as a function of neutrino mass. Try to see whether the observed rate differs significantly from the calculated rate with $m_\nu = 0$. Some examples follow.

Nuclear β-decay: One can look at the beta spectrum in $(Z, A) \to (Z{+}1, A){+}$ $e^- + \overline{\nu}_e$ (Kurie plot) or corresponding positron decay. The shape of the curve

can be calculated assuming $m_{\nu_e} = 0$. If, however the mass is not zero, the observed count will fall short of the calculated one as the electron energy approaches the total decay energy $E_0 = M_i - M_f$, where M_i and M_f are the masses of the initial atom and the final ion. The fraction of decays when the electron energy is close to E_0 becomes rapidly smaller for beta decays with higher Q values. It is therefor, imperative to select a candidate with low Q. The lowest known Q value (18.6 keV) for this process occurs for ^{3}H β-decay.

Pion decay: One can look for the muon energy in $\pi^+ \to \nu^+\nu_\mu$ (or its charge conjugate decay). Obviously this energy depends on the ν_μ mass.

Tau decay: There are various decay modes of the tau. One can use the kinematics of the final state to find the mass of the ν_τ.

Direct Kinematic tests [Kraus et al., 2004, Assamagan et al., 1996, Roney, 2001] have yielded the results

$$\begin{aligned} m_{\nu_e} &< 2.2\,\text{eV} \quad (95\%\ \text{CL,from}\ ^3\text{H} \to ^3\text{He} + e^- + \overline{\nu}_e), \\ m_{\nu_\mu} &< 170\,\text{keV} \quad (90\%\ \text{CL,from}\ \pi^+ \to \mu^+ + \nu_\mu), \\ m_{\nu_\tau} &< 15.5\,\text{MeV} \quad (95\%\ \text{CL,from}\ \tau \to 5\pi + \nu_\tau). \end{aligned}$$

Strictly speaking, these experiments do not measure m_{ν_e}, m_{ν_μ}, or m_{ν_τ}, which are not the neutrino mass eigenstates. Instead they measure some average values of $m_1 \equiv m(\nu_1)$, m_2, and m_3.

1.8. Summary

Table 1.2 summarizes the current state of knowledge of the neutrino parameters. Ignoring the phases and assuming $\theta_{13} = 0$, the "best-fit PMNS matrix" reads:

$$U^{BF}_{PMNS} = \begin{bmatrix} 0.83 & 0.56 & 0 \\ -0.39 & 0.59 & 0.71 \\ 0.39 & -0.59 & 0.71 \end{bmatrix} \tag{1.34}$$

TABLE 1.2. The current state of knowledge of the neutrino parameters

Parameter	Best-fit value	Range
Δm^2_{21}	$8.0^{-5}\,\mathrm{eV}^2$	$(7.7-8.4)\times 10^{-5}\,\mathrm{eV}^2$ $(\pm 1\sigma)$
$\lvert\Delta m^2_{31}\rvert$	$2.43\times 10^{-3}\,\mathrm{eV}^2$	$(2.30-2.56)\times 10^{-3}\,\mathrm{eV}^2$ $(\pm 1\sigma)$
θ_{12}	33.9°	$32.3^\circ - 35.5^\circ$ $(\pm 1\sigma)$
θ_{13}	unknown	$0^\circ - 11.4^\circ$ (90% $C.L.$)
θ_{23}	45°	$36.8^\circ - 53.2^\circ$ (90% $C.L.$)
δ_{CP}	unknown	
m_{lightest}	unknown	$0 - 2.2\,\mathrm{eV}$ (95% $C.L.$)
Hierarchy	unknown	
Dirac or Majorana	unknown	

Chapter 2

The MINOS Experiment

The Main Injector Neutrino Oscillation Search (MINOS) is a long-baseline neutrino oscillation experiment that performs precision measurements of the neutrino oscillation parameters in the "atmospheric neutrino" sector. The neutrinos are generated by the Main Injector (NuMI) facility at the Fermi National Accelerator Laboratory (Fermilab). The MINOS Near Detector is located on-site at Fermilab, 1 km away from the beam source, while the MINOS Far Detector is located at 735 km downstream of Soudan Underground Laboratory in northern Minnesota. The two detectors are magnetized steel-scintillator tracking calorimeters. Comparison of the neutrino energy spectra and flavor composition of the beam at the two detectors will allow measurement of neutrino oscillation parameters. This chapter describes the NuMI beam line and the details of the MINOS detectors. This is followed by a review of the detector calibration and event reconstruction chain.

2.1. The Fermilab Accelerator

The NuMI neutrino beam is created at Fermilab using 120 GeV protons from the Main Injector. Figure 2.1 shows the schematic drawing of the Fermilab accelerators. First, inside of the Cockcroft-Walton accelerator, hydrogen gas is ionized to create a negative ion, H^- particle with an energy of 750 keV. These particles will travel through the Linac, the LINear ACcelerator. The Booster takes 400 MeV H^- ions (where electrons will be taken off) from the Linac. After 20000 cycles in the Booster, the remaining proton will reach 8 GeV, and will enter (by a magnet kicker displacement) the Main Injector (MI). MI can accelerate the particles to 120 GeV, and then

send them to the Pbar target, which yields 8 GeV anti-protons, or to the NuMI target, which produce neutrinos for the NuMI experiments. Alternatively, it can accelerate proton to 150 GeV for collider experiments in Tevatron. Presently, for a typical main injector cycle, injection, acceleration and resetting, takes 2.2 s for 11-batch injection.

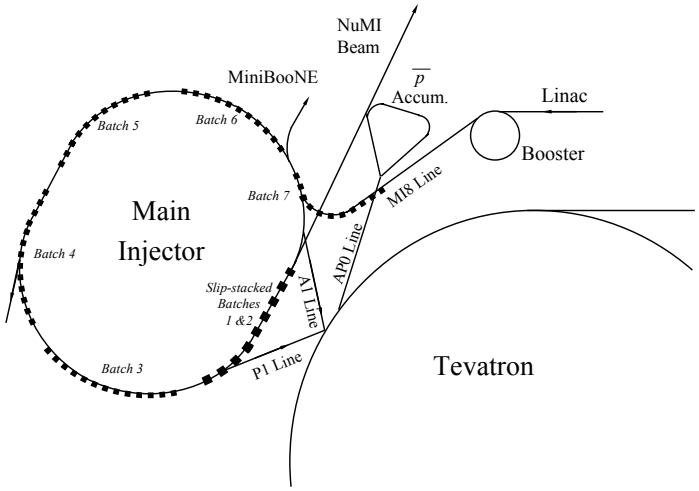

FIGURE 2.1. The Fermilab accelerators. Those used in generation of the NuMI beam are LINAC, Booster, and Main Injector [Zwaska].

The main injector circumference is exactly 7 times the booster circumference, so there is room for 7 booster batches. However, one slot must remain empty to allow the injection kicker to ramp down. A fast single turn extraction kicker was required for the NuMI project to spill 120 GeV protons onto a target. The extraction kicker has to rise in the $\sim 1.5\,\mu s$ abort gap of the Main Injector and then extract $\sim 1.6\,\mu s$ of beam (a single batch) for anti-proton production and $8.0\,\mu s$ of beam (5 batches) to NuMI. This mode is referred to as "mixed mode". There is a second operational mode which is referred to as "NuMI only mode". In this mode, $9.6\,\mu s$ (6 batches) of beam is extracted to NuMI [Jensen and Krafczyk].

A technique called "slip stacking" is utilized to increase the number of protons available for both the anti-proton production and the NuMI neutrino production at Fermilab. This involves stacking two booster batches end to end but with slightly different momenta, into the Main Injector. The two batches have different periods of revolution and 'slip' relative to each other azimuthally and finally overlap. When

they overlap they are captured using a single RF which is the average of the initial frequencies associated with the two batches [Shukla et al.].

Starting 2008, a "multi-batch slip stacking" mode becomes the standard operational mode. In this mode, five batches are loaded into the MI, and six more batches are loaded and slipped with the first five to make two batches for the anti-proton production and nine for NuMI. This mode is referred to as "2+9" mode. The NuMI beam intensity is greatly improved in this operational mode. A typical beam intensity is 3.1×10^{13} ppp for the "mixed mode" and 3.7×10^{13} ppp for the "NuMI only mode" with 8 booster turns. The corresponding beam power is 230 kW and 270 kW, respectively.

2.2. The NuMI Neutrino Beam

The Neutrinos at the Main Injector (NuMI) facility at Fermilab began operations in late 2004. The NuMI neutrino beam generates neutrinos mainly from the decays of pion and kaon secondary particles produced in the NuMI target, with a small contribution from muon decay [Adamson et al., 2008a]. Protons of 120 GeV are extracted from the main injector accelerator in 10 μs spill, bent downward by 58 mrad to point at the Far Detector, and impinged upon the NuMI hadron production target. The global positioning system (GPS) defined the survey beam direction to within 12 m of the Far Detector. A schematic diagram of the NuMI beam line is shown in Figure 2.2.

2.2.1. Target and horns. The production target is a rectangular graphite rod, segmented longitudinally into 47 segments. The target dimensions are 6.4 mm in width, 15 mm in height and 940 mm in length (1.9 interaction lengths). The typical beam-spot r.m.s. at the target is 1.1-1.2 mm. A collimating baffle upstream of the target provides protection for the target, its colling lines, as well as downstream beam components. The baffle is a 1.5 m long graphite rod with an 11 mm diameter inner

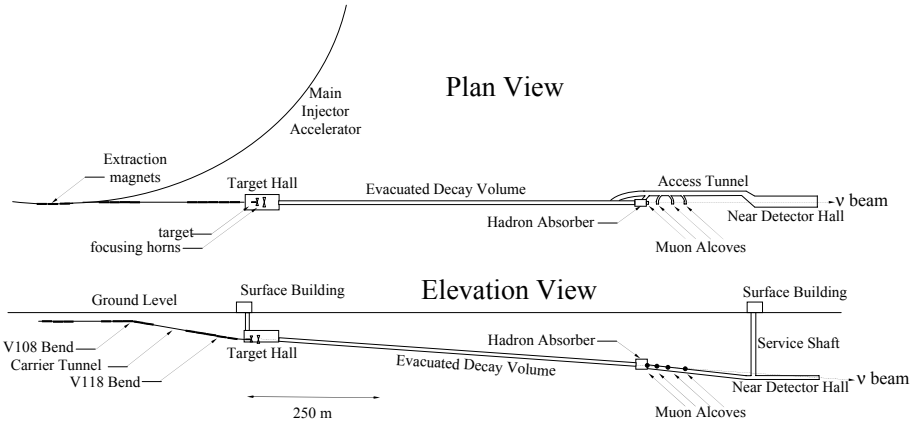

FIGURE 2.2. Plan and elevation views of the NuMI beam facility. A proton beam is directed onto a target, from which the secondary pions and kaons are focused into a decay volume via magnetic horns. Ionization chambers at the end of the beam line measure the uninteracted primary beam, secondary hadron beam and tertiary muon beam [Zwaska et al., 2006].

bore. The target is water cooled via stainless steel lines at the top and bottom of each fin, as shown in Figure 2.3.

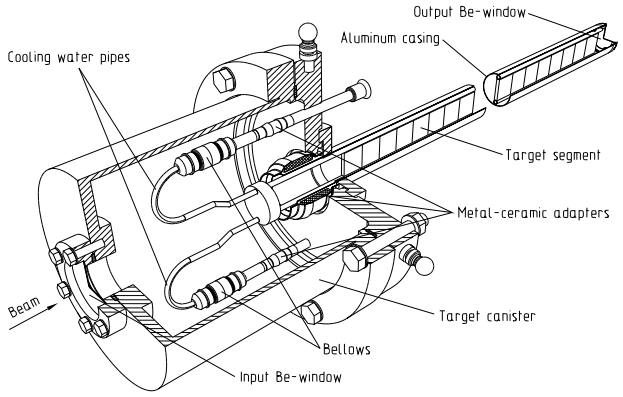

FIGURE 2.3. Schematic of the NuMI production target, which consists of 47 graphite segments [Garkusha et al., 2007].

The particles produced in the target are focused by two magnetic parabolic-shape horns [Abramov et al., 2002], as shown in Figure 2.4. The absolute value of the current flowing through the horns was calibrated to within $\pm 0.5\%$ and was observed to vary less than 0.2% over the course of the data collection period. The alignment of the target and horn system relative to the beam axis was checked using the proton beam itself [Zwaska et al., 2006]. The relative longitudinal positions of the two horns

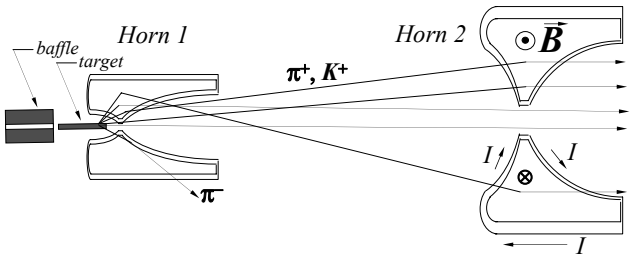

FIGURE 2.4. Hadrons produced in the NuMI target are focused by a system of two magnetic horns. The horns are separated by 10 m and each consists of an outer cylindrical conductor and inner parabolic conductor. The vertical scale is 4 times that of the horizontal (beam axis) scale [Adamson et al., 2008a].

and the target optimizes the momentum focus for pions and kaons and therefore the typical neutrino energy. To fine-tune the beam energy, the target is mounted on a rail-drive system with 2.5 m of longitudinal travel, permitting remote change of beam energy without directly accessing the horns and target. The beam has been designed so as to adjust the energy spectrum of neutrinos in order to maximize sensitivity to oscillation parameter Δm^2. Most of the time the beam line is configured in the "low energy" mode with $\langle E_\nu \rangle \sim 4\,\text{GeV}$. In its furthest downstream location, the target is cantilevered approximately 65 cm into the first parabolic horn. Moving the target upstream directs smaller-angle, higher-momentum particles into the magnetic fields of the focusing horns, resulting in a higher-energy neutrino beam, as shown in Figure 2.5.

2.2.2. Decay pipe and absorber. The focused beam particles enters into a 675 m long, 2 m diameter steel pipe, evacuated to ∼0.5 Torr to reduce meson absorption and scattering. This length is approximately the decay length of a 10 GeV pion. The entrance to the decay pipe is sealed by a two-piece aluminum-steel window. The central (radius < 50 cm) portion of the window is made of 1 mm thick aluminum and is strengthened by an outer (radius > 50 cm) section made of 1.8 cm thick steel. The design reduces scattering in the window while maintaining vacuum integrity. The

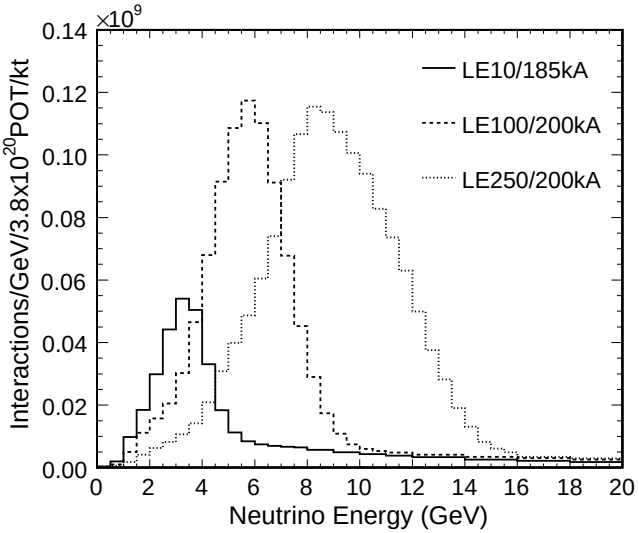

FIGURE 2.5. Calculated rate of ν_μ charged-current interactions in the MINOS Near Detector. Three spectra are shown, corresponding to the low, medium, and high neutrino energy positions of the target. In these configurations, the target is located 10, 100, and 250 cm upstream of its fully-inserted position [Adamson et al., 2008a].

decay volume is surrounded by 2.5-3.5 m of concrete shielding. Neutrinos are produced by decays of the secondaries, e.g. $\pi^+(K^+) \to \mu^+\nu_\mu$. At the end of the decay pipe there is a water-cooled absorber with an aluminum core encased in steel to stop any remaining primaries and undecayed secondaries. Any muons passing through the absorber are stopped by 240 m of dense Dolomite rock before they reach the Near Detector cavern. Ionization chambers are used to monitor the secondary and tertiary particle beams. One array is located immediately upstream of the absorber, and three others are located at the muon alcoves, one downstream of the absorber, one after 8 m of rock, and a third after an additional 12 m of rock. The first array monitors the remnant hadrons at the end of the decay pipe, and the other three arrays monitor the tertiary muon from the π and K decays.

The flavor composition of the beam will be predominantly ν_μ (92.9%). Small contributions of $\overline{\nu}_\mu$ (5.8%) will come from μ^+ decays and target produced π^- decays. A 1.2% ν_e component of the beam results from μ^+ decays and target-produced K^+_{e3} decays. The contribution from $\overline{\nu}_e$ is small (0.1%).

2.3. The MINOS Detectors

MINOS consists of two neutrino detectors separated by a long baseline. A third detector, called the calibration detector, was exposed to test beams at CERN to establish detector response to hadrons, electrons and muons with momenta in the range 0.2-10 GeV/c. The Near Detector at Fermilab is used to characterize the neutrino beam and its interactions and is located about 1 km from the primary proton beam target, the source of the neutrino parent particles. The Far Detector performs similar measurements 735 km downstream. The essence of the experiment is to compare the rates, energies and topologies of events at the Far Detector with those at the Near Detector, and from those comparisons determine the relevant oscillation parameters. The detectors have been designed to be as similar as possible to reduce systematic errors. In this section, we will first describe the main feature of the MINOS detectors, and then discuss the unique feature of each individual detector.

2.3.1. MINOS Detector Technologies. The MINOS detectors are magnetized steel/scintillator tracking/sampling calorimeters with an absorber layer of steel and an active layer of plastic scintillator. The steel and scintillator is arranged into a "sandwich" structure: a layer of 1 cm thick scintillator is attached to a layer of 2.54 cm thick steel to form a plane. There is a 2.41 cm air gap between two successive planes for mechanical reasons. The scintillator is divided up into 4.1 cm wide strips, and each plane has one "view" of strips, with the next plane having the orthogonal view to give a three-dimensional tracking capability. The two views are at 45° relative to vertical in order to avoid having strip readout connections at the bottom of the detector. One view is referred to as "U view" and the other view is referred to as "V view".

The detectors use a solid scintillator that is made by extruding polystyrene into long thin strips. The polystyrene is doped with the PPO (1%) and POPOP (0.03%). Fiber readout of extruded scintillator was chosen as opposed to direct readout of

cast scintillator in order to reduce costs. Each scintillator strip has a 2.3 mm-deep by 2.0 mm-wide groove cut into its wider edge which runs along the length of the strip. A 1.2 mm diameter wavelength shifting (WLS) fiber-optic cable is glued into the groove. WLS fibers minimize self-absorption by absorbing blue light peaked at 420 nm and re-emitting the green light peak at 470 nm. The blue photons from the scintillator are absorbed in the WLS fiber and re-emitted isotropically. Those resulting photons whose directions fall within the total internal reflection cones are transported along the fiber to the edges of the detector, subsequently being routed to the photo detectors. The scintillator surface is covered by a thin (0.25 mm) co-extruded titanium-dioxide (TiO_2)-loaded polystyrene layer that serves as a diffuse reflector. The scintillator and TiO_2 coating are co-extruded in a single process, a standard technique in the plastics industry. The fiber must be completely contained inside the groove to ensure efficient light collection. A specularly reflective strip of aluminized Mylar tape is placed over the groove after the WLS fiber has been glued in place. The cutaway drawing of a single scintillator strip is shown in Figure 2.6.

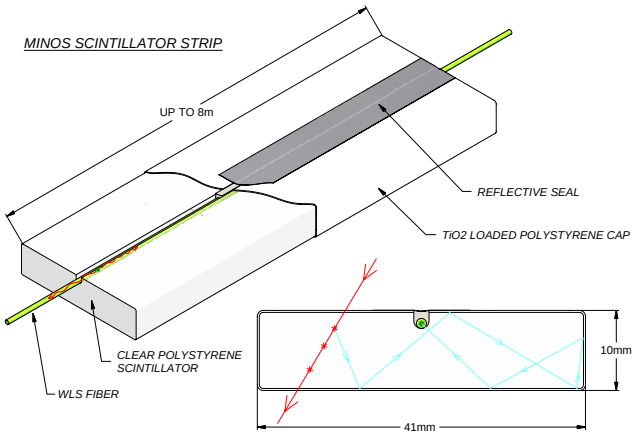

FIGURE 2.6. Cutaway drawing of a single scintillator strip. Light produced by ionizing particle is multiply reflected inside the strip by the outer reflective coating. Light absorbed by a WLS fiber is re-emitted isotropically. Those resulting photons whose directions fall within the total internal reflection cones are transported along the fiber to the edge of the detector, subsequently being routed to the photodetectors [Michael et al., 2008].

The scintillator strips are encased in light-tight aluminum (0.05 cm thick) modules, which contain between 20 and 28 strips. After exiting the strips the WLS fibers run together in a manifold before they terminate in a connector. Clear fiber cables connect to the module and transmit light from the edges of the detector to centralized locations where the multi-anode photomultiplier tubes (PMTs) and readout electronics are mounted. A light injection system illuminates the WLS fibers near their ends with LED-generated UV light to monitor the stability and linearity of the PMTs. The MINOS detector are read out by Hamamatsu 64-anode (M64) PMTs for the Near Detector and and 16-anode (M16) PMTs for the Far Detector. The PMTs are housed in light-tight, steel enclosures containing clear fiber bundles which are interlaced from cable connectors to PMT pixels. In the Near Detector each M64 resides in an individual enclosure. In the Far Detector each enclosure (called a "MUX box") houses three M16 PMTs. Figure 2.7 illustrates the scintillator system readout for a module.

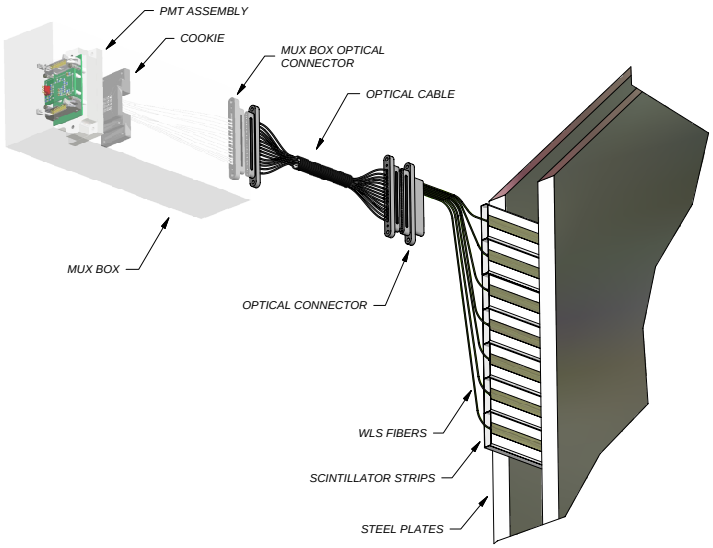

FIGURE 2.7. Schematic drawing of the scintillator system readout for a module [Michael et al., 2008].

The phototube signals are digitized using a modified version of the Viking VA chips mode designed by the Norwegian company IDEA ASA at the Far Detector [Oliver

et al., 2004] and FNAL "QIE" chips [Cundiff et al., 2006] at the Near Detector to meet the fast demands of the high event rate at the near site. In both cases, circuitry is installed to inject known amounts of charge into the digitization circuits for calibration of the digitization. Data are gathered into custom mid-level VME cards for readout by the data acquisition. The data acquisition reads charge and time information (called "digits") for each phototube signal, combines such data from all parts of the detector, and arranges them into time-ordered "snarl" of data that correspond to physical events.

Both the Near and Far Detectors are magnetized with a current-carrying coil producing an average magnetic field of 1.3(1.4) T in the Near(Far) Detector. A coil running down the center of the detector and back outside of the detector is used to create the field. At the Near Detector the coil is offset by 50 cm from the detector center so as to give a large fiducial volume around the neutrino beam spot. MINOS is unique in that it is the only large, underground detector with a magnetic field. The magnetic field allows charge separation between the μ^+ and μ^-, and therefore charged current interactions of ν_μ and $\overline{\nu}_\mu$. A comparison of atmospheric oscillation properties for the two would be a test of CPT symmetry in neutrino masses and mixing. The magnetic field also allows the muon momentum to be measured through the curvature of tracks that are only partially contained within the detector. It also focuses negative particles (i.e. μ^-) created in the beam ν_μ CC interactions increasing the proportion that are fully contained. The energy resolution on the curvature measurements is approximately 14% at 10 GeV muon momentum. Multiple scattering of the muons in the steel is the predominant limitation on the accuracy of these measurements. For muons that stop in the detector a much better measurement of their momenta can be obtained from a range measurement. The energy resolution for stopping muons from a range measurement is approximately 6%. In the energy range of interest, the average muon momentum is roughly 2 GeV/c. Those low energy muons are most like to stop in the detector and their momenta are measured through the range accordingly.

The data acquisition (DAQ) and timing system synchronize and continuously read out the front-end electronics. Software triggering in the DAQ provides flexible event selection and data processing. Various triggers are implemented in the DAQ system. The triggers fall into three categories: special triggers for debugging and calibration, bias-free triggers based on spill signals or spill times to gather beam events, and triggers based on the clustering of hits in the detector to gather out-of-spill events. GPS timestamps allow data from the two detectors to be synchronized with the beam pulses. The two detectors have different front-end electronics due to the disparate rates of neutrino interactions and cosmic-ray crossings at the two sites.

2.3.2. The Far Detector. The Far Detector has mass of 5.4 kt. It is the largest of the three MINOS detectors and is located 714 m below the Earth's surface (2070 m water equivalent) in the Soudan Underground Laboratory, Northern Minnesota. It consists of 286 8 m wide octagonal planes, arranged in 2 super-modules of 249 and 237 planes, of which 248 and 236 are instrumented with scintillator. The division of the detector into two super-modules is made due to restrictions on the length of the magnetic coil, thus each super-module is independently magnetized. The first and second super-modules were completed in August 2002, and June 2003, respectively. Collection of cosmic-ray and atmospheric neutrino data for each super-module has begun since shortly after the completion of each super-module. Each of the scintillator planes is divided up into 192 strips. The 192 scintillator strips are encased in 8 modules. The center four modules contain twenty 8 m long strips. The outer modules contain 28 strips varying in length from 3.4 m to 8 m. The center two modules must provide clearance for the detector's magnet coils. A semi-circular hole of radius 197 mm is cut into the aluminum over of the affected modules and short lengths of scintillator strips passing through the hole are also cut away. However, the WLS fiber passing through the affected strips are not cut. Rather, a "bypass" channel routes them around the hole, as shown in Figure 2.8.

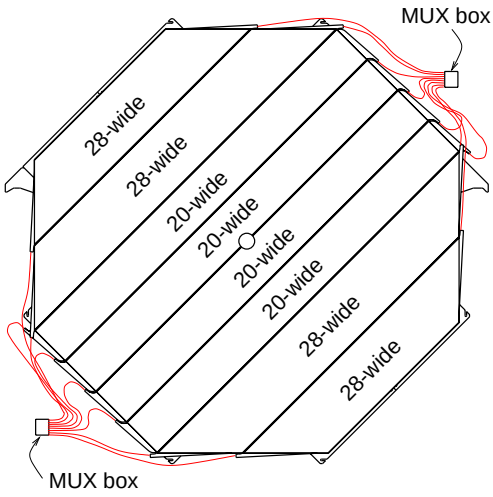

FIGURE 2.8. Layout of far detector scintillator modules. The center four modules contain twenty strips and the outer modules contain 28 strips.

The scintillator strips are read out at both ends by Hamamatsu M16 PMTs with 16 pixels. To reduce the large instrumentation load, a multiplexing technique (optical summing) is employed so that 8 strips from each plane are read out by the same PMT pixel. This is feasible because the transverse spread of hadronic/electromagnetic showers from beam neutrinos is limited to a $\sim$1 m region. To enable determination of which strip was actually hit, the 8 strips read out by a single pixel on one side of detector are read out by 8 different pixels on the other side.

The front-end electronics (FEE) at the Far Detector [Oliver et al., 2004] were specifically designed for the low-rate underground environment. A block diagram of the readout structure is shown in Figure 2.9. The readout is based on the front-end ASIC VA32_HDR11, developed in collaboration with the Norwegian company IDEA ASA. Each VA chip is responsible for sampling and holding the signals from one of the three PMTs in a MUX box. Three VA chips are mounted onto a single VA Front-end Board (VFB), located on the outside of the PMT MUX box. The VFB provides support circuitry for power distribution and biasing of the VA chips. It also contains a discriminator chip ASDLite ASIC, which compares the dynode signals from the

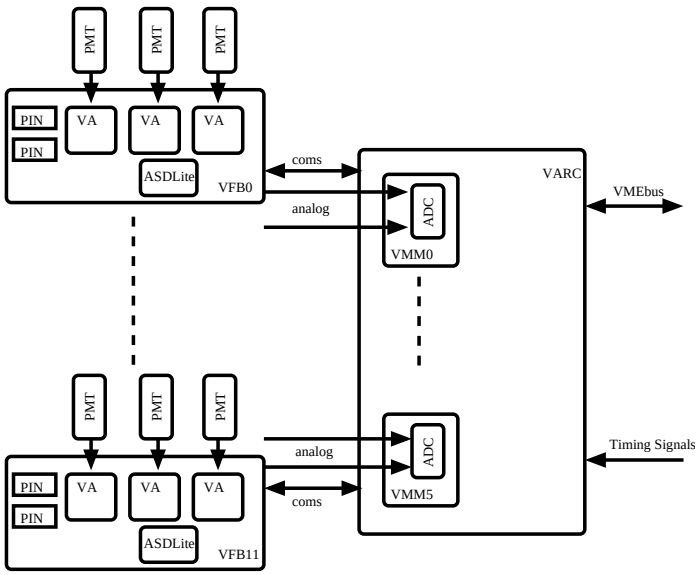

FIGURE 2.9. Schematic overview of the Far Detector readout electronics. Three PMTs are connected with short flat ribbon cables to the VFB, which also houses two PIN diodes to monitor the light level of the light injection system. The VA ASIC amplifies and holds the PMT signals, which are multiplexed via an analog link onto an ADC on the VARC. The VFB is controlled through a digital link by the VARC [Michael et al., 2008].

PMTs with a common programmable threshold to provide a discriminated signal for time-stamping and readout initiation. The VFB is operated in slave mode and fully controlled by the VA readout controller (VARC) described below.

The analog signals from the VA chip are multiplexed onto an ADC, which is located on a VA Mezzanine Module (VMM). Two VFBs are connected to each VMM. The VARC houses 6 VMMs and controls the signal digitization, triggering, timestamping and bias of the VA chips. Each VARC can thus service up to 36 PMTs of 16 channels each.

The VARC is implemented as a 9U VME card. Three VARCs, a timing card, and a Motorola VME processor share a single VME crate. The VARC receives the discriminated dynode signal of each PMT. It time-stamps these signals with an effective 640 MHz TDC, and then generates the hold signals for the VA ASIC. The signals held

in the VA ASIC are then multiplexed to a commercial 14-bit 10 MHz ADC. The digitization sequence is started if the VARC receives at least two discriminated dynode signals from different PMTs in a 400 ns window. This so-called 2-out-of-36 trigger reduces the dead time due to dark noise in the PMTs and fiber noise in the scintillator, without compromising the recording of physics events. The entire detector readout is synchronized by a 40 MHz optical timing distribution signal slaved to a GPS clock from True Time.

Once the data are digitized they are transmitted to a local FIFO and stored there for further processing. The pedestal is subtracted and data above an individually settable specification threshold are written to an on-board VME memory. This memory is read out by the DAQ system. The VARC also controls pedestals and charge injection calibration runs.

To aid the atmospheric neutrino analysis in the Far Detector, a cosmic ray veto shield has been erected around the top and sides of the detector. This allows cosmic rays to be tagged and reduces the cosmic ray background by a factor of approximately 100. The shield is made of the same scintillator strips as the main detector and the data is read out in the same fashion. Due to the steepness of the cosmic tracks and knowledge of the spill time, cosmic ray muons are not a significant source of background for the beam analysis, so shield information is not used for the accelerator neutrino analysis.

2.3.3. The Near Detector. The Near Detector has a mass of 0.98 kt. It is located a short distance from the neutrino source at Fermilab, 100 m below the surface (225 m water equivalent). The design of the Near Detector takes advantage of the high neutrino flux at this location to define a relatively small target fiducial volume for selection of events for the near/far comparison. At the beam intensity of 2.2×10^{13} POT/spill, an average of 16 neutrino interactions occurred in the Near Detector during each 10 μs spill in the low-energy beam configuration [Adamson et al., 2008a]. The Near Detector consists of 282 planes. It has an elongated octagonal cross-section,

3.8 m high and 4.8 m wide. Only 153 of the 282 planes are active. The upstream 120 planes of the detector, the calorimeter section, contains the target fiducial volume in which every plane is instrumented. The downstream part, the spectrometer section, is used to measure the momenta of energetic muons and has only every fifth plane instrumented with scintillator. Active planes are instrumented with four distinct scintillation module patterns: full U-view (FU), full V-view (FV), partial U-view (PU), and partial V-view (PV). The area of partial coverage is set to ensure the complete measurement of neutrino events occurring in the Near Detector fiducial volume. The full-view coverage extends around the coil hole in order to track long range muons downstream of neutrino interactions. The layout of different scintillator modules are shown in Figure 2.10. The spectrometer section of the Near Detector, plane 121-281, is used to measure the momenta of energetic muons and only every fifth plane is fully-instrumented scintillator.

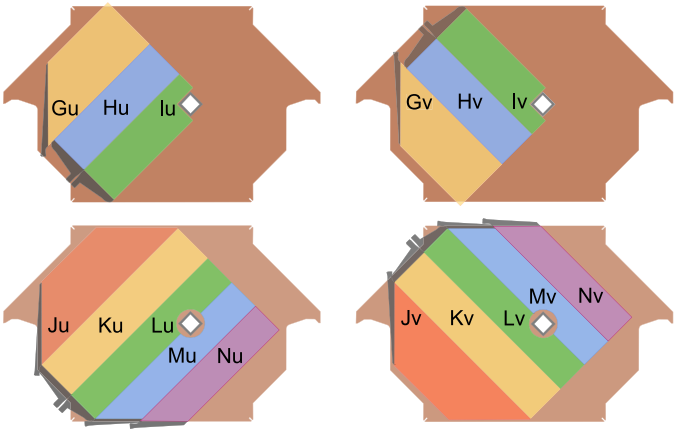

FIGURE 2.10. The four different configurations of planes used in the Near Detector, showing the different layouts of the scintillator modules. The upper two figures show partially instrumented planes ("calorimeter region") while the lower two figures show the fully instrumented ones ("tracking region"). The G-N notations denote the different shapes of the scintillator modules. The beam is centered midway between the coil hole and the left side of the plane, hence the scintillator need only cover that area in the target region [Michael et al., 2008].

In contrast to the Far Detector, scintillator strips in the Near Detector need only be read out on one end; their relatively short lengths (typically 2.8 m compared to 8 m

at the Far Detector) ensure that enough photons reach the PMTs to detect the passage of a minimum ionizing particle efficiently. The other end of the strip is covered with reflective aluminized mylar tape to increase the light yield. The scintillator strips are read out by Hamamatsu M64 PMTs with 64 pixels. A partially-instrumented plane has 64 strips so is read out by a single PMT. A fully-instrumented plane has 96 strips so is read out by 1.5 PMTs. Furthermore, to reduce the instrumentation, a 4-fold electrical summing technique is employed in the muon-spectrometer region. Each PMT is split into groups of 4 pixels and the signal from the 4 anodes are fed into a single electronics channel. The consequence of the electrical summing is that a "seed" track in the forward region (calorimeter) is needed to project into the muon-spectrometer for unambiguous reconstruction.

Due to the multiple events occurring each beam spill, dead-timeless, high-speed front-end electronics is required for the Near Detector. In the Near Detector front-end electronics [Cundiff et al., 2006], each PMT pixel is digitized continuously at the frequency of the beam RF structure of 53.103 MHZ (18.83 ns). This is achieved with an individual front-end channel unit consisting of a small mezzanine printed circuit board (PCB) called a MENU (MINOS Electronics for Neutrinos). The principal MENU components are an ASIC named the *Charge Integrator and Encoder* (abbreviated "QIE"), a commercial flash analog-to-digital converter ("FADC"), and a data buffer. A MENU board also contains circuitry for measuring source current and circuitry for injecting DC current into the QIE for performing electronics calibration. Sixteen MENUs reside on a VME type-6U PCB (called a MINDER - MINOS Near Detector Electronics Readout), with four MINDERs required for each fully used M64 PMT.

The QIE input signal current, I, is split into eight binary-weighted "ranges" with values $I/2$, $I/4$, $I/8$, ..., and integrated onto a capacitor for each range. A bias current is added to ensure that the capacitor voltage on one and only one range is within the predetermined input limits of the FADC. The QIE selects that voltage for output to

the FADC, and also outputs a 3-bit number representing the range value. Each QIE is equipped with four independent copies of the current splitter, integration, and output circuits to permit continuous dead-timeless operation. Each QIE data word consists of 13 bits including an 8-bit FADC value, a 3-bit range value, and a 2-bit code for the identification of the current splitter and capacitor circuit (known as "CapID").

Data from the front-end, consisting of range, FADC value, and CapID, are transfered to VME type-9U modules called MASTERs (MINOS Acquisition, Sparsifier, and Time-stamper for Event Readout), which read out up to eight MINDERs each. The MASTERs linearize the data words using a lookup table which represents the results of a charge injection calibration of each MENU. The resulting linearity is better than 0.5% over the entire dynamic range.

To provide uniformity, a centralized Near Detector clock system is used to distribute a continuous 53 MHz reference, spill signals, and other control signals to all front-end modules. Clock signals are also used to synchronize the readout of data by the VME processors and the DAQ system. The Near Detector clock is synchronized to the Fermilab accelerator but the phase of timing signals relative to an independent GPS system is used to allow accurate reconstruction of the absolute UTC event time.

2.4. Triggering

The DAQ systems at both detectors are functionally identical and run on standard commercial PCs [Boehm]. When they receive a trigger signal the DAQ records the readout from the detector to disk. The data are distributed to online monitors and event displays as well as transferred to the Fermilab mass storage facility via the internet. The primary trigger conditions are summarized as follows:

- **Spill trigger:** All digitization that occur within the spill gate (100 μs around the spill) are recorded, which is used by the Near Detector to record the spill signal.

- **Remote spill trigger:** As the direct spill signal is not available at the Far Detector, the near timing system is used to generate time-stamps of the spill signals. These time-stamps are transmitted to the Far Detector over the internet. All digitization that occur within a configurable window around the spill are recorded. As the Far Detector DAQ has large buffering, it is possible to allow for significant delays in the spill time arriving. This trigger is approximately 99% efficient.
- **Fake remote spill trigger:** Fake spill triggers are randomly generated between spills in order to sample detector activity. Spills triggered by these events will be used for measuring the cosmic background.
- **Plane trigger:** M out of N contiguous planes must contain at least one hit strip. In general this is set to a 4 in 5 configuration.
- **Energy trigger:** M contiguous planes in the detector have a summed raw pulse height greater than threshold energy E and distributed across at least N hit strips. In general this is set to M=4, E=1500 ADC, N=6. This mode is not in standard use at the Near Detector.
- **Activity trigger:** There is activity in any N detector planes, N is nominally 20.
- **Special trigger:** This set of triggers is used primary for calibration runs or detector component debugging tests.

The choice of trigger will result in different biases in the physics events recorded. For this reason separate offline reconstruction is used for processing of the minimum bias spill based triggers (primary beam events) and the triggers based on detector activity (primary cosmic and noise events).

2.5. Detector Calibration

The detector calibration is very important for the MINOS measurements. The MINOS detectors measure hadronic and electromagnetic shower energy by calorimetry. The relative detector energy calibration is critical for neutrino oscillation studies that rely on comparisons of energy spectra and event characteristics in the Near and Far Detectors. The task of calibration for MINOS comprises: removing detector variation within each detector, relating energy deposits from different detectors (relative calibration) and finally translating detector responses for different types of particles to energy in GeV (absolute calibration).

2.5.1. Calibration Tools. The principle tools for calibrating the detector response are an LED based light-injection (LI) system, a test-bench scan of the scintillator modules with a radioactive source, and cosmic ray muons.

A light-injection (LI) calibration system has been designed for the MINOS detectors to map the linearity of the instrumentation, to monitor the stability of the PMTs and electronics over time, to evaluate the single-photoelectron gain, and to monitor the integrity of the optical path and readout system [Adamson et al., 2002]. The system is based upon pulsed blue light-emitting diodes (LEDs). A rack-mounted box, known as a "pulser box", contains a set of 20 LEDs, each of which has an optical fanout allowing it to illuminate multiple individual fibers. These fibers carry light to a set of optical connectors on the back panel of the pulser box. From the pulser box, optical fibers carry the light to the outer edges of the MINOS detector. A set of highly reflective cavities situated there, the "light-injection modules" (LIM), allows the blue LED light to illuminate the green wavelength-shifting fibers, thus producing pulse of light that mimic the signals from the scintillator.

Cosmic ray muons are used at each detector to measure scintillator related quantities. Through-going cosmic ray muons have an average energy of 200 GeV at the

Far Detector and a rate of 0.5 Hz. At the Near Detector, the mean energy is 55 GeV and the rate is 10 Hz.

2.5.2. Relative Calibration. The main branch of this calibration is convert raw ADC's into calibrated muon Energy Units (MEU). The first step towards achieving this is to make the response of each individual detector uniform. The calibration corrects for scintillator light output variations as well as nonuniformities of light transmission and collection in the fibers, PMTs and readout electronics. The charge-injection system is used to measure the linearity of electronics. The light-injection system is used to measure the linearity and time variation of the readout response. The cosmic ray muons are used to measure scintillator strip light output variation with time and position, specifically to record inter-strip and intra-strip non-uniformities. The next step is to relate energy deposits in one detector with those in another. This can be done by using particle of known energy and comparing the detector responses. MINOS uses stopping muons from cosmic rays to do the inter-detector calibration.

The detector is calibrated in a multistage procedure that converts the raw photomultiplier signal $Q_{\mathrm{raw}}(i,t,x,d)$ measured by channel i at time t for an energy deposition at position x into a fully corrected signal Q_{cor}. Each calibration stage produces a "calibration constant". The fully corrected Q_{cor} is defined as the product of $Q_{\mathrm{raw}}(i,t,x)$ and the calibration constant from each stage:

$$Q_{\mathrm{cor}} = Q_{\mathrm{raw}}\left(i,t,x,d\right) \times D\left(d,t\right) \times L\left(i,d,Q_{\mathrm{raw}}\right) \times S\left(d,i,t\right) \times A\left(i,x,d\right) \times M(d)$$

where D, L, S, A and M refer to:

Drift correction $D\left(d,t\right)$**:** The channel gains and their variation over time are measured with the LED based light-injection system, demonstrating that short term (<24 h) gain variations are small and occurred mostly due to

environmental changes in the detector hall. Light-injection data were eventually superseded by measurements of the median pulse height per plane induced by through-going muon data, which were also able to correct for variations in the scintillator, WLS fiber and electronics. The detector response varies by $< 5\%$ over the data-taking period as shown in Figure 2.11. The decreasing response is likely due to the aging of the scintillator.

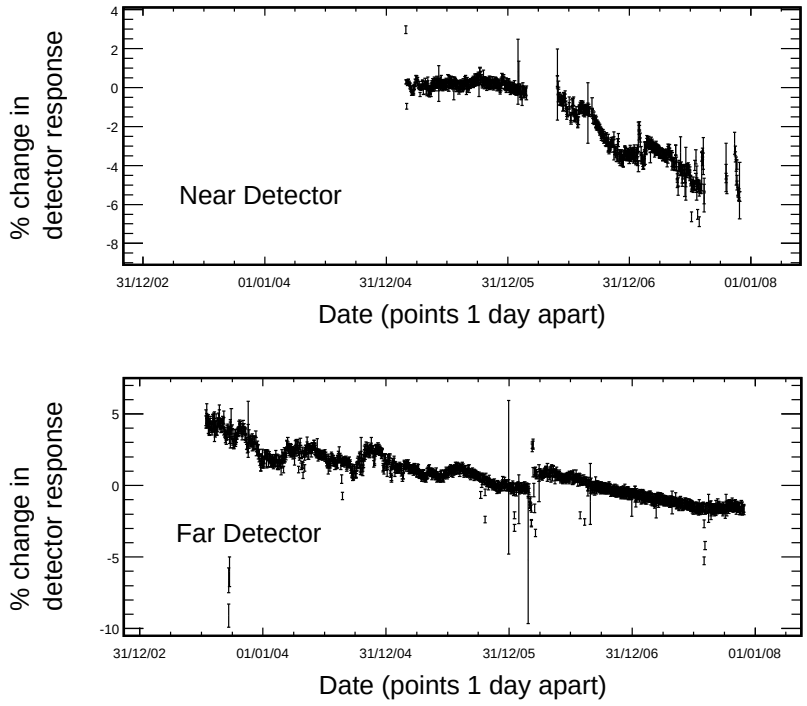

FIGURE 2.11. Variation in the median signal per plane deposited by through-going muon cosmic ray muons. The time dependence is largely due to variations in the environmental conditions in the Near and Far Detector halls and aging of the scintillator. [Michael et al., 2008]

Linearity Correction $L\left(i, d, Q_{\mathbf{raw}}\right)$: The response of the MINOS PMTs becomes non-linear at the 5-10% level when signal approach 100 photoelectrons. We need to use the light-injection system to measure the non-linearity curve and make the correction. The intensity of injected light is monitored by PIN photodiodes that are read out simultaneously with the PMTs. Although the PIN photodiodes themselves are measured to be quite linear, non-linearities

on the order of 1-2% are apparent in the readout response from both detectors because of the electronics noise. In the Near Detector, PIN diodes are amplified with high gain in order to suppress the electronics noise. In the Far Detector, the readout is still very non-linear even with high-gain PIN diodes. Therefore, the PIN diodes are not used in the Far Detector. Instead, the readout of the other end (far end) of the flashed strip end (near end) is used to monitor the intensity of injected light.

Strip-to-Strip Correction $S(d,i,t)$**:** Through-going cosmic ray muon data are used to measure the strip-to-strip (channel-by-channel) time dependent response of the detector. This calibration relates the mean response of each strip end to the detector average. This calibration incorporates several detector effects that vary channel-by-channel, including scintillator light yield, WLS fiber collection efficiency, readout fiber attenuation, PMT quantum efficiency and PMT gain. Once this calibration is performed, the response from the center of any strip is the same.

Attenuation Correction $A(i,x,d)$**:** A radioactive source, ^{137}Cs, was used to map out the response of each scintillator module at many positions along each strip. This was done on a test-bench setup prior to installation of the modules in the Near and Far Detectors. Through-going comic ray muons can also be used to correct the variation in light caused by attenuation along the WLS fiber in a scintillator strip. The pulse height from a strip hit by a track is plotted as a function of the longitudinal track position. The attenuation of light along the WLS fiber is described by two characteristic attenuation lengths. The strong absorption of light at short wavelength is characterized by a short attenuation length; and the attenuation of remaining longer wavelength light is characterized by a longer attenuation length. These

data are fit to a double exponential:

$$A(x) = A_1 e^{-x/L_1} + A_2 e^{-x/L_2} \tag{2.1}$$

where x is the track position along the strip and L_1, L_2 stand for two attenuation lengths. A fit is performed for each strip and the resulting parameters are used to correct the data. The resulting parameters are used to correct the reconstructed shower energy for attenuation based on the reconstructed shower position. The relative size of the correction varies by about 30% over the 8 m length of a Far Detector scintillator strip when signal from both ends are added, and by about 50% over the 3 m length of a Near Detector strip. Figure 2.12 shows the double exponential fit to the cosmic ray muon and mapper data.

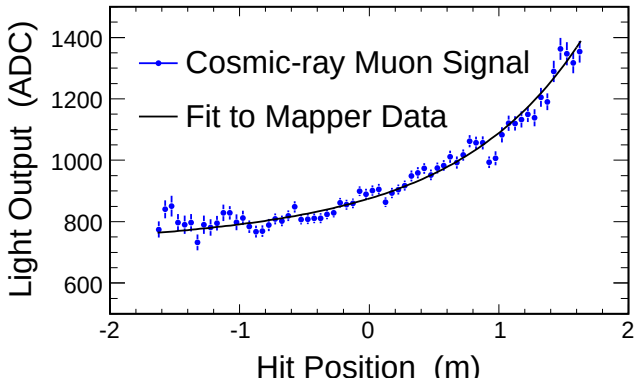

FIGURE 2.12. The attenuation curve measured by cosmic ray muon and the double exponential fit to the mapper data.

Inter-Detector Correction $M(d)$**:** The final stage in the relative calibration chain, before a conversion to absolute energy deposition in GeV, is the inter-detector calibration. This calibration step serves to relate energy deposits in one detector with those in another. Stopping cosmic ray muon data are used for this task because they are abundant enough at all detectors and their energy deposition in each plane can be accurately determined from range measurements. A "track window" technique was developed for this

calibration. This technique measures the response of muons only when their momenta are between 0.5 and 1.1 GeV. This avoids using data from the end of the track where the rapid increase in ionization occurs. The stopping power of muons is shown in Figure 2.13. After the inter-detector calibration a particle, of given energy and type, passing through a plane of scintillator in any of the three detectors gives an identical response (to within the errors of the calibration). A universal energy unit, the Muon Energy Unit (MEU, also referred to as a Minimum Ionizing Particle, MIP) is defined as the detector response to a perpendicular 1 GeV muon transversing 1 plane of scintillator.

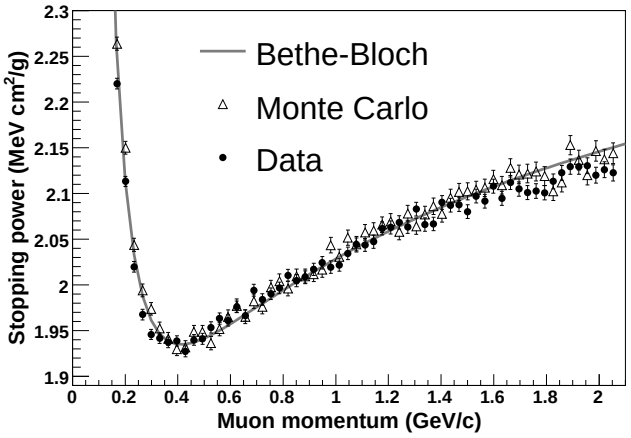

FIGURE 2.13. Stopping power of muons. The Bethe-Block predicted muon stopping power in polystyrene scintillator (gray) compared to the Far Detector data (black circles) and the GEANT Monte Carlo (open triangles). Both data and Monte Carlo have been scaled to match the calculation at the minimum ionizing points. [Michael et al., 2008]

2.5.3. Absolute Calibration. MINOS physics analysis require a good understanding of the detector response to muon, electrons and hadrons with energy below 10 GeV. One need to understand not only the overall energy scale and resolution, but also the event shape characteristics. The calibration detector [Adamson et al., 2006] was exposed to test beams at CERN to establish the response to hadrons, electrons and muons with momenta in the range 0.2-10 GeV/c. The measurements were used to normalize Monte Carlo simulations and to establish the uncertainty on the hadronic

and electromagnetic energy scales. The data from the calibration detector were compared with events simulated using the same GEANT3 base Monte Carlo used for the Near and Far detectors.

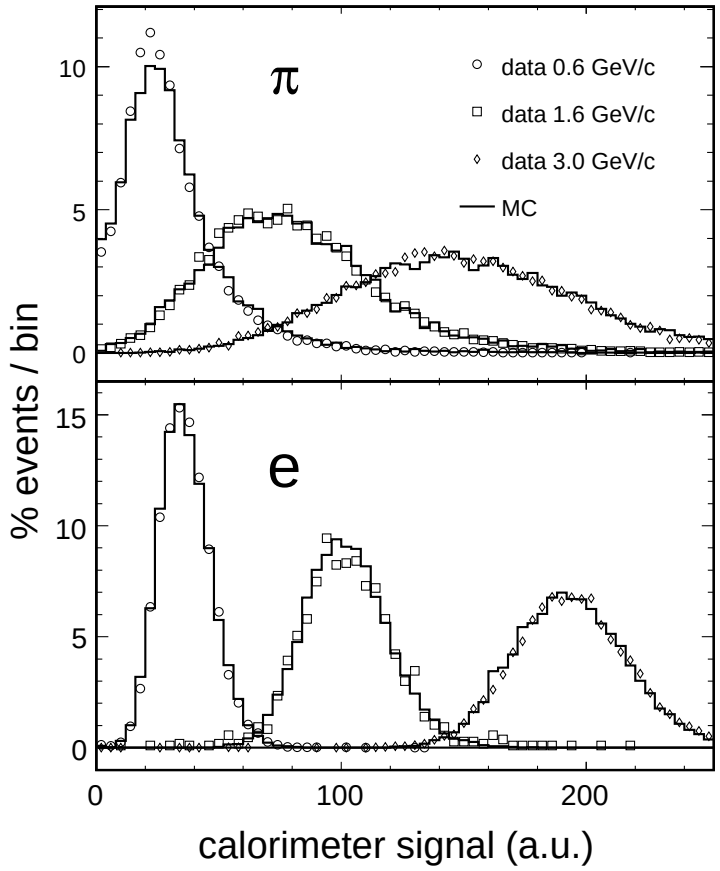

FIGURE 2.14. The calorimeter-signal scale is in arbitrary units. The data (open symbols), obtained from the calibration detector exposure to CERN test beams, are compared to distributions from Monte Carlo simulations. Pion induced showers are simulated using the GCALOR shower code [Michael et al., 2008].

Figure 2.14 shows the measured detector response to pions and electrons compared with the simulation result. The simulated calorimetric response to electrons agreed with the data to better than 2% in the electron momentum range 0.2-10 GeV/c [Vahle]. Pion and proton induced showers were compared with events simulated using the GHEISHA, GEANT-FLUKA and GCALOR shower codes. The GCALOR-based simulation was in best agreement with the data and was adopted as the default

shower code. The Monte Carlo reproduces the response to pion and proton induced showers to better than 6% at all momentum settings [Kordosky]. The energy resolution was adequately reproduced by the simulation and may be parameterized as $56\%/\sqrt{E} \bigoplus 2\%$ for hadron showers and $21.4\%/\sqrt{E} \bigoplus 4\%/E$ for electrons, where E is expressed in GeV.

2.6. Monte Carlo Simulation

Monte Carlo (MC) simulation is an important part of all the MINOS analysis. We measure the neutrino interactions in the Near Detector and we use the MC to extrapolate the Near Detector spectrum to predict the unoscillated Far Detector spectrum to compare with data for evidence of spectral distortion. The prediction must take into account the ND and FD spectral differences that are present, even in the absence of oscillations, due to pion decay kinematics and beam-line geometry.

The modeling of the neutrino beam-line includes a simulation of the hadrons produced by 120 GeV/c protons incident on the NuMI target and the propagation of those hadrons and their progeny through the magnetic focusing elements, along the decay pipe and into the primary beam absorber allowing for decay of unstable particles. The production of secondary mesons in the NuMI target was calculated using the FLUKA05 Monte Carlo, which has uncertainties at the 20%-30% level stemming from a lack of relevant thick-target hadron production data. Particles exiting the target are recorded and later propagated in the GEANT3 simulation of the NuMI beam-line (GNuMI). The simulation describes the magnetic focusing horns, surrounding shielding, decay pipe and beam absorber. The GEANT-FLUKA code is used to model the secondary interactions in the horn and decay pipe as well as the full particle decay chains. Decays in which a neutrino is produced are saved and later used as input for neutrino event simulation in the Near and Far Detectors.

Neutrino interactions are modeled by the NEUGEN program. NEUGEN simulates both (quasi-)elastic and inelastic neutrino scattering. The latter includes

a Rein-Sehgal based treatment of neutrino-induced resonance production, charged and neutral-current coherent pion production and modified leading order deep inelastic scattering (DIS) model extended to improve the treatment in the transition region between DIS and resonant production. The neutrino-induced hadronic multi-particle production is simulated using the AGKY program, which employs the PYTHIA/JETSET model to simulate interactions with high invariant masses and a phenomenological model to simulate the low invariant masses. Hadrons produced in the neutrino scattering are allowed to interact while exiting the target nucleus ("final state interaction"). The final state interactions are calculated using the INTRANUKE code from within NEUGEN. The calculation incorporates pion elastic and inelastic scattering, single charge exchange and absorption.

The response of the detector is simulated using GEANT3 with the GCALOR model of hadronic interactions. The simulation randomly samples neutrinos from the flux predicted by the beam simulation and traces them through the Near and Far Detector halls. The simulation includes a detailed geometric model of the detector. The position of individual scintillator strips was determined with a precision of approximately 1 mm using cosmic-ray tracks. The magnetic field is modeled via finite element analysis driven by bench measurements of the steel B-H curve.

The final step in the simulation chain involves photon generation in the scintillator, capture and transmission of photons through internal reflection in the WLS fibers and conversion of photons to photoelectrons in the PMTs. This step uses a program written in Object Oriented (OO) C++ and based in the ROOT framework. It simulates many features including PMT cross-talk (some signal can be detected on adjacent pixels to the one being illuminated), noise, non-linearity (PMT, VA and QIE) and triggers.

2.7. Reconstruction

Neutrino interactions are reconstructed using energy deposition, timing and topology of the scintillator strips that has been "hit" by traversing particles. Since a typical 10 μs spill contains overlapping events, a spill is "sliced" into individual candidate events based on spatial and timing information of the hits. Tracks and showers are constructed from the slices which are then put together to form events. Several properties (vertex, length, angle, energy etc.) are assigned to the reconstructed tracks, showers and events.

The reconstruction software consists of an ordered chain of algorithms, each of which builds a set of calibration objects (digits, strips, slices, tracks, showers and events) that are passed to the next reconstruction algorithm. The reconstruction chain is listed below [Marshall]:

- **Digit formation** The input to the reconstruction consists of the raw data collected during a particular block of time, such as a beam spill. The input is converted into a lists of digits, each of which contains a digitized measurement of the pulse height recorded in an electronics channel, a digitized timing measurement and a list of possible associated strip ends. In the Far Detector, separate digits are formed from the scintillation light observed at the two ends of each strip, whilst the multiplexing means that every digit has eight possible associated strip end.
- **Demultiplexing** The stage of the reconstruction attempts to identify which of the eight strip ends associated with each Far Detector digit is really responsible for the scintillation light. The demultiplexing algorithm compares digits from the two sides of the detector in order to produce a list of the possible solutions in each plane. Unambiguous digit combinations are identified whenever only one pairing of strip ends can place two digits on the same strip. These unambiguous combinations, together with timing information, are used to constrain the possible event region.

- **Strip formation** The reconstruction software analyzes the list of digits in order to form strip objects, which each represent a single energy deposit in a scintillator strip. At Far Detector, strip objects are created by simply combining the digits recorded at the two ends of each scintillator strip. At the Near Detector, the scintillator strips are only read out at one end, but multiple digits can be produced for each energy deposit. Groups of digits originating at similar times from a single scintillator strip are combined to form a strip object.
- **Slicing** The high event rate at the Near Detector means that multiple neutrino interactions are expected per spill. In order to simplify the reconstruction of individual events, the list of strip objects is divided into slices. Each slice contains strips that are closely associated in space and time and which are likely to originate from a single neutrino interaction. At the Far Detector, the event rate is so low that only one slice will typically be formed. The remaining reconstruction processes are all performed separately for each slice.
- **Track finding** The primary signature of a charged current (CC) ν_μ interaction in the MINOS detectors is the presence of a muon track with a contained vertex. It is therefore very important to identify the strips produced by muon tracks and to reconstruct the kinematic properties of the muons. The track reconstruction is performed in two stages: track finding and track fitting. The track finding algorithm analyzes the topology of the strips in each slice in order to identify "seed tracks" (which specify the basic structure of a muon track).
- **Track fitting** In the second stage of track reconstruction, each seed track is used as the input to a Kalman filter. The Kalman filter uses knowledge of muon propagation in order to refine the track strip selection, extrapolate tracks into the Near Detector spectrometer and calculate many important

track properties. The muon charge sign and momentum are estimated from the curvature of the track in the magnetic field, whilst a further momentum estimate is obtained from the track range.

- **Shower finding** Within each slice, any strips that are clustered together in time and space are combined to form a shower. The energy of the shower can be calculated from the total pulse height deposited in the shower strips, after subtraction of pulse height contribution from any tracks with which strips are shared. For accurate energy reconstruction in CC ν_μ interactions, the most important showers are the vertex hadronic showers associated with the interaction between the neutrino and nucleus.
- **Event formation** The final step in the reconstruction process is the combination of tracks and showers to form events. The optimal combinations are identified by examining the spatial and temporal separations of the different tracks and showers in each slice. The reconstructed events represent the best estimates of the energy deposits associated with individual neutrino interactions. For a reconstructed ν_μ CC event, the neutrino energy is specified as the sum of the vertex shower energy and the energy of the longest track.

After the formation of events, the reconstruction process is complete. The details of each reconstructed event, including the estimated neutrino energy and properties of the tracks and showers, are recorded for the analysis.

Chapter 3

Neutrino Flux Prediction

The $\nu_\mu \to \nu_\tau$ oscillation is firmly established. The task ahead is to measure with increasing precision the oscillation parameters, $\sin^2 2\theta_{23}$ and Δm^2_{23}. The most sensitive determination of these parameters is conducted by measuring the disappearance of ν_μ during the 735 km flight of ν_μ from the source, Near Detector (ND) at Fermilab, to the Far Detector (FD) at the Soudan mine. A question of fundamental import is: is $\sin^2 2\theta_{23}$ unity? Furthermore, precision on $\sin^2 2\theta_{23}$ has a direct impact on the search for θ_{13} and the CP-violating parameter, δ_{CP}. Additionally, sensitive search of $\sin^2 2\theta_{13}$ down to a few percent level is one of the goals of the NuMI/MINOS program. Finally searches for anomalous oscillation phenomena in the $\overline{\nu}_\mu$ induced charged-current (CC) events — unique to MINOS — and the neutrino induced neutral current (NC) interactions are an integral part of the oscillation research program.

Measurements and discoveries of the elements of the neutrino mass matrix outlined above critically depends upon the precision with which one can predict the neutrino flux ratio in the Far Detector with respect to the Near Detector as a function of the neutrino energy (E_ν) and the ν_e/ν_μ flux ratio.

3.1. Error in Neutrino Flux Prediction

The error in neutrino flux prediction arises from the following factors:

- Poor measurements of the secondary meson production in p-Nucleus Collision: The cross section ($\frac{d^2\sigma}{dx_F dp_T}$) of secondary mesons, $\pi^\pm$, $K^\pm$, and K^0_L, produced in the 120 GeV proton-Carbon collision is either poorly measured or non-existent.

- Beam focusing error: The misalignment of target and horn, the mis-calibration of horn current and baffle scraping can cause a systematic difference between the predicted neutrino flux and the true neutrino flux.
- Poor measurement of the neutrino-nucleon/nucleus cross section at $E \leq 10\,\mathrm{GeV}$.
- Error in the neutrino energy scale: The total neutrino energy is measured by adding the muon energy (E_μ) which is systematically well measured ($\pm 2\%$ for stopping muon and $\pm 4\%$ for through-going muon), and the hadronic energy (E_{Had} or ν) which is systematically poorly measured ($\simeq 10\%$ in MINOS).
- Neutrino event reconstruction and background estimates

3.2. Composition of Neutrino Flux

The NuMI neutrino beam contains ν_μ, $\overline{\nu}_\mu$, ν_e, and $\overline{\nu}_e$.

- The ν_μ, produced by π^+ and K^+ decays, is entirely dominated by π^+ contributions in $E_\nu \leq 20\,\mathrm{GeV}$ region. The K^+ contributions are discernible beyond 25 GeV, and dominate the ν_μ flux for $E_\nu \geq 35\,\mathrm{GeV}$ or so.
- The $\overline{\nu}_\mu$ is dominated by the "wrong sign" π^-; only at highest energies K^- significantly contribute.
- The ν_e flux is produced by μ^+ (from π^+), K^+, and K^0_L decays. Below E_ν of 10 GeV, the μ^+ contributions ($\simeq 85\%$)dominate; in the intermediate region $10 \leq E_\nu \leq 20\,\mathrm{GeV}$, half the ν_e come from μ^+ and the rest from kaons; above 20 GeV kaons dominate. The K^0_L is estimated using the K^+ and K^-.
- The $\overline{\nu}_e$ flux is produced by μ^- (from π^-), K^-, and K^0_L decays.

3.3. Determination of Relative Neutrino Flux using low ν Events

3.3.1. Introduction. The determination of neutrino flux as a function of E_ν using the low ν events was first presented in [Mishra, 1990] . The method provides

the flux up to an overall normalization factor. We first outline the conceptual idea behind the method.

The dynamics of neutrino-nucleon scattering implies that the number of events in a given energy bin with $E_{\rm Had} \leq \nu_0$ is proportional to neutrino (antineutrino) flux in that energy bin up to corrections $\mathcal{O}(\nu_0/E)$ and $\mathcal{O}(\nu_0/E)^2$. The method follows from the general expression of the neutrino-nucleon differential cross section. With the assumptions of locality, Lorentz invariance, CP-invariance, and the V-A Lorentz structure of the weak current, one can derive an expression for neutrino (antineutrino) differential cross section in terms of structure functions, $2xF_1(x,Q^2)$, $F_2(x,Q^2)$, and $xF_3(x,Q^2)$:

$$\begin{aligned} \frac{d\sigma^{\nu(\bar{\nu})}}{dxdy} &= \frac{G_F^2 ME}{\pi} \times \\ &\left[\left(1-y-\frac{Mxy}{2E}\right)F_2^{\nu(\bar{\nu})} + \frac{y^2}{2}2xF_1^{\nu(\bar{\nu})} \pm y\left(1-\frac{y}{2}\right)xF_3^{\nu(\bar{\nu})}\right] \end{aligned} \quad (3.1)$$

where G_F is the Fermi weak coupling constant, M is the proton mass, E is the incident neutrino energy in the lab frame, and y, the inelasticity, is the fraction of the energy transferred into the hadronic system. The xF_3 term is added for neutrino interactions and is subtracted for antineutrinos. $R_L(x,Q^2)$, the ratio of the cross section for scattering from longitudinally to transversely polarized W-bosons relates $F_2(x,Q^2)$ and $2xF_1(x,Q^2)$

$$2xF_1 = F_2\left(\frac{1+(\frac{2Mx}{Q})^2}{1+R_L(x,Q^2)}\right) \quad (3.2)$$

Structure functions depend on x, the Bjorken scaling variable, the Q^2, the four momentum squared of the virtual W-boson.

The above expression is independent of specifics of nucleon composition. In particular no assumption about quark/partons as nucleon constituents need be invoked.

Furthermore the expression includes all of CC — Quasi-Elastic (QEL), Resonance (RES), and Deep-Inelastic Scattering (DIS) processes.

Using $\nu = E \times y$, and integrating the differential cross section given in Equation 3.1 over x (from 0 to 1) gives

$$\frac{d\sigma}{d\nu} = A\left(1 + \frac{B}{A}\frac{\nu}{E} - \frac{C}{A}\frac{\nu^2}{2E^2}\right) \tag{3.3}$$

where the coefficients are given by,

$$\begin{aligned} A &= \frac{G_F^2 M}{\pi}\int F_2(x)dx \\ B &= -\frac{G_F^2 M}{\pi}\int \left(F_2(x) \mp xF_3(x)\right)dx \\ C &= B - \frac{G_F^2 M}{\pi}\int F_2(x)R_{TERM}dx \end{aligned} \tag{3.4}$$

where

$$R_{TERM} = \frac{1 + \frac{2Mx}{\nu}}{1 + R_L} - \frac{Mx}{\nu} - 1$$

depends on the longitudinal structure function, $R_L(x)$. The coefficient B has a minus sign in the integral for neutrinos and a plus sign for antineutrinos.

The integration over x at fixed ν_0 (some hadronic energy cut) gives an implicit Q^2 dependence, $Q^2 = 2Mx\nu$. The implicit Q^2 dependence in the integral gives a ν dependence to the value of the coefficients A, B, and C shown above. For different value of ν the integral will be over different ranges in Q^2 . In our case, the integrals will be carried out at a fixed value of ν and the Q^2 dependence will be accounted for in the theoretical model used.

As $\nu \to 0$ the cross section Equation 3.3 becomes independent of energy. Multiplying both sides of Equation 3.3 by the flux $\Phi(E)$ gives the number of events

$$\frac{dN}{d\nu} = \Phi(E)A\left(1 + \frac{B}{A}\frac{\nu}{E} - \frac{C}{A}\frac{\nu^2}{2E^2}\right) \tag{3.5}$$

the number of events in a given energy bin (E_ν) with hadronic energy less than ν, is proportional to the flux, $\frac{dN}{d\nu} \to \Phi(E_\nu)A$. The cross section is evaluated at a small but finite value of ν, thus one must account for the energy dependence introduced by the $\frac{\nu}{E}$ terms in the cross section. The relative flux is then given by

$$\Phi(E_\nu) \propto \int_0^{\nu_0} \frac{\frac{dN(E)}{d\nu}}{1 + \langle\frac{B}{A}\rangle\left(\frac{\nu}{E} - \frac{\nu^2}{2E^2}\right) + \frac{\nu^2}{2E^2}\frac{\int F^2 R_{TERM}}{\int F_2(x)}} d\nu \tag{3.6}$$

A summary of the low ν method and, especially, the correction is well summarized in the cross section work done by [Bhattacharya].

So long as the corrections are small, the error in the relative flux will be small. Since our primary interest is relative flux determination, i.e. neutrino flux in an energy bin relative to another energy bin, variations in the coefficients do not affect the relative flux.

The prescription for the relative flux determination is as follows: we count the number of ν_μ-CC events below a certain small value of hadronic energy (ν_0). The observed number of events, up to the correction due to the finite ν_0 of the order $\mathcal{O}(\nu_0/E)$, in each total visible energy bin, which is dominated by the corresponding energy of the lepton, is proportional to the relative flux. Smaller the factor ν_0/E, smaller is the correction.

3.3.2. ν_0 Correction for ν_μ and $\overline{\nu}_\mu$ Events. The ν_0 correction computed using the NEUGEN MC does not assume the Callan-Gross relation nor does it ignore terms involving Mxy/E_ν. For a discussion of the ν_0-correction, please see [Bhattacharya]. For identical cuts, the correction function is the same. We have computed the ν_0-correction for ν_μ and $\overline{\nu}_\mu$ events for 1.0 GeV cuts as a function of E_ν, showed in Figure 3.1.

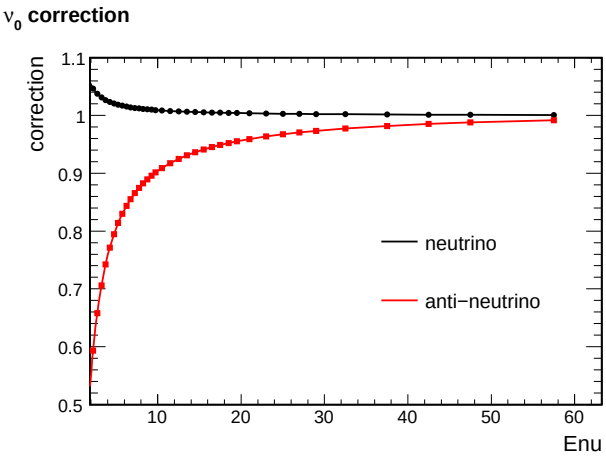

FIGURE 3.1. $\nu_0 = 1.0\,\text{GeV}$ correction as a function of E_ν for ν_μ and $\overline{\nu}_\mu$

3.3.3. A Summary of Low ν Flux Method. From the above discussion we glean that the low ν method of relative flux determination relies upon the cross section formula which can be derived without invoking the specifics of the nucleon structure and types of neutrino interactions such as scaling (DIS) or non-scaling (QEL/RES).

3.4. Empirical Parameterization of $\pi^\pm$ and $K^\pm$ using the Low ν Events in the Near Detector

Our analysis entails an empirical prarametrization (EP) of the secondary $\pi^\pm$ and $K^\pm$ production in 120 GeV p-NuMI target as a function of x_F and p_T using the relative flux determined by the low ν events in the Near Detector. The analysis should be contrasted with the 'traditional' method of using the low ν events, as in CCFR/NuTEV and in the MINOS Near Detector: start with data charged-current events with $E_{\text{Had}} \leq \nu_0$; correct for acceptance and smearing; apply the ν_0 correction to obtain the relative neutrino flux at Near Detector. (The analysis of the inclusive ν_μ cross section by Bhattacharya and Naples [Adamson et al., 2010] essentially use this method.)

The advantage of the EP analysis is as follows:

- **ND and FD Flux:** The EP constraints of pions and kaons allow us to accurately predict the Far Detector flux predicated on the Near Detector low ν events.
- **The ν_e and $\overline{\nu}_e$ Flux:** Constraining the normalization and energy dependence of π^+, and, hence, of μ^+, and K^+ allows us to predict the ν_e/ν_μ ratio at the Near and Far Detectors.
- **The Functional Form:** The EP functional form provides additional critical constraint, especially at low neutrino energies, which the traditional method lacks. This significantly alleviates the uncertainties in the coefficients, B/A and C/A, used in the ν_0 correction.

The disadvantages of the EP method are:

- **The level of agreement with the low ν ND events:** The precision of EP prediction at the Near and Far Detectors, is at best as good as the fit to the data. Our goal, however, is to obtain the ratio of FD/ND as a function of E_ν; and ν_e/ν_μ. Many systematic errors in the EP flux cancel or diminish while measuring the FD/ND and ν_e/ν_μ ratio.
- **Errors associated with beam focusing:** The traditional method is largely independent of the details of the beam focusing. The EP analysis must quantify the error in the flux prediction, and in the FD/ND ratio, due to various beam focusing related errors.
- **Functional form:** Whereas the EP functional form provides additional constraints on the flux, it also introduces uncertainty arising from different functions. Although this was one of the toughest errors to confront, it is found to be smaller than other errors.

3.4.1. Steps in the EP Analysis — Method-1. The conceptual modus operandi of the EP analysis is as follows:

(1) **Parameterization of the BMPT flux:** Using a given x_F and p_T function (see section 3.7) describing the π^+ and K^+ differential cross section, fit the BMPT flux.

(2) **Acceptance correction:** Obtain the acceptance-smearing matrix using the ν_μ-CC Monte Carlo for events with $E_{\rm Had} \leq \nu_0$. The standard "cocktail" of QEL/RES/DIS is used. [1]

(3) **Selection of ν^μ CC data with $E_{Had} \leq \nu_0$:** The data are selected using cuts identical to the standard CC selection.

(4) **Non-prompt background:** Obtain the non-prompt (NP) background (NC-induced events for ν_μ) for low ν events using the Monte Carlo. The estimates of the NP, overall level and energy dependence, is taken from the standard Monte Carlo. Unless mentioned otherwise NP backgrounds are not changed — although there are large uncertainties in the NP estimates in the MINOS Monte Carlo.

(5) **Fit the EP function:** The EP-flux is obtained by reweighting the FLUKA-flux. For a given iteration of the EP-flux, fold in the ν_0 correction; fold in the acceptance-smearing; add the non-prompt background; fit the resulting "reconstructed" MC to the data; iterate parameters till the fit converges.

We call this Method-1.

3.4.2. Steps in the EP Analysis — Method-2. An equivalent method, called Method-2, differs from Method-1 (see Sec 3.4.1) as follows:

(1) **Use the Standard ν_μ-CC Monte Carlo:** Use the standard reconstructed ν_μ charged-current Monte Carlo and the non-prompt background.

(2) **Fit the EP function:** The EP-flux is obtained by tuning the reconstructed ν_μ charged current events to the data. (One does not need to apply either

[1]The acceptance and the energy almost entirely depend upon the muon since the hadron energy is small. What matters is the acceptance of an ν_μ-CC with $E_{\rm Had} \leq \nu_0$ regardless of QEL, or RES, or DIS.

the acceptance-smearing or the ν_0 correction since the correction coefficients are computed using the Monte Carlo.)

The two methods within statistical errors yield identical flux as shown in Section 3.9.2. Our default method is the simpler Method-2.

3.5. Constraining the Electron-Neutrino Flux using Muon-Neutrinos

From the discussion above (Section 3.2), it follows that in the crucial oscillation region $E_\nu \leq 20\,\text{GeV}$ the ν_e and $\overline{\nu}_e$ are strongly constrained by the precision with which $\pi^\pm$ are determined using ν_μ and $\overline{\nu}_\mu$ data.

The empirical constraint on the ν_e and $\overline{\nu}_e$ using the ν_μ and $\overline{\nu}_\mu$ fits was first suggested, and derived, in the Dec/06 Collaboration meeting [Godley and Ling, 2006]. Table 3.1 shows an approximate composition of the sources of ν_e in NuMI. Since the ν_μ data imposes strict constraint on the shape and the normalization of the π^--induced events, it automatically yields the absolute μ^-. Godley and Ling [2006] showed that the ν_e/ν_μ ratio can be constrained at the 7% level using the EP constraints derived from ν_μ and $\overline{\nu}_\mu$.

Table 3.1. An Approximate Composition of the ν_e in two E_ν-bins.

ν_e Source	ND	
	$E_\nu \leq 5\,\text{GeV}$	$5 \leq E_\nu \leq 15\,\text{GeV}$
μ^+	87%	54%
K^+	10%	33%
K^0_L	3%	13%

3.6. Fit Technique

The goal of the fit is to minimize the differences between the beam MC prediction and the measured charged-current events at the Near Detector. This is achieved by adjusting the FLUKA05 π/K predictions with some function form. The data is binned in energy with 130 bins.

We use MINUIT to find the set of parameters that minimizes the χ^2 function defined in the following way:

$$\chi^2 = \sum_{\nu_\mu,\overline{\nu}_\mu} \sum_i \frac{(e_i - o_i)^2}{\sigma_{e_i}^2 + \sigma_{o_i}^2} + \sum_j \frac{p_j^2}{\sigma_{p_j}^2} \tag{3.7}$$

where i runs over the bins in data histograms and j runs over the penalty terms. The e_i and o_i are expected and observed number of events in i-th bin respectively. The expectations e_i are functions of the inputs to the Monte Carlo, such as the π/K yields off that target. The σ_{e_i} and σ_{o_i} are corresponding statistical errors.

Some of the parameters in the fit are constrained to particular values that are known with some certainty. To use the information we introduce penalty terms that are added to the function that is being minimized in the fit. The p_j is the value of certain parameter and σ_{p_j} is the penalty term for that parameter.

3.7. Hadron Production Reweighting Functional Forms

3.7.1. EP1 — BMPT-Like Function Form. We use a BMPT [Bonesini et al., 2001] type functional form to reweight the meson cross sections:

$$\begin{aligned} \left(E \times \frac{d^3\sigma}{dp^3}\right) &= A\,(1 - x_R)^\alpha\,(1 + Bx_R)x_R^{-\beta} \times \\ &\quad \left(1 + a'(x_R)p_T + b'(x_R)p_T^2\right) e^{-a'(x_R)p_T} \end{aligned} \tag{3.8}$$

where $a'(x_R) = a/x_R^\gamma$ and $b'(x_R) = a^2/2x_R^\delta$. The scaling variable $x_R = E^*/E^*_{max}$ is defined as the ratio of the energy of the meson in the center-of-momentum frame and the maximum kinematically available energy. Positive and negative mesons are assumed to have the same p_T distributions. The ratio r of positive to negative meson (π^+/π^- or K^+/K^-) is parameterized using the formulae:

$$r(\pi) = r_0 \cdot (1 + x_R)^{r_1} \tag{3.9}$$

$$r(K) = r_0 \cdot (1 - x_R)^{r_1} \tag{3.10}$$

Phenomenological rationale, following Bonesini et al. [2001], for the choice of the function is summarized below. The BMPT formula assumes an approximate factorization in x_R and p_T. The $(1 - x_R)^{\alpha}$ behavior at large x_R is theoretically motivated on the basis of quark counting rules. The $x_R^{-\beta}$ behavior empirically accounts for the non-direct hadron formation mechanism at small x_R. The p_T behavior is modelled by the known exponential fall of soft interactions and a polynomial behavior to interpolate the low p_T part of the spectrum. The x_R dependence of $a'(x_R)$ and $b'(x_R)$ is introduced to parameterize the violation of p_T invariance observed in the data. Models based on the parton structure of the hadrons predict a p_T^{-n} dependence of the cross section at large p_T, where hard scattering processes take over.

The shape of the positive to negative meson ratios is supported by some phenomenological analysis of pp data suggesting that $r(\pi) \simeq 1$ for $x_R \simeq 0$ and rises to about 5 for $x_R \to 1$, closely following the u/d ratio of valence quarks in the projectile proton, while $r(K)$ has a $(1-x_R)^{-3}$ behavior for $x_R \to 1$. Data from NA56/SPY and NA20 cover the fragmentation region of the proton at large x_R and the central region. At large x_R a functional behavior similar to that exhibited by pp data is expected.

Table 3.2 presents the default values of the BMPT parameters.

TABLE 3.2. Default values of the BMPT parameters

	A (mb/GeV^2)	B	α	β	a (GeV^{-1})	γ	δ	r_0	r_1
π	62.3	1.57	3.45	0.517	6.10	0.153	0.478	1.05	2.65
K	7.74	-	2.45	0.444	5.04	0.121	2γ	1.15	-3.17

The EP function is calculated by changing the values of A, B, α, β, a, γ, δ, r_0 and r_1 of $\pi^{\pm}$ and $K^{\pm}$.

$$\begin{aligned}
A'_{\pi} &= A_{\pi} \cdot (1 + par[0]) \qquad A'_{K} = A_{K} \cdot (1 + par[9]) \\
B'_{\pi} &= B_{\pi} \cdot (1 + par[1]) \qquad B'_{K} = 0 \\
\alpha'_{\pi} &= \alpha_{\pi} \cdot (1 + par[2]) \qquad \alpha'_{K} = \alpha_{K} \cdot (1 + par[10]) \\
\beta'_{\pi} &= \beta_{\pi} \cdot (1 + par[3]) \qquad \beta'_{K} = \beta_{K} \cdot (1 + par[11]) \\
\gamma'_{\pi} &= \gamma_{\pi} \cdot (1 + par[4]) \qquad \gamma'_{K} = \gamma_{K} \cdot (1 + par[13]) \\
\delta'_{\pi} &= \delta_{\pi} \cdot (1 + par[5]) \qquad \delta'_{K} = 2 \cdot \gamma'_{K} \\
a'_{\pi} &= a_{\pi} \cdot (1 + par[6]) \qquad a'_{K} = a_{K} \cdot (1 + par[12]) \\
r'_{0\pi} &= r_{0\pi} \cdot (1 + par[7]) \qquad r'_{0K} = r_{0K} \cdot (1 + par[14]) \\
r'_{1\pi} &= r_{1\pi} \cdot (1 + par[8]) \qquad r'_{1K} = r_{1K} \cdot (1 + par[15])
\end{aligned}$$

Unlike the muon neutrino flux spectrum, electron neutrino spectrum has a significant component coming from K^0_L. These neutral kaons give rise to ν_e and $\overline{\nu}_e$ through $K^0_L \to \pi e \nu$ (K^3_{e3}) decays. By fitting muon neutrinos we don't have any sensitivity to K^0_L, however the number of produced neutral kaons can be correlated with number of charged kaons in the simple parton model:

$$N(K^0_L) = N(K^0_S) = \frac{N(K^+) + 3N(K^-)}{4} \tag{3.11}$$

This model agrees with K^0_S production within 15% up to $x_R = 0.5$ [Pavlovic].

3.7.2. EP2 — SKZP-Like Function Form. The second functional form, EP2, followed the parameterization by Pavlovic.

$$\frac{d^2N}{dx_F dp_T} = [A + Bp_T] \cdot exp\left(-Cp_T^{3/2}\right) \tag{3.12}$$

Parameters A, B and C are functions of x_F, which is defined as $x_F = 2p_L^*/\sqrt{s}$, where p_L^* and $\sqrt{s}$ are the longitudinal momentum of the detected particle and the total energy in the center-of-momentum frame. The parameter A determines the yield at low p_T, B determines the rising edge, and C determines how fast the function falls off at high p_T.

Values of A, B, and C can be found as function of x_F by fitting the p_T distributions in distinct bins of x_F. The results from the fits to A, B, and C take the form:

$$\begin{aligned} A(x_F) &= a_1 * (1 - x_F)^{a_2} * (1 + a_3 * x_F) * x_F^{-a_4} \\ B(x_F) &= b_1 * (1 - x_F)^{b_2} * (1 + b_3 * x_F) * x_F^{-b_4} \\ C(x_F) &= c_1/x_F^{c_2} + c_3 \qquad\qquad (\text{for } x_F \leq 0.22) \\ &= c_1 * e^{(c_2(x_F - c_3))} + c_4 x_F + c_5 \quad (\text{for } x_F \geq 0.22) \end{aligned} \tag{3.13}$$

To describe the hadron production, 16 parameters are introduced: 6 for π^+ and K^+ and 2 for π^- and K^-. The six parameters for the positive mesons are defined as follows:

$$\begin{aligned} A'(x_F) &= (par[0] + par[1] \cdot x_F)\, A(x_F) \\ B'(x_F) &= (par[2] + par[3] \cdot x_F)\, B(x_F) \\ C'(x_F) &= (par[4] + par[5] \cdot x_F)\, C(x_F) \end{aligned} \tag{3.14}$$

The EP Weight function for positive mesons is calculated using:

$$W(\pi^+, K^+) = \frac{[A' + B' p_T] \cdot exp\left(-C' p_T^{3/2}\right)}{[A + B p_T] \cdot exp\left(-C p_T^{3/2}\right)} \tag{3.15}$$

The weights for the negative mesons are defined as follows:

$$\begin{aligned} W(\pi^-) &= (par[12] + par[13] \cdot x_F) * W(\pi^+) \\ W(K^-) &= (par[14] + par[15] \cdot x_F) * W(K^+) \end{aligned} \tag{3.16}$$

The functional forms of BMPT (EP1) and SKZP (EP2) are quite distinct. The two functions, EP1 and EP2, provide a measure to bracket the uncertainty in the the flux prediction.

3.8. Event Selection

The analysis uses the Daikon04 version of the Monte Carlo simulation and the cedar-phy-bhcurve version of the reconstruction. The selection of the Near Detector events for the EP analysis is detailed in Table 3.3. Data are from Run1. The Table 3.3 shows the reduction of events for ν_μ and $\overline{\nu}_\mu$.

Table 3.3. The Near Detector ν_μ and $\overline{\nu}_\mu$ CC-like event selection for 1×10^{20} POT.

ν_μ selection cuts	ND	
	Data	MC
Fiducial Volume Cuts	3.38×10^6	3.03×10^6
Track Quality Cuts	3.37×10^6	3.02×10^6
Coil Hole Cuts	2.79×10^6	2.51×10^6
Low ν Cuts	8.27×10^5	7.54×10^5
ν_μ PID Cuts	6.09×10^5	5.41×10^5
$\overline{\nu}_\mu$ PID cuts	7.01×10^4	6.06×10^4

3.9. Test Studies with Mock Data

In order to test our EP fit method, we summarize a set of studies conducted with the mock data. We reweight a Monte Carlo sample with a set of hadron production tuning parameters and treat them as our "fake data".

3.9.1. The ν_μ and $\overline{\nu}_\mu$ Fits to the Mock Data. Figure 3.2 shows the ν_μ and $\overline{\nu}_\mu$ LE fit with $E_{\rm Had} \leq 1\,{\rm GeV}$. The ability of the EP-fit to reproduce the mock data satisfies a necessary systematic condition; and it also prove that our fit procedure is working well.

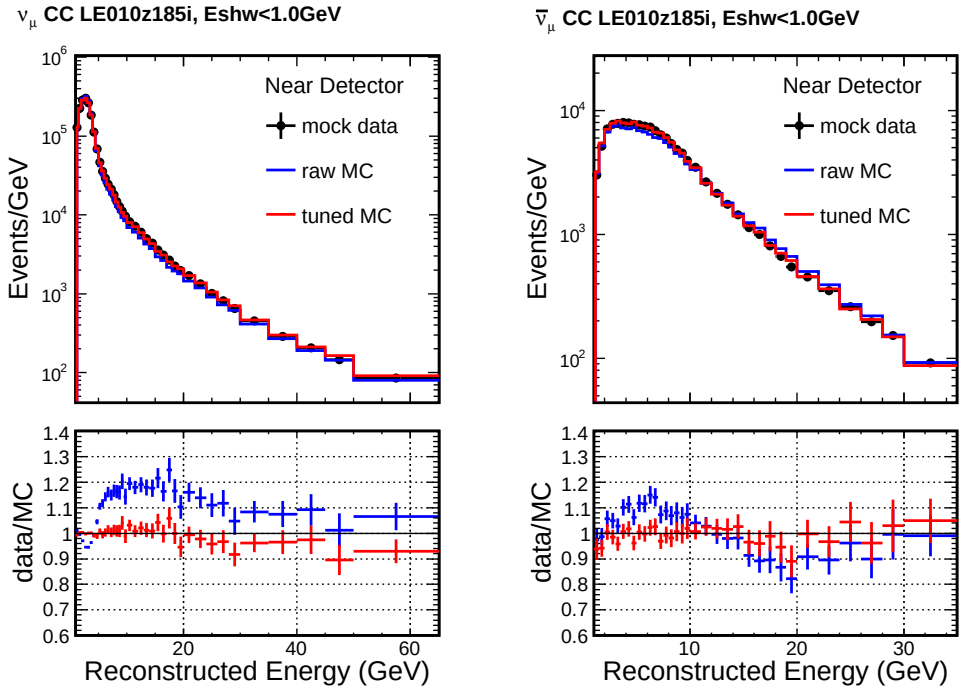

FIGURE 3.2. The EP fits to the ν_μ (left) and $\overline{\nu}_\mu$ (right) LE mock data with $E_{\rm Had} \leq 1\,{\rm GeV}$ are shown in the expanded energy range. The ratio of Data/Fit is shown below.

3.9.2. Method-1 versus Method-2. We next show the equivalence of Method-1 (Section 3.4.1) and Method-2 (Section 3.4.2). The EP fits are made to the same mock data following the two methods. Figure 3.3 compares the fitted ν_μ flux in ND, FD, and the FD/ND for the two methods. The two methods yield consistent flux in the two detectors; And more importantly, the ratio between the two ratio is unity. The $\overline{\nu}_\mu$ study, pictured in Figure 3.4, shows the same equivalence between the two methods. As we mentioned before, Method-2 is selected as our default fitting method according to its simplicity.

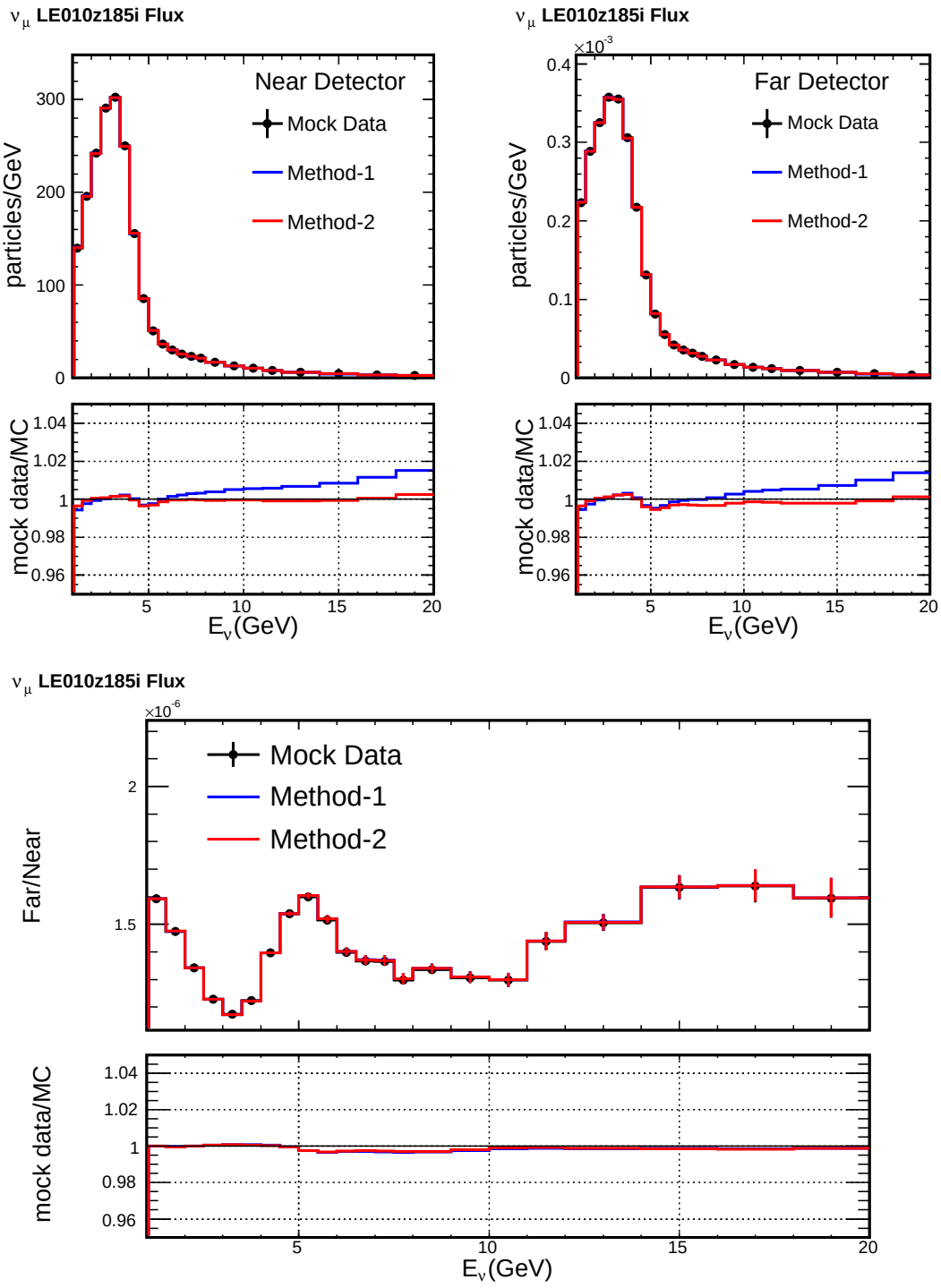

FIGURE 3.3. The fitted ν_μ flux in Method-1 .vs. Method-2: The comparison shows that the two methods of EP-fit are equivalent.

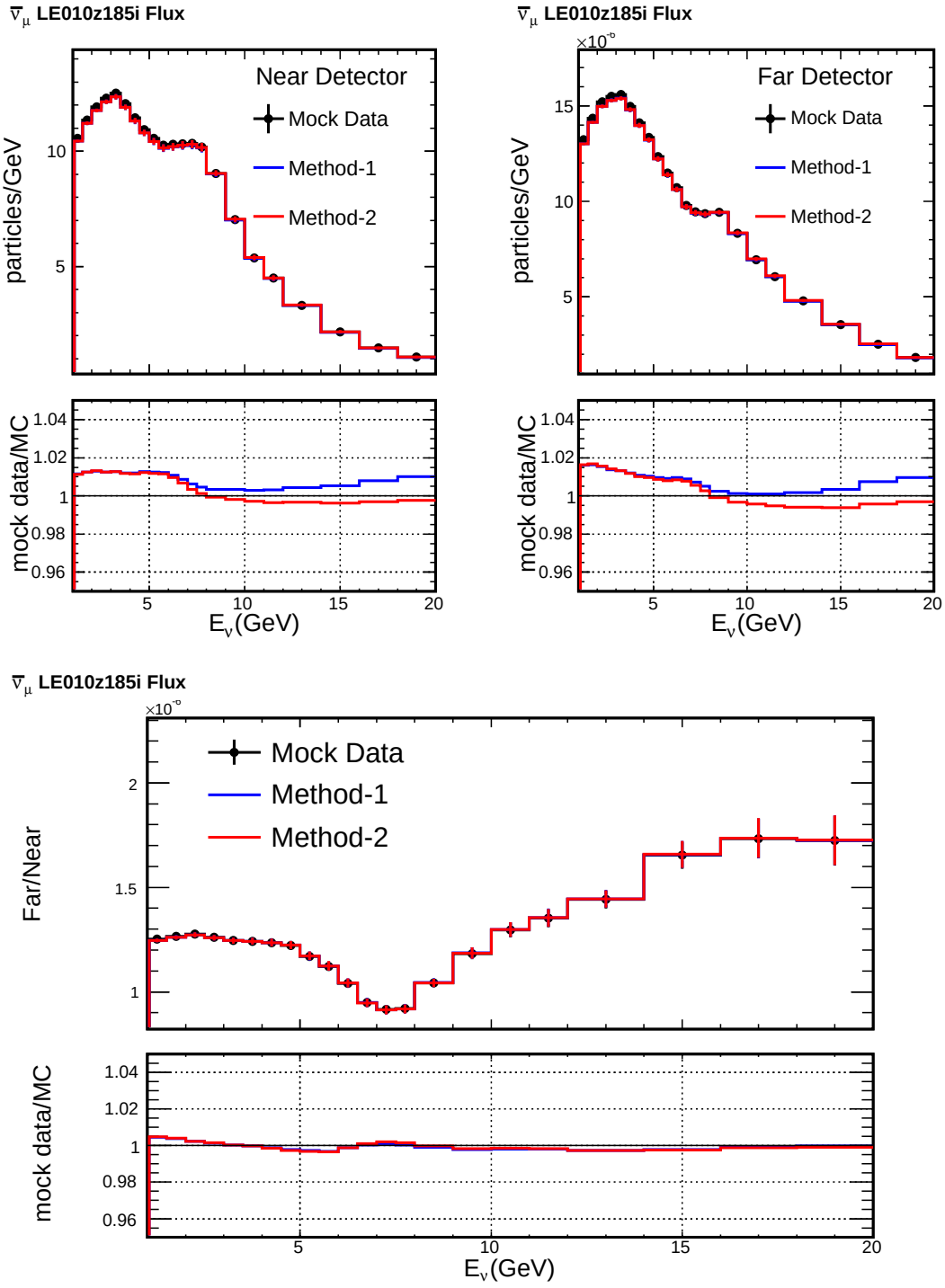

FIGURE 3.4. The fitted $\bar{\nu}_\mu$ flux in Method-1 .vs. Method-2: The comparison shows that the two methods of EP-fit are equivalent.

3.10. The EP Fit to Data

In this section we present the EP fits to the MINOS Near Detector data. First we fit the LE(L010z185i) data alone (Run1 and Run2); next we present a combined fit to the LE(L010z185i) and HE(L100z250i) data.

3.10.1. The EP Fit to the Run1 LE Data. We present the EP fit to the LE-data alone in Run1. As discussed earlier, the default EP uses the BMPT-like function, and the ν_0 cut is 1 GeV. Figure 3.5 compares the ν_μ and $\overline{\nu}_\mu$ low ν data with the corresponding EP-fits in the energy region $1 \leq E_\nu \leq 20\,\text{GeV}$ and $1 \leq E_\nu \leq 65\,\text{GeV}$. The ν_μ fit agrees with the data within 5%, or better. The $\overline{\nu}_\mu$ fit agrees within 10% although above $E_\nu \geq 20\,\text{GeV}$ the ratio is off by 20%.

The EP parameters obtained by fitting the ND Run1 data with $E_{\text{Had}} \leq 1\,\text{GeV}$ cut are shown in Table 3.4.

Table 3.4. The best fit EP parameters using ND Run1 data with $E_{\text{Had}} \leq 1\,\text{GeV}$.

	$p0$	$p1$	$p2$	$p3$	$p4$	$p5$	$p6$	$p7$
best fit	0	1.86	0.133	-0.0101	-1.96	-1.52	1.2	0
error	0	0.262	0.0235	0.0461	0.159	0.169	0.115	0
	$p8$	$p9$	$p10$	$p11$	$p12$	$p13$	$p14$	$p15$
best fit	0	-0.00205	-0.172	0.0632	1.59	-2.92	0	0
error	0	0.176	0.0787	0.159	0.169	0.264	0	0

Comparisons of the meson production cross sections obtained from the EP fits with those measured in MIPP (Main Inject Proton Production) are presented in Section 3.12.

3.10.2. The EP Fit to the Run2 LE Data. The section details the EP fits to the Run2 LE data. Compared with Run1 LE target position, during the Run2 LE running period the target position was observed be to be shifted by about 1 cm (LE009z185i).

The EP fit is carried out with the shifted target position by 1 cm. Figure 3.6 shows the ν_μ and $\overline{\nu}_\mu$ data and EP fit comparison in the $1 \leq E_\nu \leq 20\,\text{GeV}$ and $1 \leq E_\nu \leq$

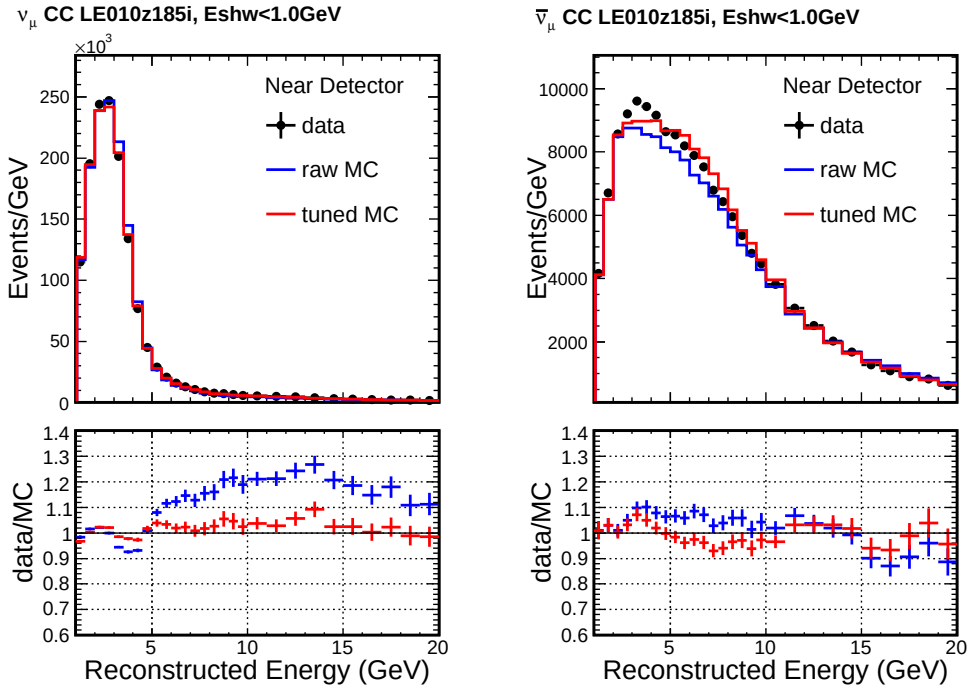

(a) Zoomed

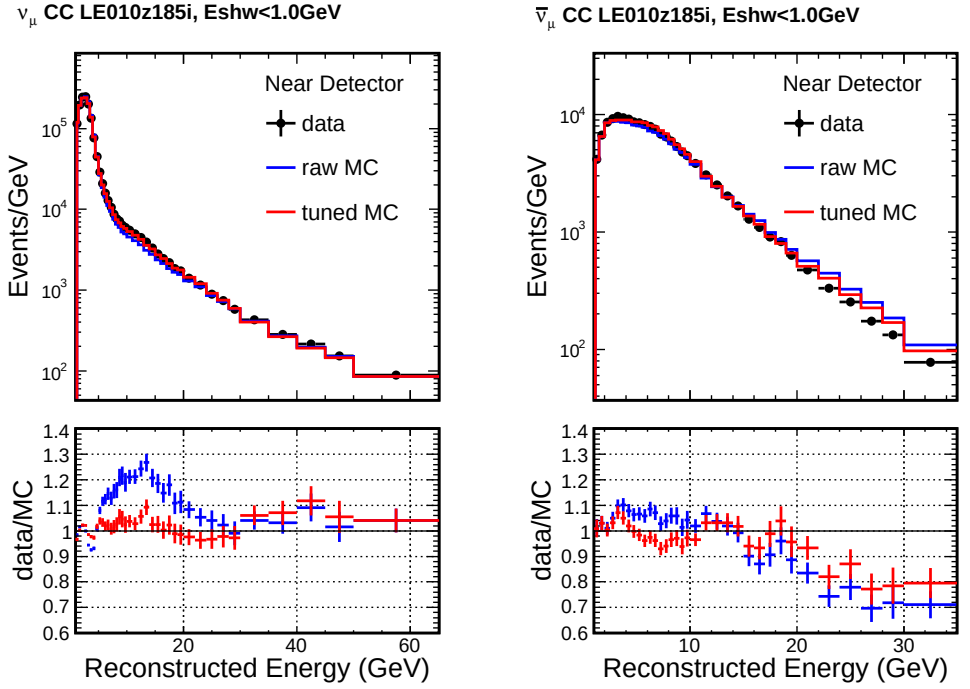

(b) All

FIGURE 3.5. The EP fit to LE Run1 data: The EP fits to the ν_μ and $\overline{\nu}_\mu$ LE-Run1 data with $E_{\mathrm{Had}} \leq 1\,\mathrm{GeV}$. The ratio of Data/Fit is shown below.

65 GeV region. The fit quality is very similar to that of Run1. The ν_μ fit agrees with the data within 5%. The $\overline{\nu}_\mu$ fit agrees within 10% although above $E_\nu \geq 20\,\text{GeV}$ the ratio is off by 20%. The EP parameters obtained by fitting the ND Run2 data with $E_{\text{Had}} \leq 1\,\text{GeV}$ cut are shown in Table 3.5.

TABLE 3.5. The best fit EP parameters using ND Run2 data with $E_{\text{Had}} \leq 1\,\text{GeV}$.

	$p0$	$p1$	$p2$	$p3$	$p4$	$p5$	$p6$	$p7$
best fit	0	1.82	0.0943	0.029	-2.06	-1.64	1.35	0
error	0	0.264	0.0231	0.045	0.158	0.179	1.205	0
	$p8$	$p9$	$p10$	$p11$	$p12$	$p13$	$p14$	$p15$
best fit	0	0.0549	-0.174	0.0576	1.76	-2.96	0	0
error	0	0.212	0.0889	0.179	0.173	0.250	0	0

3.10.3. The EP Fit to the Combined LE/HE Data from Run1 and Run2. In order to cross check the EP fit, we also preformed the EP fit to the combined LE and HE data in Run1 and Run2. Figure 3.7 compares the ν_μ and $\overline{\nu}_\mu$ low ν data in LE mode with the corresponding EP-fits; while the Figure 3.8 and compares the ν_μ and $\overline{\nu}_\mu$ low ν data in HE mode with the corresponding EP-fits. The quality of combined fit in LE mode is similar to that when using the LE alone. The HE fit, however, shows a $\pm 10\%$ variation and is very similar to the raw MC. This may imply that the disagreement between data and MC is not caused by hadron production. And the EP fit is more sensitive to the LE-data than that displayed by the HE data because of the statistics. The $\overline{\nu}_\mu$ data in HE agree with the fit in the statistically significant $E_{\text{vis}} \leq 20\,\text{GeV}$.

3.11. The EP-Predicted Composition of the ν_μ, $\overline{\nu}_\mu$, ν_e, and $\overline{\nu}_e$ Flux

The section presents the composition of the ν_μ, $\overline{\nu}_\mu$, ν_e, and $\overline{\nu}_e$ flux as predicted by the analysis. We show the composition for the Run1 fits. The composition for Run2 fits are very similar. Figure 3.9 shows the low ν ν_μ data and the MC composition

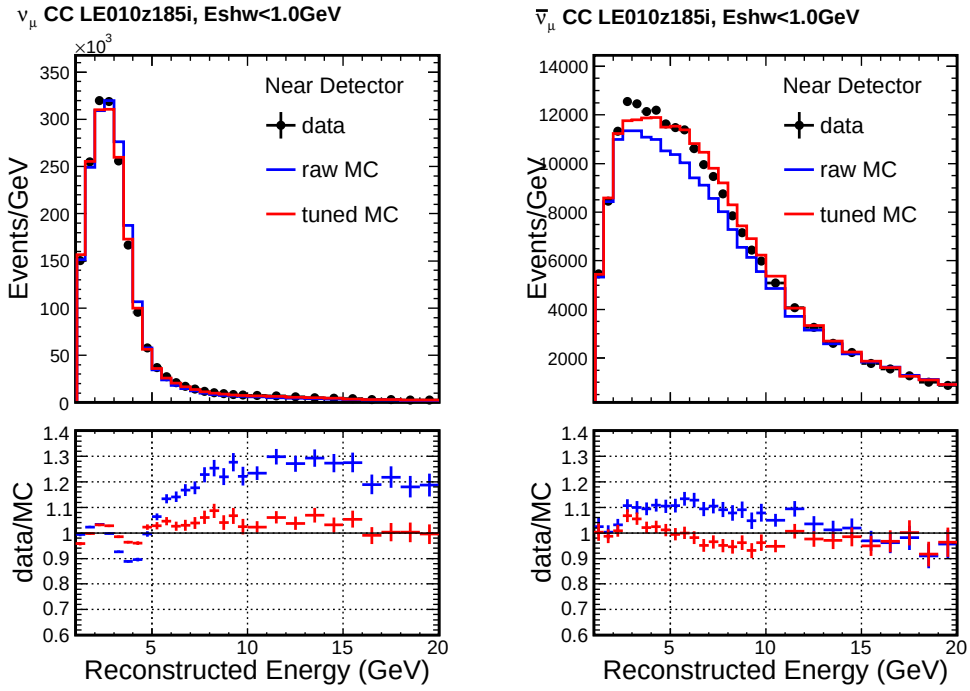

(a) Zoomed

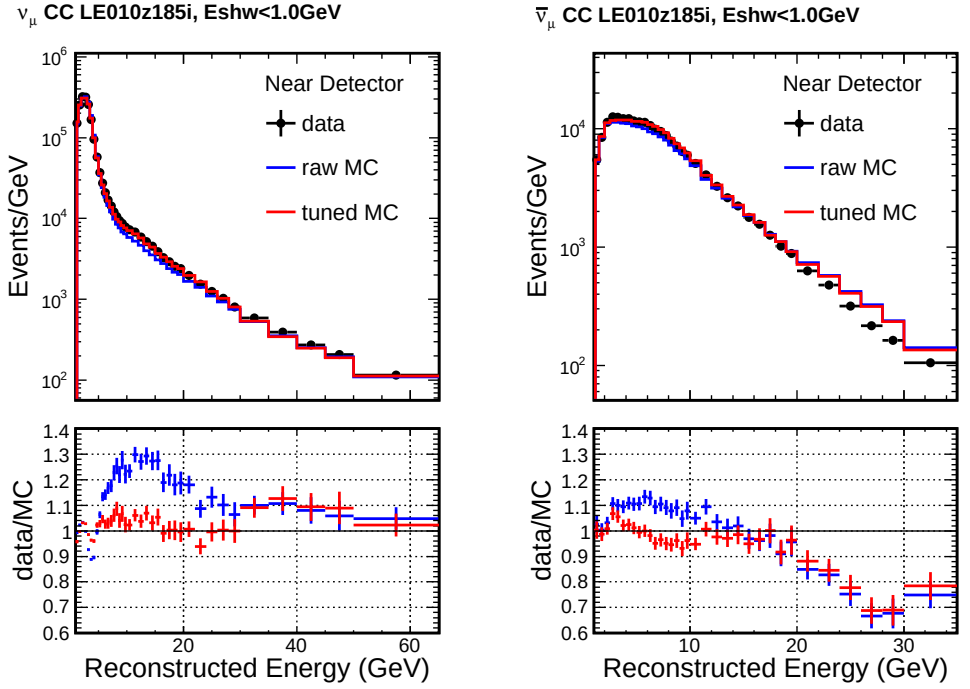

(b) All

FIGURE 3.6. The EP fit to LE Run2 Data With Shifted Target: The EP fits to the ν_μ and $\overline{\nu}_\mu$ LE-Run2 data with $E_{\text{Had}} \leq 1\,\text{GeV}$. The ratio of Data/Fit is shown below.

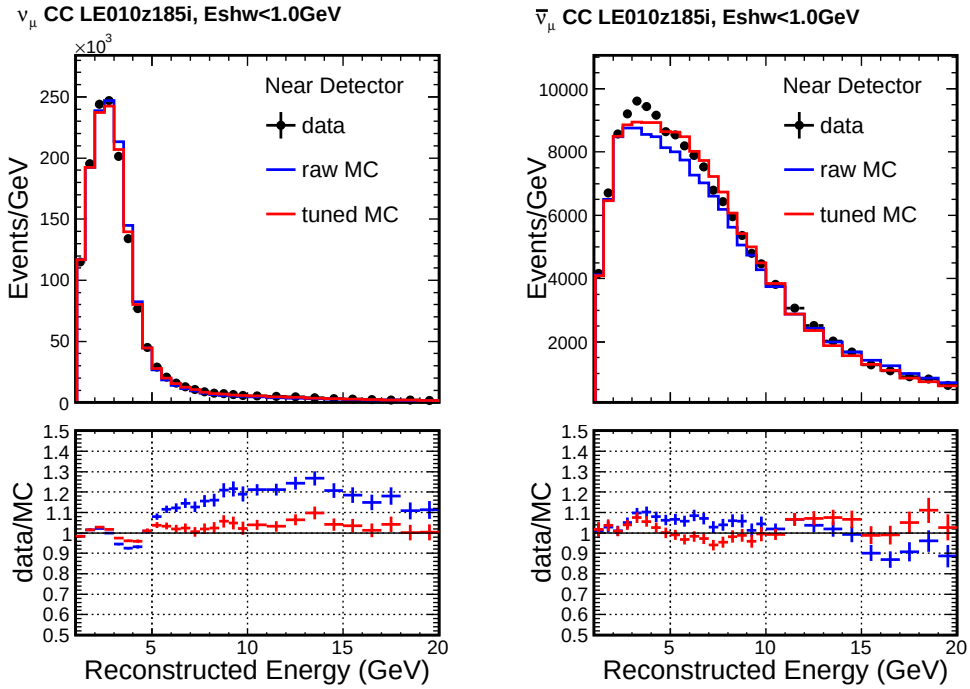

(a) Zoomed

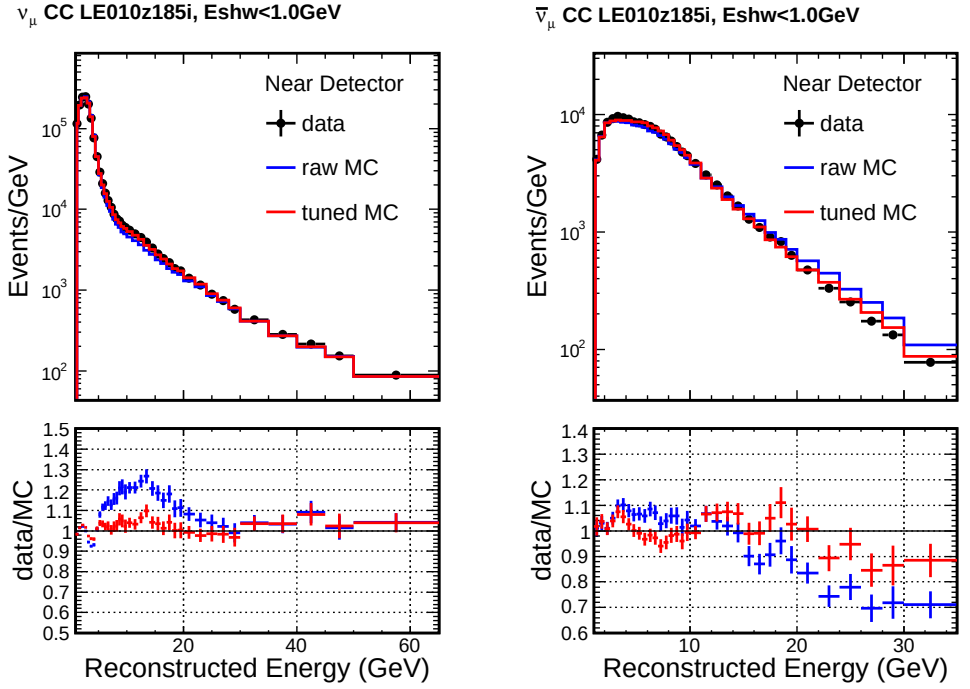

(b) All

FIGURE 3.7. The Combined EP fit to LE (Run1) and HE (Run2) Data: The EP fits to the ν_μ and $\overline{\nu}_\mu$ LE-Run1 data with $E_{\mathrm{Had}} \leq 1\,\mathrm{GeV}$. The ratio of Data/Fit is shown below.

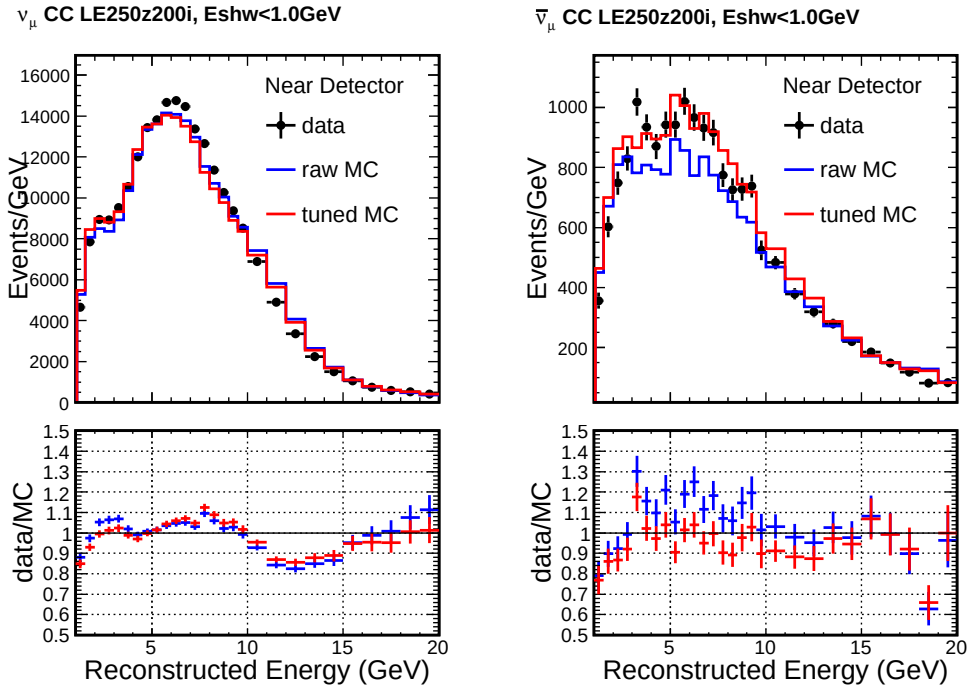

(a) Zoomed

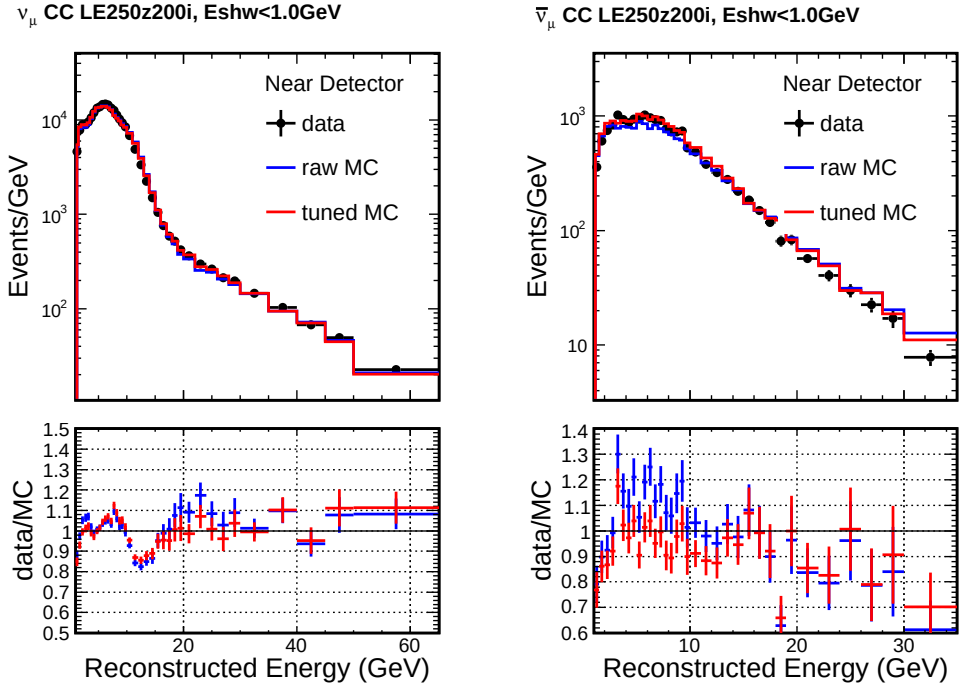

(b) All

FIGURE 3.8. The Combined EP fit to LE (Run1) and HE (Run2) Data: The EP fits to the ν_μ and $\overline{\nu}_\mu$ HE-Run2 data with $E_{\mathrm{Had}} \leq 1\,\mathrm{GeV}$. The ratio of Data/Fit is shown below.

predicted by the EP fits on a linear and log scale. The corresponding composition for $\overline{\nu}_\mu$ is presented in Figure 3.10 Finally, the EP predicted ν_e and $\overline{\nu}_e$ flux composition are shown in Figure 3.11.

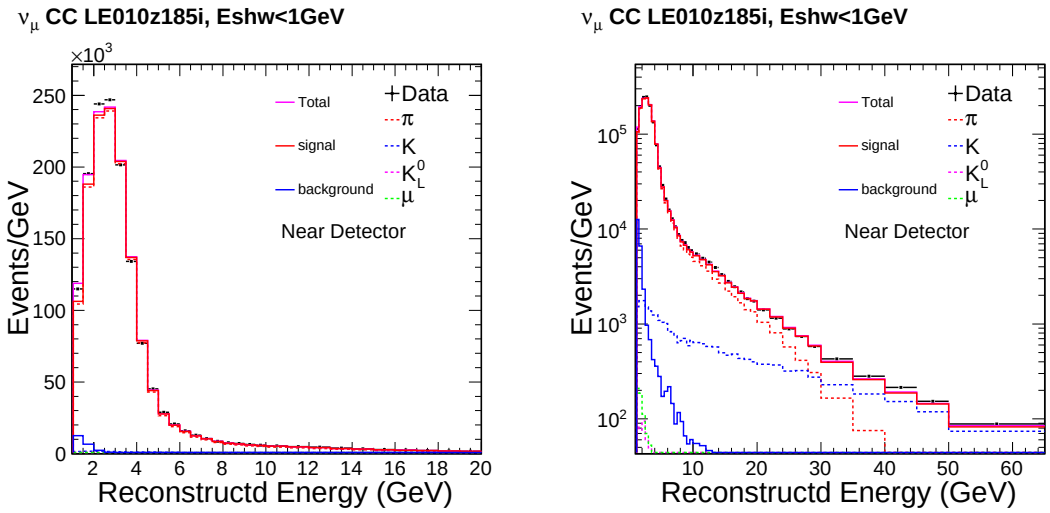

(a) Zoomed (b) All

FIGURE 3.9. Run1 low ν data sample composition for ν_μ

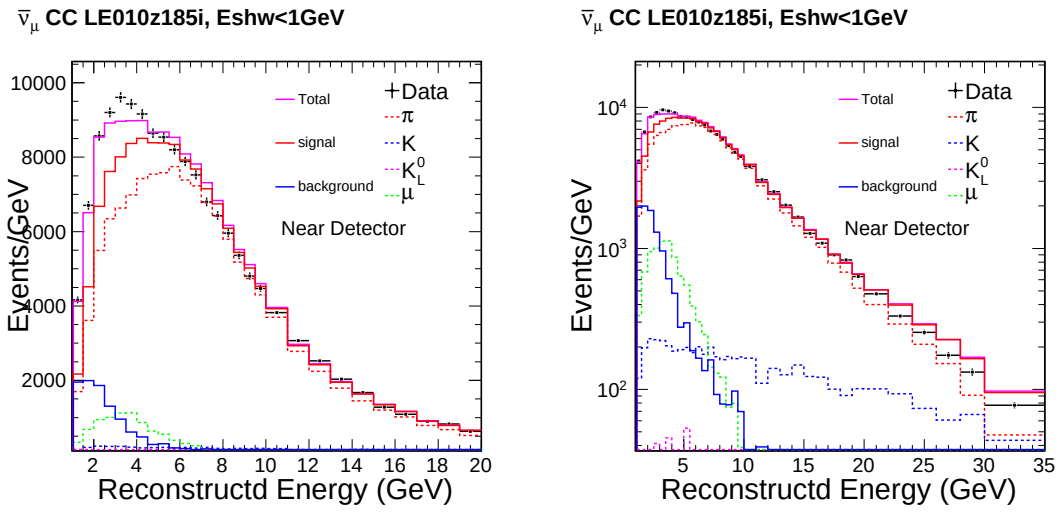

(a) Zoomed (b) All

FIGURE 3.10. Run1 low ν data sample composition for $\overline{\nu}_\mu$

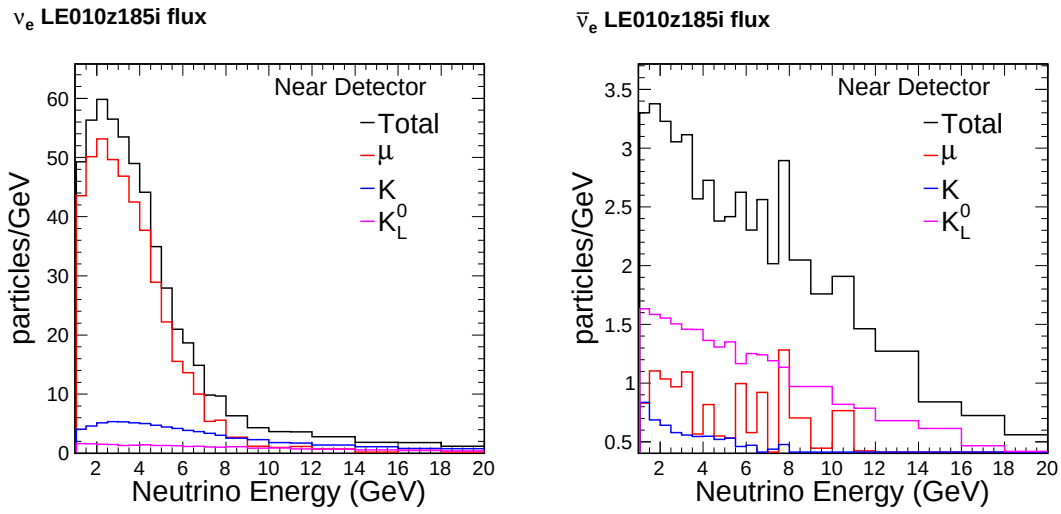

(a) ν_e (b) $\overline{\nu}_e$

FIGURE 3.11. Run1 low ν data sample composition for ν_e and $\overline{\nu}_e$

3.12. RATIO OF CROSS SECTION OF MESONS

This section presents a comparison of the ratios of meson cross section as a function of energy in p_T bins. The comparison is between the EP-fits, the available data, and other parameterizations.

Main Injector Particle Production (MIPP) experiment measures the hadron interactions at Fermilab. It also measures the secondary hadron production spectra of 120 GeV proton and NuMI target interaction. Based on the study done by Lebedev and Seun [2008] , the π^-/π^+, K^-/K^+, K^+/π^+ and K^-/π^- ratios for momenta above 20 GeV are provided. Although the statistic and systematic uncertainties associated with these ratios are quite large, we can still compare our best fit results with their measurement.

First, we present a comparison of π^-/π^+ cross section. Figure 3.12 shows that the EP fits agree with the data in the crucial region $0 \leq p_T \leq 0.4$ GeV. At higher p_T bins that minimally contribute to the MINOS neutrino data, the agreement is poor. Since we fix the π^-/π^+ ratio as the BMPT function, we have the exact same π^-/π^+

ratio as the BMPT. Comparatively, the FLUKA05 have a very different π^-/π^+ ratio from the MIPP measurement.

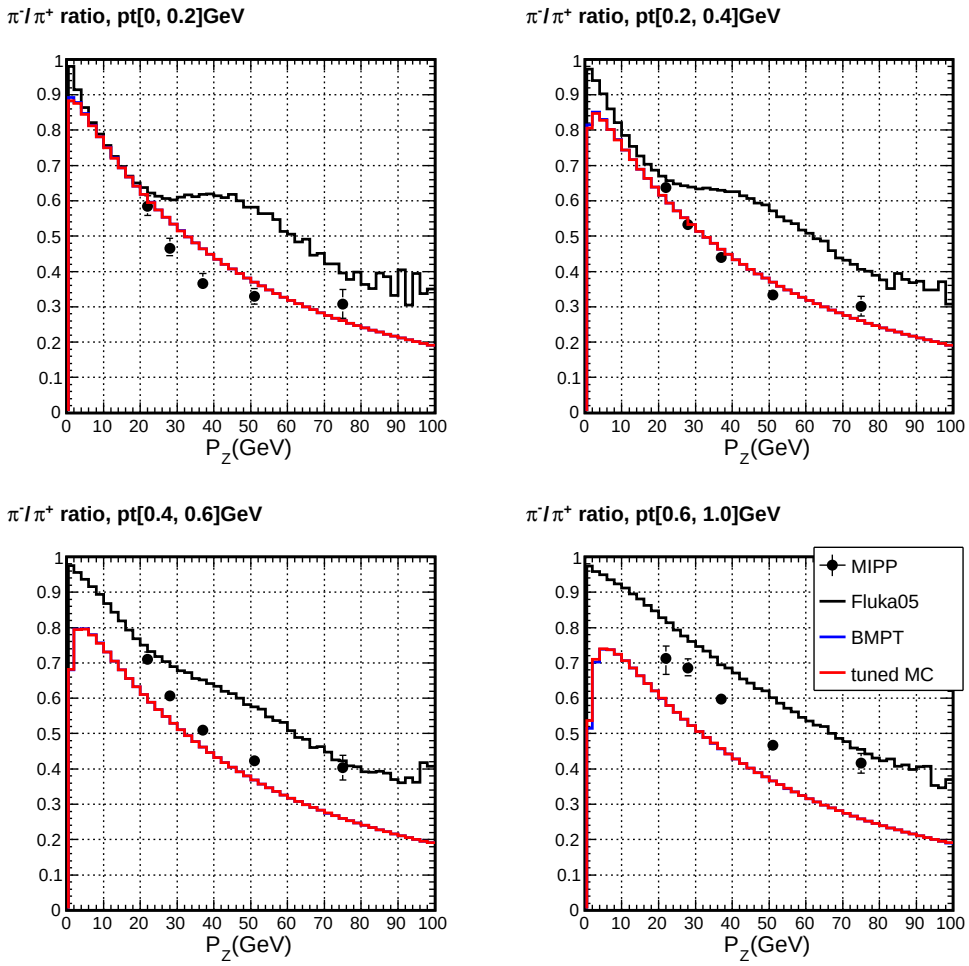

FIGURE 3.12. Comparison of Ratio of π^-/π^+ as a Function of Energy in p_T-bins: The EP-fits are compared to the available data and other parametrizations.

Next, we present a comparison of K^+/π^+ cross section. Figure 3.13 shows that the EP fits agree with the data at energies below 50 GeV; at higher energies the agreement is poor. But for the ν_e analysis this is not critical since at high energies the inherent ν_μ induced by K^- are well constrained.

Next, we present a comparison of K^-/π^- cross section. The ratios in the different transverse momentum regions are shown in Figure 3.14, all the models agree with

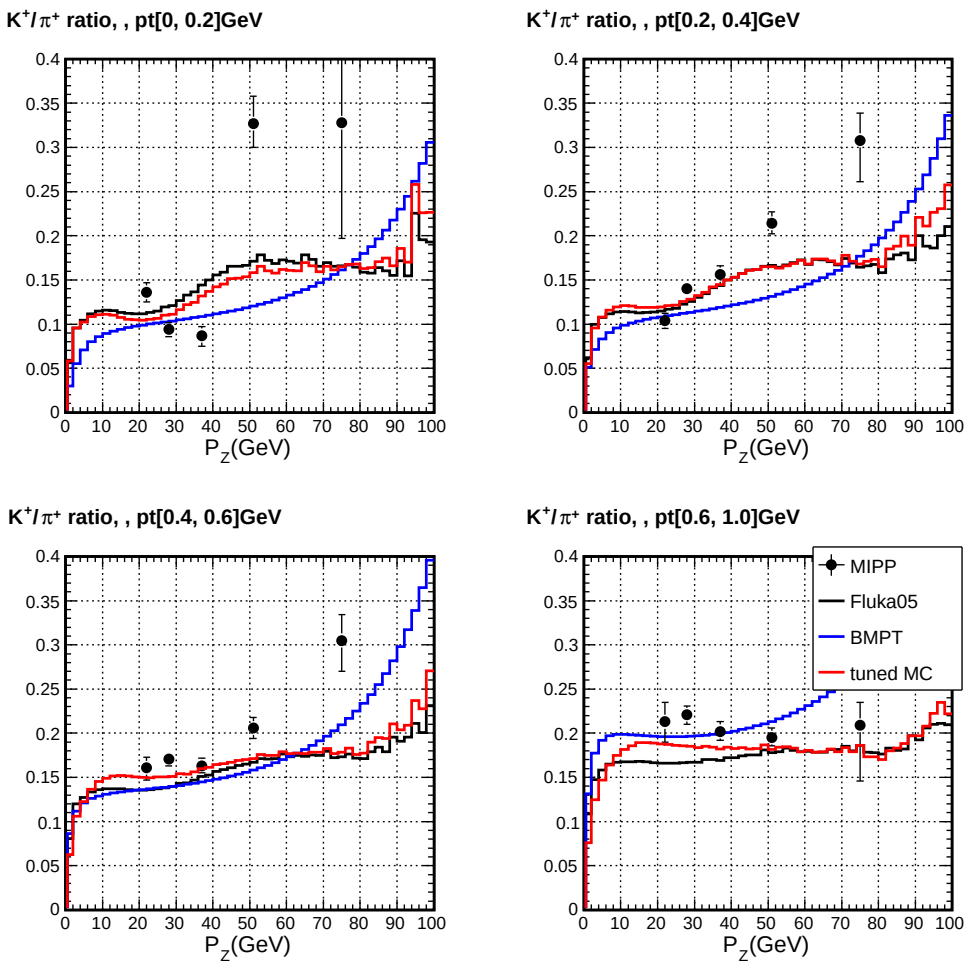

FIGURE 3.13. Comparison of Ratio of K^+/π^+ as a Function of Energy in p_T-bins: The EP-fits are compared to the available data and other parameterizations.

the data fairly well except in the $0 \leq p_T \leq 0.2\,\text{GeV}$ region where data have fairly big errors.

Finally, we present a comparison of K^-/K^+ cross section in Figure 3.15. The EP fits agree with the data fairly well.

3.13. The EP Weights for the Mesons

This section presents the EP weights associated with the π^+, π^-, K^+, and K^- in 3.16(a), 3.16(b), 3.16(c), and 3.16(d). The largest discrepancy between the data and Monte Carlo is at the high-energy tail as shown in Figure 3.5. To compensate

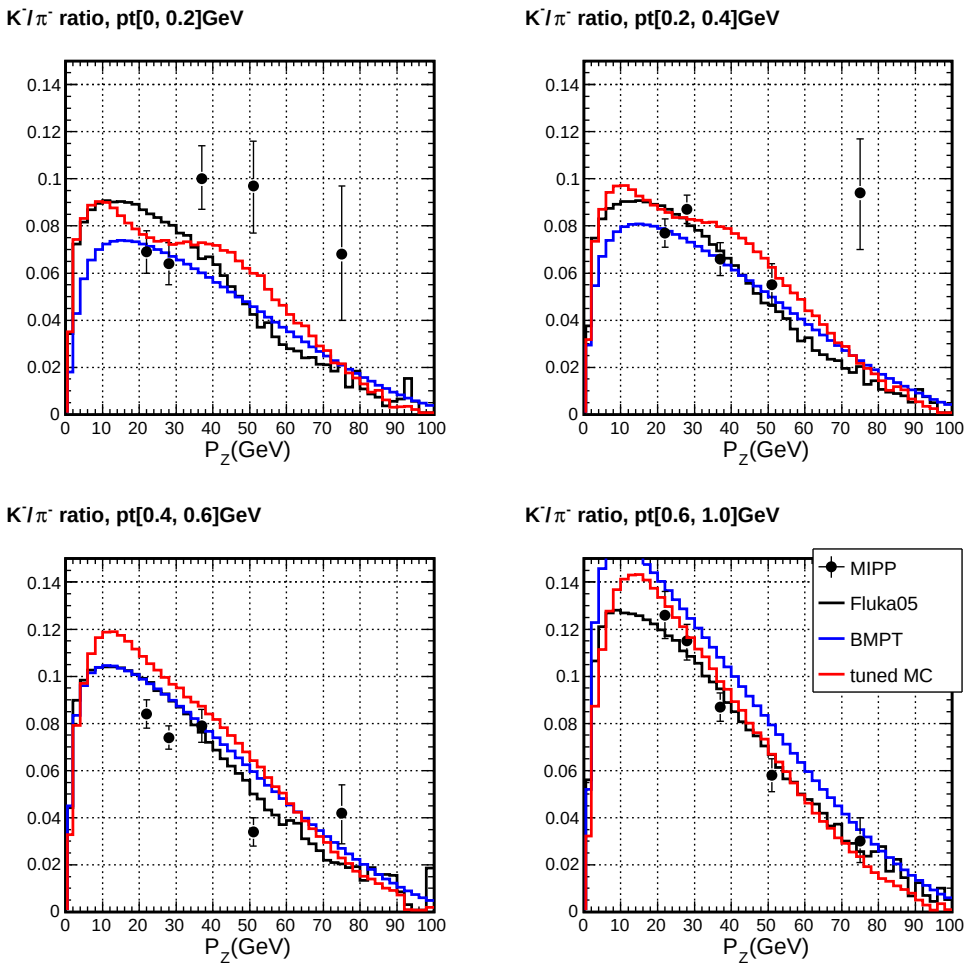

FIGURE 3.14. Comparison of Ratio of K^-/π^- as a Function of Energy in p_T-bins: The EP-fits are compared to the available data and other parameterizations.

for this, the fit should increase the relative number of hadrons at low p_T as shown in 3.16(a) and 3.16(c).

3.14. Statistical Uncertainties after the Fit

Some residual uncertainties remain due to the statistical uncertainty on the parameters used in the fit. How these uncertainties propagate into the neutrino flux can be estimated by looking at how varying the parameters of the fit affects the neutrino flux. Varying all the parameters simultaneously within 1σ away from their best-fit value is not a good way of estimating the error. Since some of the parameters are

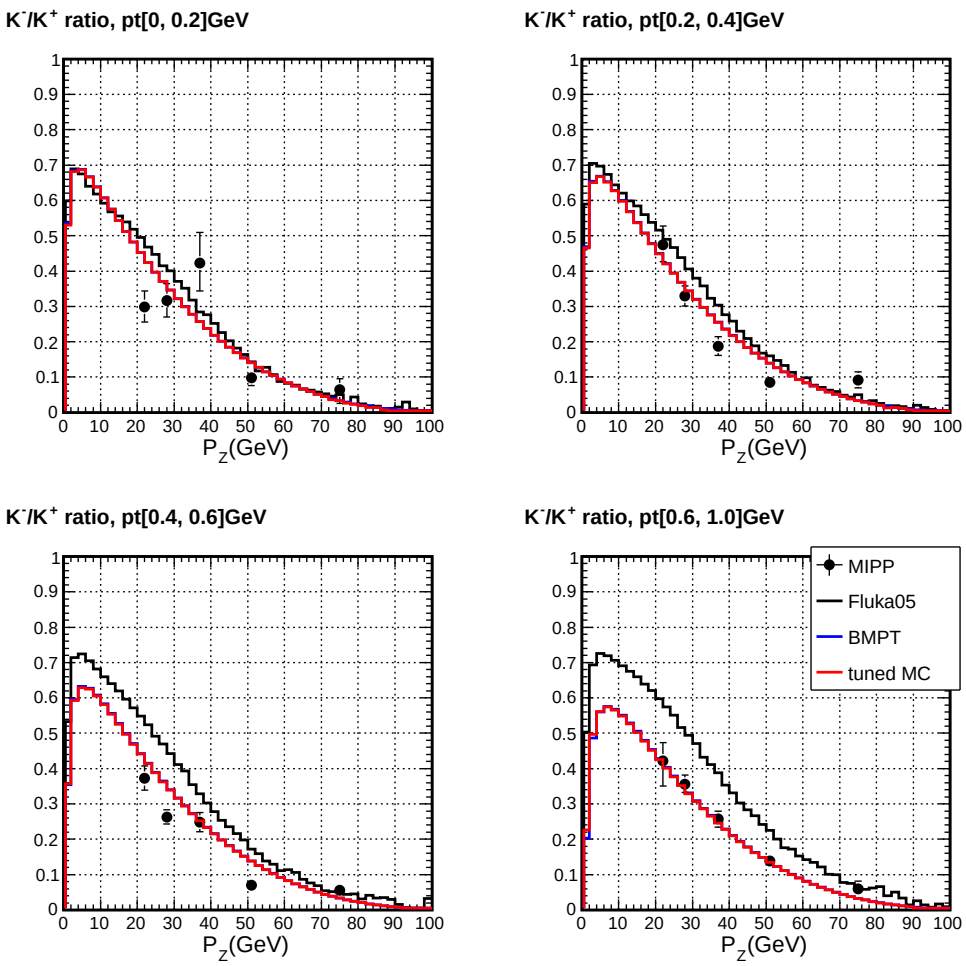

FIGURE 3.15. Comparison of Ratio of K^-/K^+ as a Function of Energy in p_T-bins: The EP-fits are compared to the available data and other parameterizations.

correlated or anti-correlated with each other. We need to take the correlation into account. Figure 3.17 shows the correlation matrix of the fit variables. Significant correlation is seen between the hadron production parameters, the cause of this is the BMPT parameterization method chosen.

Firstly, we vary each parameter by $\pm 1\sigma$ separately and calculate the ND, FD and FD/ND flux deviations of each parameter on each energy bin.

Secondly, we use the Formula 3.17 to calculate the flux errors for each energy bin, where $\mathcal{F}$ is the deviation associated with the flux, p_i is the deviation for each parameter and V_{ij} is the covariance matrix of the parameters.

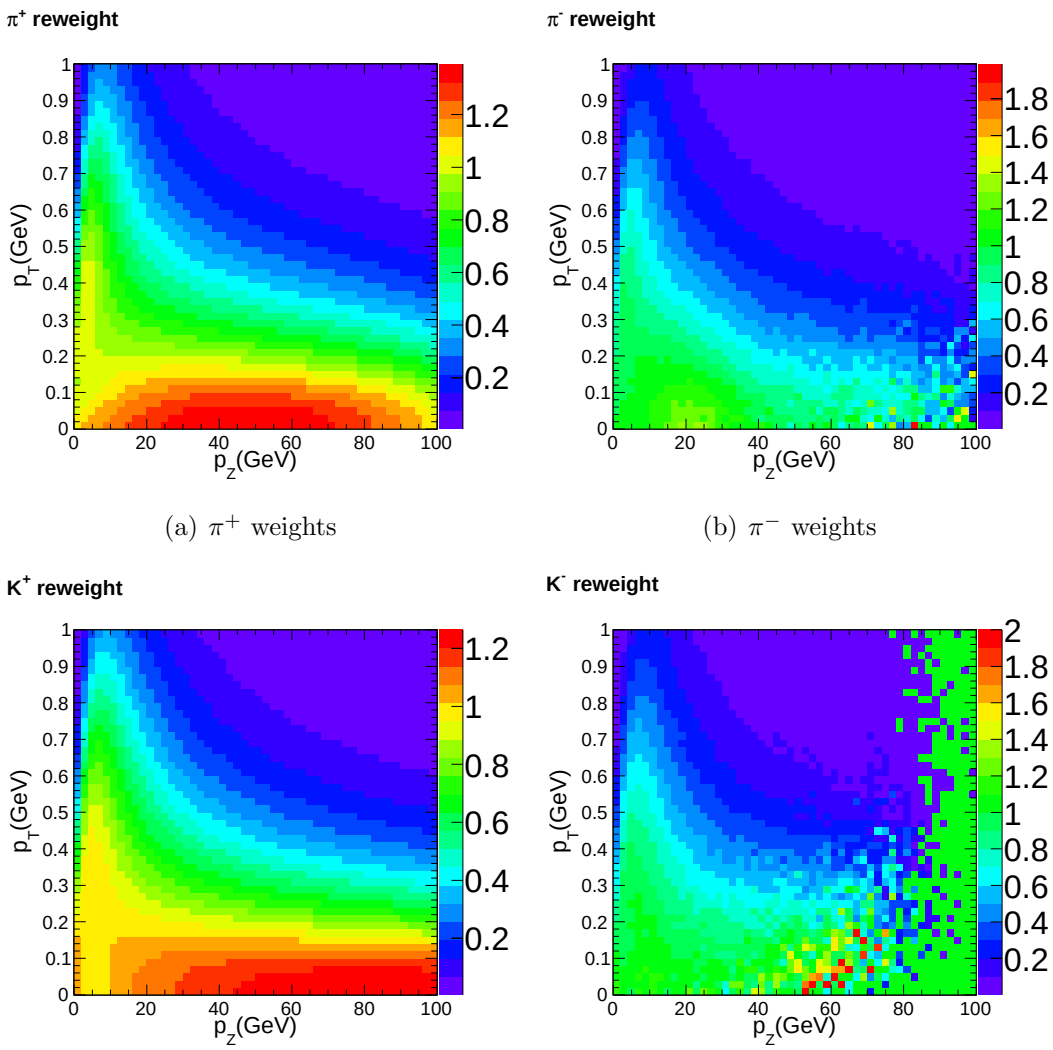

(a) π^+ weights

(b) π^- weights

(c) K^+ weights

(d) K^- weights

FIGURE 3.16. The EP Weights for the Mesons as a Function of p_T versus p_z

$$\sigma^2_{\mathcal{F}} \approx \sum_{i,j=1} \left[\frac{\partial \mathcal{F}}{\partial p_i} \frac{\partial \mathcal{F}}{\partial p_j} \right]_{\vec{p}=\vec{\mu}} V_{ij} \tag{3.17}$$

Table 3.6 shows the result for ν_μ and $\overline{\nu}_\mu$ flux. It is about 4% uncertainty for individual detector. The uncertainty in FD/ND is very tiny, less than 1%.

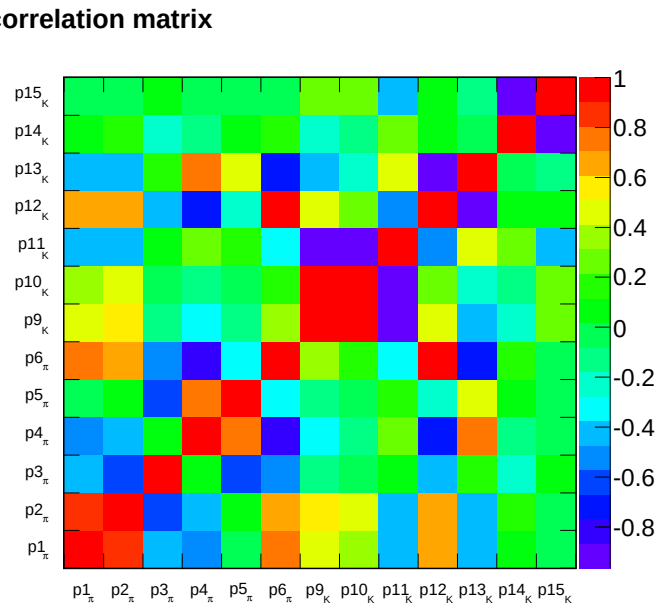

FIGURE 3.17. Correlation of fit parameters.

TABLE 3.6. Statistical uncertainties after the fit in the ν_μ and $\overline{\nu}_\mu$ flux in coarse E_ν bins: error of the number of ν_μ and $\overline{\nu}_\mu$ in the ND, FD, and the double ratio FD/ND error.

Statistical uncertainties after the fit						
E_ν		[1, 5]	[5, 10]	[10, 20]	[20, 65]	[1, 65]
ν_μ	**ND**	0.040	0.041	0.042	0.045	0.041
	FD	0.040	0.044	0.046	0.052	0.042
	F/N	0.000	0.003	0.003	0.005	0.001
$\overline{\nu}_\mu$	**ND**	0.030	0.045	0.035	0.042	0.040
	FD	0.035	0.043	0.040	0.051	0.004
	F/N	0.005	0.002	0.005	0.011	0.005

3.15. SYSTEMATICS OF EP FLUX

As mentioned in Section 3.1, there are several systematic uncertainties associated with the EP flux. In this section, we are trying to evaluate how they are going to affect the EP flux prediction for each individual detector and the F/N ratio.

3.15.1. Systematic Variation of QEL/RES/DIS Components. In Section 3.3 and Section 3.4 we argued for the conceptual insensitivity of the EP analysis of low

ν_0 flux to the QEL/RES/DIS composition of the CC-MC. Here we explicitly carry this systematic check.

According to the uncertainties associated with the quasi-elastic and resonance components, we shifted the quasi-elastic and resonance components by ±15%. The KNO parameters, which describe the resonance and deep inelastic mixed region, are changed by ±50%. All these changes are applied in the ν_μ-CC and $\overline{\nu}_\mu$-CC Monte Carlo. The EP fits are carried out for each variation and compared with the standard.

The effect of ±15% QEL-variation on the ν_μ and $\overline{\nu}_\mu$ flux are shown in Table 3.7. It quantifies the corresponding percentage systematic variation in the EP-flux, with respect to the standard, in four coarse E_ν-bins. The 15% variation in QEL causes the EP-flux in ND or FD to change by at most $\simeq 1.5\%$; there is at most 1% change in the FD/ND ratio. The systematic effect on the fitted $\overline{\nu}_\mu$ flux are similar to ν_μ with slightly larger errors.

TABLE 3.7. A ±15% QEL-variation in the ν_μ and $\overline{\nu}_\mu$ flux in E_ν bins: Shown are the ratio, variance/standard, for ν_μ and $\overline{\nu}_\mu$ in the ND, FD, and the double ratio F/N.

QEL variation ratios							
E_ν			[1, 5]	[5, 10]	[10, 20]	[20, 65]	[1, 65]
ν_μ	**ND**	-15%	1.000	0.999	1.003	1.012	1.000
		+15%	1.001	1.001	0.994	0.995	1.000
	FD	-15%	0.999	0.993	0.998	1.018	0.999
		+15%	1.001	1.006	1.002	1.011	1.002
	F/N	-15%	0.999	0.994	0.996	1.002	1.000
		+15%	1.001	1.005	1.009	1.016	1.013
$\overline{\nu}_\mu$	**ND**	-15%	1.007	1.009	1.011	1.034	1.009
		+15%	0.969	0.985	0.981	0.987	0.978
	FD	-15%	1.007	1.007	1.009	1.045	1.009
		+15%	0.986	0.992	0.992	1.008	0.990
	F/N	-15%	1.000	0.997	0.998	1.011	1.008
		+15%	1.017	1.007	1.012	1.022	1.020

The effect of ±15% Res-variation on the ν_μ and $\overline{\nu}_\mu$ flux are shown in Table 3.8. The 15% variation in RES causes the EP-flux in ND or FD to change by at most

$\simeq 2\%$; there is no perceptible change in the FD/ND ratio. The effect of this systematic variation on $\overline{\nu}_\mu$ is similar.

TABLE 3.8. A $\pm 15\%$ resonance variation in the ν_μ and $\overline{\nu}_\mu$ flux in E_ν bins: Shown are the ratio, variance/standard, for ν_μ and $\overline{\nu}_\mu$ in the ND, FD, and the double ratio F/N.

Resonance variation ratios							
E_ν			[1, 5]	[5, 10]	[10, 20]	[20, 65]	[1, 65]
ν_μ	**ND**	-15%	0.999	0.996	0.989	1.002	0.998
		+15%	1.000	1.002	1.006	1.004	1.001
	FD	-15%	0.998	0.998	0.991	1.013	0.998
		+15%	1.000	1.001	1.008	1.015	1.001
	F/N	-15%	1.000	1.002	1.002	1.010	1.007
		+15%	1.001	0.998	1.003	1.008	1.006
$\overline{\nu}_\mu$	**ND**	-15%	0.991	0.991	0.987	1.005	0.991
		+15%	0.983	1.001	1.004	1.014	0.995
	FD	-15%	0.999	0.993	0.990	1.019	0.996
		+15%	0.992	1.003	1.009	1.031	1.001
	F/N	-15%	1.008	1.003	1.004	1.015	1.012
		+15%	1.009	1.002	1.006	1.017	1.014

The effect of $\pm 50\%$ KNO-variation on the ν_μ and $\overline{\nu}_\mu$ flux are shown in Table 3.9. The 50% variation in KNO causes EP-flux to change by at most 1% for each detector and FD/ND ratio. The systematic effect on the fitted $\overline{\nu}_\mu$ flux is somewhat larger than that for ν_μ flux.

3.15.2. Systematic Variation of Functional Form. As shown in Section 3.7, we have introduced two functional forms to conduct the EP analysis. The two EP fits converged well. For the ν_μ flux, two parametrization methods vary by $\leq 2\%$ at individual detectors and the FD/ND ratio; and for the $\overline{\nu}_\mu$ flux, they vary by $\simeq 3\%$ at individual detectors and the FD/ND ratio in Table 3.10.

3.15.3. Systematic Variation of $\pm 20\%$ in K/π ratios. In Section 3.12, we compared our K^+/π^+ and K^-/π^- ratio with FLUKA05, BMPT and the MIPP experiment. Since in our beam fit we set the penalty term of the variation of K/π ratio at about 20% level, we need to study the systematic errors on the 20% shift on the K/π ratios.

TABLE 3.9. A ±50% KNO variation in the ν_μ and $\overline{\nu}_\mu$ flux in E_ν bins: Shown are the ratio, variance/standard, for ν_μ and $\overline{\nu}_\mu$ in the ND, FD, and the double ratio F/N.

KNO variation ratios							
E_ν			[1, 5]	[5, 10]	[10, 20]	[20, 65]	[1, 65]
ν_μ	**ND**	-50%	1.000	0.999	0.995	1.002	1.000
		+50%	1.001	0.998	0.997	1.003	1.000
	FD	-50%	1.001	0.999	0.997	1.012	1.000
		+50%	1.001	0.998	0.999	1.014	1.001
	F/N	-50%	1.000	1.000	1.002	1.009	1.007
		+50%	1.000	0.999	1.003	1.009	1.007
$\overline{\nu}_\mu$	**ND**	-50%	0.990	0.995	0.994	1.009	0.993
		+50%	0.982	0.995	0.995	1.009	0.990
	FD	-50%	0.998	0.998	0.998	1.023	0.999
		+50%	0.992	0.998	1.000	1.027	0.997
	F/N	-50%	1.008	1.002	1.005	1.015	1.012
		+50%	1.010	1.002	1.006	1.018	1.015

TABLE 3.10. Functional-form variation in the ν_μ and $\overline{\nu}_\mu$ flux in coarse E_ν bins: ratio of the number of ν_μ and $\overline{\nu}_\mu$ in the ND, FD, and the double ratio FD/ND.

Functional form variation ratios						
E_ν		[1, 5]	[5, 10]	[10, 20]	[20, 65]	[1, 65]
ν_μ	**ND**	1.001	1.000	0.995	1.029	1.001
	FD	1.001	0.988	1.001	1.051	1.001
	F/N	1.000	0.988	1.010	1.025	1.019
$\overline{\nu}_\mu$	**ND**	0.973	1.022	0.979	0.978	0.993
	FD	0.994	1.021	0.990	1.021	1.003
	F/N	1.022	1.000	1.017	1.040	1.038

Table 3.11 quantifies the corresponding percentage systematic variation in the EP-flux, with respect to the standard, in four coarse E_ν-bins. We show the effect of $\pm 20\% K/\pi$ ratio on the ν_μ and $\overline{\nu}_\mu$ flux in Table 3.11. The 20% variation in K/π ratio causes EP-flux at most 1% changes in ND, FD and FD/ND ratio; the systematic effect on the fitted $\overline{\nu}_\mu$ flux is similar.

3.15.4. Systematic Variation of ν_0 Cuts. The EP-analysis was conducted with ν_0 cuts of 0.5, 1.0, 1.5. Satisfactory fits were obtained for all these cuts for

TABLE 3.11. K/π ratio variation in the ν_μ and $\overline{\nu}_\mu$ flux in coarse E_ν bins: Ratio of the number of ν_μ and $\overline{\nu}_\mu$ in the ND, FD, and the double ratio FD/ND.

K/π variation ratios							
E_ν			[1, 5]	[5, 10]	[10, 20]	[20, 65]	[1, 65]
ν_μ	**ND**	K/π -20%	1.000	0.998	0.999	1.000	1.000
		K/π +20%	1.000	1.002	1.001	1.001	1.000
	FD	K/π -20%	1.000	0.996	0.996	1.003	0.994
		K/π +20%	1.000	1.004	1.004	0.997	1.001
	F/N	K/π -20%	0.998	0.997	0.998	0.999	0.999
		K/π +20%	1.000	1.003	1.002	1.000	1.001
$\overline{\nu}_\mu$	**ND**	K/π -20%	1.000	1.001	1.008	0.988	1.001
		K/π +20%	1.001	0.999	0.992	1.012	0.999
	FD	K/π -20%	0.997	0.999	1.007	0.994	1.000
		K/π +20%	1.003	1.001	0.993	1.005	1.000
	F/N	K/π -20%	0.998	0.998	1.000	0.998	0.998
		K/π +20%	1.002	1.002	1.000	1.001	1.001

ν_μ and $\overline{\nu}_\mu$ data. Here we compare the fitted EP flux for three different ν_0 cuts, $\leq$ 0.5 GeV, $\leq$ 1.0 GeV, and $\leq$ 1.5 GeV, at the ND, FD, and the FD/ND.

Table 3.12 quantifies the corresponding effect on the ν_μ and $\overline{\nu}_\mu$ flux. For ν_μ flux, the agreement among the fluxes is within $\pm$0.5%. The agreement among the $\overline{\nu}_\mu$ fluxes is very similar.

TABLE 3.12. ν_0 (E_{Had} cut) variation in the ν_μ and $\overline{\nu}_\mu$ flux in coarse E_ν bins: ratio of the number of ν_μ and $\overline{\nu}_\mu$ in the ND, FD, and the double ratio FD/ND.

ν_0 cut variation ratios							
E_ν			[1, 5]	[5, 10]	[10, 20]	[20, 65]	[1, 65]
ν_μ	**ND**	$\nu_0 = 0.5$	0.998	1.007	1.001	1.018	1.001
		$\nu_0 = 1.5$	1.001	0.992	0.998	1.002	0.999
	FD	$\nu_0 = 0.5$	0.999	1.004	0.997	1.006	1.000
		$\nu_0 = 1.5$	1.001	0.995	1.001	1.010	1.001
	F/N	$\nu_0 = 0.5$	1.000	0.996	0.997	0.994	0.995
		$\nu_0 = 1.5$	1.000	1.003	1.003	1.006	1.005
$\overline{\nu}_\mu$	**ND**	$\nu_0 = 0.5$	1.022	1.020	1.016	1.038	1.021
		$\nu_0 = 1.5$	0.980	0.983	0.986	0.976	0.982
	FD	$\nu_0 = 0.5$	1.016	1.018	1.013	1.024	1.017
		$\nu_0 = 1.5$	0.984	0.985	0.989	0.986	0.986
	F/N	$\nu_0 = 0.5$	0.995	0.998	0.997	0.999	0.998
		$\nu_0 = 1.5$	1.005	1.002	1.003	0.999	1.000

3.15.5. Systematic Variation of Beam Focusing Uncertainties. Incorrect alignment or modeling of the focusing will change the neutrino energy spectrum. They includes the following uncertainties: the uncertainty on the number of proton on target; the alignment of horn and target; the modelling of current in the horn and the fraction of the beam scraping the upstream shielding components.

Uncertainties from these effects can be calculated by the Monte Carlo simulation. However since we can constrain the neutrino flux uncertainty with the Near Detector data, it will have a slightly different systematic change to the pure Monte Carlo simulation.

According to the systematic uncertainties quoted by Pavlovic [2006], we shifted each beam transport uncertainty systematically by $\pm 1\sigma$ and refit to the Near Detector data.

Table 3.13, Table 3.14, Table 3.15 and Table 3.16 quantifies the corresponding percentage systematic variation associated with ν_μ and $\overline{\nu}_\mu$ flux in ND, FD and FD/ND. Baffle scrapping and horn one offset uncertainties have almost no effects on the predicted ν_μ and $\overline{\nu}_\mu$ fluxes. The horn current variation and horn current distribution will change the ν_μ and $\overline{\nu}_\mu$ flux about 1.5% separately.

TABLE 3.13. Baffle scrapping uncertainty in the ν_μ and $\overline{\nu}_\mu$ flux in coarse E_ν bins: ratio of the number of ν_μ and $\overline{\nu}_\mu$ in the ND, FD, and the double ratio FD/ND.

Baffle scrapping variation ratio						
E_ν		[1, 5]	[5, 10]	[10, 20]	[20, 65]	[1, 65]
ν_μ	**ND**	0.999	1.004	0.999	1.000	1.000
	FD	1.000	1.001	0.998	0.999	1.000
	F/N	1.000	0.997	0.999	0.998	0.998
$\overline{\nu}_\mu$	**ND**	1.002	0.997	0.998	1.003	0.999
	FD	1.000	0.996	0.996	1.002	0.998
	F/N	0.998	0.999	0.998	0.999	0.999

3.15.6. Systematic Variation of the E_{Had}-Scale Uncertainty. The error on the energy scale is dominated by the hadronic energy scale. The estimate on the E_{Had}-scale error is about 10% excluding the error on the E_{Had} in FD relative to ND.

TABLE 3.14. Horn1 position offset in the ν_μ and $\overline{\nu}_\mu$ flux in coarse E_ν bins: ratio of the number of ν_μ and $\overline{\nu}_\mu$ in the ND, FD, and the double ratio FD/ND.

Horn1 offset variation ratio						
E_ν		[1, 5]	[5, 10]	[10, 20]	[20, 65]	[1, 65]
ν_μ	**ND**	0.999	1.004	0.999	1.002	1.000
	FD	1.000	1.003	0.997	1.001	1.000
	F/N	1.000	0.999	0.998	0.998	0.998
$\overline{\nu}_\mu$	**ND**	1.004	0.998	1.001	1.006	1.001
	FD	1.001	0.997	0.998	1.005	0.999
	F/N	0.997	0.998	0.998	0.998	0.998

TABLE 3.15. Horn current distribution variation in the ν_μ and $\overline{\nu}_\mu$ flux in coarse E_ν bins: ratio of the number of ν_μ and $\overline{\nu}_\mu$ in the ND, FD, and the double ratio FD/ND.

Horn current distribution variation ratios							
E_ν			[1, 5]	[5, 10]	[10, 20]	[20, 65]	[1, 65]
ν_μ	**ND**	-1σ	1.000	0.997	1.003	0.997	1.000
		$+1\sigma$	0.999	1.004	0.997	1.006	1.000
	FD	-1σ	1.004	1.000	1.017	1.007	1.005
		$+1\sigma$	0.996	1.001	0.982	0.995	0.996
	F/N	-1σ	1.006	1.006	1.014	1.021	1.018
		$+1\sigma$	0.994	0.994	0.985	0.978	0.981
$\overline{\nu}_\mu$	**ND**	-1σ	0.992	1.010	0.994	0.970	0.999
		$+1\sigma$	1.006	0.991	1.005	1.029	1.001
	FD	-1σ	1.006	1.019	1.007	0.977	1.009
		$+1\sigma$	0.995	0.983	0.992	1.022	0.992
	F/N	-1σ	1.013	1.010	1.014	1.012	1.012
		$+1\sigma$	0.989	0.991	0.986	0.987	0.987

The EP flux analysis using the low ν events promises to alleviate the E_{Had}-scale error in the oscillation measurement. This is because the analysis relies on the muon energy — *the only energy scale accurately measured in MINOS.*

To check the effect of the E_{Had}-scale error on the ν_μ and $\overline{\nu}_\mu$ flux, we use the mock data. The E_{Had} of the data is changed by $\pm 10\%$ — multiplied by 0.9 and 1.1. The EP fits with $E_{Had} \leq 1\,\text{GeV}$ are carried out on the two E_{Had}-shifted sets and compared with the standard EP. We find the following:

TABLE 3.16. Horn current variation in the ν_μ and $\overline{\nu}_\mu$ flux in coarse E_ν bins: ratio of the number of ν_μ and $\overline{\nu}_\mu$ in the ND, FD, and the double ratio FD/ND.

Horn current variation ratios							
E_ν			[1, 5]	[5, 10]	[10, 20]	[20, 65]	[1, 65]
ν_μ	**ND**	-1σ	0.998	1.009	1.001	0.996	1.000
		$+1\sigma$	1.001	0.992	0.999	1.004	1.000
	FD	-1σ	1.002	1.016	1.014	1.010	1.004
		$+1\sigma$	0.998	0.985	0.985	0.991	0.996
	F/N	-1σ	1.006	1.008	1.013	1.024	1.020
		$+1\sigma$	0.995	0.992	0.985	0.975	0.979
$\overline{\nu}_\mu$	**ND**	-1σ	0.997	1.005	0.990	0.972	0.998
		$+1\sigma$	1.003	0.995	1.010	1.029	1.002
	FD	-1σ	1.007	1.014	1.001	0.978	1.007
		$+1\sigma$	0.993	0.988	0.998	1.021	0.994
	F/N	-1σ	1.011	1.009	1.012	1.013	1.012
		$+1\sigma$	0.991	0.992	0.987	0.985	0.986

Table 3.17 contrasts the standard ν_μ and $\overline{\nu}_\mu$ flux with the E_{Had}-shifted flux. The ND or FD flux change by at most a few percent, but the FD/ND ratio is not affected.

TABLE 3.17. E_{Had} scale variation in the ν_μ and $\overline{\nu}_\mu$ flux in coarse E_ν bins: ratio of the number of ν_μ and $\overline{\nu}_\mu$ in the ND, FD, and the double ratio FD/ND.

E_{Had} scale variation ratios							
E_ν			[1, 5]	[5, 10]	[10, 20]	[20, 65]	[1, 65]
ν_μ	**ND**	-10%	1.002	0.987	1.008	1.010	1.001
		+10%	0.999	1.004	0.987	0.995	0.999
	FD	-10%	1.002	0.982	1.009	1.022	1.001
		+10%	0.999	1.009	0.987	1.000	0.999
	F/N	-10%	1.001	0.995	1.001	1.003	1.002
		+10%	0.999	1.003	1.000	1.009	1.007
$\overline{\nu}_\mu$	**ND**	-10%	0.962	0.988	1.000	1.017	0.981
		+10%	1.018	0.999	0.994	1.014	1.006
	FD	-10%	0.970	0.988	1.004	1.042	0.986
		+10%	1.021	1.001	0.995	1.014	1.009
	F/N	-10%	1.008	0.992	1.006	1.021	1.017
		+10%	1.004	1.002	0.999	1.007	1.005

3.15.7. Systematic Variation of the E_μ-Scale Uncertainty. The systematic error on the muon-energy (E_μ) scale is much smaller than that on the hadronic energy.

For the muons that range-out, the E_μ error is about 4%; for the muons that are measured by range, E_μ error is about 2%;

The EP flux analysis using the low ν events heavily relies on the precision with which the E_μ-scale is determined. To quantify the effect of the E_μ-scale error on the ν_μ and $\overline{\nu}_\mu$ flux, we again use the mock data. The E_μ of the data is changed by $\pm 2\%$ and $\pm 4\%$ for the range and curvature momentum measurement. The EP fits with $E_{Had} \leq 1\,\text{GeV}$ are carried out on the two E_μ-shifted sets and compared with the standard EP.

Table 3.18 and Table 3.19 contrast the standard ν_μ and $\overline{\nu}_\mu$ flux with the E_μ-shifted flux. The ND or FD flux change by as much as 7%. However, the FD/ND ratio is about 1-2%.

TABLE 3.18. E_μ range momentum scale variation in ν_μ and $\overline{\nu}_\mu$ flux in coarse E_ν bins: ratio of the number of ν_μ and $\overline{\nu}_\mu$ in the ND, FD, and the double ratio FD/ND.

E_μ range momentum variation ratios							
E_ν			[1, 5]	[5, 10]	[10, 20]	[20, 65]	[1, 65]
ν_μ	**ND**	-2%	1.006	0.950	0.982	1.000	0.999
		+2%	0.995	1.053	1.010	1.003	1.002
	FD	-2%	1.005	0.931	0.959	0.996	0.994
		+2%	0.995	1.074	1.032	1.026	1.006
	F/N	-2%	0.998	0.979	0.977	0.970	0.973
		+2%	1.000	1.019	1.022	1.030	1.026
$\overline{\nu}_\mu$	**ND**	-2%	0.986	0.983	1.009	1.064	0.992
		+2%	0.982	1.007	0.985	0.967	0.991
	FD	-2%	0.970	0.970	0.992	1.076	0.980
		+2%	1.023	1.027	1.009	0.989	1.020
	F/N	-2%	0.983	0.986	0.983	1.000	0.995
		+2%	1.041	1.021	1.026	1.028	1.028

3.15.8. Systematic Variation of the Decay Pipe Uncertainty. The decay production, or downstream production, refers to the neutrino that come from the decay of hadrons produced in the decay pipe rather than in the target. There are couple uncertainties associated with the decay pipe production. First it does not produce the same spectrum in the Near and Far Detectors so errors in production cross

TABLE 3.19. E_μ curvature scale variation in the ν_μ and $\overline{\nu}_\mu$ flux in coarse E_ν bins: ratio of the number of ν_μ and $\overline{\nu}_\mu$ in the ND, FD, and the double ratio FD/ND.

E_μ curvature momentum variation ratios							
E_ν			[1, 5]	[5, 10]	[10, 20]	[20, 65]	[1, 65]
ν_μ	**ND**	-4%	1.000	1.003	0.976	0.926	0.998
		+4%	1.001	0.988	1.020	1.077	1.002
	FD	-4%	1.000	0.999	0.978	0.935	0.998
		+4%	1.002	0.990	1.021	1.094	1.003
	F/N	-4%	1.000	0.998	1.002	1.013	1.010
		+4%	1.002	1.001	1.003	1.012	1.009
$\overline{\nu}_\mu$	**ND**	-4%	1.038	1.008	0.947	0.912	1.006
		+4%	0.955	0.976	1.033	1.098	0.982
	FD	-4%	1.051	1.010	0.939	0.910	1.007
		+4%	0.959	0.977	1.044	1.131	0.991
	F/N	-4%	1.013	1.002	0.992	1.006	1.004
		+4%	1.005	1.000	1.013	1.028	1.023

section do not cancel between two detectors. Second, the downstream production is modeled with GFLUKA, not FLUKA05, our preferred and tuned hadron interaction model.

The decay pipe production uncertainty is one of the hardest systematic error to evaluate. We change the mock data decay pipe production by ±20%. The EP fits are carried out on the decay pipe production-shifted sets and compared with the standard EP. We find the following: Table 3.20 contrasts the standard ν_μ and $\overline{\nu}_\mu$ flux with the decay pipe production-shifted flux. We can see that for ν_μ flux, ND or FD flux change by at most a few percent, and the FD/ND ratio is affected by about 1%. However, it has more impact on the $\overline{\nu}_\mu$ flux, about 6% for each detector and about 3% for the FD/ND ratio.

3.15.9. Summary of Systematic Errors. In this section, we summarize the composite systematic errors associated with the ν_μ and $\overline{\nu}_\mu$ flux at ND, at FD and the FD/ND ratio. The total ν_μ systematic uncertainties at the Near Detector is shown in Figure 3.18 and FD/ND ratio in Figure 3.19; the total $\overline{\nu}_\mu$ systematic uncertainties at the Near Detector is shown in Figure 3.20 and FD/ND ratio in Figure 3.21.

TABLE 3.20. Decay pipe production variation in the ν_μ and $\overline{\nu}_\mu$ flux in coarse E_ν bins: ratio of the number of ν_μ and $\overline{\nu}_\mu$ in the ND, FD, and the double ratio FD/ND.

Decay Pipe Production Uncertainty							
E_ν			[1, 5]	[5, 10]	[10, 20]	[20, 65]	[1, 65]
ν_μ	**ND**	-20%	1.003	0.989	0.989	0.991	1.001
		+20%	0.998	1.007	1.003	1.013	1.000
	FD	-20%	1.004	0.997	1.003	1.011	1.003
		+20%	0.997	1.000	0.993	1.012	0.998
	F/N	-20%	1.002	1.008	1.015	1.018	1.016
		+20%	0.998	0.992	0.990	0.995	0.997
$\overline{\nu}_\mu$	**ND**	-20%	0.914	0.963	0.977	0.975	0.945
		+20%	1.056	1.027	1.014	1.043	1.037
	FD	-20%	0.939	0.974	0.998	1.012	0.966
		+20%	1.047	1.020	1.002	1.037	1.028
	F/N	-20%	1.027	1.011	1.025	1.033	1.030
		+20%	0.991	0.935	0.987	1.000	0.997

In the Near Detector, the total systematic uncertainty associated with ν_μ relative flux is about 5-7%; And the uncertainty for the FD/ND ratio is less than 3%, especially in the low energy region, $1 \leq E_\nu \leq 5\,\text{GeV}$. The main contributions are from the muon energy scale (range measurement in the low energy region and curvature measurement in the high energy region), beam focusing uncertainties and function form.

For the $\overline{\nu}_\mu$ flux, since the antineutrino parents, π^- and K^-, are defocused by the horn magnet field and detector magnetic field, it has quite larger and different systematic uncertainties from ν_μ flux. In the Near Detector, the total systematic uncertainty is about 10%, except in the low energy region, $E_\nu \leq 2\,\text{GeV}$; And the uncertainty for the FD/ND ratio is about 4%. The largest systematic uncertainties come from the decay pipe production, muon range measurement, beam focusing and functional form.

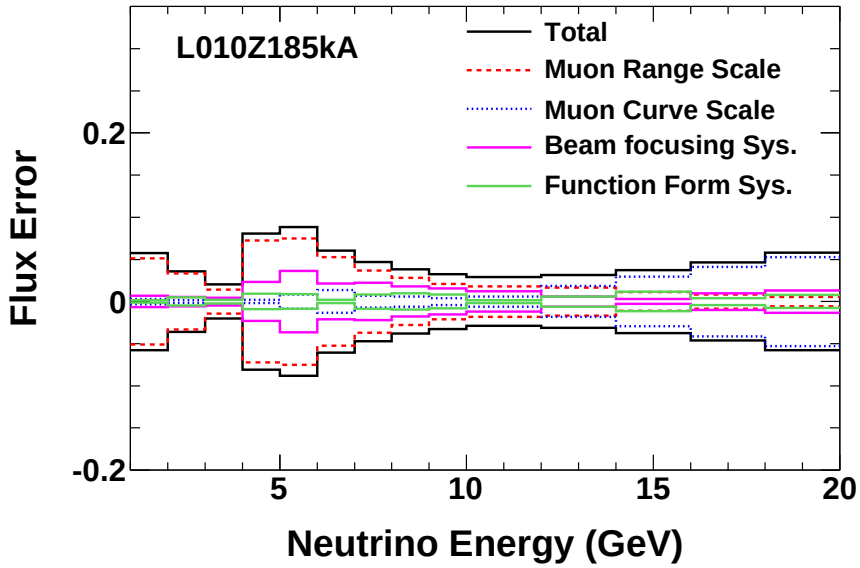

FIGURE 3.18. Total Systematic error on the EP-Determined ν_μ flux in the Near Detector.

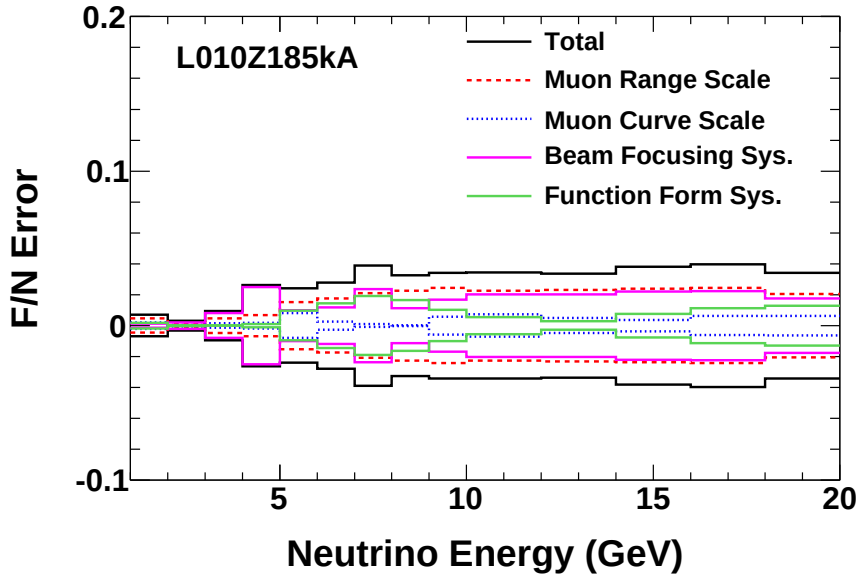

FIGURE 3.19. Total Systematic error on the EP-Determined ν_μ flux of the Far/Near ratio.

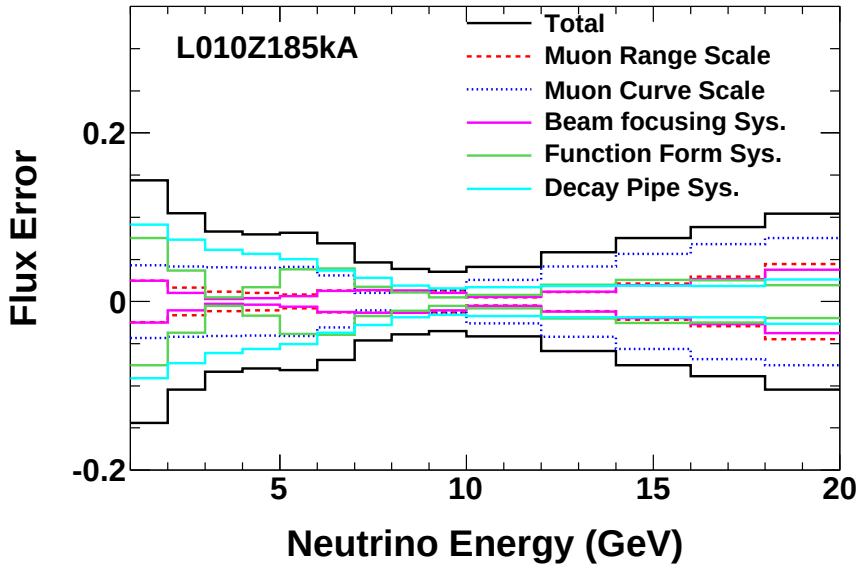

FIGURE 3.20. Total Systematic error on the EP-Determined $\overline{\nu}_\mu$ flux in the Near Detector.

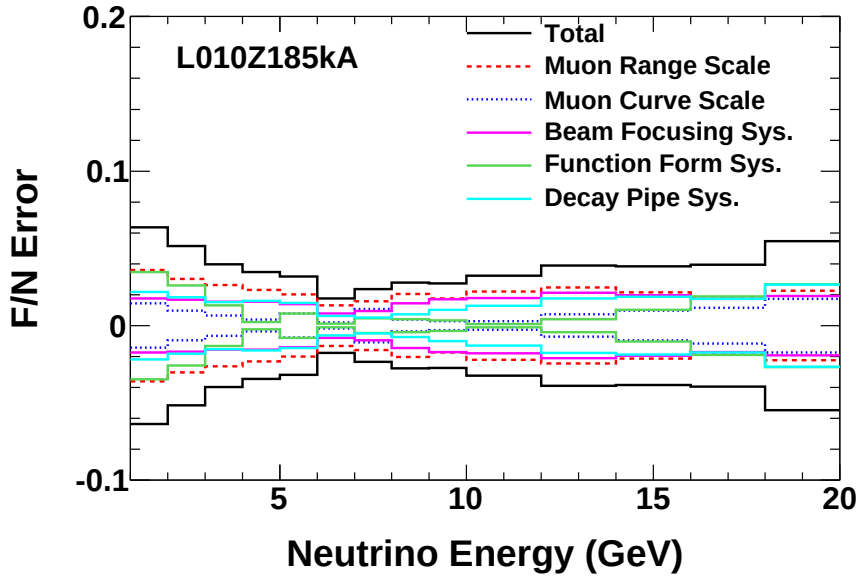

FIGURE 3.21. Total Systematic error on the EP-Determined $\overline{\nu}_\mu$ flux of the Far/Near ratio.

Chapter 4

Near Detector Data

After EP fit is done in Chapter 3, a direct comparison of all of the data in the Near Detector can be made. This serves as an important check for the EP fit. The tuned Monte Carlo should be checked with different physics distributions to see if any problems or discrepancies result from the tuning. We also need to extrapolate the Near Detector data and make the unoscillated prediction for the Far Detector. A detailed comparison will be done for the data sets that will be used in the oscillation analysis: the le010z185i(Run1) and le010z185i(Run2) configuration.

4.1. Selection Cuts

The following cuts were determined by the collaboration at large to provide a standard sample of CC-like events selected with high efficiency.

- **Data quality:** The bad runs are rejected based on a run by run scan of the online monitoring files. An entire run was flagged as bad if at any time in the run there were problems.
- **Beam quality:** Require that the spill come from a time with reliable beam quality.
- **Coil current:** Require that the current in the coil be at the nominal value and that the data was taken with the field orientation in which negative particles are focused.
- **Fiducial Volume:** The fiducial volume is defined as a cylinder around the beam center. The longitudinal z position of the vertex is between 1 m and 5 m and the transverse position of the vertex to be within 0.8 m around the

beam center. Figure 4.1 shows the fiducial volume cuts in the x and y 2D direction.

- **Track quality:** Each event is required to have a reconstructed track. The track is required to pass the track fitting algorithm or satisfy the track reclamation cut. The track reclamation cut can reclaim tracks for which the track fitter failed to converge, but the momentum can be reliably reconstructed from range. This reduces a bias seen in the track fitter where more Near Detector data events were seen to fail compared to Monte Carlo.
- **CC-Pid and negative curvature selection:** Select μ^- tracks. For detail information, see Section 4.2.

The Near Detector data cut table is shown in Table 4.1. And the spectrum of the neutrino events is quite flat as a function of time in Figure 4.2.

TABLE 4.1. The cut table of the Near Detector event selection of different run period.

Cut	Run1 (1.25×10^{20} POT)	Run2 (1.67×10^{20} POT)
Track in Fiducial	2.73×10^6	3.57×10^6
Track Quality	2.73×10^6	3.56×10^6
Track PID	1.83×10^6	2.38×10^6

4.2. Charged-Current Event Selection

The MINOS experiment measures the muon neutrino disappearance rate by comparing the ν_μ charged-current event rates at the Near and Far Detectors. These events are identified by the observation of a muon track. Low energy muons produce short tracks, which are difficult to distinguish from background tracks. These background tracks are found in the neutral current interactions, and they contribute a systematic error for the measurement of the ν_μ disappearance rate by the MINOS experiment.

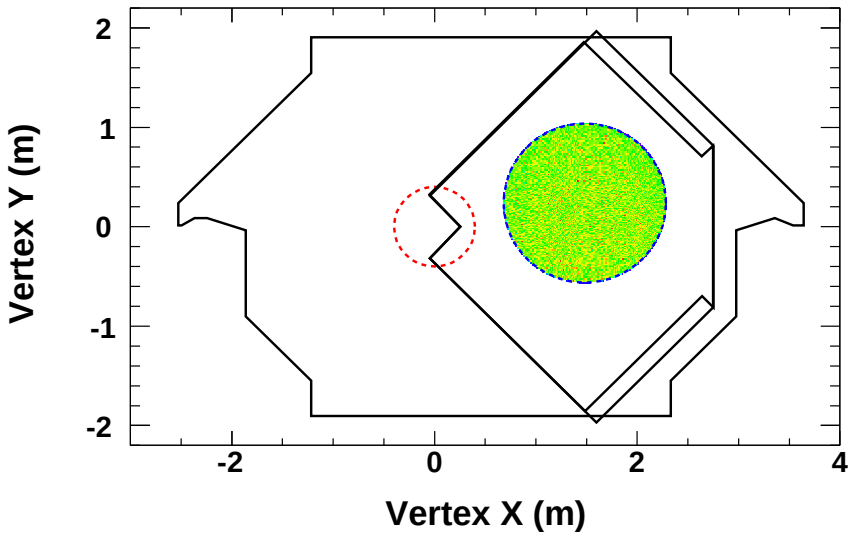

(a) Run1

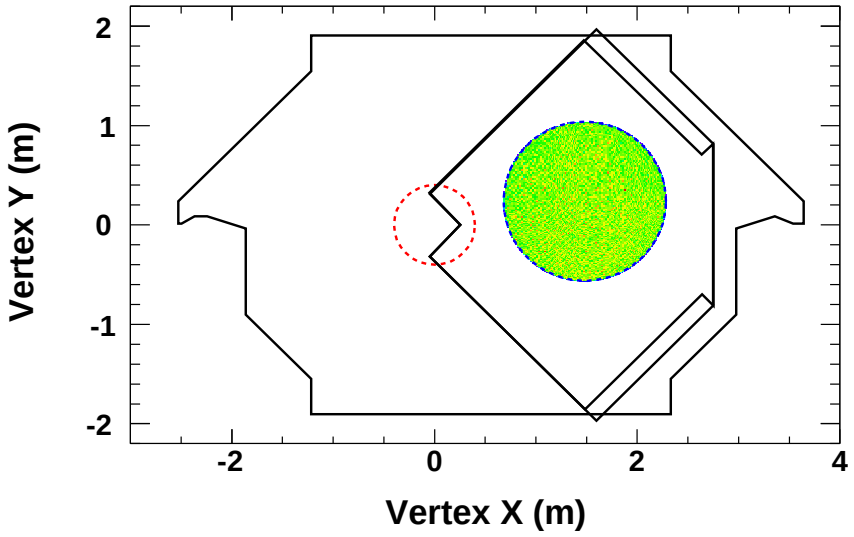

(b) Run2

FIGURE 4.1. 2D plots in the x and y plane of event vertex position for LE Run1 (top) and Run2 (bottom). The blue line indicates the fiducial volume cut and the red line indicates the coil hole region.

In order to distinguish the muon tracks with other hadron tracks, we need to develop a ν_μ charged-current classification algorithm that can improve the CC and NC separation.

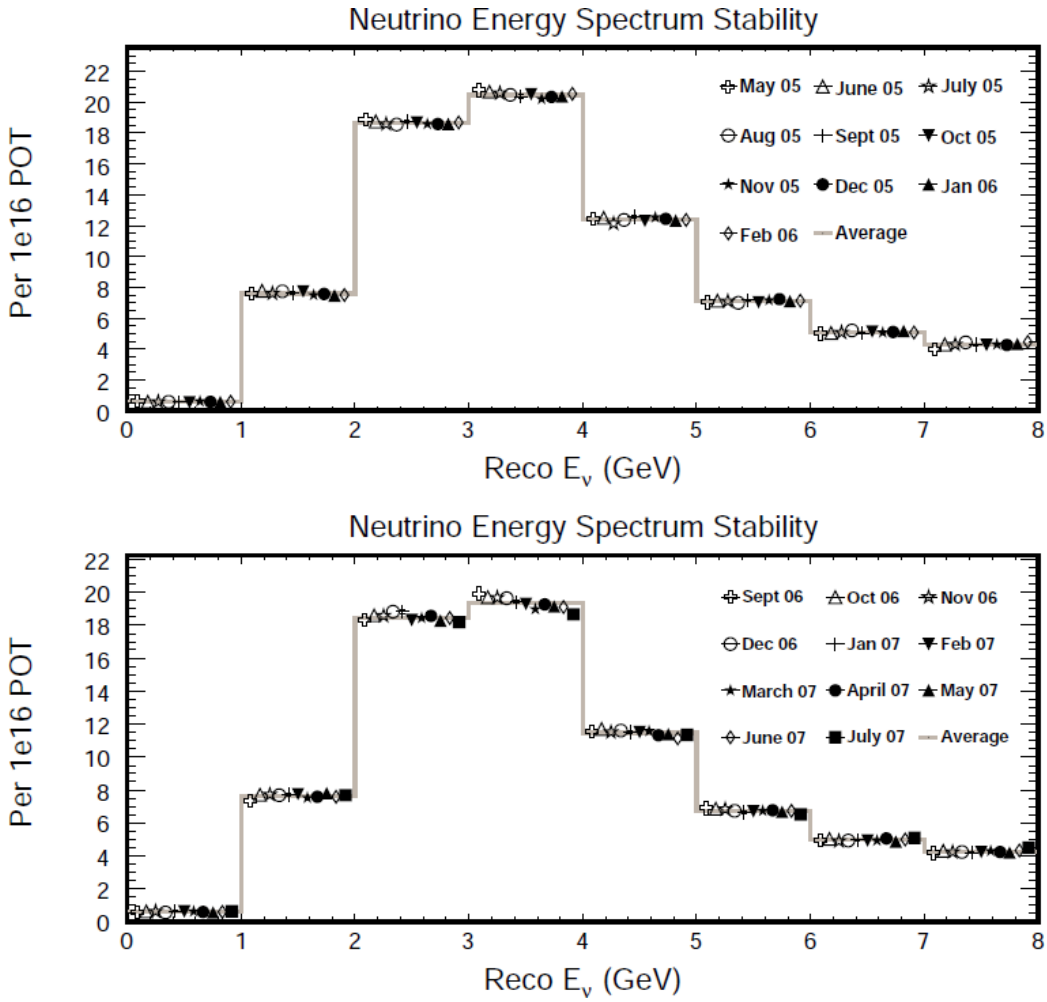

FIGURE 4.2. The number of neutrino events over time as a function of energy. The top plot is from Run1 and the bottom from Run2. Figure courtesy Mark Dorman.

In the low energy beam configuration, the ν_μ charged-current interactions produce muons with momentum peaked around 2 GeV. The muon with 2 GeV momentum are easily distinguished by a long track through the multiple detector planes.

However, many short reconstructed tracks are a part of hadronic shower with track-like features. These non-muon tracks are produced in neutral current interactions and, if not correctly identified, may lead to mis-classification of an event as a ν_μ charged-current interaction. The second most significant source of the non-muon tracks are from ν_μ charged-current events in which a large fraction of the neutrino energy is transfered to a hadronic shower. In these events, the muons are obscured

by a hadronic shower causing these events to be essentially indistinguishable from the neutral current events. As a result, reconstructed tracks in these events do not have the characteristic of a muon track.

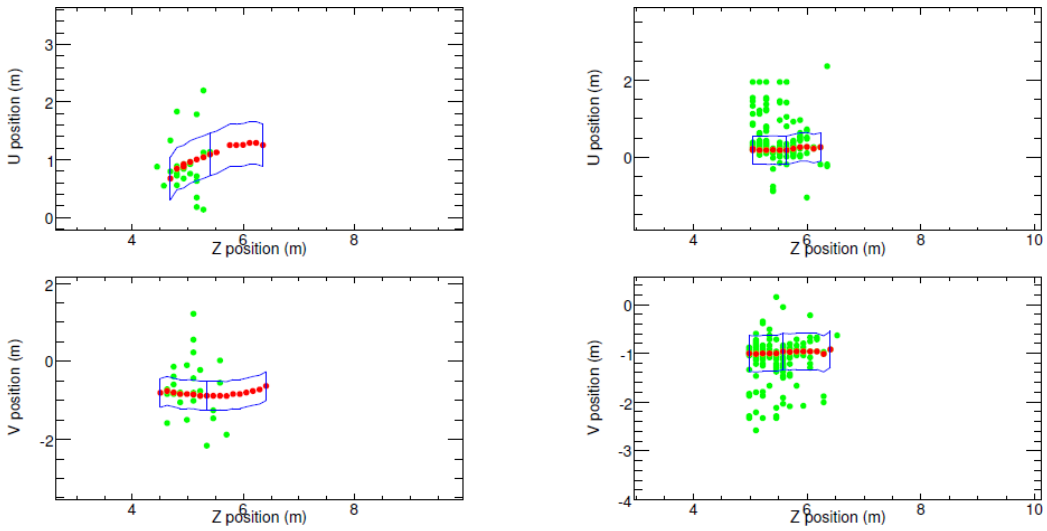

FIGURE 4.3. Event displays show two reconstructed events from the MC simulation. The left figure shows a true ν_μ charged-current event, and the right figure shows a true neutral current event. The reconstructed track hits are shown in red; the reconstructed shower hits are shown in green. The track is split into two segments, outlined by the blue boxes [Ospanov].

4.2.1. KNN Input Variables. I will describe a ν_μ charged-current event identification method for the ν_μ disappearance analysis: k-nearest neighbor (kNN) method. The kNN method was developed by Ospanov. The kNN algorithm use four track variables that serve as inputs to a multi-variate classification algorithm:

(1) **Number of Scintillator Planes:** This variable is proportional to the length of the muon track within the detector. Muon can travel a long distance through matter (compared with hadrons), so long reconstructed tracks are easily identified as muon tracks. For example, a typical 1 GeV muon travels through approximately 20-30 detector planes. The distribution is shown in Figure 4.4.

(2) **Mean pulse height of track hits:** The muon pulse height of track hits measures the average energy loss in the MINOS scintillator strips. The minimum ionizing particles such as muons deposit the same average energy for each plane. The distribution is shown in Figure 4.5.

(3) **Signal fluctuation:** This variable measures fluctuations in the energy deposited in the MINOS scintillator strips. Hadronic showers have larger fluctuations in deposited energy, than muons. This variable is constructed by sorting the track hits in order of ascending pulse height. The hits are then divided into two samples the low and high pulse height hits. The variable is defined as the ratio of the mean of the low pulse height hits to the mean of the high pulse height hits. The distribution is shown in Figure 4.6.

(4) **Transverse profile:** The pulse height of all detector hits that fall within a 4 strip window and a 37.36 ns time window is compared to the pulse height of the track. A muon track should have few stray hits around the track and will have typically one hit per plane. The distribution is shown in Figure 4.7.

These four variables probe the physics of the muon propagation through the MINOS detectors, and they have different distributions for the muon and non-muon tracks, as shown from Figure 4.4 to Figure 4.7. For the last three variables, the first 30% of the track near the hadronic shower was excluded to enhance the sensitivity to the differences between muon and non-muon tracks.

4.2.2. Construct KNN PID. An event classification is a decision to assign an event to one of several predetermined classes. A typical classification problem has two classes: signal and background. The goal of the classification procedure is to select a maximum number of signal events while keeping a number of background events at a reasonable level.

In the previous section, the four track variables were described. These variables probe the physics of the muon propagation through the MINOS detectors, and they have different distributions for the muon and non-muon tracks. The MC simulation

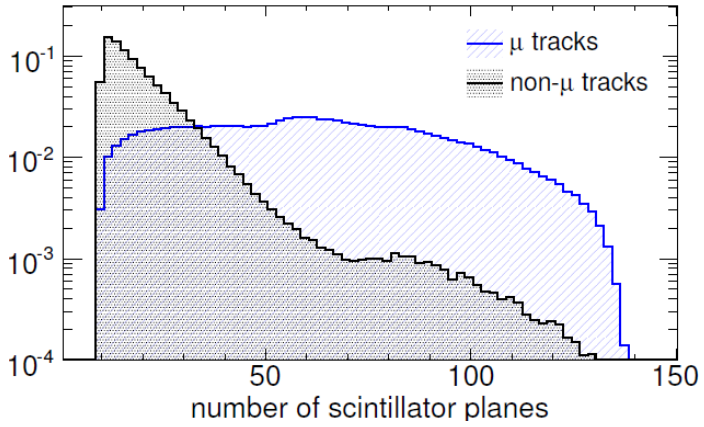

FIGURE 4.4. Number of track scintillator planes for reconstructed muon and non-muon tracks [Ospanov].

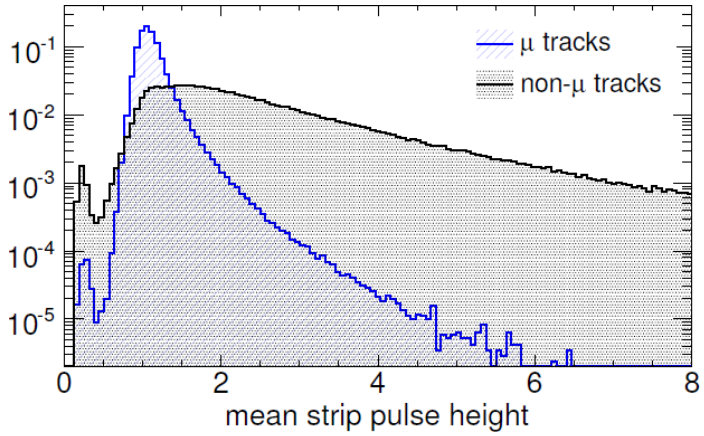

FIGURE 4.5. A mean pulse height of the track hits for reconstructed muon and non-muon tracks [Ospanov].

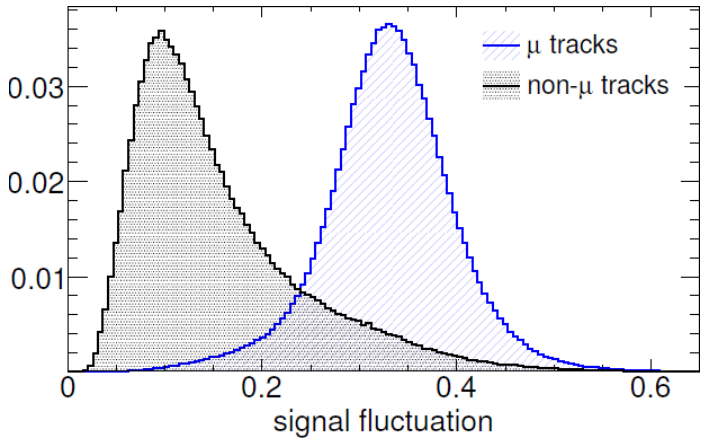

FIGURE 4.6. A signal fluctuation variable is the ratio of the mean of low pulse height hits over the mean of high pulse height hits [Ospanov].

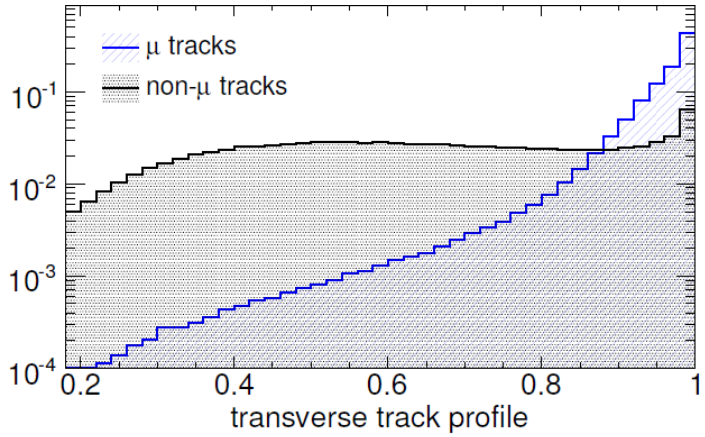

FIGURE 4.7. A transverse profile variable for the reconstructed muon and non-muon tracks [Ospanov].

was used to compute probability density functions for these four variables. In general, a set of events with a known class (in this case, a muon or non-muon track) is called a training sample (set). The classification decision is made by comparing a query event with the events in the training set.

The KNN algorithm uses a training set to estimate a density for the signal and background events in a small neighborhood around the query event. The KNN algorithm estimates a multidimensional probability density function by counting the number of signal and background events in this small neighborhood. Typically, the signal and background events occupy distinct, but overlapping, regions in the parameter space creating distinguishing features that separate these two classes of events. The KNN algorithm finds the k nearest events from the training set for each query event:

$$k = k_S + k_B$$

where k_S is the number of the signal events, and k_B is the number of the background events. The probability that the query event is the signal event is approximated by the following expression:

$$P_S = \frac{k_S}{k_S + k_B} = \frac{k_S}{k} \tag{4.1}$$

This variable is used as a discriminant variable for the event classification.

A vector X_i represents a point in a multidimensional parameter space; this vector is constructed using the classification variables for the event i. The distance function, D, between two events are calculated as the Euclidean distance function:

$$D = \sqrt{\sum_{i=1}^{d} |X_i^T - X_i^Q|^2} \tag{4.2}$$

where d is the number of variables, X_i^T are the variables of the event from a training set, and X_i^Q are the variables of the query event. The k events with the smallest values of D are the k-nearest neighbors. A value of k determines the average size of the neighborhood over which probability density functions are evaluated. Figure 4.8 illustrates event classification with the k-nearest neighbor algorithm.

The discriminant variable KNN is shown in Figure 4.9. The events with KNN > 0.3 are identified as the ν_μ charged-current events. The 0.3 value was obtained in a sensitivity study for an analysis of the ν_μ disappearance. As implemented, this algorithm requires events to have at least 5 hits in each view. Since reconstructed tracks are required to have at least 2 planes in each view, a small fraction of tracks found by the reconstruction will not be assigned a kNN output. Studies have shown that these events are dominantly NC events and therefore are discarded from the analysis.

The performance of the KNN algorithm is evaluated using two quantities: signal efficiency and purity. Figure 4.10 shows the efficiency and purity for the low energy beam configuration. The selected ν_μ charged-current events at the Far Detector include the estimated 0.6% background contamination from the neutral current interactions. A smaller background contamination can reduce systematic errors for the measurement of the muon neutrino oscillation parameters.

Study shows the efficiency is the same for three beam configurations, so it does not depend on the MC energy spectrum [Ospanov]. The purity for the high energy

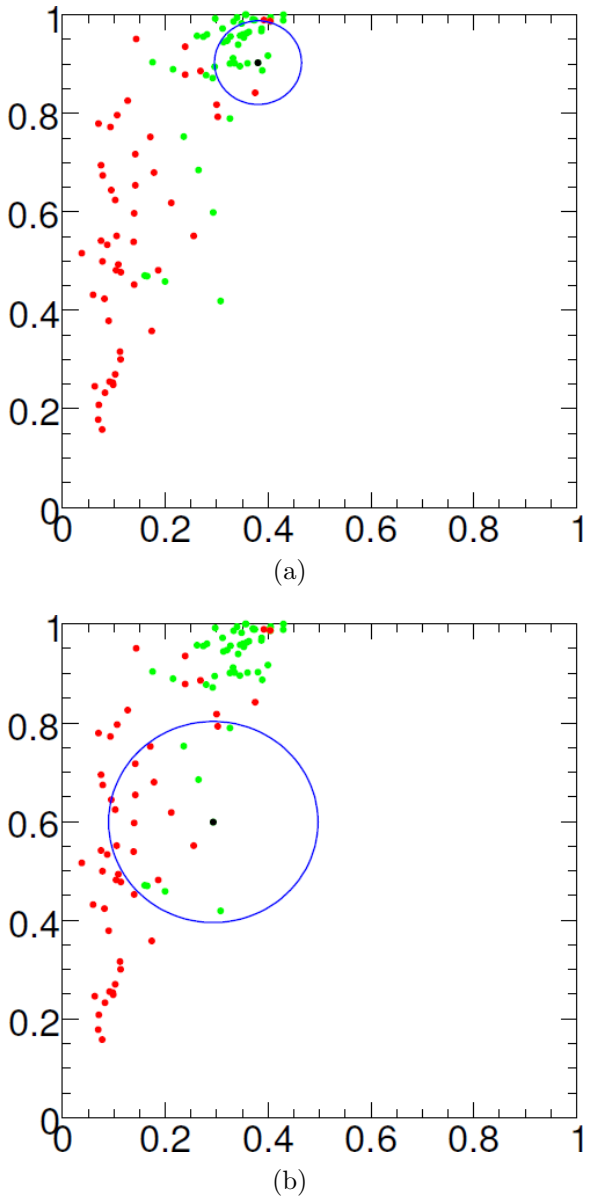

FIGURE 4.8. Example of KNN classification for two variables. Signal events are shown in green; background events are shown in red; and a query event is shown in black. A neighborhood enclosing the 20 nearest neighbors is shown in blue. Top: the neighborhood contains 19 green points and 1 red point - the query event is classified as a signal event. Bottom: the neighborhood contains 7 green points and 13 red points - the query event is classified as a background event [Ospanov].

beam is lower, because the number of neutral current background events from the high energy tail is increased.

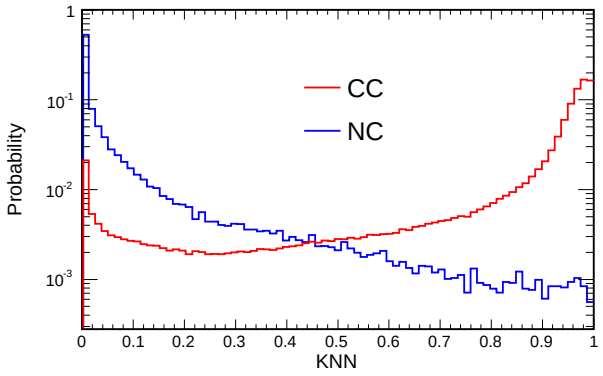

FIGURE 4.9. K-nearest neighbor variable for tracks and events. The variables are computed using the 80 nearest neighbors.

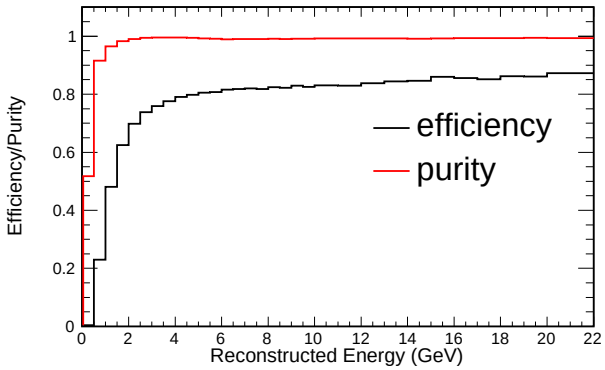

FIGURE 4.10. The efficiency and the purity for the ν_μ charged current selection.

4.2.3. KNN Distributions for Data and MC. Figure 4.11 shows the KNN distributions for the LE Run1 and Run2 Near Detector data and Monte Carlo. After beam retuning, the Monte Carlo agree with the data distribution quite well. The data and Monte Carlo comparison for the Far Detector will be shown in Figure 6.5 in Chapter 6.

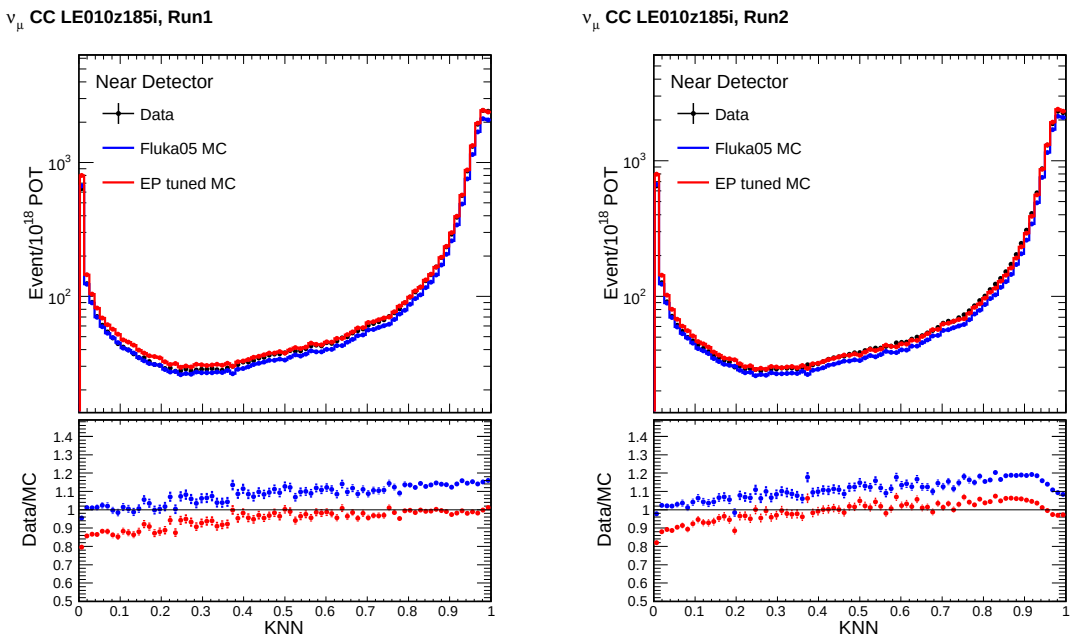

(a) Run1 (b) Run2

FIGURE 4.11. KNN distributions for the LE Run1 (left) and Run2 (right) Near Detector data and Monte Carlo. Data is represented with black points. Blue and red lines represent the untuned FLUKA05 and EP tuned Monte Carlo. The ratio of data/MC ratios are shown in bottom.

4.3. DATA AND MC COMPARISON

The Monte Carlo distributions shown in the following pages use the reweighting from the Near Detector fit described in the previous chapter. The CC-PID selection cut has been applied to all the plots:

- **Energy related distributions:** reconstructed event energy, reconstructed track energy, reconstructed shower energy and the number of tracks and showers.
- **Vertex and track end:** Track begin vertex x, y, z and the track end vertex x, y, z.
- **CC-PID input variable distribution:** Contains the four variables used in the standard CC selection algorithm including scintillator planes, mean

pulse height, mean low pulse height / mean high pulse height, the transverse profile.

4.3.1. LE Run1 data/MC comparison. This section compares different distributions in the Near Detector for data and Monte Carlo for LE Run1 data from Figure 4.12 to Figure 4.16.

4.3.2. LE Run2 data/MC comparison. This section compares different distributions in the Near Detector for data and Monte Carlo for LE Run2 data from Figure 4.17 to Figure 4.21.

4.3.3. Summary. Overall there is good agreement in the Near Detector after Monte Carlo tuning has been applied. Run2 generally has a slightly worse data/MC agreement compared with Run1. The worse agreement between Run2 data and MC may imply that target degradation become more phenomenal than Run1. Some general features in the data and MC disagreement:

- **Event with low y:** There is more data in the low y region than Monte Carlo even after retuning.
- **Muon track end position:** Track end x doesn't agree well for the stopping muons near the center of the detector where the coil is located.
- **Transverse variable:** The transverse profile of the muon track window is affected by the cross talk simulation. We expect a better data/MC agreement with a new version of cross talk modeling.

Although some of the sources of these discrepancies are not fully understood, these problems do not pose a significant setback for extrapolation purpose, since some of these discrepancies will be cancelled for two detectors.

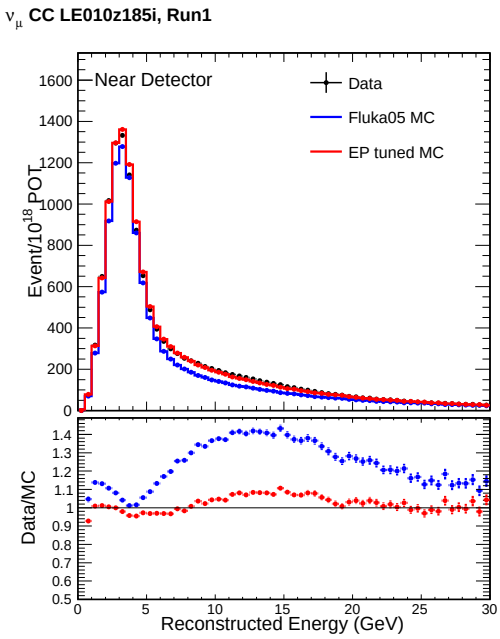

(a) Reconstructed event energy

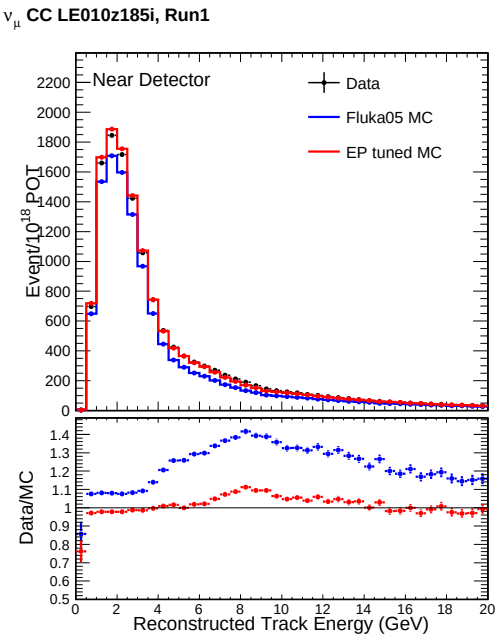

(b) Reconstructed track energy

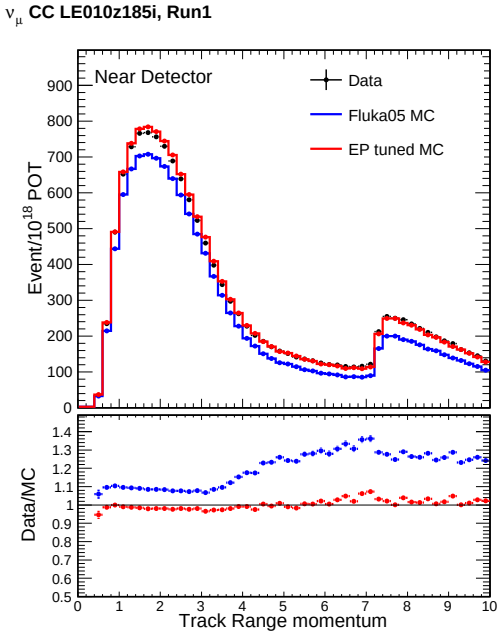

(c) Reconstructed track range momentum

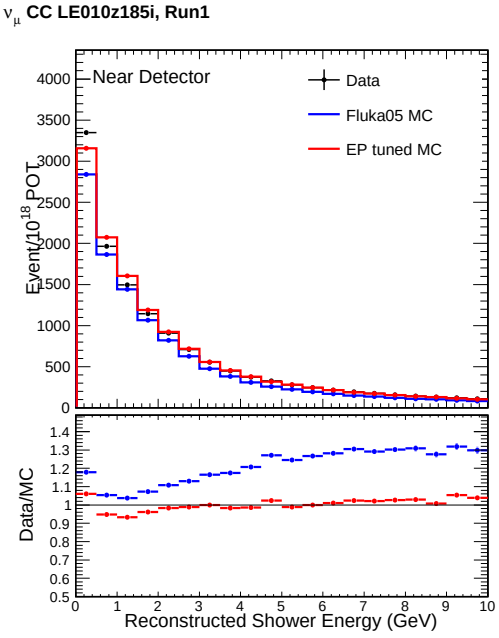

(d) Reconstructed shower energy

FIGURE 4.12. Energy distributions for the LE Run1 Near Detector data and Monte Carlo. Data is represented with black points. Blue and red lines represent the untuned FLUKA05 and EP tuned Monte Carlo. The data/MC ratios are also shown.

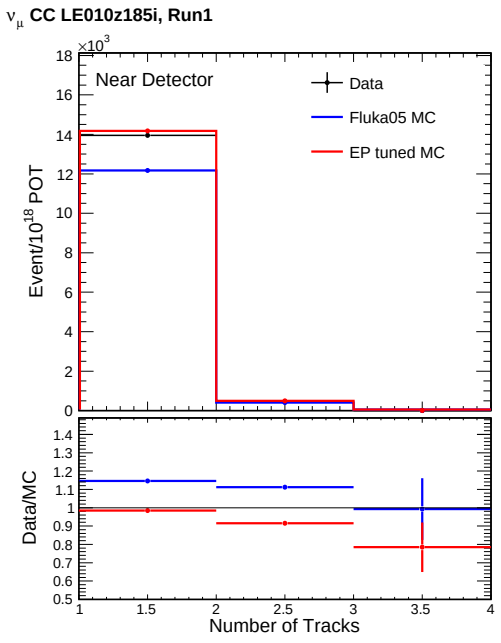

(a) No. of tracks

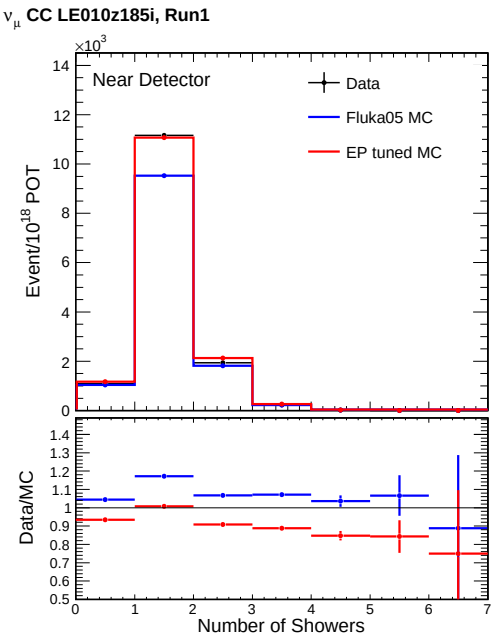

(b) No. of showers

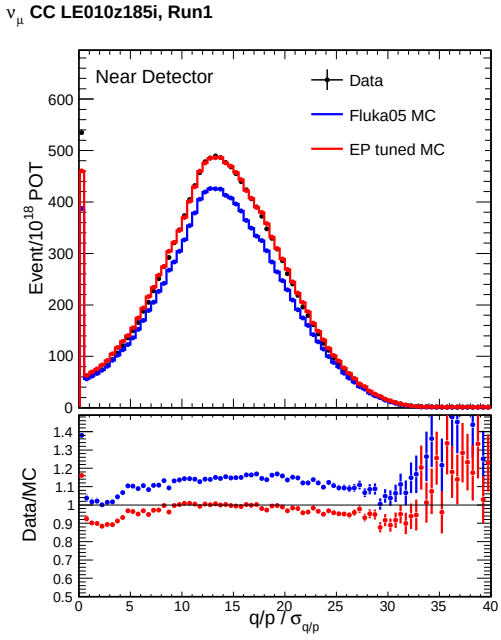

(c) Track q/p/$\sigma_{q/p}$

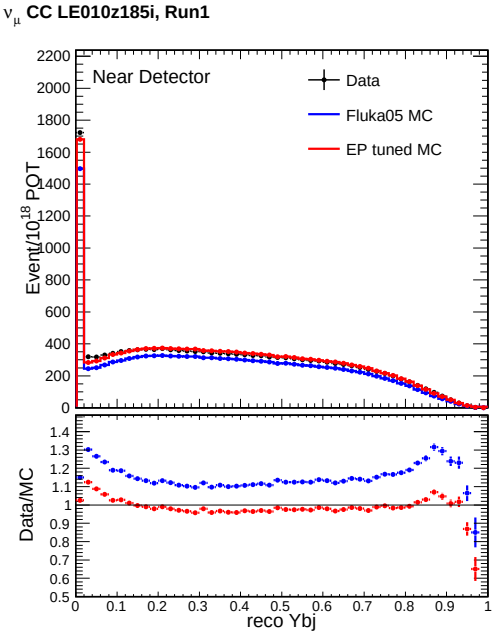

(d) Reconstructed Ybj

FIGURE 4.13. Track and shower distributions for the LE Run1 Near Detector data and Monte Carlo. Data is represented with black points. Blue and red lines represent the untuned FLUKA05 and EP tuned Monte Carlo. The data/MC ratios are also shown.

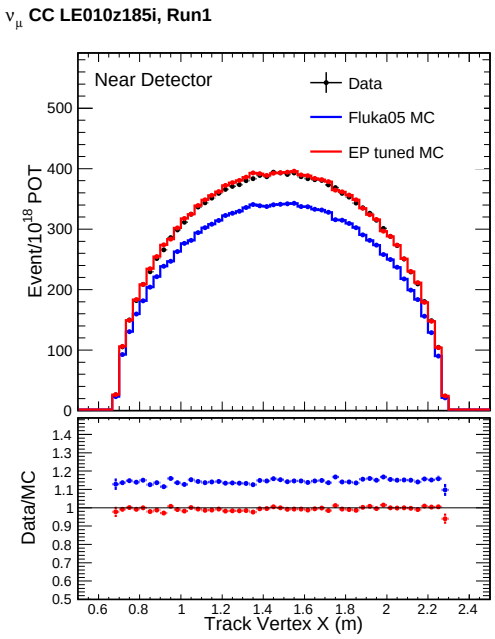

(a) Track vertex X (m)

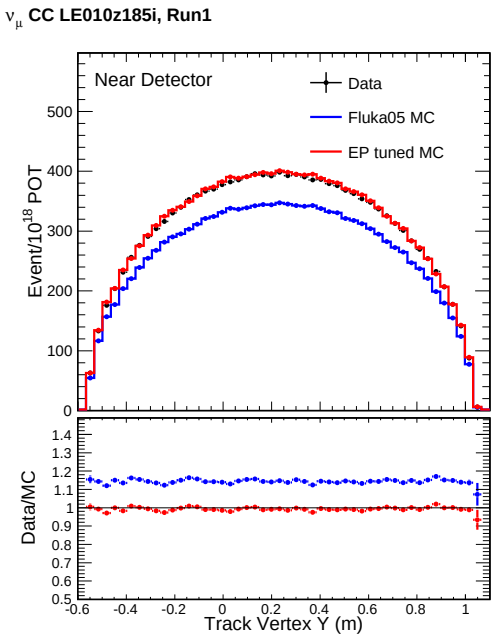

(b) Track vertex Y (m)

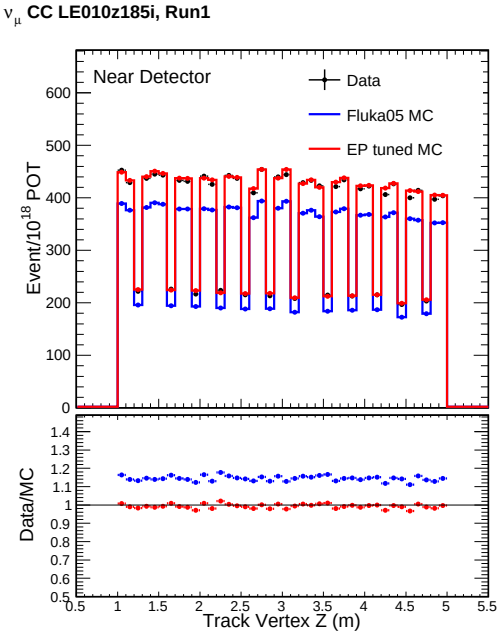

(c) Track vertex Z (m)

FIGURE 4.14. Track vertex distributions for the LE Run1 Near Detector data and Monte Carlo. Data is represented with black points. Blue and red lines represent the untuned Fluka05 and EP tuned Monte Carlo. The data/MC ratios are also shown.

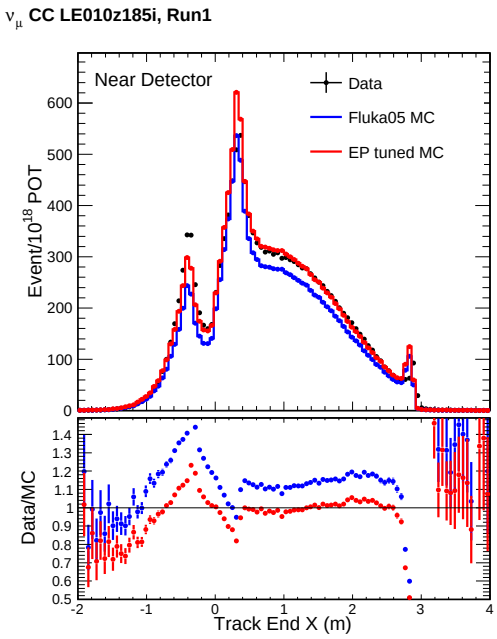

(a) Track end X (m)

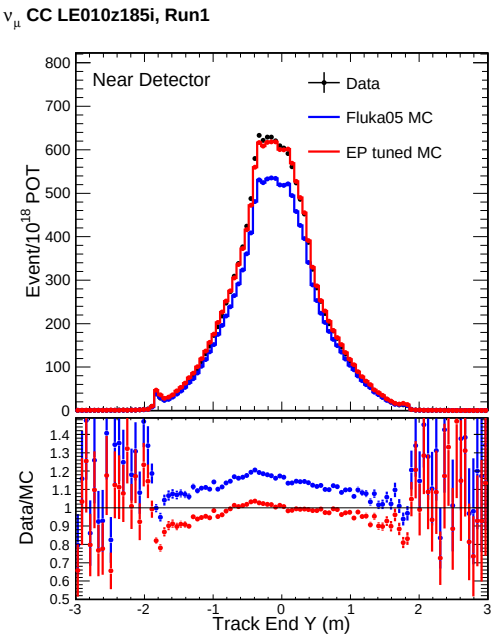

(b) Track end Y (m)

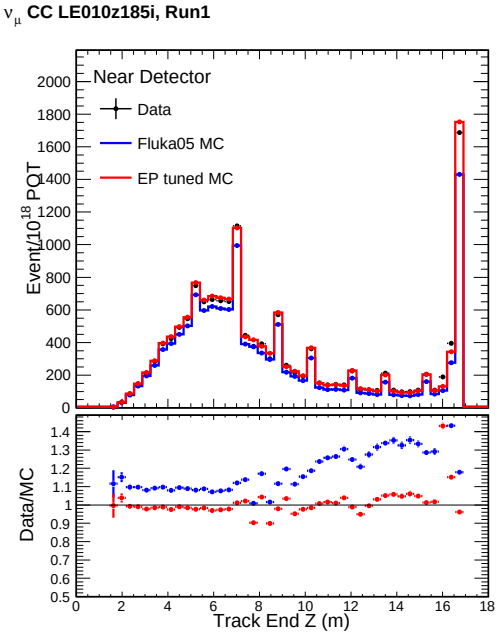

(c) Track end z (m)

FIGURE 4.15. Track end distributions for the LE Run1 Near Detector data and Monte Carlo. Data is represented with black points. Blue and red lines represent the untuned Fluka05 and EP tuned Monte Carlo. The data/MC ratios are also shown.

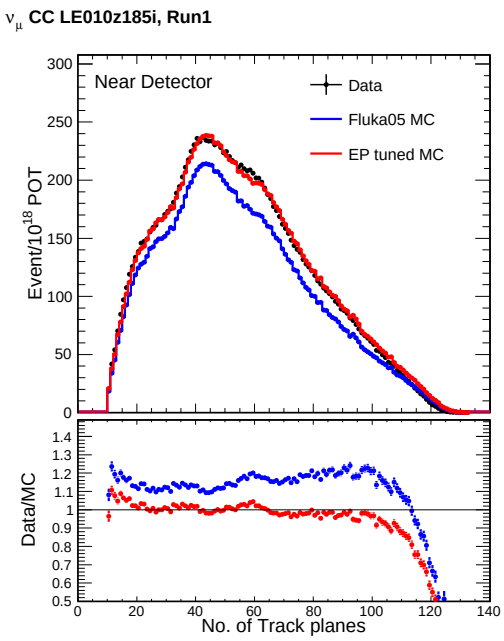

(a) No. of track planes

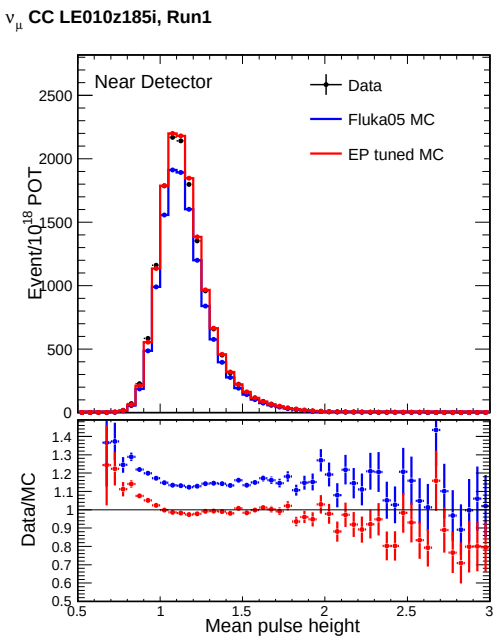

(b) Mean pulse height

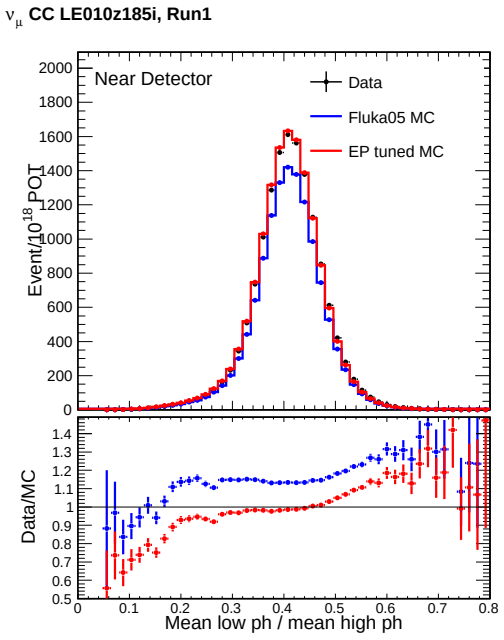

(c) Mean low/high pulse height

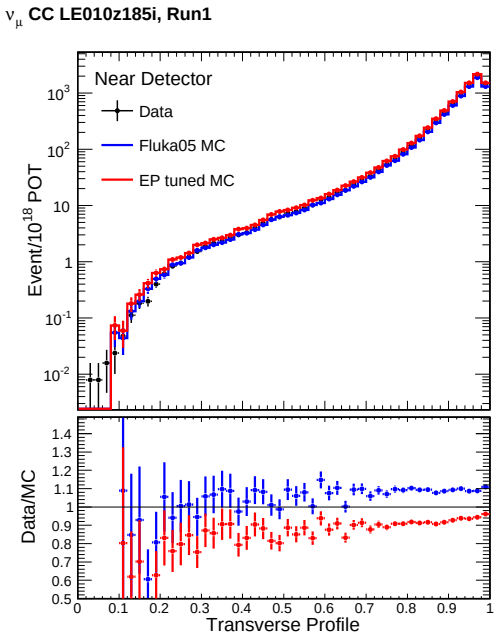

(d) Transverse profile

FIGURE 4.16. KNN input variables for the LE Run1 Near Detector data and Monte Carlo. Data is represented with black points. Blue and red lines represent the untuned Fluka05 and EP tuned Monte Carlo. The data/MC ratios are also shown.

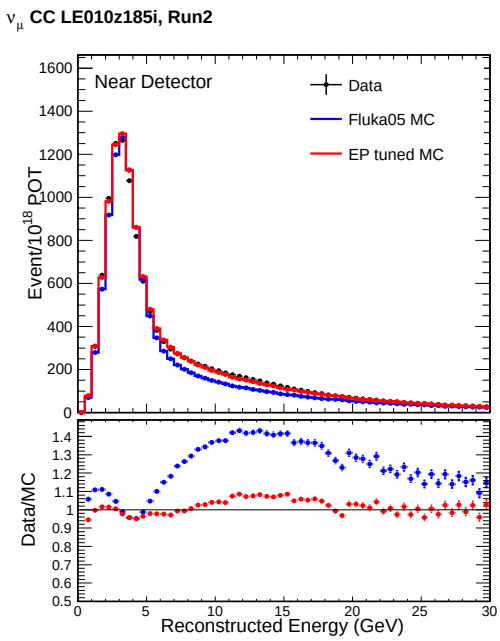

(a) Reconstructed event energy

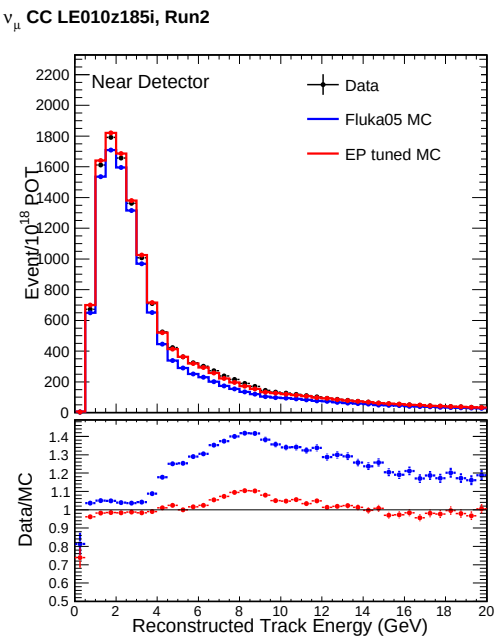

(b) Reconstructed track energy

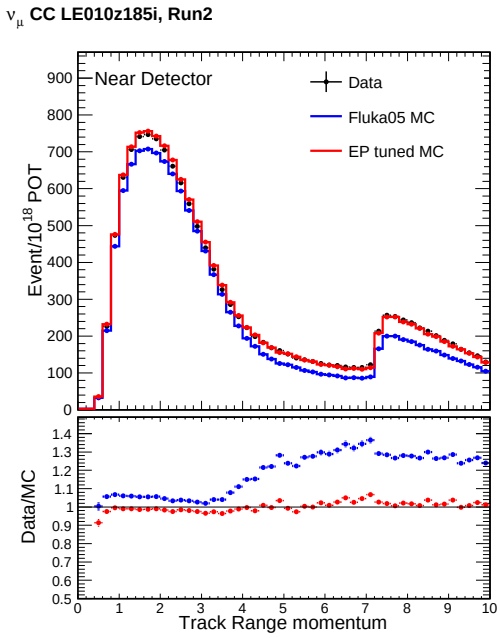

(c) Reconstructed track range momentum

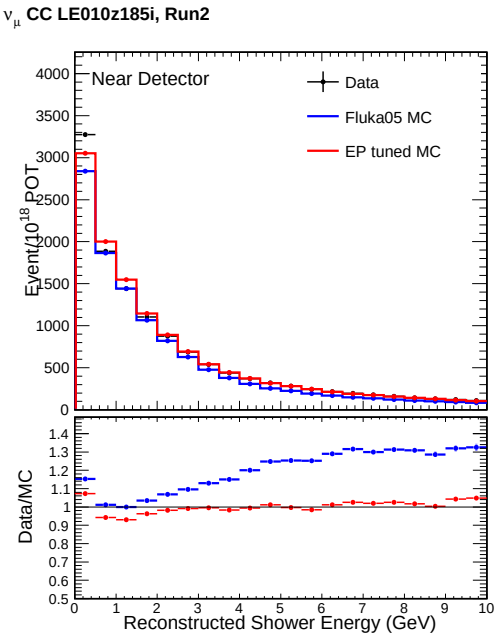

(d) Reconstructed shower energy

FIGURE 4.17. Energy distributions for the LE Run2 Near Detector data and Monte Carlo. Data is represented with black points. Blue and red lines represent the untuned Fluka05 and EP tuned Monte Carlo. The data/MC ratios are also shown.

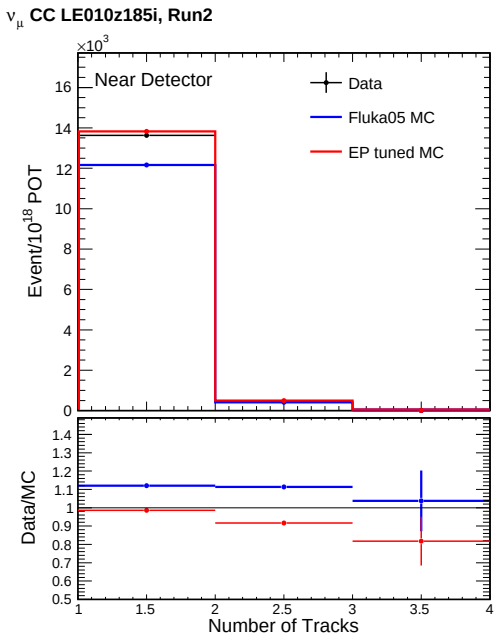

(a) No. of tracks

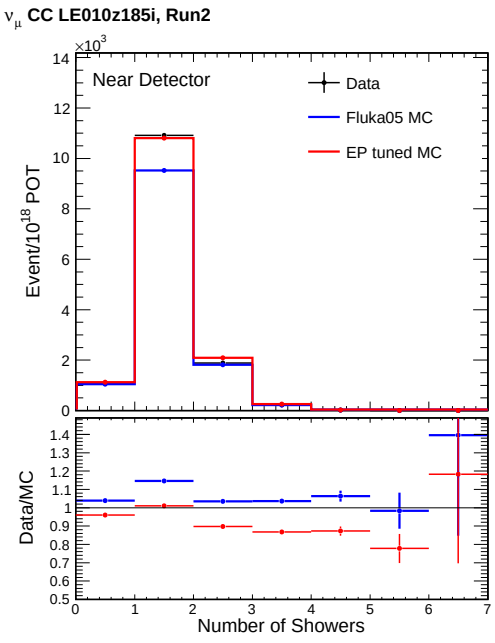

(b) No. of showers

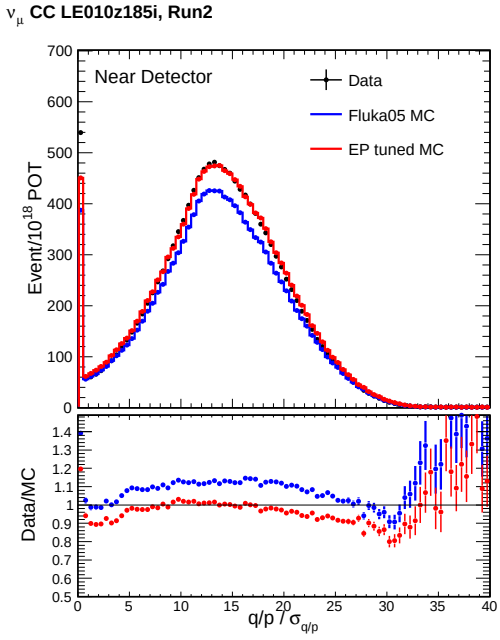

(c) Track q/p/$\sigma_{q/p}$

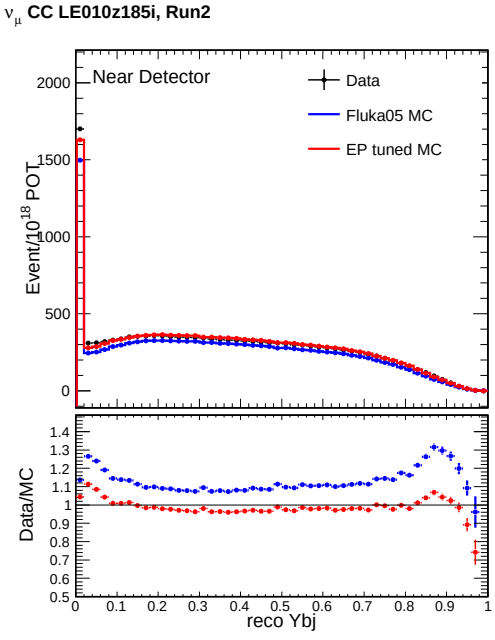

(d) Reconstructed Ybj

FIGURE 4.18. Track and shower distributions for the LE Run2 Near Detector data and Monte Carlo. Data is represented with black points. Blue and red lines represent the untuned FLUKA05 and EP tuned Monte Carlo. The data/MC ratios are also shown.

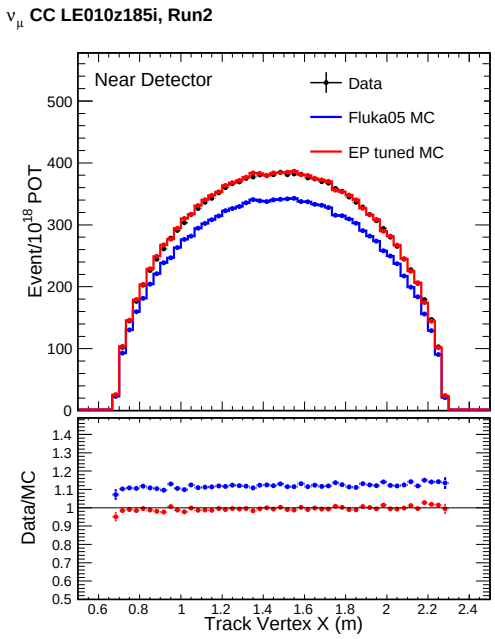

(a) Track vertex X (m)

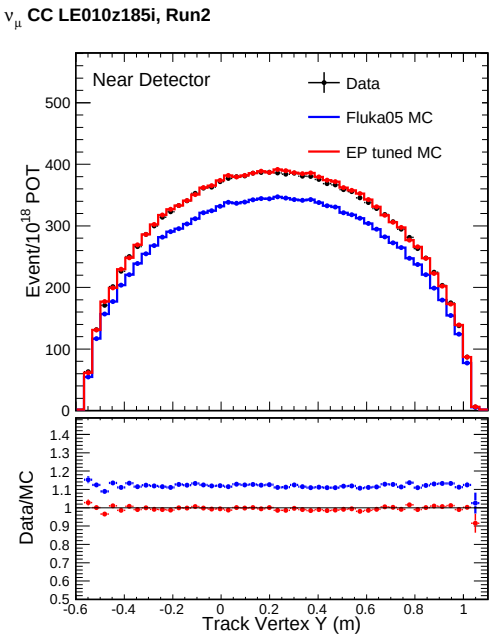

(b) Track vertex Y (m)

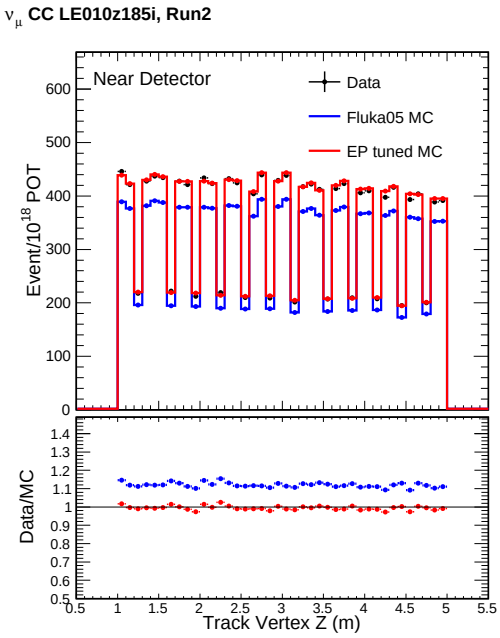

(c) Track vertex Z (m)

FIGURE 4.19. Track vertex distributions for the LE Run2 Near Detector data and Monte Carlo. Data is represented with black points. Blue and red lines represent the untuned Fluka05 and EP tuned Monte Carlo. The data/MC ratios are also shown.

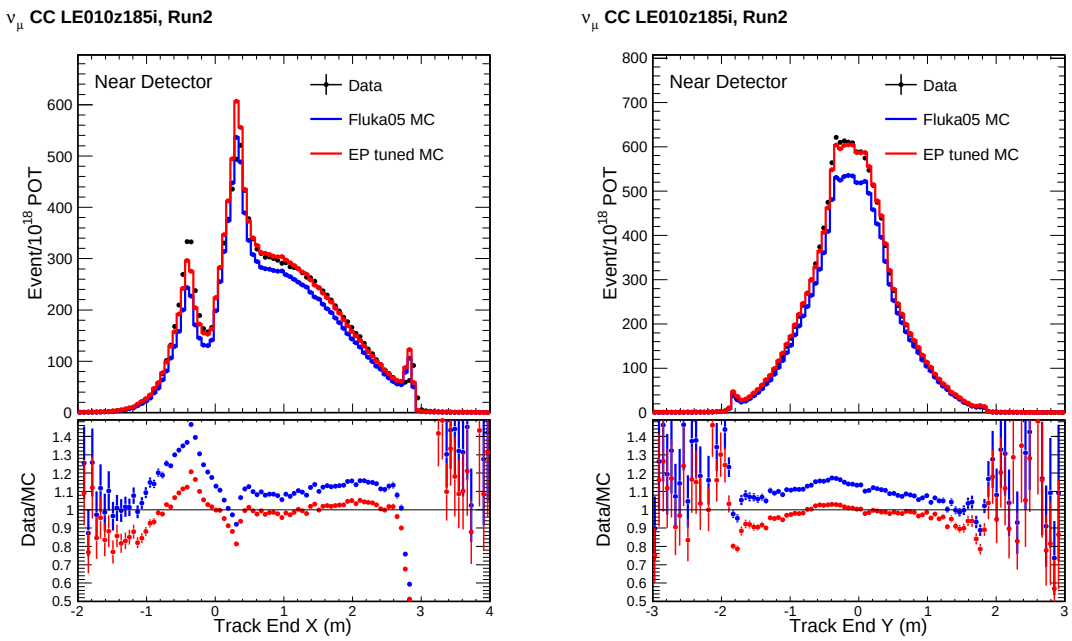

(a) Track end X (m)

(b) Track end Y (m)

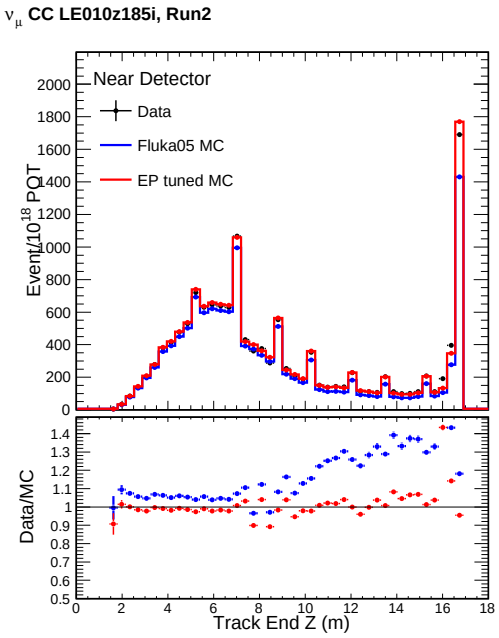

(c) Track end Z (m)

FIGURE 4.20. Track end distributions for the LE Run2 Near Detector data and Monte Carlo. Data is represented with black points. Blue and red lines represent the untuned FLUKA05 and EP tuned Monte Carlo. The data/MC ratios are also shown.

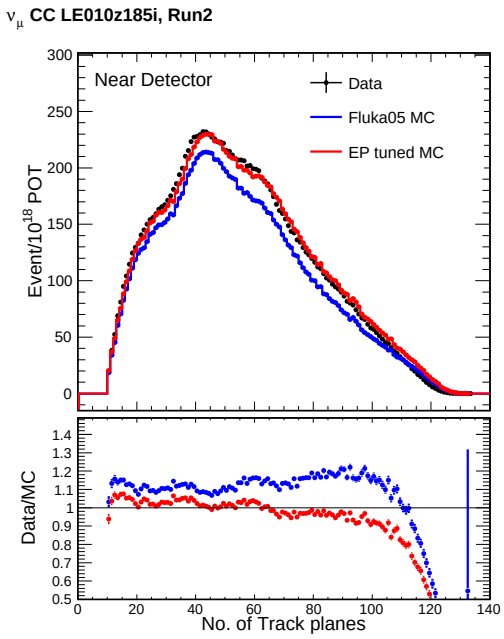

(a) No. of track planes

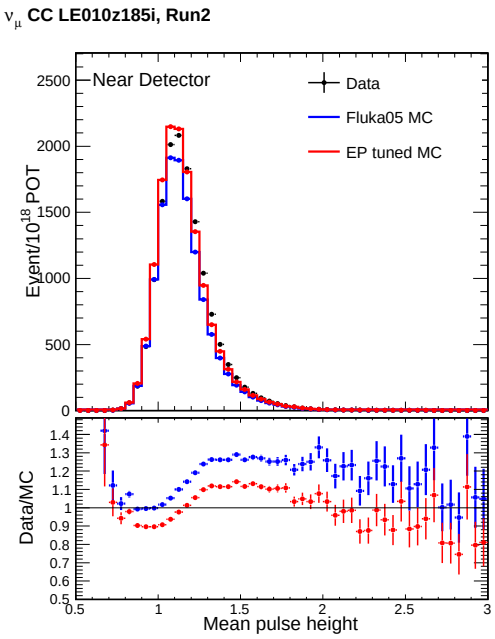

(b) Mean pulse height

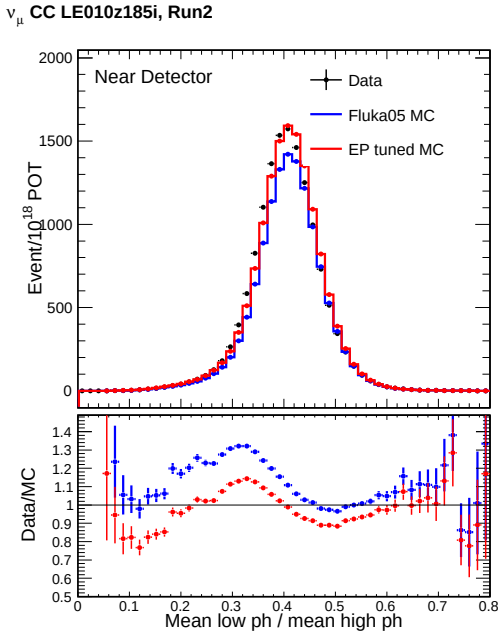

(c) Mean low/high pulse height

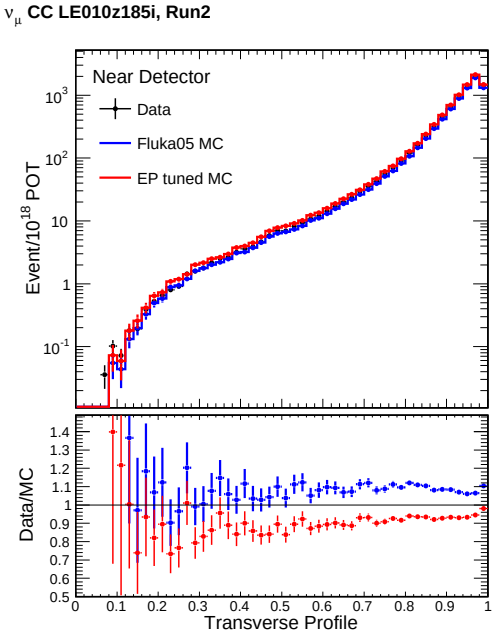

(d) Transverse profile

FIGURE 4.21. KNN input variables for the LE Run2 Near Detector data and Monte Carlo. Data is represented with black points. Blue and red lines represent the untuned FLUKA05 and EP tuned Monte Carlo. The data/MC ratios are also shown.

Chapter 5

Prediction of the Far Detector Spectrum

The basic philosophy of two almost identical detectors used in the MINOS experiment is to cancel some systematic uncertainties, such as neutrino flux, neutrino interaction cross section, hadronic shower modeling and energy calibration.

5.1. Flux Differences

If the energy spectrum of neutrinos at the Near Detector and Far Detector are identical, then the Near Detector flux would be a direct measure of the expected Far Detector flux, to be scaled by the relative solid angles [Kopp et al.]:

$$\Phi^i_{far} = \left(\frac{z_{near}}{z_{far}}\right)^2 \Phi^i_{near} \tag{5.1}$$

where Φ_i is the flux of neutrinos in an energy bin i and $z_{near} = 1000\,\mathrm{m}$ is the distance of the Near Detector from the NuMI target and $z_{far} = 735{,}000\,\mathrm{m}$.

However this is not exactly true. Three effects modify the above approximation. These are pictured schematically in Figure 5.1

(1) The Near Detector distance of $z_{near} = 1000\,\mathrm{m}$ is comparable to the mean decay length of pion ($\gamma\beta c\tau \sim 560\,\mathrm{m}$ for a $10\,\mathrm{GeV}$ pion). This means that soft pions will decay significantly upstream of the ND, while fast pion will decay right in front of it exaggerating their flux contribution to the ND by nearly a factor of two.

(2) Soft pions are typically under-focused by the horns, so have a larger divergence as they enter the decay pipe. Fast pions, because of their boost, are at smaller entrance angles.

(3) The energy of neutrino reaching the detector is a non-trivial function of the parent π/K energy and the angle of the neutrino with respect to the π/K direction:

$$E_\nu \approx \left(1 - \frac{m_\mu^2}{M^2}\right) \frac{E}{1 + (\gamma \tan \theta_\nu)^2} \tag{5.2}$$

where m_μ and M are the muon and parent hadron masses, E the parent hadron energy, $\gamma = E/M$ is the parent's Lorentz boost, and θ_ν is the angle (in the lab) between the neutrino and parent hadron directions.

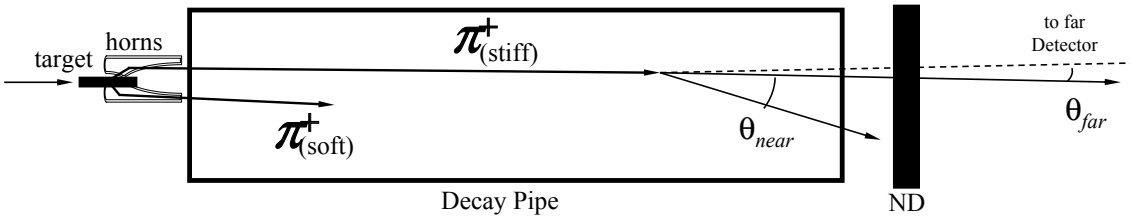

FIGURE 5.1. Schematic view of pion decay leading to neutrinos that reach Near and Far Detectors. The differences in the Near and Far Detectors spectra are due to the different angular acceptance of the two detectors and the proximity of the Near Detector to the beam line [Kopp et al.].

The competing effects above lead to systematic distortions between the ND and FD flux at the 20-30% level. Figure 5.2 shows the neutrino energy spectrum at the Near and Far Detectors.

5.2. Extrapolation Method

The Near Detector measures the neutrino energy spectrum close to the source and before oscillations have occurred. We can use the Near Detector data to predict the Far Detector spectrum as "extrapolation". Any difference between the prediction and the Far Detector data may then be interpreted as neutrino oscillations or some other hypothesis.

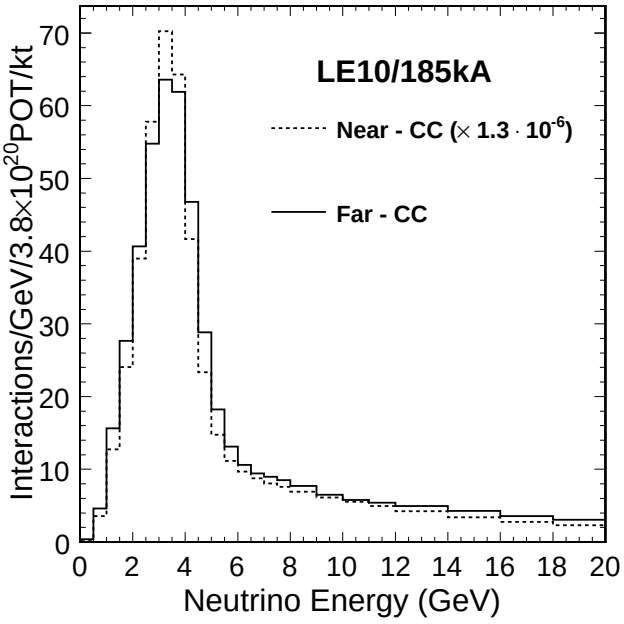

FIGURE 5.2. Comparison of the neutrino energy spectrum at the Near and Far Detectors. The two are not identical, due to solid angle difference between the two detectors [Adamson et al., 2008a].

Various extrapolation methods has been developed by the MINOS collaboration. In this thesis I will mainly introduce "the F/N method" and the "beam matrix method".

5.2.1. The F/N method. "The F/N method" is the most straightforward method to extrapolate the Near Detector spectrum to the Far Detector. We can use the Monte Carlo simulation to derive a transfer function.

The far to near flux ratio of Figure 5.3 is itself nearly a transfer function except that it is expressed in true neutrino energy and does not account for detector energy resolution, detector acceptance and fiducial mass.

A suitable replacement can be evaluated by applying the ν_μ charged-current selection to fully simulated events in both detectors to derive neutrino event rates, n_i and f_i in bins i of reconstructed neutrino energy. The Near Detector data N_i are then used to predict the far spectrum:

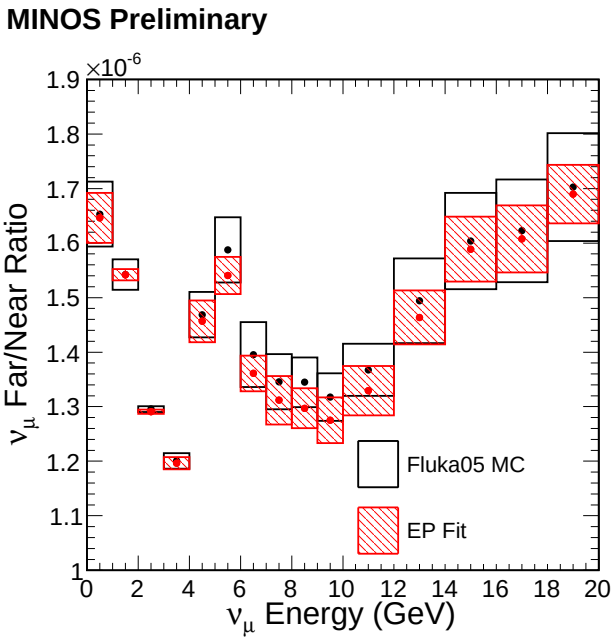

FIGURE 5.3. The predicted ratio (F/N) of ν_μ flux at the two detectors before and after the beam fitting.

$$F_i^{predicted} = N_i \times \frac{f_i}{n_i} \tag{5.3}$$

This technique is referred to as the "F/N method" but is equivalent to scaling each bin in the simulated Far Detector reconstructed neutrino energy spectrum by the ratio of the number of observed to expected events in the corresponding Near Detector reconstructed neutrino energy bin.

5.2.2. The Beam Matrix Method. The beam matrix method was chosen as the primary analysis extrapolation method for MINOS. It was first proposed by Szleper and A.Para [2001].

Neutrinos having a given energy in the Near Detector come from decays which would, collectively, yield neutrinos covering a range of energies in the Far Detector as indicated in Figure 5.4. The fact that a single energy in the Near Detector corresponds to a range in the Far Detector suggests that the neutrino energy spectra may be related by a two-dimensional matrix rather than a one-dimensional ratio. This "beam matrix"

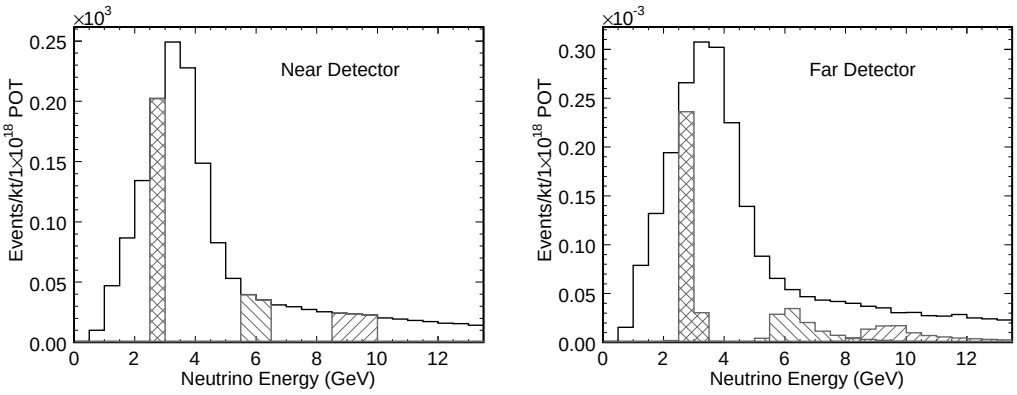

(a) (b)

FIGURE 5.4. The relationship between energy of neutrinos observed in the Near Detector with those observed in the Far Detector. Decays producing neutrinos with a given energy in the Near Detector would produce a range of energies in the Far Detector, yielding the energy smearing seen here [Adamson et al., 2008a].

B_{ij} is shown in Figure 5.5. Each cell represents the number of neutrinos expected in energy bin i at the Far Detector for one neutrino in bin j in the Near Detector.

The matrix is constructed from the beam simulation using the known geometric acceptance of the two detectors.

In the MINOS beam simulation, the neutrino is forced to pass through either the Near or Far Detectors, with probability for the particular meson decay given by

$$\frac{dP}{d\Omega_\nu} \approx \frac{1}{4\pi} \frac{4\gamma^2(1+\tan^2\theta_\nu)^{3/2}}{(1+\gamma^2\tan^2\theta_\nu)^2} \quad , \tag{5.4}$$

The energy dependence of the ν_μ charged-current cross section is included in the calculation but is most relevant for the small off-diagonal elements.

As with the F/N ratio, the matrix can only be employed after accounting for detector acceptance and inefficiencies. The corrected true ν_μ charged-current energy spectrum at the Near Detector, organized in energy bins, is treated as a m-dimensional column vector N_i and multiplied by the $m \times m$ dimensional matrix B_{ij} to estimate the true ν_μ charged-current energy at the Far Detector

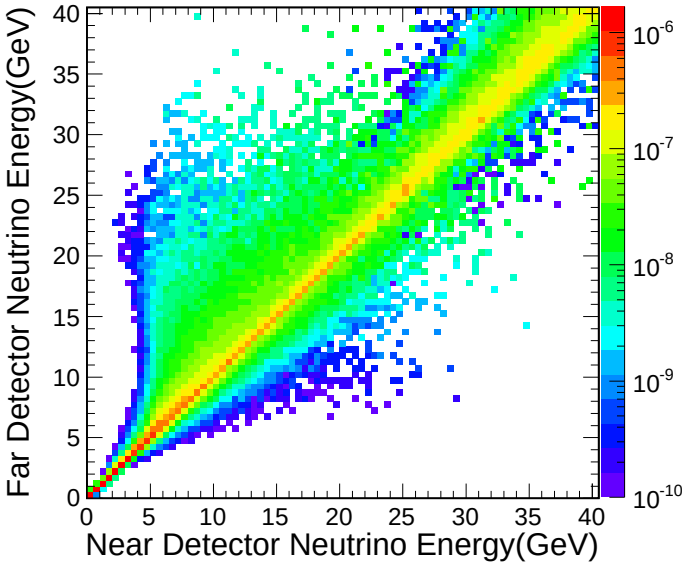

FIGURE 5.5. The joint distribution of neutrino energies observed in the Near and Far Detectors. The contents of each cell represent the mean number of ν_μ events expected in the Far Detector for one event in the Near Detector. This distribution may be treated as a matrix to relate the energy spectra measured in the Near Detector to those in the Far Detector.

$$F_i = \sum_{j=0}^{m} B_{ij} N_j \tag{5.5}$$

5.2.3. Summary. Generally speaking, "F/N Method" and "Beam Matrix Method" are quite similar. Both of them can reduce the effect that uncertainties in hadron production, neutrino cross sections and detector acceptance have on the prediction of the neutrino energy spectrum at the Far Detector.

5.3. Predicted Far Detector Spectrum

These two Extrapolation methods can be separated into the following steps:

(1) $N_{reco}(E) \rightarrow N_{true}(E)$ with Near Detector acceptance correction

(2) $N_{true}(E) \rightarrow F_{true}(E)$ with "F/N" or "beam matrix" extrapolation

(3) $F_{true}(E) \rightarrow F_{reco}(E)$ with Far Detector acceptance correction

5.3.1. Calculating the Near Detector True Spectrum. In order to get the Near Detector true energy spectrum, we need to apply purity, smearing and efficiency correction on the Near Detector reconstructed energy spectrum. All the correction are calculated with the Near Detector Monte Carlo.

The purity is defined as the ratio of selected signal events and total selected events in the fiducial volume.

$$Pur^{N}_{recoE} = \frac{(\text{NO. of signal events selected})_{recoE}}{(\text{NO. of total events selected})_{recoE}} \tag{5.6}$$

The smearing correction is to transfer reconstructed energy into true energy, $Smr^{N}_{recoE,trueE}$. It is a matrix, which can be built by the correspondent reconstructed energy and true energy for each Monte Carlo signal event.

The Efficiency is defined as the ratio of selected signal events and total generated signal events in the fiducial volume.

$$Eff^{N}_{trueE} = \frac{(\text{NO. of signal events selected})_{trueE}}{(\text{NO. of total events generated})_{trueE}} \tag{5.7}$$

Combining all the corrections, we can get the Near Detector true energy spectrum,

$$Spec^{N}_{trueE} = Spec^{N}_{recoE} \times \frac{Pur^{N}_{recoE} \times Smr^{N}_{recoE,trueE}}{Eff^{N}_{trueE}} \tag{5.8}$$

5.3.2. Calculating the Far Detector True Spectrum. As mentioned in the previous section, we can use either "F/N method" or "beam matrix method" to extrapolate the Near Detector true energy spectrum to the Far Detector true energy spectrum. The F/N ratio and beam matrix is shown in Figure 5.3 and Figure 5.5.

$$Spec^{F}_{trueE} = Spec^{N}_{trueE} \times BMM^{F,N}_{trueE} \times \frac{(Mass)^{F}_{Fid}}{(Mass)^{N}_{Fid}} \tag{5.9}$$

$$\text{or} \quad Spec^{F}_{trueE} = Spec^{N}_{trueE} \times (F/N)_{trueE} \times \frac{(Mass)^{F}_{Fid}}{(Mass)^{N}_{Fid}} \tag{5.10}$$

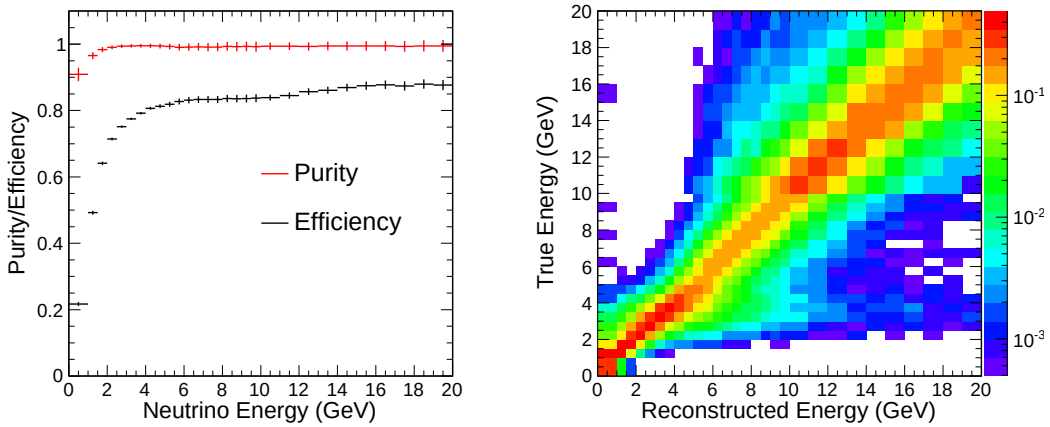

(a) Efficiency and Purity (b) Energy Smearing

FIGURE 5.6. The Near Detector acceptance correction.

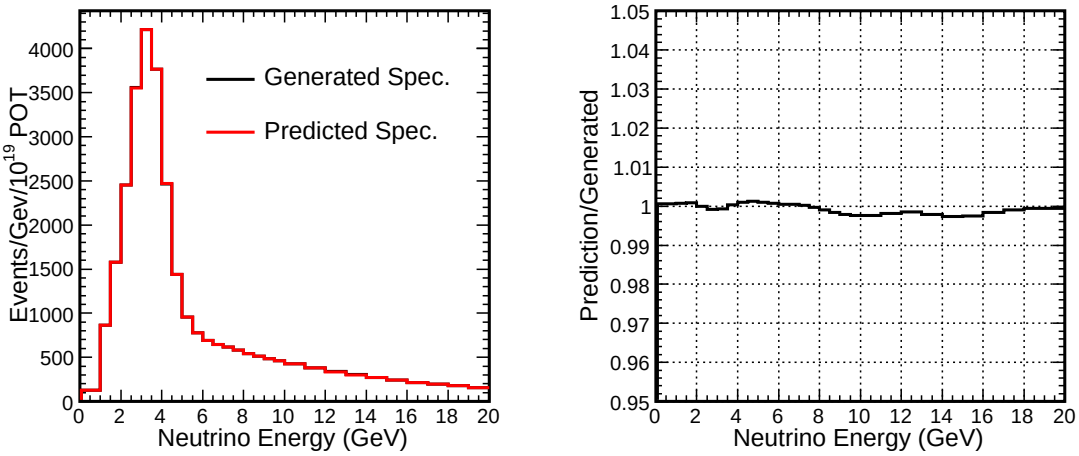

FIGURE 5.7. The Near Detector true energy spectrum prediction.

5.3.3. Calculating the Far Detector Reconstructed Spectrum. For the Far Detector reconstructed energy spectrum, we just need to reverse the correction order of the Near Detector corrections. Of course, all the corrections are calculated with the Far Detector Monte Carlo.

$$Spec^{F}_{recoE} = Spec^{F}_{trueE} \times \frac{Eff^{F}_{trueE} \times Smr^{F}_{trueE,recoE}}{Pur^{F}_{recoE}} \tag{5.11}$$

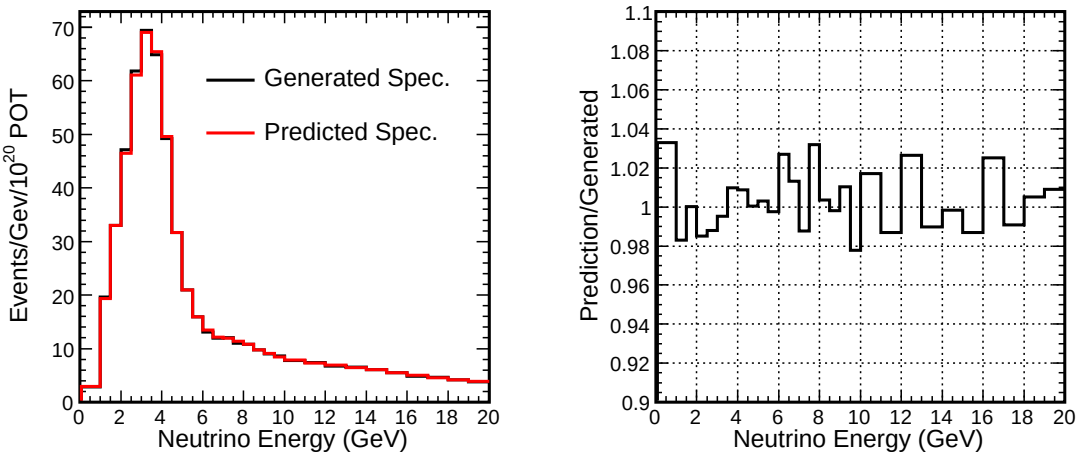

FIGURE 5.8. The Far Detector true energy spectrum prediction.

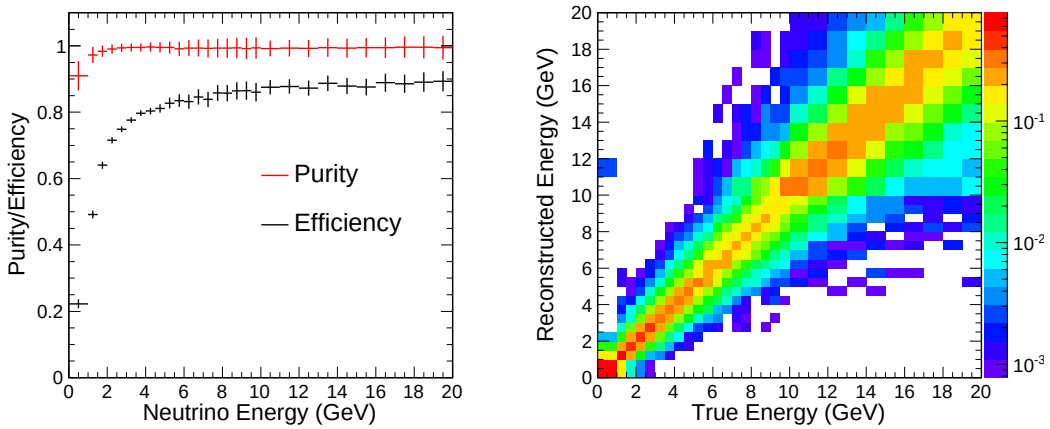

(a) Efficiency and Purity

(b) Energy Smearing

FIGURE 5.9. The Far Detector acceptance correction.

5.4. SYSTEMATIC UNCERTAINTY

Systematic errors can potentially affect the values of the measured oscillation parameters. This section will describe the sources of systematic error that are most important for the atmospheric oscillation analysis. The errors and their associated systematic uncertainties are evaluated by the Monte Carlo sample.

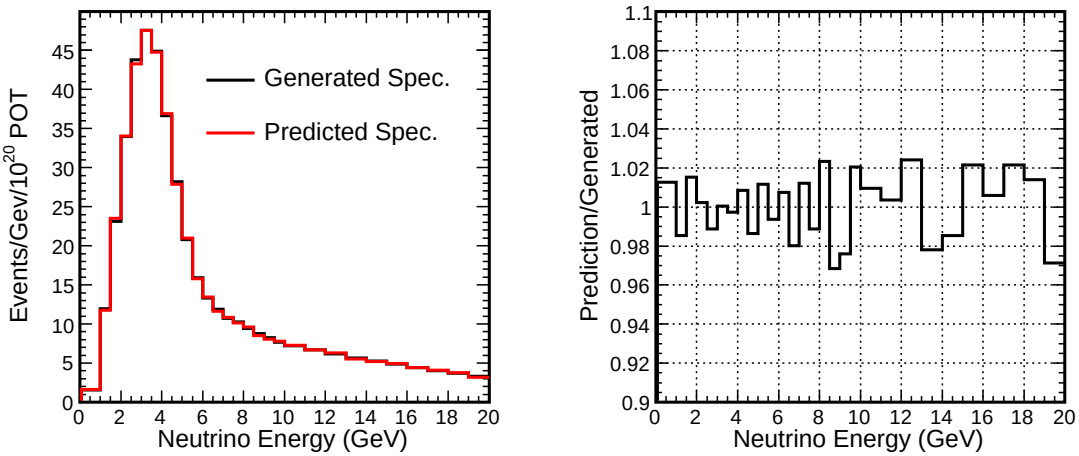

FIGURE 5.10. The Far Detector reconstructed energy spectrum prediction.

5.4.1. Relative Normalization. The uncertainty on the relative normalization between Near and Far has been estimated to be 4% [Adamson et al., 2008a]. This number has three sources: 2% from fiducial mass calculations, 1% from the live time, and 3% from reconstruction differences.

The normalization uncertainty from reconstruction can be calculated as:

$$\text{Uncertainty} = 1 - \frac{\left(R_{\text{tracking}} \times R_{\text{sign}} \times R_{\text{fiducial}}\right)_{\text{Far}}}{\left(R_{\text{tracking}} \times R_{\text{sign}} \times R_{\text{fiducial}}\right)_{\text{Near}}} \tag{5.12}$$

where R is the ratio of the efficiencies between the data and Monte Carlo for track identification, charge sign determination and fiducial volume effects.

The tracking efficiency estimates how often reconstructed tracks are misidentified in CC events and missed in NC events. The sign efficiency identifies tracks obviously reconstructed with the wrong curvature. The fiducial efficiency accounts for events with an incorrect vertex position.

5.4.2. Hadron Energy Scale. The estimated error from the shower or hadronic energy scale consists of the absolute energy scale (including single hadron response,

intranuclear effects, calibration) and the relative energy scale between the Near and Far Detectors.

The Calibration Detector provided the single hadron response for the MINOS detectors. Table 5.1 lists the different components of the uncertainty. A total uncertainty of 5.6% was derived for the absolute scale uncertainty.

TABLE 5.1. Uncertainties from the Calibration Detector for use in calculating the absolute energy scale [MINOS, 2007].

Sources	Uncertainty
Tuning MC to CalDet data	2.5-5%
CalDet beam	2%
CalDet stopping muon	1.4%
Spill .vs. Cosmic Response	1%
Total	5.6%

Hadron produced from neutrino interaction can re-interact in the target nucleus. This process is referred to as final state interaction or intranuclear re-scattering. The uncertainty in these final state interactions must be accounted for in the calculation of the resulting shower energy as measured in the MINOS detectors. The total uncertainty was estimated by selecting the important parameters and then shifting each component by 1 σ and evaluating the resulting shift in the shower energy. The total maximum uncertainty from these effects is 8.2% in the lowest energy bin.

By comparing the calibration procedures in the Near and Far Detectors a relative uncertainty can be found: The total uncertainty in the Near Detector is 2.3% while the Far Detector is 2.4%. Combining these in quadrature gives a Near-to-Far relative calibration of 3.3%. The largest uncertainty in both the Near and Far detector is the result of difference in the spatial variation of the response when comparing the data to the Monte Carlo.

The total hadronic energy uncertainty is obtained by adding in quadrature the values from the intranuclear re-scattering, 5.6% uncertainty from CalDet, and the 2.4% uncertainty from the Far Detector calibration. This is a shower dependent value with a maximum of 10.3%.

5.4.3. Muon Momentum. A Range-Curvature task force studied the systematic error on the muon energy as measured by range. They found the error to be 2% by comparing GEANT Monte Carlo predictions to external data. To establish the uncertainty on the momentum determination from curvature, a comparison of the muon energy from range and curvature was carried out. The agreement was found to be good with 2%, making the total systematic error on the muon energy from curvature to be 4% [Hatcher et al., 2007].

5.4.4. Neutral Current Contamination. The Monte Carlo model are not reliable to estimate the NC background due to the uncertainties in the hadronization, intranuclear process and NC cross section. This requires constraints from the Near Detector data to understand these uncertainties. MINOS use a data driven study to estimate the uncertainty on the NC background using muon removed events. Muon hits were removed from CC events to create NC-like or "fake" NC events. By comparing these fake NC events, an estimate of the track finding efficiency in hadronic showers can be obtained.

The fake NC events are reprocessed through the reconstruction chain applying the CC event selection cuts. This sample can be used to study differences in the reconstruction of background NC events. Fitting the ratio after the PID cut gives an efficiency correction factor. The result of the fit gives an energy dependent correction factor that addresses the differences in finding tracks in NC events.

After correction of the Monte Carlo to match the selection efficiency of NC data events, the uncertainties in the NC cross section can be directly addressed. This is a simple process and involves scaling the NC PID distribution so that the best possible agreement is achieved between the overall MC and data Pid distributions.

The typical efficiency error is about 20%, while the typical normalization correction is about 10%. Assuming these numbers are uncorrelated, the NC background is calculating to be 25%. Given that the muon removed events have inherent difference from the NC events, the value was doubled to 50% [Marshall, 2007].

5.4.5. Cross Section. Estimates the uncertainty of the charged current neutrino cross section can be broken down into different parts: uncertainties on the quasi-elastic and resonance axial mass M_A and uncertainties on the behavior of the cross-section in the transition region from resonance to deep inelastic scattering.

The low energy region is governed by the two M_A values. Both are dipole parametrization of the neutrino-nucleon cross-section. The value of M_A^{QE} and M_A^{RES} used in the simulation, based on preexisting data are 0.99 and 1.12 respectively. Both of these measurements have an uncertainty of 15% which takes into account evidence that the data may not be described by the simple dipole parametrization and effects in iron nuclei. These classes of events make up a majority of the events in the oscillation region, and therefore uncertainties for DIS events are not considered.

5.5. Impact on the Oscillation Measurements

The strategy used to quantify the impact of the systematic errors on the oscillation parameters proceeds as follows:

(1) Create a "fake" data set for the Near and Far Detectors from the Monte Carlo. Oscillate the data using the input parameters of $\sin^2(2\theta_{23}) = 1.0$ and $\Delta m^2_{32} = 2.38 \times 10^{-3}\,\mathrm{eV}^2$.
(2) Apply 1σ systematic shift on the fake data for both Near and Far Detectors.
(3) Use the beam matrix method to predict the unoscillated Far Detector spectrum.
(4) Fit the Monte Carlo to the fake Far Detector data and find out how far the oscillation parameters have shifted from the input values.

Table 5.2 lists the systematic shifts on the measurement of $|\Delta m^2_{32}|$ and $\sin^2(2\theta_{23})$ for various sources of systematic error. The values quoted are the maximum shifts for ± 1 standard deviation variations in each of the systematic parameters. The

largest systematic uncertainties come from the normalization, absolute hadronic energy scale and neutral current contamination. These three systematic parameters will be included as nuisance parameters in the fit for the Far Detector data in Chapter 6.

TABLE 5.2. Systematic shifts on the measurement of $|\Delta m^2_{32}|$ and $\sin^2(2\theta_{23})$ for various sources of systematic error.

Uncertainty	$\lvert\Delta m^2_{32}\rvert(10^{-3}\,\mathrm{eV}^2/\mathrm{c}^4)$	$\sin^2(2\theta_{23})$
Normalization ±4%	0.08	0.005
Abs. hadronic E scale ±11%	0.05	0.005
NC contamination ±50%	0.02	0.020
Rel. hadronic E scale ±3%	0.01	0.010
flux uncertainty $\pm1\sigma$	0.01	0.005
Track E scale ±2%	0.03	0.005
$M_A^{QE} \pm 15\%$	0.00	0.005
$M_A^{RES} \pm 15\%$	0.00	0.005
KNO parameters ±50%	0.00	0.010
Total Sys. Error	0.10	0.027

Chapter 6

Far Detector Data

This chapter will describe the selection of events in the Far Detector data and perform the oscillation fit to the selected data sample.

The data sets used for the oscillation analysis are the Run1 and Run2 LE beam configuration. The number of proton on target (POT) for Run1 is 1.27×10^{20}, for Run2 is 1.94×10^{20}. The total is 3.2×10^{20}.

6.1. Selection Cuts

The following selection cuts were applied to select neutrino events from the NuMI beam:

- **Data Quality Cut:** Require the high voltage, coil and timing system to be fully operational.
- **Spill Timing Cut:** Require the time difference between an event and the nearest spill to be $\leq 20\,\mu$s and $\geq -30\,\mu$s, as shown in Figure 6.1.
- **Light Injection Cut:** The calibration system used an LED light injection system to character the detector response. An algorithm identifies light injection events and remove them from the data sample.
- **Track Cut:** Events must have at least one track the passes the track fitter.
- **Fiducial Volume Cut:** The fiducial volume of the Far Detector is defined such that the z is $\geq 0.5\,$m and $\leq 29.4\,$m except between the super module region $\geq 14.5\,$m and $\leq 16.5\,$m. The distance, d, from the vertex to the center of the detector must satisfy $d \geq 0.4\,$m to eliminate events close to the magnetic coil and $d \leq \sqrt{14}\,$m, as shown in Figure 6.3.

- **Track Angle Cut:** In order to select the neutrino events from the beam instead of the cosmic rays, we require the angle between the reconstructed track and the beam direction is required to be within 53°, as shown in Figure 6.2.
- **Charge Current Selection Cut:** Select CC events by requiring the output of the KNN algorithm be greater than 0.3.

Table 6.1 shows the event cut table for the Far Detector data sample. The total number of events after the selection cuts is 708, 270 in Run1 and 438 in Run2. And the total selected event rate as a function of time is flat as shown in Figure 6.4.

TABLE 6.1. The cut table of the Far Detector event selection of different run period.

Cut	Run1	Run2	Sum	percentage(%)
Track in Fiducial	400	657	1057	100
Track Direction	376	616	992	93.8
Track Quality	374	615	989	93.6
Track charge	315	515	830	78.5
Track PID	270	438	708	67.0

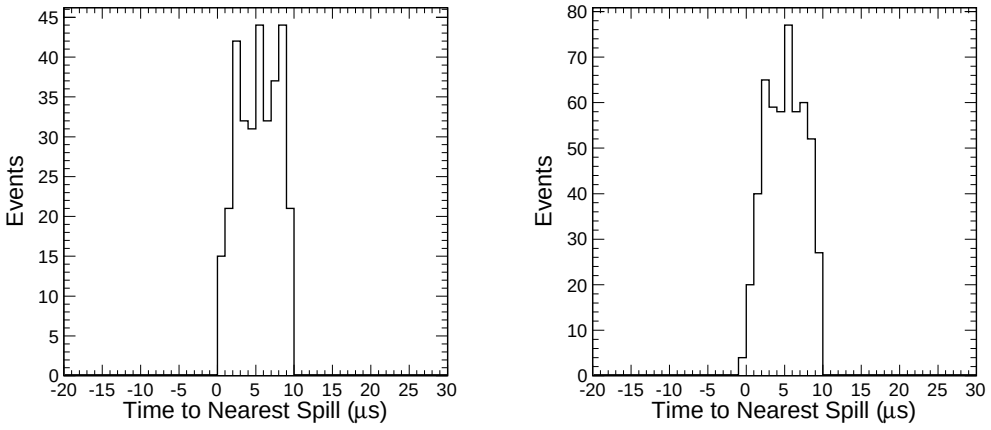

(a) Run1 Data (b) Run2 Data

FIGURE 6.1. The relative time between neutrino events and the closest spill time.

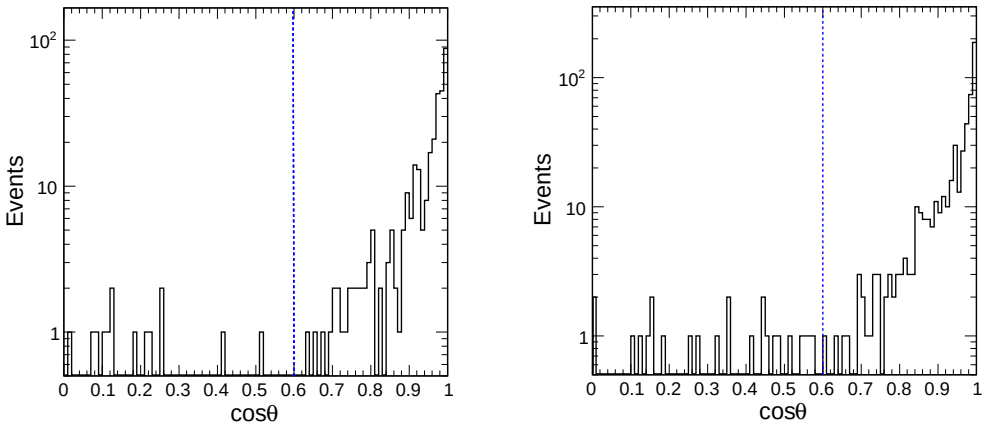

(a) Run1 Data (b) Run2 Data

FIGURE 6.2. The cosine of angle between the reconstructed track and the beam direction. The blue dotted line shows the selection cut.

6.2. DATA AND MC COMPARISON

6.2.1. Event Deficit. In the following few pages, The comparison between the data and unoscillated Monte Carlo extrapolation and a fit to the oscillation hypothesis. Clear evidence is seen of a suppression of the low energy events.

From the Far Detector data and Monte Carlo comparison, we can see a clear event deficit. Assuming no oscillation, the predicted number of Far Detector events is 923 ± 52 (syst.). The observed number of Far Detector events is 708. The deficit corresponds to a significance of 3.6 standard deviations, where both statistical and systematic errors on the total rate are taken into account.

6.2.2. LE Run1 data/MC comparison. This section compares different distributions in the Far Detector for LE Run1 data and unoscillated and oscillated Monte Carlo from Figure 6.6 to Figure 6.10.

6.2.3. LE Run2 data/MC comparison. This section compares different distributions in the Far Detector for LE Run2 data and unoscillated and oscillated Monte Carlo from Figure 6.11 to Figure 6.15.

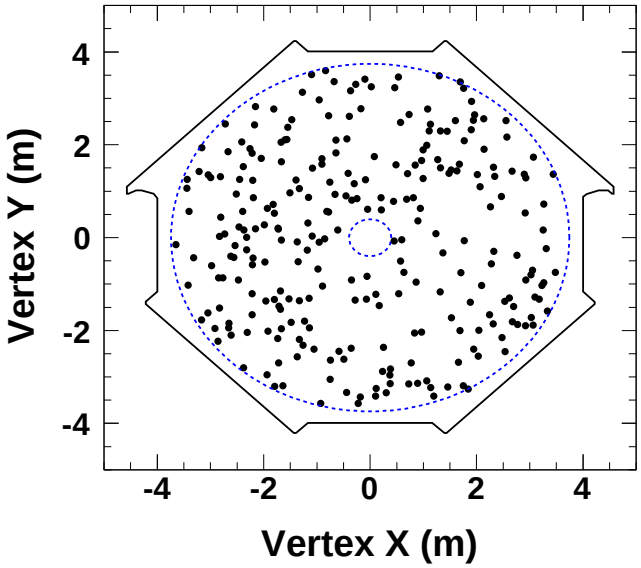

(a) Run1 Data

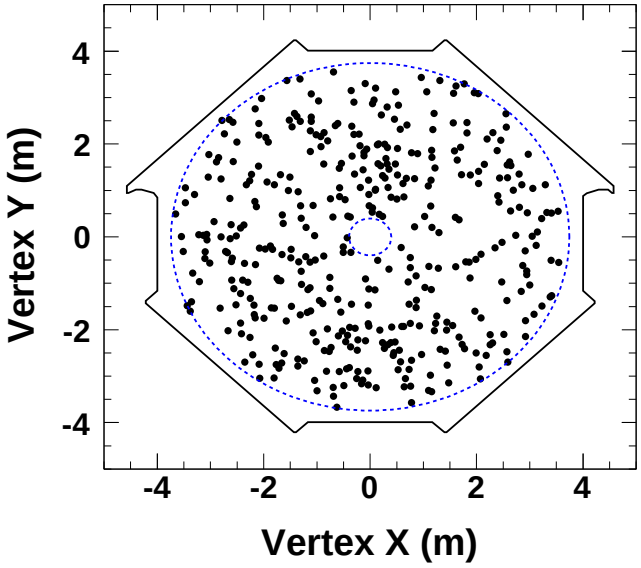

(b) Run2 Data

FIGURE 6.3. 2D plots in the x and y plane of event vertex position for LE Run1 (top) and Run2 (bottom). The blue line indicates the fiducial volume of the Far Detector.

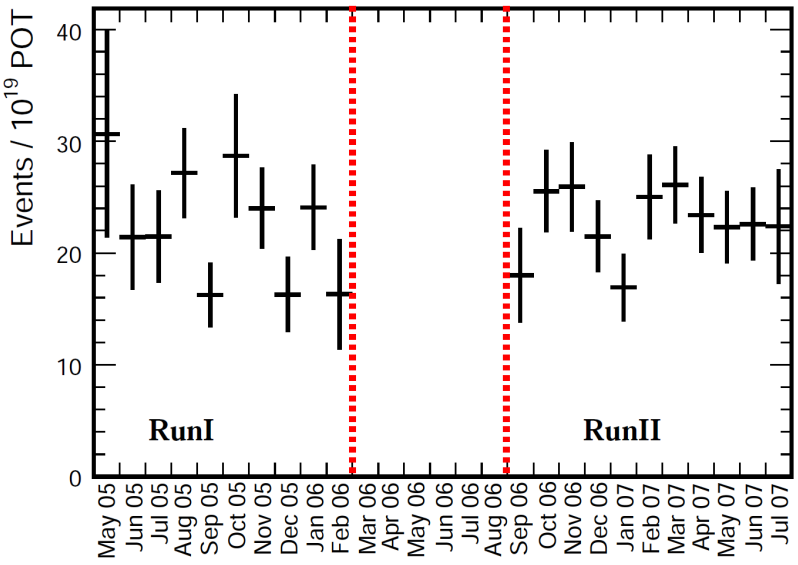

FIGURE 6.4. The number of CC-like events as a function of month [Armstrong].

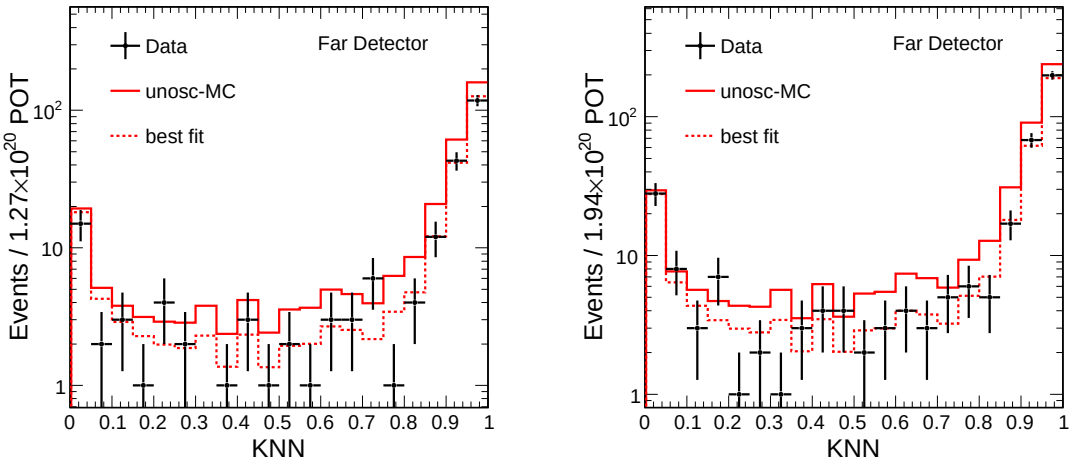

(a) Run1

(b) Run2

FIGURE 6.5. KNN distributions for the LE Run1 (left) and Run2 (right) Far Detector data and Monte Carlo. Data is represented with black points. The red solid and dotted lines represent the unoscillated and oscillated Monte Carlo.

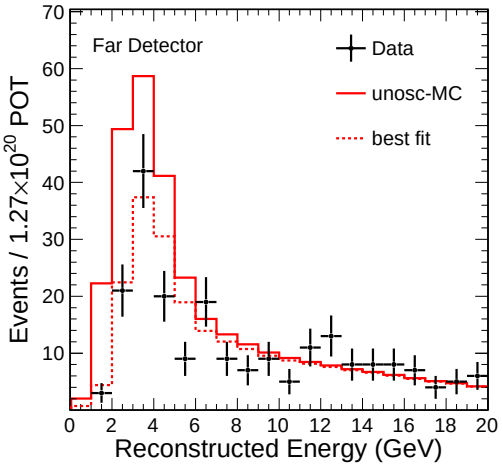

(a) Reconstructed event energy

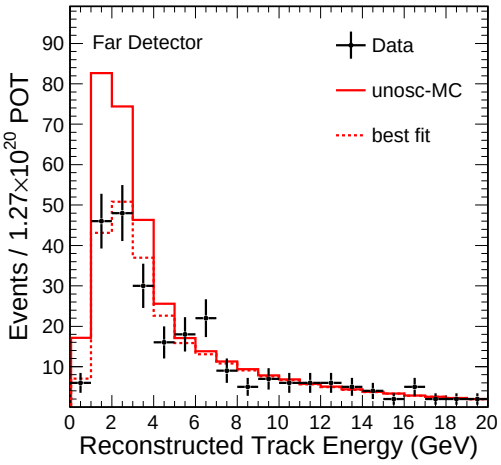

(b) Reconstructed track energy

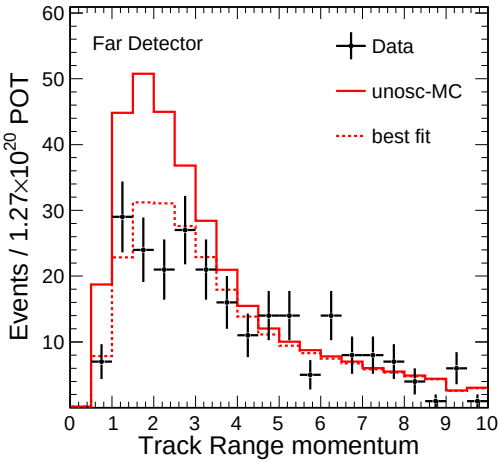

(c) Reconstructed track range momentum

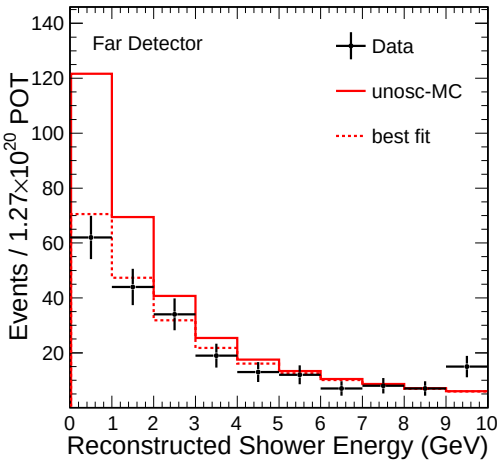

(d) Reconstructed shower energy

FIGURE 6.6. Energy distributions for the LE Run1 Far Detector data and Monte Carlo. Data is represented with black points. The black points represent data, the red solid and dotted lines represent the unoscillated and oscillated Monte Carlo.

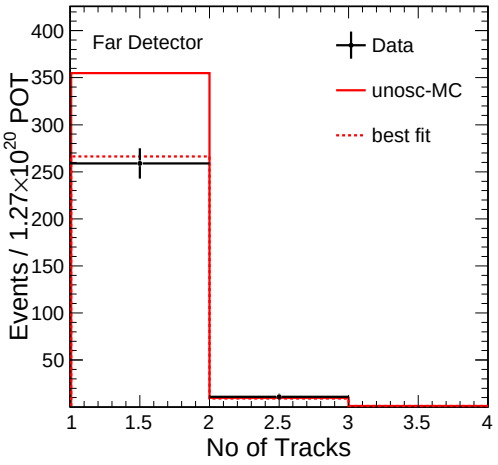

(a) No. of tracks

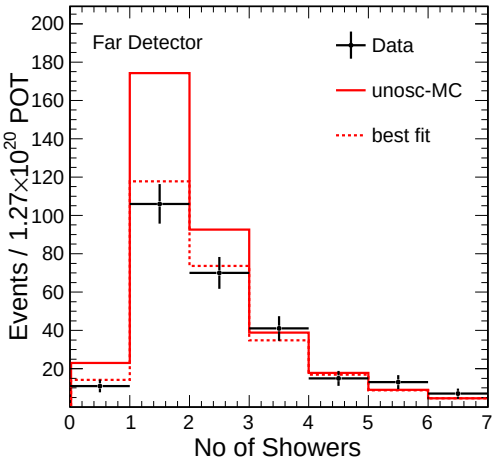

(b) No. of showers

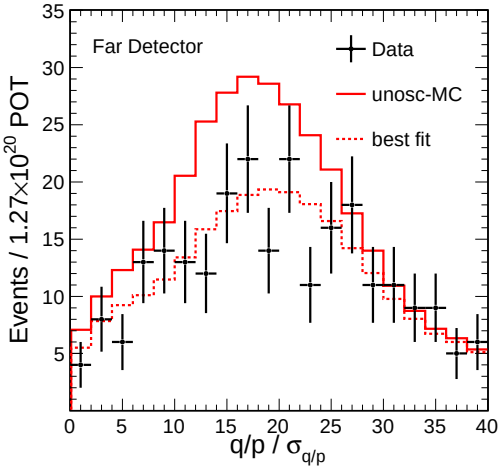

(c) q/p/$\sigma_{q/p}$

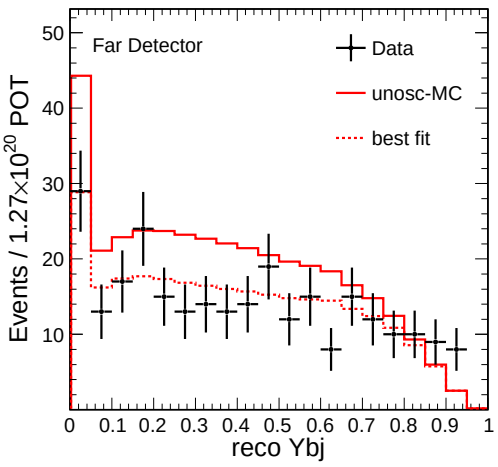

(d) Reconstructed Ybj

FIGURE 6.7. Track and shower distributions for the LE Run1 Far Detector data and Monte Carlo. Data is represented with black points. The red solid and dotted lines represent the unoscillated and oscillated Monte Carlo.

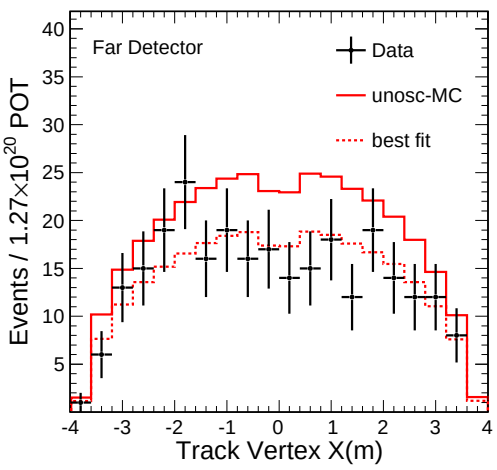

(a) Track vertex X (m)

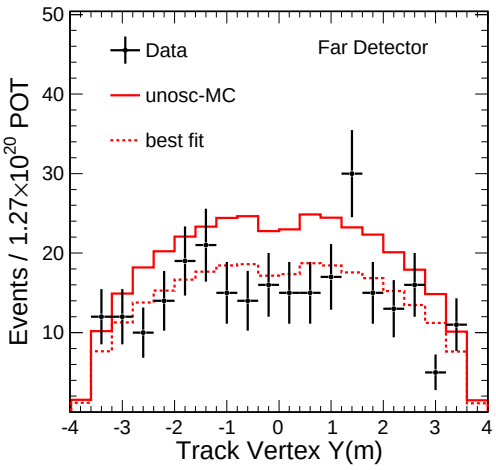

(b) Track vertex Y (m)

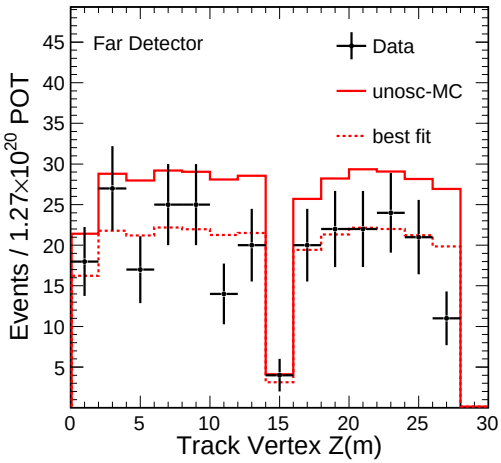

(c) Track vertex Z (m)

FIGURE 6.8. Track vertex distributions for the LE Run1 Far Detector data and Monte Carlo. Data is represented with black points. The red solid and dotted lines represent the unoscillated and oscillated Monte Carlo.

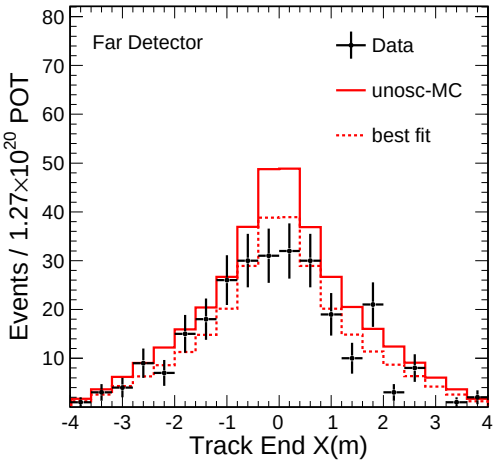

(a) Track end X (m)

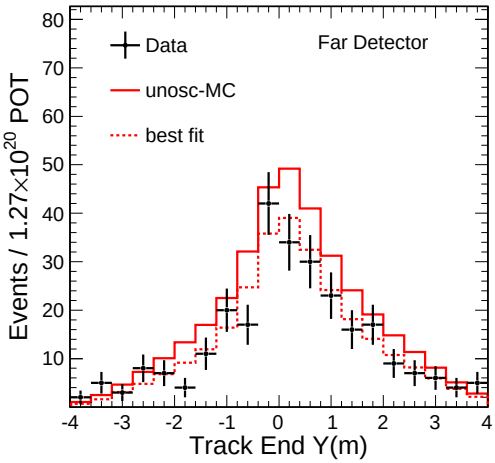

(b) Track end Y (m)

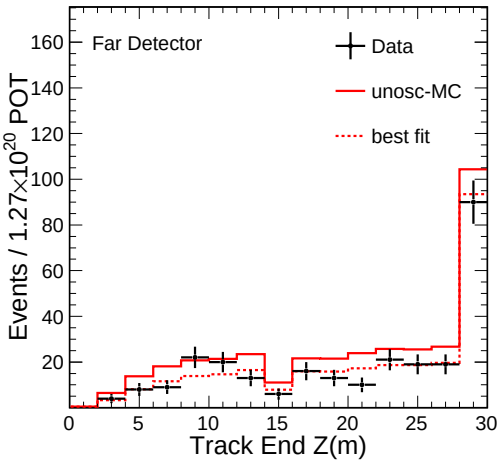

(c) Track end Z (m)

FIGURE 6.9. Track end distributions for the LE Run1 Far Detector data and Monte Carlo. Data is represented with black points. The red solid and dotted lines represent the unoscillated and oscillated Monte Carlo.

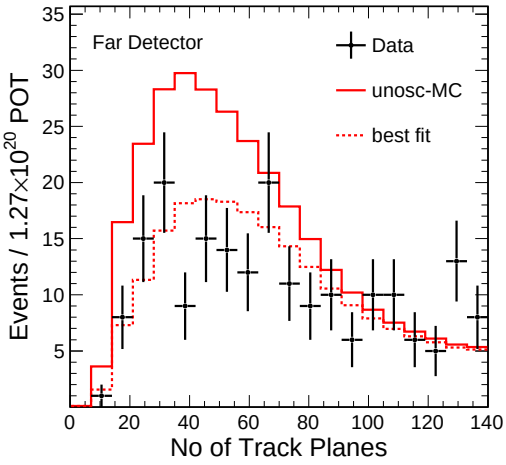

(a) No. of track planes

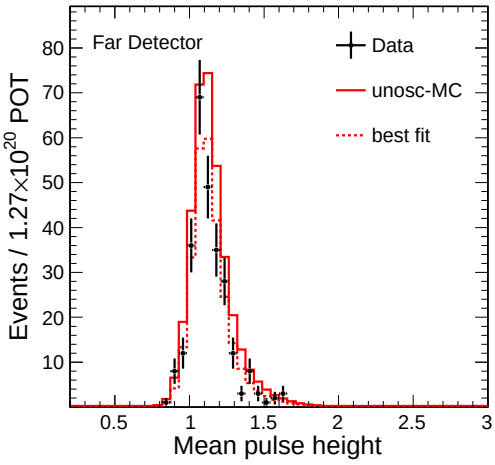

(b) Mean pulse height

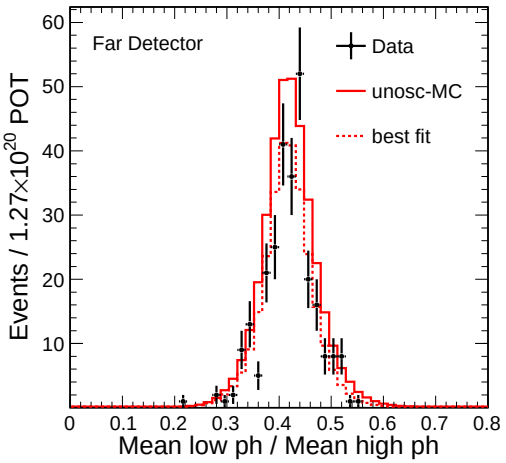

(c) Mean low/high pulse height

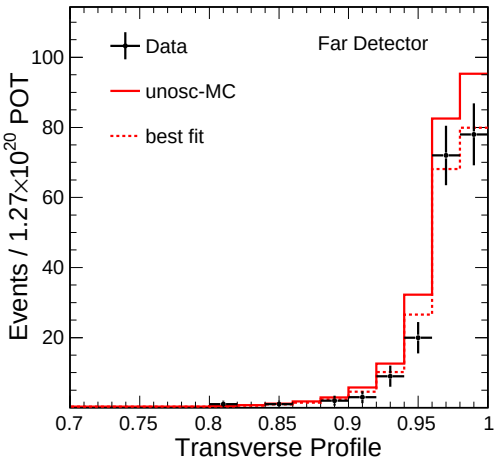

(d) Transverse profile

FIGURE 6.10. KNN input variables for the LE Run1 Far Detector data and Monte Carlo. Data is represented with black points. The red solid and dotted lines represent the unoscillated and oscillated Monte Carlo.

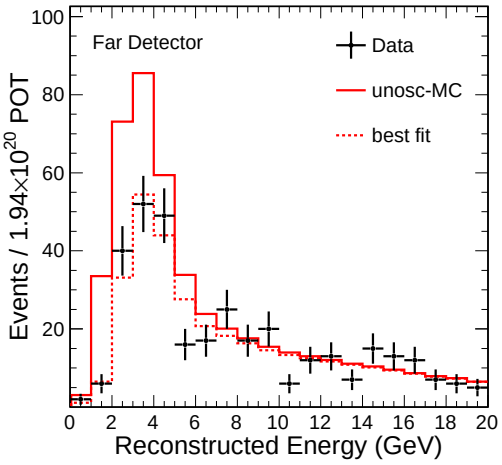

(a) Reconstructed event energy

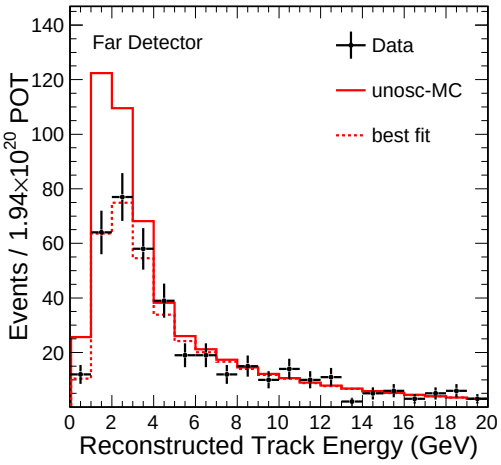

(b) Reconstructed track energy

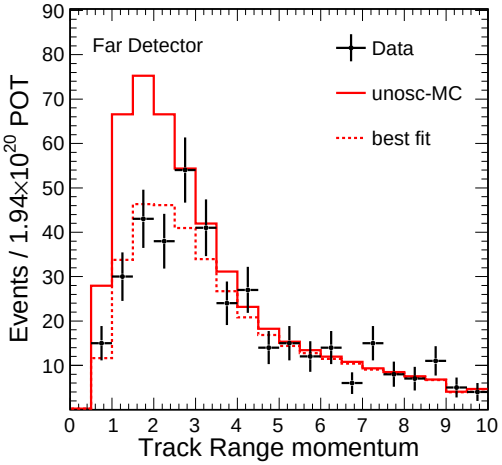

(c) Reconstructed track range momentum

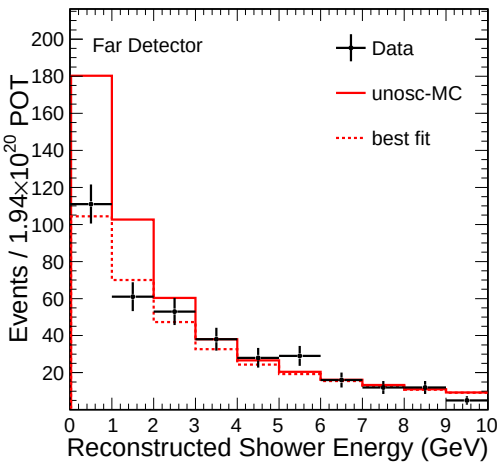

(d) Reconstructed shower energy

FIGURE 6.11. Energy distributions for the LE Run2 Far Detector data and Monte Carlo. Data is represented with black points. The black points represent data, the red solid and dotted lines represent the unoscillated and oscillated Monte Carlo.

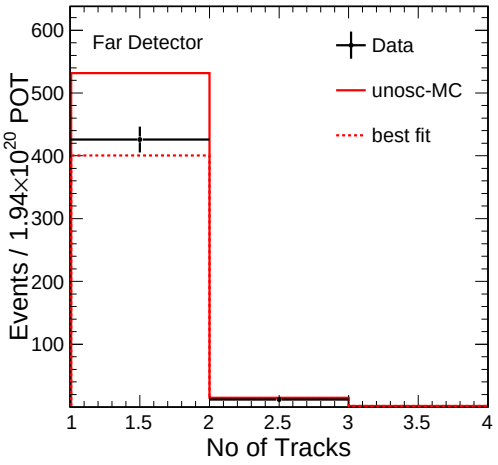

(a) No. of tracks

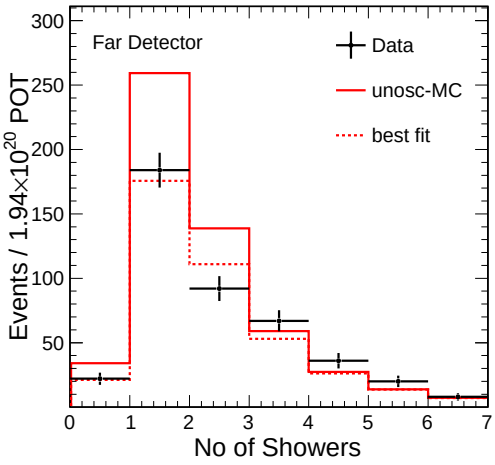

(b) No. of showers

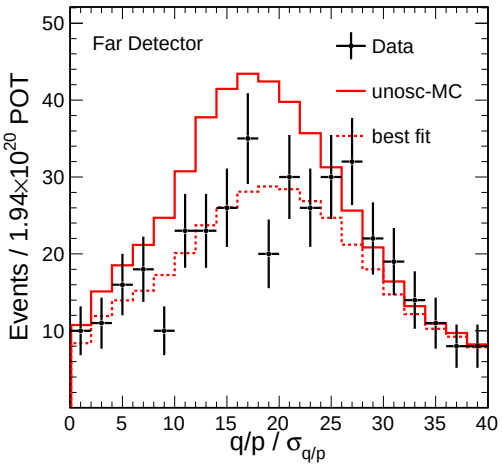

(c) q/p/$\sigma_{q/p}$

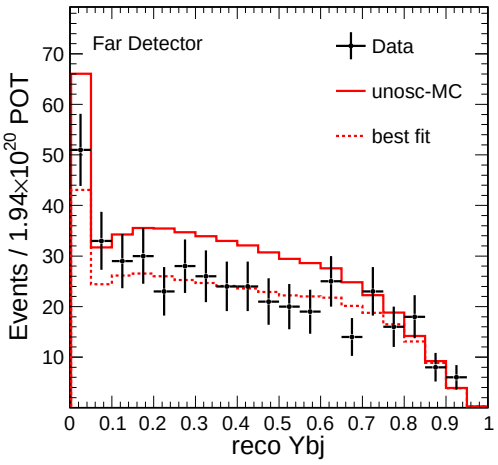

(d) Reconstructed Ybj

FIGURE 6.12. Track and shower distributions for the LE Run2 Far Detector data and Monte Carlo. Data is represented with black points. The red solid and dotted lines represent the unoscillated and oscillated Monte Carlo.

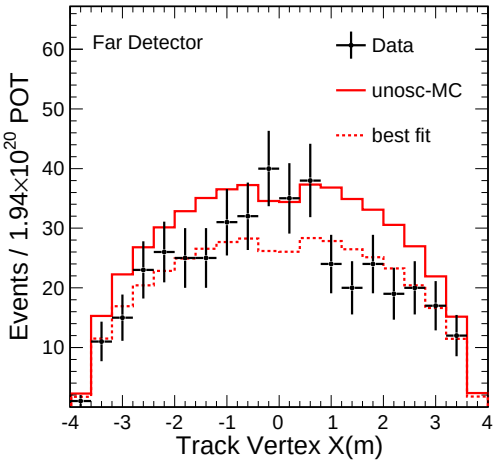

(a) Track vertex X (m)

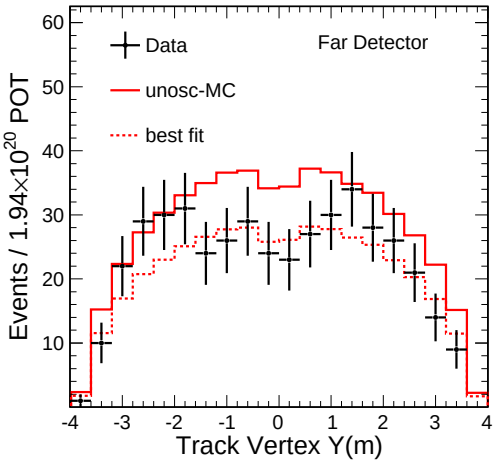

(b) Track vertex Y (m)

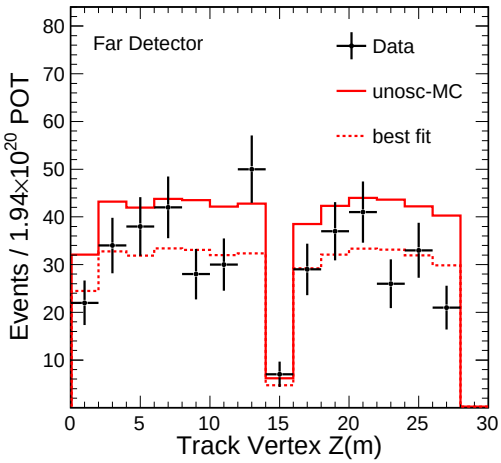

(c) Track vertex Z (m)

FIGURE 6.13. Track vertex distributions for the LE Run2 Far Detector data and Monte Carlo. Data is represented with black points. The red solid and dotted lines represent the unoscillated and oscillated Monte Carlo.

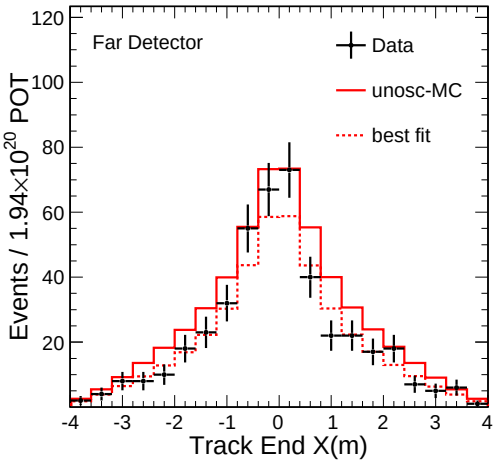

(a) Track end X (m)

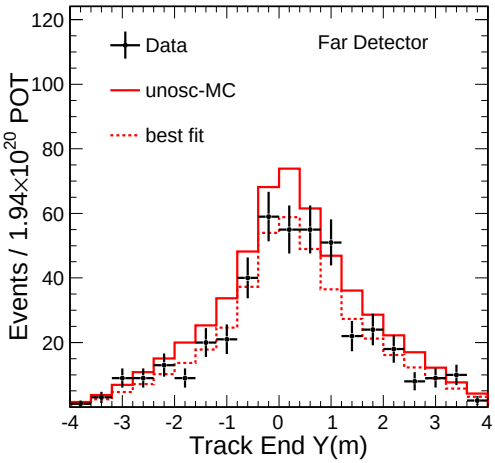

(b) Track end Y (m)

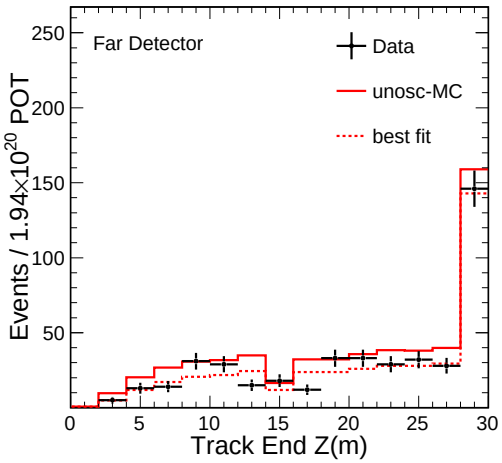

(c) Track end Z (m)

FIGURE 6.14. Track end distributions for the LE Run2 Far Detector data and Monte Carlo. Data is represented with black points. The red solid and dotted lines represent the unoscillated and oscillated Monte Carlo.

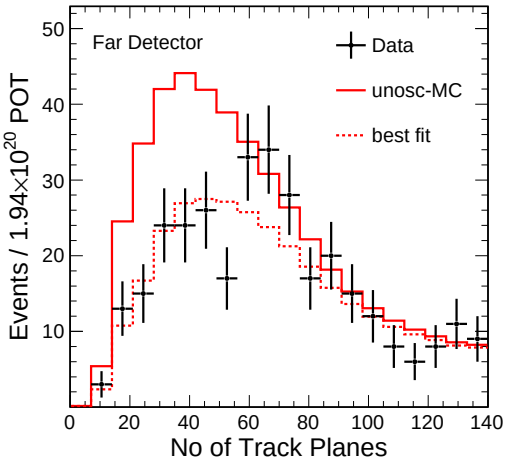

(a) No. of track planes

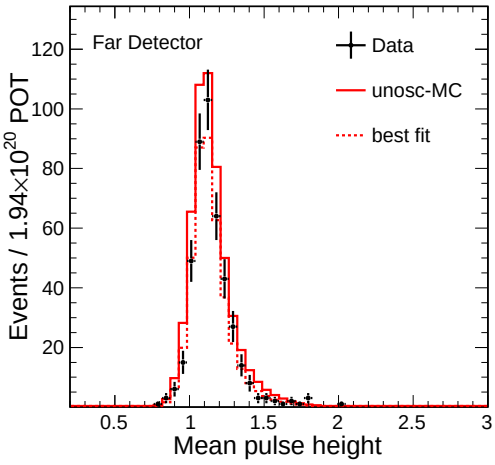

(b) Mean pulse height

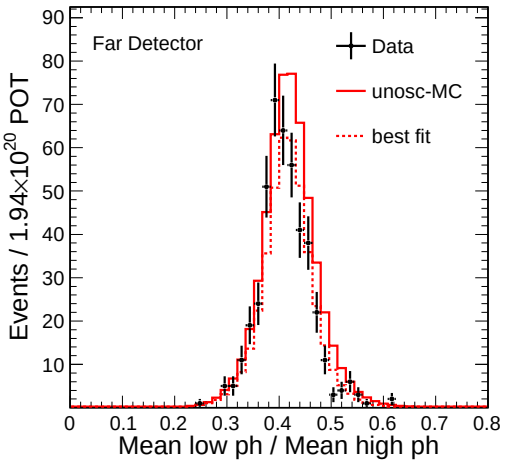

(c) Mean low/high pulse height

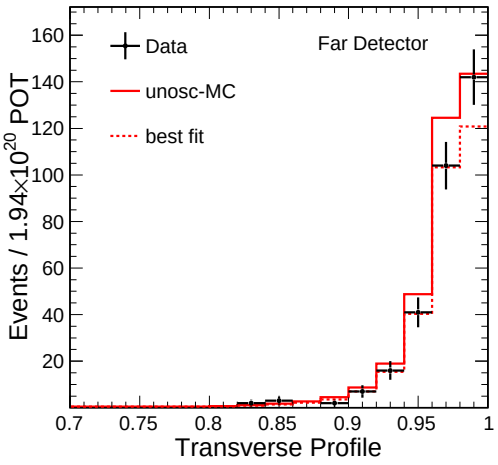

(d) Transverse profile

FIGURE 6.15. KNN input variables for the LE Run2 Far Detector data and Monte Carlo. Data is represented with black points. The red solid and dotted lines represent the unoscillated and oscillated Monte Carlo.

6.3. Oscillation Fit

Based on the two-flavor $\nu_\mu \to \nu_\tau$ oscillation assumption, the muon neutrino survival probability is given by:

$$P(\nu_\mu \to \nu_\mu) = 1 - \sin^2(2\theta_{23}) \sin^2(1.267 \Delta m^2_{32} L/E) \tag{6.1}$$

In order to measure the oscillation parameters $|\Delta m^2_{32}|$ and $\sin^2(2\theta_{23})$, we can fit the Equation 6.1 to the Far Detector data. The likelihood function is defined as:

$$\chi^2 = \sum_{i}^{bins} 2(N_i^{exp} - N_i^{obs} + 2N_i^{obs} ln(N_i^{obs}/N_i^{exp})) + \sum_{j=1}^{3} \left(\frac{\Delta \alpha_j}{\sigma_{\alpha_j}} \right)^2 \tag{6.2}$$

where N_i^{obj} and N_i^{exp} are the numbers of observed and expected events in bin i of the reconstructed energy distribution, the α_j are fitted systematic parameters, with associated errors σ_{α_j}.

Figure 6.16, Figure 6.17 and Figure 6.18 shows the neutrino energy spectrum for the Far Detector data compared with the unoscillated prediction and the best fit prediction. The best fit prediction came from a simultaneous fit to the data from run1 and run2 LE configurations.

The allowed regions at 68%, 90% and 99% C.L. in the $|\Delta m^2_{32}|$, $\sin^2(2\theta_{23})$ plane are shown in Figure 6.19 and Figure 6.20. Here the confidence level intervals are obtained using the Gaussian approximation ($\Delta\chi^2 = 2.3, 4.6, 9.2$). These confidence level intervals were found to be in good agreement with those obtained from a study using the unified approach of Feldman and Cousins [Adamson et al., 2008a].

Ignoring for the moment the effect of the systematic errors, the best fit points for oscillation parameters were found at $|\Delta m^2_{32}| = 2.36 \times 10^{-3}\,\mathrm{eV}^2$ and $\sin^2(2\theta_{23}) = 1.00$. The result had a $\chi^2 = 63.5$ for 62 degrees of freedom.

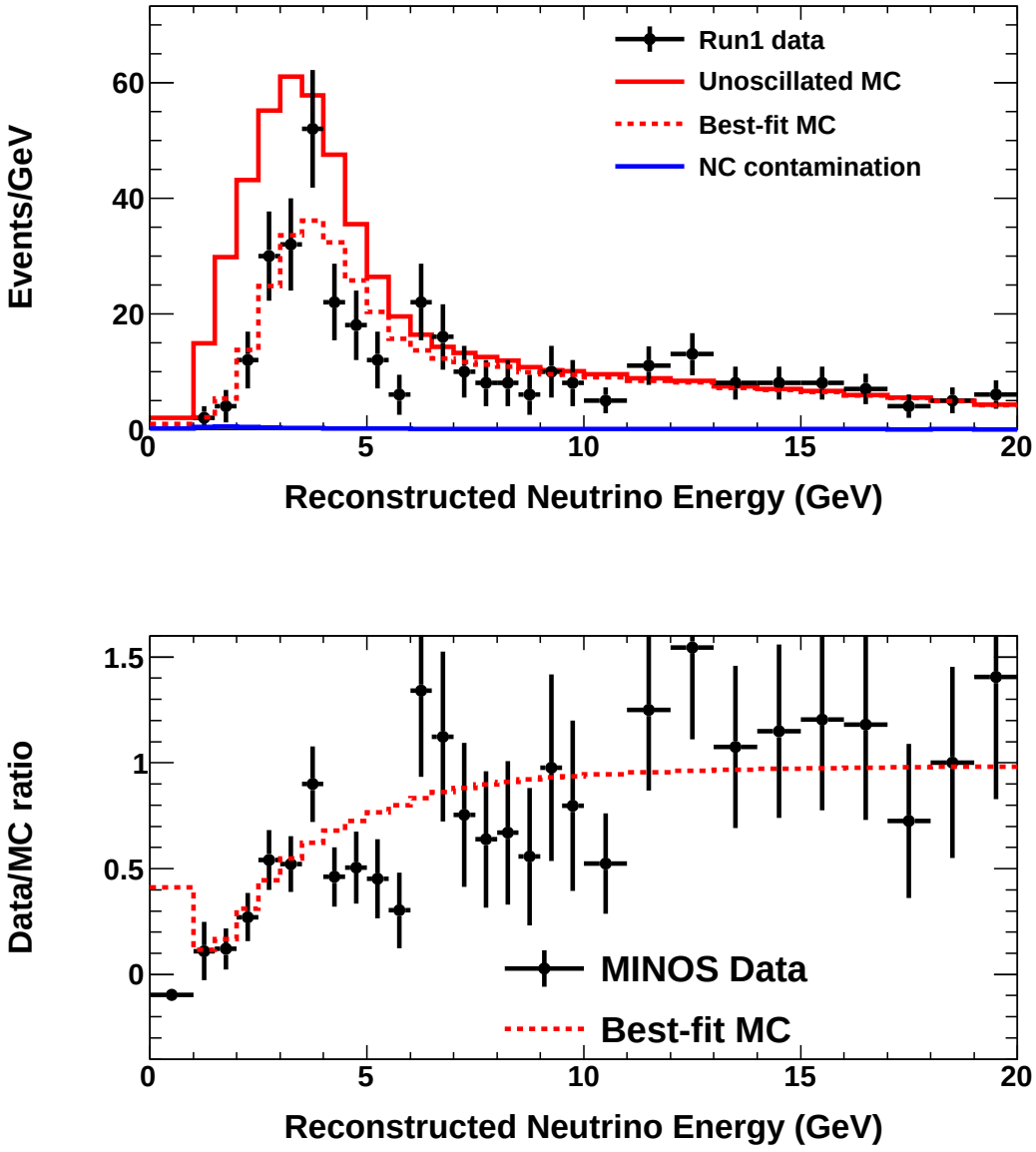

FIGURE 6.16. The top plot shows the neutrino energy spectrum from the LE Run1 configuration with the unoscillated prediction and best-fit oscillated spectrum overlaid. The bottom plot shows the ratio of the observed spectrum to the unoscillated Far Detector prediction, where the expected neutral-current background has been subtracted.

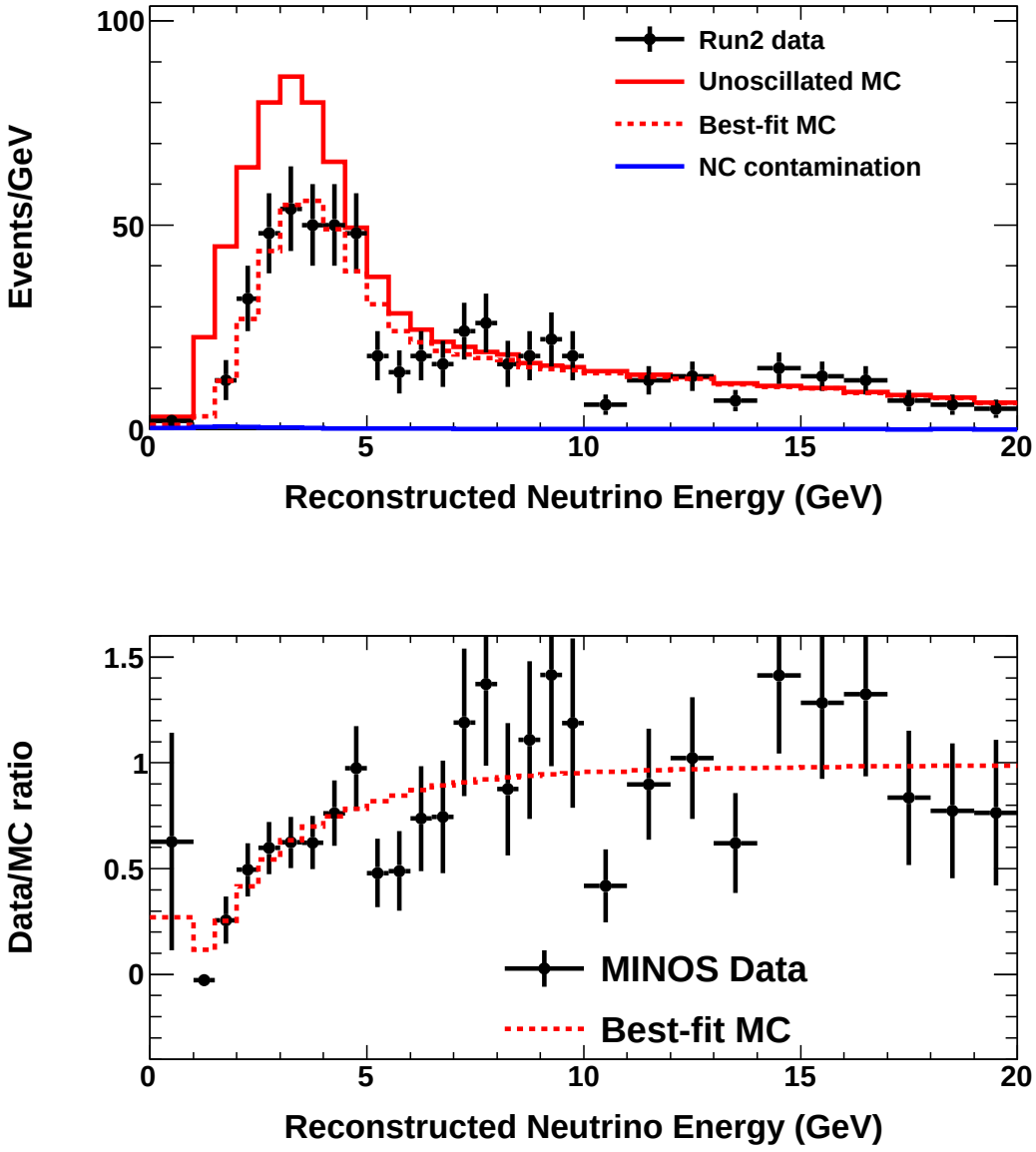

FIGURE 6.17. The top plot shows the neutrino energy spectrum from the LE Run2 configuration with the unoscillated prediction and best-fit oscillated spectrum overlaid. The bottom plot shows the ratio of the observed spectrum to the unoscillated Far Detector prediction, where the expected neutral-current background has been subtracted.

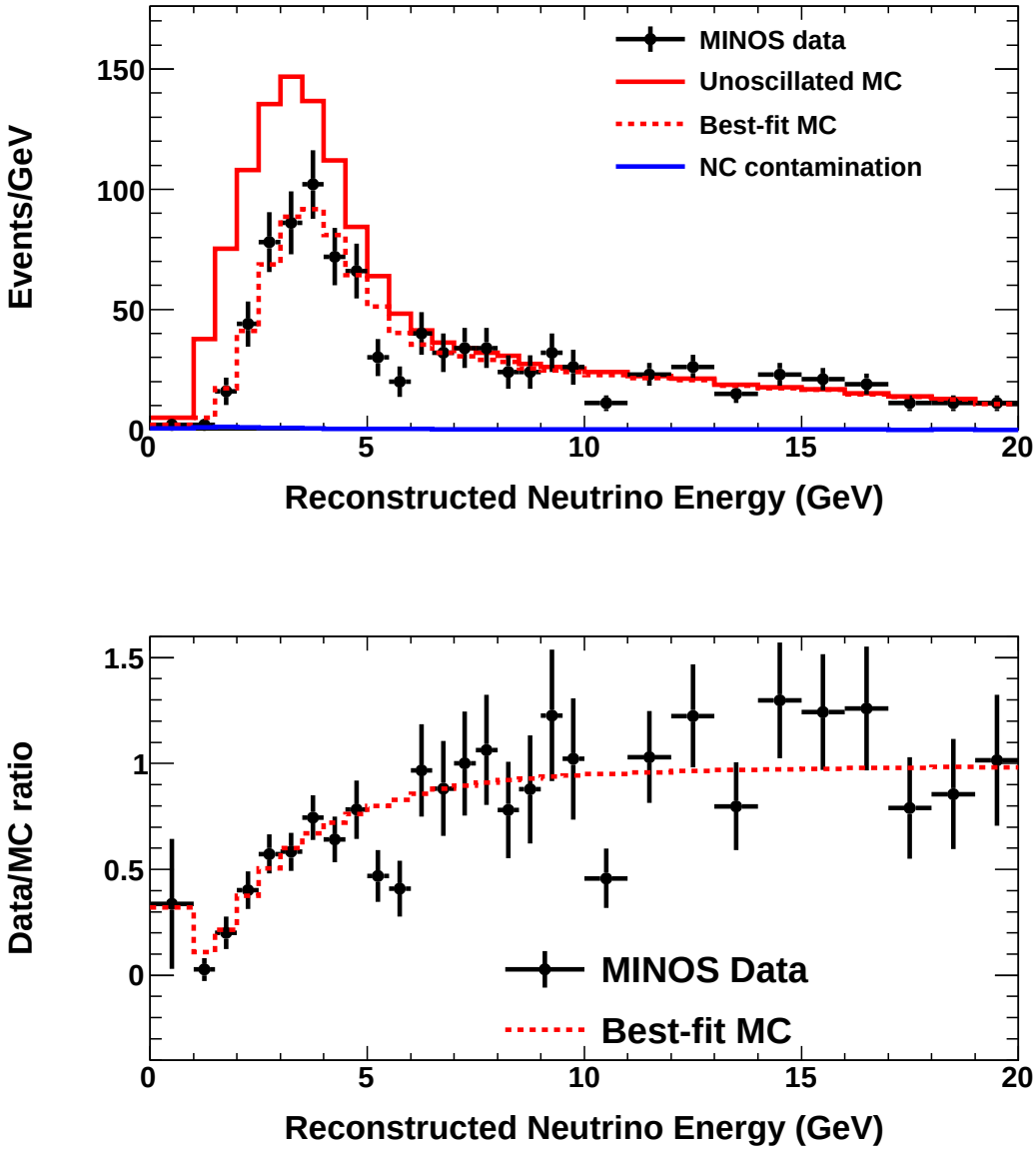

FIGURE 6.18. The top plot shows the neutrino energy spectrum from the LE Run1 and Run2 configuration with the unoscillated prediction and best-fit oscillated spectrum overlaid. The bottom plot shows the ratio of the observed spectrum to the unoscillated Far Detector prediction, where the expected neutral-current background has been subtracted.

If we put the 3 largest systematic errors into the fit calculation, the best-fit parameters are $|\Delta m^2_{32}| = 2.44 \times 10^{-3}\,\mathrm{eV}^2$ and $\sin^2(2\theta_{23}) = 1$, where the fit has been constrained to the region $\sin^2(2\theta_{23}) \leq 1$. The allowed ranges of these parameters are:

$$2.28 \times 10^{-3} < |\Delta m^2_{32}| < 2.56 \times 10^{-3}\mathrm{eV}^2$$

$$\sin^2(2\theta_{23}) > 0.955 \quad (68\%\ \mathrm{C.L.})$$

$$2.20 \times 10^{-3} < |\Delta m^2_{32}| < 2.70 \times 10^{-3}\mathrm{eV}^2$$

$$\sin^2(2\theta_{23}) > 0.900 \quad (90\%\ \mathrm{C.L.})$$

The best fit result of $|\Delta m^2_{32}|$ has been changed by $0.08 \times 10^{-3}\,\mathrm{eV}^2$, which is consistent with the uncertainty quoted in Table 5.2 in Chapter 5. And the best fit result requests we need to increase the F/N relative normalization by 1%, decrease the absolute hadronic energy scale by 5% and decrease the neutral-current contamination by 5%.

Table 6.2 shows the best-fit oscillation parameters and χ^2 when fitting each data run alone and combined. It also shows the best-fit results when the physical boundary constraint ($\sin^2(2\theta_{23}) \leq 1$) is removed. Figure 6.21 shows the fit contours for the different running period.

The one-dimensional projection of the χ^2 surface for $\sin^2(2\theta_{23})$ and $|\Delta m^2_{32}|$ are shown in Figure 6.22, the value of χ^2 has been minimized at each point with respect to $|\Delta m^2_{32}|$ and $\sin^2(2\theta_{23})$.

TABLE 6.2. The best-fit oscillation parameters when fitting each data run alone.

Data Set	$\lvert\Delta m^2_{32}\rvert(10^{-3}\,\mathrm{eV}^2)$	$\sin^2(2\theta_{23})$	χ^2/d.o.f
LE Run1 Only	2.60	1.000	28.96 / 30
LE Run1 Only (Unconstrained)	2.36	1.065	28.17 / 30
LE Run2 Only	2.34	1.000	32.42 / 30
LE Run2 Only (Unconstrained)	2.38	1.070	31.22 / 30
LE Run1 + Run2	2.44	1.000	62.88 / 62
LE Run1 + Run2 (Unconstrained)	2.30	1.050	62.13 / 62

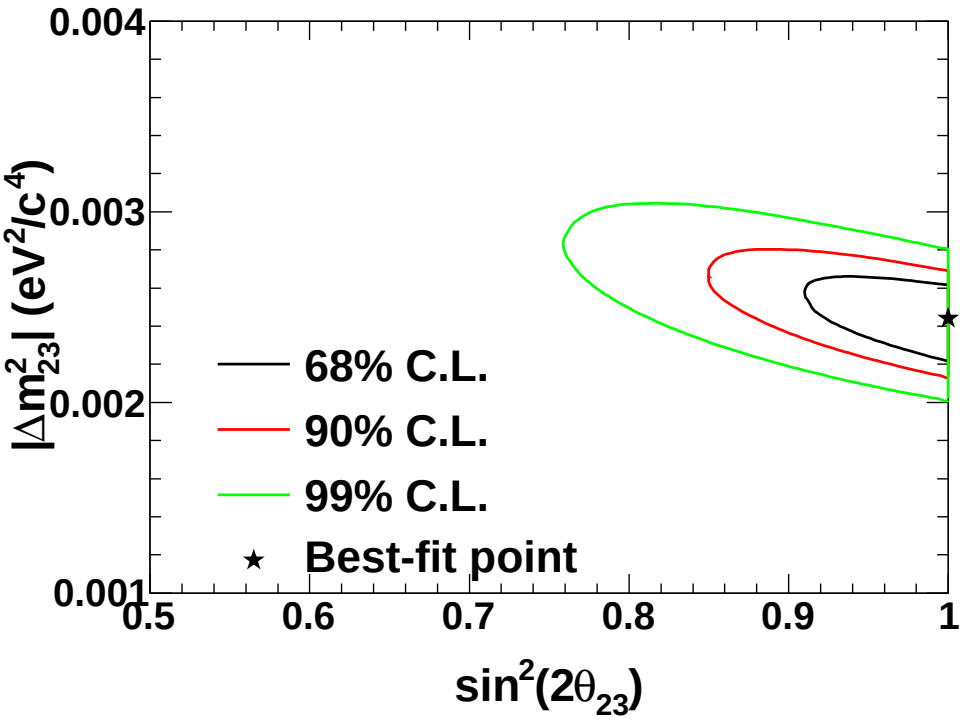

FIGURE 6.19. Allowed regions at 68%, 90%, 99% confidence level in the $|\Delta m^2_{32}|$, $\sin^2(2\theta_{23})$ plane from a fit to the Far Detector reconstructed energy spectrum, with $\sin^2(2\theta_{23})$ constrained in the physical region. The best-fit point, which occurs at $|\Delta m^2_{32}| = 2.44 \times 10^{-3}\,\mathrm{eV}^2$ and $\sin^2(2\theta_{23}) = 1$, is represented by the star.

The MINOS collaboration published oscillation results of the similar data set. This analysis served as a cross-check to that main analysis. The best-fit for the MINOS official result is : $|\Delta m^2_{32}| = (2.43^{+0.13}_{-0.13}) \times 10^{-3}\,\mathrm{eV}^2$ and $\sin^2(2\theta_{23}) = 1.00^{+0.00}_{-0.05}$. This analysis gives a very consistent result with the MINOS official result, as shown in Figure 6.23.

As shown in Figure 6.24, compared with the other atmospheric neutrino oscillation experiments, MINOS has the best constraints on $|\Delta m^2_{23}|$.

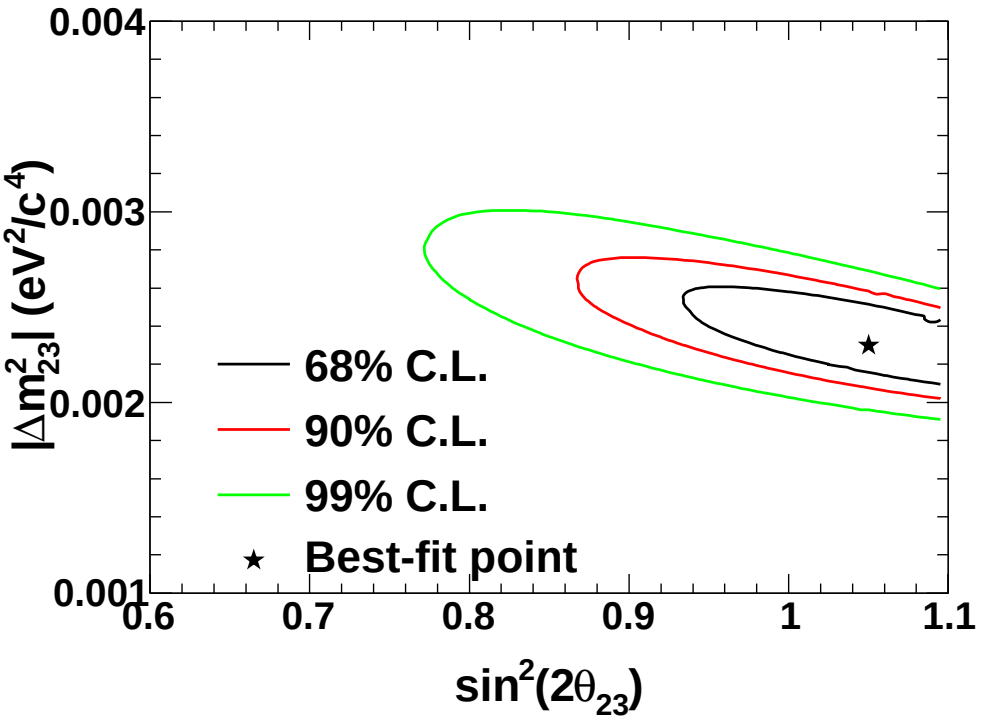

FIGURE 6.20. Allowed regions at 68%, 90%, 99% confidence level in the $|\Delta m^2_{32}|$, $\sin^2(2\theta_{23})$ plane from a fit to the Far Detector reconstructed energy spectrum where $\sin^2(2\theta_{23})$ is unconstrained. The best-fit point, which occurs at $|\Delta m^2_{32}| = 2.30 \times 10^{-3}\,\mathrm{eV}^2$ and $\sin^2(2\theta_{23}) = 1.05$, is represented by the star.

6.4. Statistical Check with Pseudo-experiments

The fit procedure is tested using Monte Carlo pseudo-experiments. The Far Detector MC simulation contains 2.57×10^{23} protons on target. The Monte Carlo pseudo-experiments are created by dividing these Monte Carlo events into statistically independent subsamples. Each subsample contains the same number of protons on target, but the number of events is allowed to fluctuate following Poisson distribution. The pseudo-experiments are created following this procedure:

(1) Oscillate the Monte Carlo with the oscillation parameters close to the minimum ($|\Delta m^2_{32}| = 2.44 \times 10^{-3}\,\mathrm{eV}^2$, $\sin^2(2\theta_{32}) = 1.0$) to generate the fake data and scale it to the desired exposure.

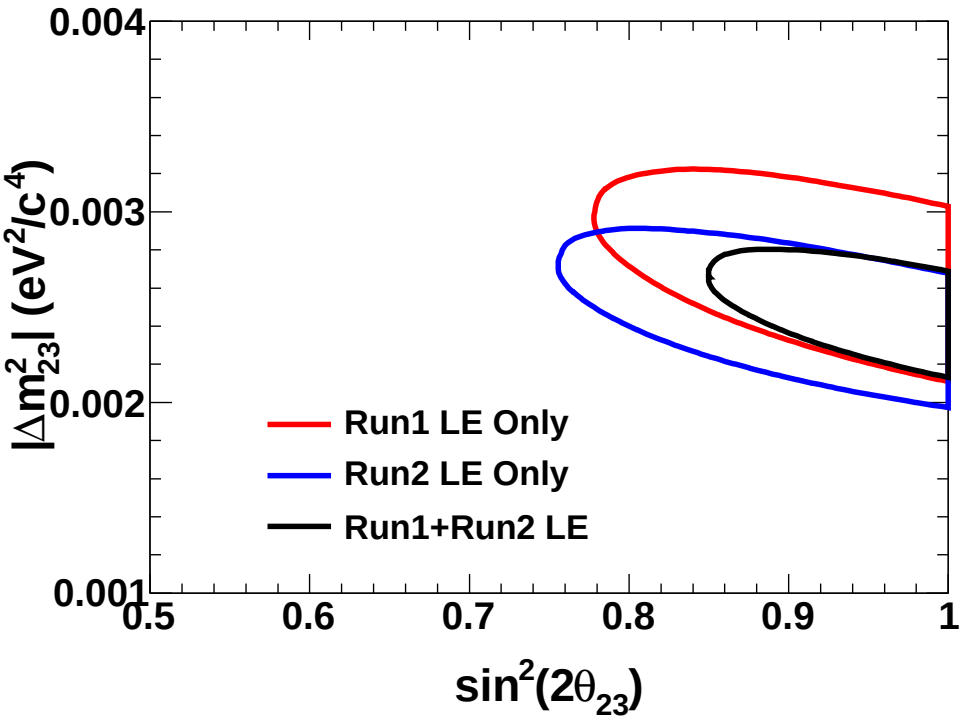

FIGURE 6.21. The 90% C.L. for individual Runs: LE Run1(red), LE Run2(blue) and combined LE runs(black).

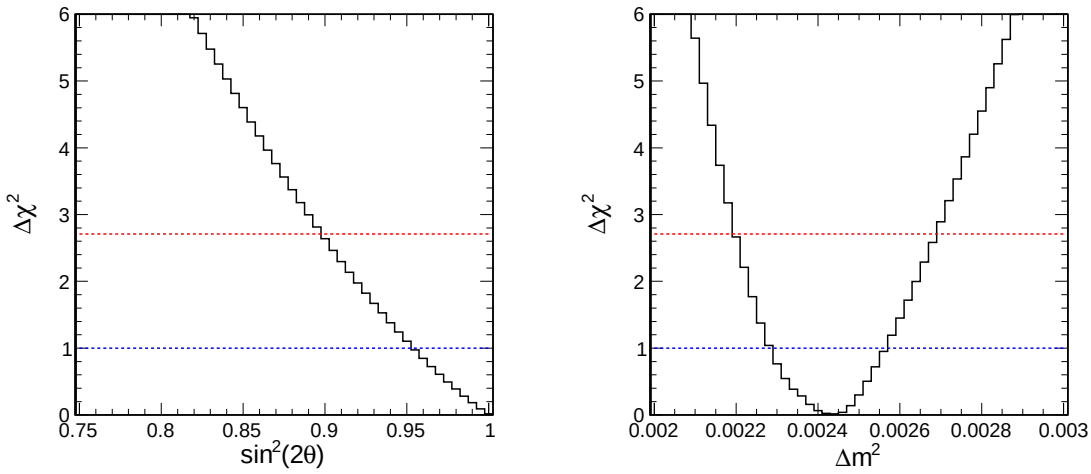

(a) (b)

FIGURE 6.22. One-dimensional projection of the $\Delta\chi^2$ surface for $\sin^2(2\theta_{23})$ and $|\Delta m^2_{32}|$. The blue and red dot line represent 68% and 90% C.L.

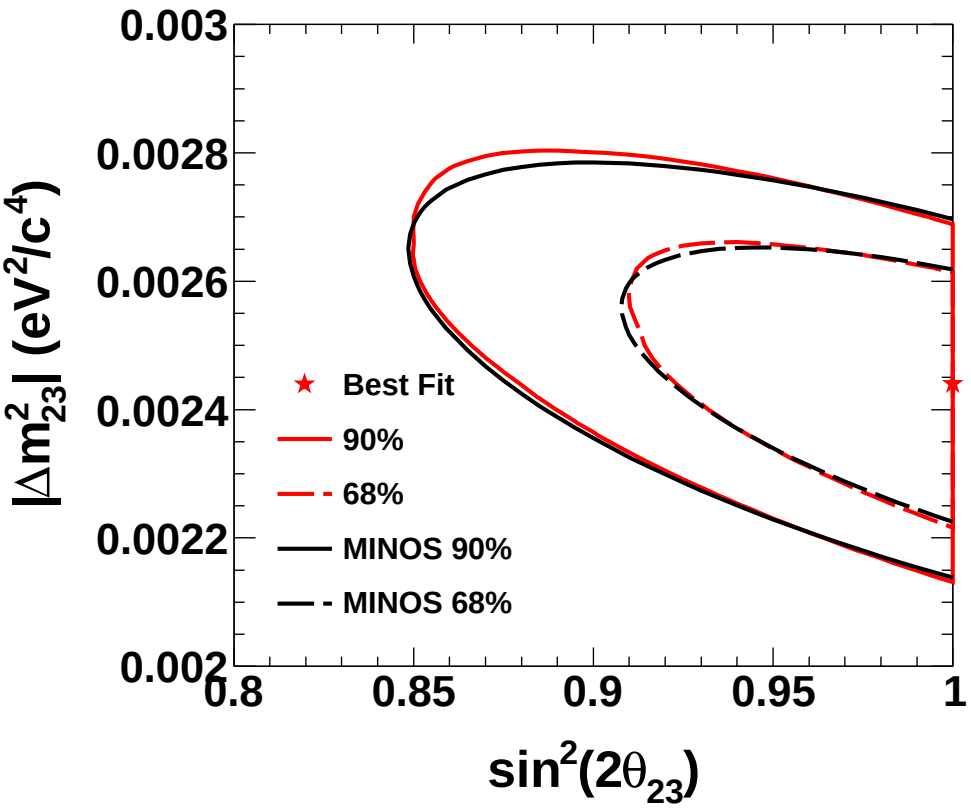

FIGURE 6.23. Comparison of the results from this thesis with the MINOS published results.

(2) Generate 300 fake experiments by Poisson fluctuating the total number of events and randomly drawing the number of events from the Monte Carlo.

(3) Fit the Monte Carlo to the randomly selected fake data and evaluate the best fit oscillation parameters comparing to the true value we put in.

Figure 6.25 shows the best fit χ^2/n.d.f distribution for the 300 pseudo-experiments. Figure 6.27 shows the best fit parameters in the $|\Delta m^2_{32}|$ and $\sin^2(2\theta_{23})$ plane. It also compares with the contours from the averaged pseudo-experiment samples. Figure 6.26 shows the best fit parameters $|\Delta m^2_{32}|$ and $\sin^2(2\theta_{23})$ distributions. The red dash lines represents the best fit parameters for these averaged pseudo-experiment samples. All the results indicate the fitting method is unbiased.

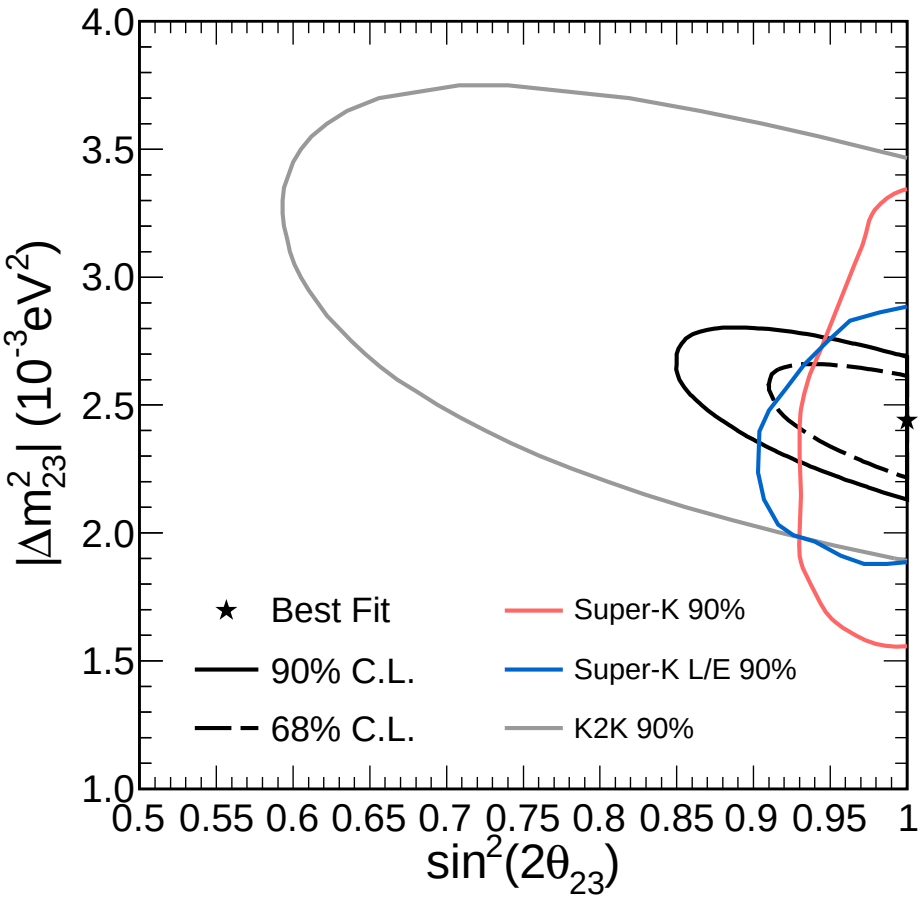

FIGURE 6.24. Comparison of the results from this thesis with other neutrino oscillation measurements from SuperKominokande (blue), the L/E analysis of SuperKamiokande (red) and K2K (gray).

6.5. FUTURE SENSITIVITY

At the current time MINOS has accumulated over 7.0×10^{20} POT, more than double the amount of data presented in this analysis. The future sensitivity to the oscillation parameters will continue to improve as shown in Figure 6.28.

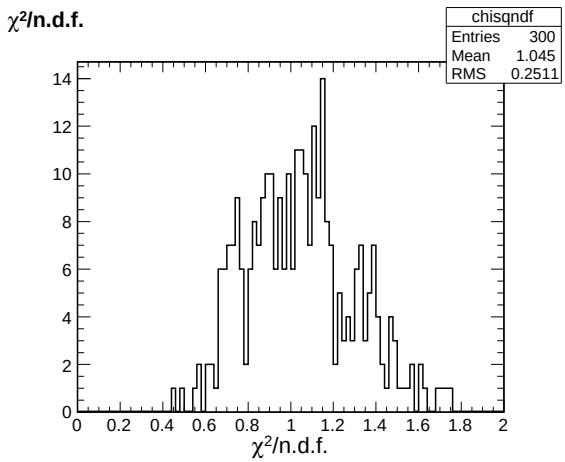

FIGURE 6.25. The χ^2/n.d.f. of 300 statistically independent pseudo-experiments. Fit parameters are constrained to the physical region: $\sin^2(2\theta_{23}) \leq 1$.

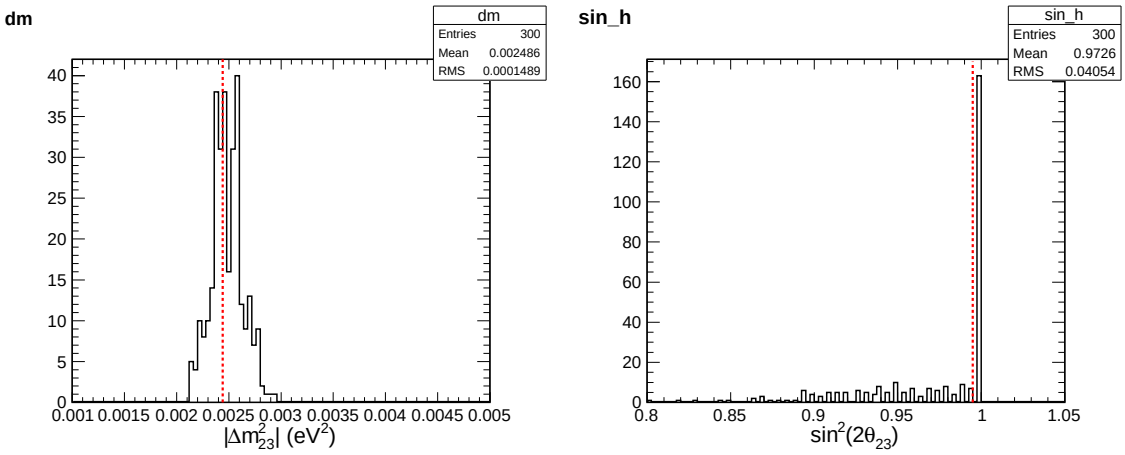

(a) (b)

FIGURE 6.26. The best fit parameters $|\Delta m^2_{32}|$ and $\sin^2(2\theta_{23})$ of 300 statistically independent pseudo-experiments. Fit parameters are constrained to the physical region: $\sin^2(2\theta_{23}) \leq 1$. The red dash lines represents the best fit parameters for the averaged pseudo-experiment samples.

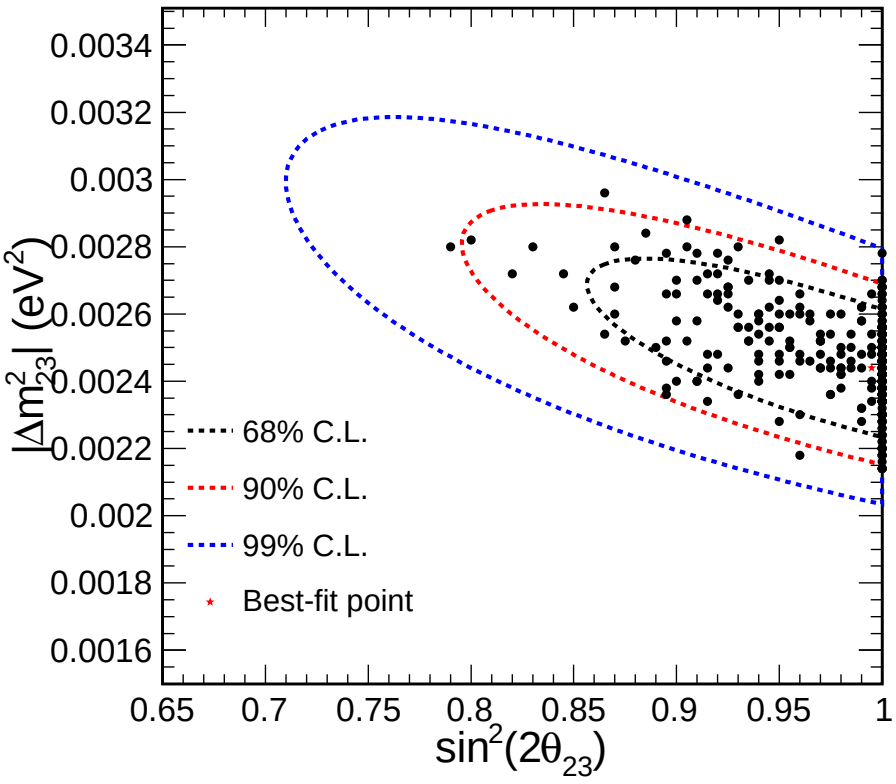

FIGURE 6.27. Allowed regions of 68%, 90%, and 99% C.L. in the $|\Delta m^2_{32}|$ and $\sin^2(2\theta_{23})$ plane with pseudo-experiments. The averaged best fit point is shown as a red star: $|\Delta m^2_{32}| = 2.44 \times 10^{-3}\,\text{eV}^2$ and $\sin^2(2\theta_{32}) = 0.995$. Best fit points for the 300 statistically independent pseudo-experiments are shown as black points.

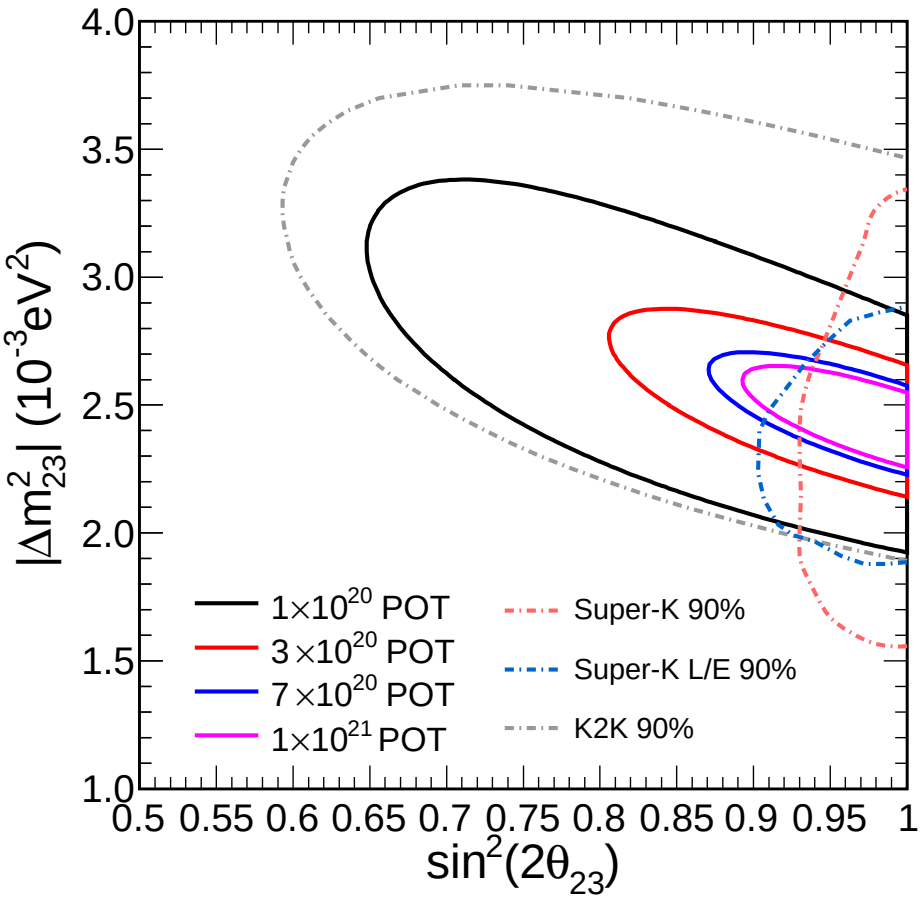

FIGURE 6.28. The sensitivity of MINOS experiment with increased POT. Statistical Only.

Chapter 7

Conclusions

This thesis has described a precision measurement of the relative neutrino flux and the atmospheric neutrino oscillation parameters in the MINOS experiments.

An empirical parameterization method to measure the relative neutrino flux was developed that used the Near Detector data to correct for our lack of knowledge of the proton hadron production. It reduced the hadron production uncertainties. The prediction from the improved Monte Carlo was used to extrapolate the flux to the Far Detector.

Three largest contributions to the systematic error for the beam matrix method are (a) the uncertainty in the relative normalization of energy spectra measured in the two detectors, (b) uncertainties in the absolute hadronic energy scale, and (c) uncertainties in the neutral-current background rate. They were included as nuisance parameters in the oscillation fit to the Far Detector data.

With an exposure of 3.2×10^{20} proton on target, the data used in this analysis were taken from May 2005 to June 2007. A total of 708 beam-coincident events are selected as ν_μ charged-current in the Far Detector. Assuming no oscillations, the predicted number of Far Detector events for this exposure is 923 ± 52 (syst.). A clear energy dependent deficit was seen for this data sample. A fit to those data to extract the mixing parameters $|\Delta m^2_{32}|$ and $\sin^2(2\theta_{23})$, within the context of two-flavor $\nu_\mu \rightarrow \nu_\tau$ oscillations. The best-fit results are $|\Delta m^2_{32}| = 2.44^{+0.12}_{-0.16} \times 10^{-3}\,\mathrm{eV}^2$ and $\sin^2(2\theta_{23}) = 1.00^{+0.00}_{-0.045}$ (68% C.L.). The $\sin^2(2\theta_{23}) \geq 0.90$ (90% C.L.) when the mixing angles is constrained to the physical region. Compared with the other neutrino oscillation experiments, MINOS has the best constraints on $|\Delta m^2_{32}|$.

Bibliography

Dzh. N. Abdurashitov et al. Results from SAGE. *Phys. Lett.*, B328:234–248, 1994. doi: 10.1016/0370-2693(94)90454-5.

A. G. Abramov et al. Beam optics and target conceptual designs for the NuMI project. *Nucl. Instrum. Meth.*, A485:209–227, 2002. doi: 10.1016/S0168-9002(01)02112-X.

P. Adamson et al. New constraints on muon-neutrino to electron-neutrino transitions in MINOS.

P. Adamson et al. The MINOS light injection calibration system. *Nucl. Instrum. Meth.*, A492:325–343, 2002. doi: 10.1016/S0168-9002(02)01293-7.

P. Adamson et al. The MINOS calibration detector. *Nucl. Instrum. Meth.*, A556: 119–133, 2006. doi: 10.1016/j.nima.2005.10.072.

P. Adamson et al. A Study of Muon Neutrino Disappearance Using the Fermilab Main Injector Neutrino Beam. *Phys. Rev.*, D77:072002, 2008a. doi: 10.1103/PhysRevD.77.072002.

P. Adamson et al. Measurement of Neutrino Oscillations with the MINOS Detectors in the NuMI Beam. *Phys. Rev. Lett.*, 101:131802, 2008b. doi: 10.1103/PhysRevLett.101.131802.

P. Adamson et al. Neutrino and Antineutrino Inclusive Charged-current Cross Section Measurements with the MINOS Near Detector. *Phys. Rev.*, D81:072002, 2010. doi: 10.1103/PhysRevD.81.072002.

A. Aguilar et al. Evidence for neutrino oscillations from the observation of anti-nu/e appearance in a anti-nu/mu beam. *Phys. Rev.*, D64:112007, 2001. doi: 10.1103/PhysRevD.64.112007.

A. A. Aguilar-Arevalo et al. A Search for electron neutrino appearance at the $\Delta m^2 \sim 1\text{eV}^2$ scale. *Phys. Rev. Lett.*, 98:231801, 2007. doi: 10.1103/PhysRevLett.98.231801.

B. Aharmim et al. Electron energy spectra, fluxes, and day-night asymmetries of B-8 solar neutrinos from the 391-day salt phase SNO data set. *Phys. Rev.*, C72:

055502, 2005. doi: 10.1103/PhysRevC.72.055502.

E. Aliu et al. Evidence for muon neutrino oscillation in an accelerator- based experiment. *Phys. Rev. Lett.*, 94:081802, 2005. doi: 10.1103/PhysRevLett.94.081802.

M. Altmann et al. Complete results for five years of GNO solar neutrino observations. *Phys. Lett.*, B616:174–190, 2005. doi: 10.1016/j.physletb.2005.04.068.

Claude Amsler et al. Review of particle physics. *Phys. Lett.*, B667:1, 2008. doi: 10.1016/j.physletb.2008.07.018.

J. C. Anjos et al. Angra neutrino project: Status and plans. *Nucl. Phys. Proc. Suppl.*, 155:231–232, 2006. doi: 10.1016/j.nuclphysbps.2006.02.058.

P. Anselmann et al. Solar neutrinos observed by GALLEX at Gran Sasso. *Phys. Lett.*, B285:376–389, 1992. doi: 10.1016/0370-2693(92)91521-A.

T. Araki et al. Measurement of neutrino oscillation with KamLAND: Evidence of spectral distortion. *Phys. Rev. Lett.*, 94:081801, 2005. doi: 10.1103/PhysRevLett.94.081801.

F. Ardellier et al. Double Chooz: A search for the neutrino mixing angle theta(13). 2006.

B. Armbruster et al. Upper limits for neutrino oscillations muon-antineutrino to electron-antineutrino from muon decay at rest. *Phys. Rev.*, D65:112001, 2002. doi: 10.1103/PhysRevD.65.112001.

Robert E. Armstrong. Muon neutrino disappearance at MINOS. FERMILAB-THESIS-2009-41.

G. Arnison et al. Experimental observation of isolated large transverse energy electrons with associated missing energy at s**(1/2) = 540-GeV. *Phys. Lett.*, B122: 103–116, 1983.

Y. Ashie et al. Evidence for an oscillatory signature in atmospheric neutrino oscillation. *Phys. Rev. Lett.*, 93:101801, 2004. doi: 10.1103/PhysRevLett.93.101801.

Y. Ashie et al. A Measurement of Atmospheric Neutrino Oscillation Parameters by Super-Kamiokande I. *Phys. Rev.*, D71:112005, 2005. doi: 10.1103/PhysRevD.71.112005.

K. Assamagan et al. Upper limit of the muon-neutrino mass and charged pion mass from momentum analysis of a surface muon beam. *Phys. Rev.*, D53:6065–6077, 1996. doi: 10.1103/PhysRevD.53.6065.

D. S. Ayres et al. NOvA proposal to build a 30-kiloton off-axis detector to study neutrino oscillations in the Fermilab NuMI beamline. 2004.

P. Bagnaia et al. Evidence for Z0 → e+ e- at the CERN anti-p p collider. *Phys. Lett.*, B129:130–140, 1983. doi: 10.1016/0370-2693(83)90744-X.

H. Bethe and R. Peierls. The 'neutrino'. *Nature*, 133:532, 1934.

Debdatta Bhattacharya. Neutrino and antineutrino inclusive charged-current cross section measurement with the MINOS near detector. FERMILAB-THESIS-2009-11.

F. Boehm et al. Final results from the Palo Verde Neutrino Oscillation Experiment. *Phys. Rev.*, D64:112001, 2001. doi: 10.1103/PhysRevD.64.112001.

Joshua Adam Alpern Boehm. Measurement of electron neutrino appearance with the MINOS experiment. FERMILAB-THESIS-2009-17.

M. Bonesini, A. Marchionni, F. Pietropaolo, and T. Tabarelli de Fatis. On particle production for high energy neutrino beams. *Eur. Phys. J.*, C20:13–27, 2001. doi: 10.1007/s100520100656.

B. T. Cleveland et al. Measurement of the solar electron neutrino flux with the Homestake chlorine detector. *Astrophys. J.*, 496:505–526, 1998. doi: 10.1086/305343.

C. L. Cowan, F. Reines, F. B. Harrison, H. W. Kruse, and A. D. McGuire. Detection of the free neutrino: A Confirmation. *Science*, 124:103–104, 1956. doi: 10.1126/science.124.3212.103.

T. Cundiff et al. The MINOS near detector front end electronics. *IEEE Trans. Nucl. Sci.*, 53:1347–1355, 2006. doi: 10.1109/TNS.2006.876771.

G. Danby et al. Observation of High-Energy Neutrino Reactions and the Existence of Two Kinds of Neutrinos. *Phys. Rev. Lett.*, 9:36–44, 1962. doi: 10.1103/PhysRevLett.9.36.

D. Decamp et al. Determination of the Number of Light Neutrino Species. *Phys. Lett.*, B231:519, 1989. doi: 10.1016/0370-2693(89)90704-1.

Y. Declais et al. Search for neutrino oscillations at 15-meters, 40-meters, and 95-meters from a nuclear power reactor at Bugey. *Nucl. Phys.*, B434:503–534, 1995. doi: 10.1016/0550-3213(94)00513-E.

E. Fermi. An attempt of a theory of beta radiation. 1. *Z. Phys.*, 88:161–177, 1934. doi: 10.1007/BF01351864.

R. P. Feynman and Murray Gell-Mann. Theory of the Fermi interaction. *Phys. Rev.*, 109:193–198, 1958. doi: 10.1103/PhysRev.109.193.

Y. Fukuda et al. Atmospheric muon-neutrino / electron-neutrino ratio in the multi-GeV energy range. *Phys. Lett.*, B335:237–245, 1994. doi: 10.1016/0370-2693(94)91420-6.

V. Garkusha et al. Design study of the NuMI Low Energy Target for Higher Power Beam. 2007. MINOS-DocDB-2778.

S. L. Glashow. Partial Symmetries of Weak Interactions. *Nucl. Phys.*, 22:579–588, 1961. doi: 10.1016/0029-5582(61)90469-2.

Andrew Godley and Jiajie Ling. Empirical Parametrisation fits for nue. 2006. MINOS DocDB-2555.

M. Goldhaber, L. Grodzins, and A. W. Sunyar. HELICITY OF NEUTRINOS. *Phys. Rev.*, 109:1015–1017, 1958. doi: 10.1103/PhysRev.109.1015.

Srubabati Goswami and Alexei Yu. Smirnov. Solar neutrinos and 1-3 leptonic mixing. *Phys. Rev.*, D72:053011, 2005. doi: 10.1103/PhysRevD.72.053011.

Xinheng Guo et al. A precision measurement of the neutrino mixing angle theta(13) using reactor antineutrinos at Daya Bay. 2007.

F. J. Hasert et al. Observation of neutrino-like interactions without muon or electron in the Gargamelle neutrino experiment. *Phys. Lett.*, B46:138–140, 1973. doi: 10.1016/0370-2693(73)90499-1.

R. Hatcher et al. Range Curvature Task Force Position Paper (2007). 2007. MINOS DocDB-3134.

K. S. Hirata et al. Observation of B-8 Solar Neutrinos in the Kamiokande-II Detector. *Phys. Rev. Lett.*, 63:16, 1989. doi: 10.1103/PhysRevLett.63.16.

J. Hosaka et al. Solar neutrino measurements in Super-Kamiokande-I. *Phys. Rev.*, D73:112001, 2006. doi: 10.1103/PhysRevD.73.112001.

Caius L. F. Howcroft. Atmospheric Neutrinos in the MINOS Far Detector. FERMILAB-THESIS-2004-71.

Y. Itow et al. The JHF-Kamioka neutrino project. 2001.

C. C. Jensen and G. A. Krafczyk. NuMI proton kicker extraction system. To appear in the proceedings of Particle Accelerator Conference (PAC 05), Knoxville, Tennessee, 16-20 May 2005.

K. K. Joo. Progress report on RENO. *Nucl. Phys. Proc. Suppl.*, 168:125–127, 2007. doi: 10.1016/j.nuclphysbps.2007.02.066.

K. Kodama et al. Observation of tau-neutrino interactions. *Phys. Lett.*, B504:218–224, 2001. doi: 10.1016/S0370-2693(01)00307-0.

Sacha Kopp et al. Position paper of the beam flux. MINOS-DocDB-1287-v1.

Michael Alan Kordosky. Hadronic interactions in the MINOS detectors. FERMILAB-THESIS-2004-34.

C. Kraus et al. Latest results from the Mainz Neutrino Mass Experiment. *Eur. Phys. J.*, C33:s805–s807, 2004. doi: 10.1140/epjcd/s2003-03-902-9.

L. D. Landau. On the conservation laws for weak interactions. *Nucl. Phys.*, 3:127–131, 1957. doi: 10.1016/0029-5582(57)90061-5.

Andrey V. Lebedev. Ratio of Pion Kaon Production in Proton Carbon Interactions. FERMILAB-THESIS-2007-76.

T. D. Lee and Chen-Ning Yang. Question of Parity Conservation in Weak Interactions. *Phys. Rev.*, 104:254–258, 1956. doi: 10.1103/PhysRev.104.254.

T. D. Lee and Chen-Ning Yang. Parity Nonconservation and a Two Component Theory of the Neutrino. *Phys. Rev.*, 105:1671–1675, 1957. doi: 10.1103/PhysRev.105.1671.

Z. Maki, M. Nakagawa, and S. Sakata. Remarks on the unified model of elementary particles. *Prog. Theor. Phys.*, 28:870, 1962. doi: 10.1143/PTP.28.870.

M. Maltoni, T. Schwetz, M. A. Tortola, and J. W. F. Valle. Status of three-neutrino oscillations after the SNO-salt data. *Phys. Rev.*, D68:113010, 2003. doi: 10.1103/PhysRevD.68.113010.

M. Maltoni, T. Schwetz, M. A. Tortola, and J. W. F. Valle. Status of global fits to neutrino oscillations. *New J. Phys.*, 6:122, 2004. doi: 10.1088/1367-2630/6/1/122.

W. Anthony Mann. Atmospheric neutrinos and the oscillations bonanza. 1999.

J. Marshall. A Data-Driven Correction to the MC NC Background (2007). 2007. MINOS-DocDB-3307.

John Stuart Marshall. A study of muon neutrino disappearance with the MINOS detectors and the NuMI neutrino beam. FERMILAB-THESIS-2008-20.

D. G. Michael et al. The Magnetized steel and scintillator calorimeters of the MINOS experiment. *Nucl. Instrum. Meth.*, A596:190–228, 2008. doi: 10.1016/j.nima.2008.08.003.

S. P. Mikheev and A. Yu. Smirnov. Resonance enhancement of oscillations in matter and solar neutrino spectroscopy. *Sov. J. Nucl. Phys.*, 42:913–917, 1985.

S. P. Mikheev and A. Yu. Smirnov. Resonant amplification of neutrino oscillations in matter and solar neutrino spectroscopy. *Nuovo Cim.*, C9:17–26, 1986. doi: 10.1007/BF02508049.

MINOS. Position Paper on Calibration, for June 2007 Box opening. 2007. MINOS-DocDB-3137-v3.

S. R. Mishra. Probing hadron structure with neutrino experiments. *Wold Scientific*, pages 84–123, 1990. Invited reivew talk presented at Workshop on Hadron Structure Function and Partion Distributions, Fermilab, Apr. 1990.

J. Oliver, N. Felt, G. Feldman, A. Lebedev, and R. Lee. Design and performance of the readout system of the MINOS Far Detector. *IEEE Trans. Nucl. Sci.*, 51: 2193–2195, 2004. doi: 10.1109/TNS.2004.834704.

Rustem Ospanov. A measurement of muon neutrino disappearance with the MINOS detectors and NuMI beam. FERMILAB-THESIS-2008-04.

W. Pauli. Dear radioactive ladies and gentlemen. *Phys. Today*, 31N9:27, 1978.

Z Pavlovic. Systematic Uncertainties in the NuMI Flux. 2006. MINOS DocDB-1283.

Zarko Pavlovic. Observation of Disappearance of Muon Neutrinos in the NuMI Beam. FERMILAB-THESIS-2008-59.

B. Pontecorvo. Neutrino experiments and the question of leptonic-charge conservation. *Sov. Phys. JETP*, 26:984–988, 1968.

J. M. Roney. Review of the tau neutrino mass. *Nucl. Phys. Proc. Suppl.*, 91:287–292, 2001. doi: 10.1016/S0920-5632(00)00953-1.

J. J. Sakurai. MASS REVERSAL AND WEAK INTERACTIONS. *Nuovo Cim.*, 7: 649–660, 1958.

Abdus Salam. On parity conservation and neutrino mass. *Nuovo Cim.*, 5:299–301, 1957. doi: 10.1007/BF02812841.

Abdus Salam. Weak and Electromagnetic Interactions. 1968. Originally printed in *Svartholm: Elementary Particle Theory, Proceedings Of The Nobel Symposium

Held 1968 At Lerum, Sweden*, Stockholm 1968, 367-377.

Kate Scholberg. Atmospheric neutrinos at Super-Kamiokande. 1999.

Thomas Schwetz. Neutrino oscillations: present status and outlook. *AIP Conf. Proc.*, 981:8–12, 2008. doi: 10.1063/1.2899010.

Sharon M Seun. Measurement of the pi/K ratio off the NuMI target in the MIPP experiment. 2008. MINOS-DocDB-5267.

S. Shukla, J. Marriner, and J. Griffin. Slip stacking in the Fermilab Main Injector. Prepared for 1996 DPF / DPB Summer Study on New Directions for High-Energy Physics (Snowmass 96), Snowmass, Colorado, 25 Jun - 12 Jul 1996.

E. C. G. Sudarshan and R. e. Marshak. Chirality invariance and the universal Fermi interaction. *Phys. Rev.*, 109:1860–1860, 1958. doi: 10.1103/PhysRev.109.1860.

M. Szleper and A.Para. Neutrino spectrum at the far detector; systematic errors. 2001. NuMI-B-781.

Patricia LaVern Vahle. Electromagnetic interactions in the MINOS detectors. doi: OSTI/15011494. FERMILAB-THESIS-2004-35.

Steven Weinberg. A Model of Leptons. *Phys. Rev. Lett.*, 19:1264–1266, 1967. doi: 10.1103/PhysRevLett.19.1264.

L. Wolfenstein. Neutrino oscillations in matter. *Phys. Rev.*, D17:2369–2374, 1978. doi: 10.1103/PhysRevD.17.2369.

C. S. Wu, E. Ambler, R. W. Hayward, D. D. Hoppes, and R. P. Hudson. EXPERIMENTAL TEST OF PARITY CONSERVATION IN BETA DECAY. *Phys. Rev.*, 105:1413–1414, 1957. doi: 10.1103/PhysRev.105.1413.

Tingjun Yang. A study of muon neutrino to electron neutrino oscillations in the MINOS experiment. FERMILAB-THESIS-2009-04.

R. Zwaska et al. Beam-based alignment of the NuMI target station components at FNAL. *Nucl. Instrum. Meth.*, A568:548–560, 2006. doi: 10.1016/j.nima.2006.08.031.

Robert Miles Zwaska. Accelerator systems and instrumentation for the NuMI neutrino beam. UMI-32-16264.

Appendix A

Retuning of Neural Network for ν_e Identification

A.1. Introduction

It is important to accurately distinguish the ν_e events from the background events to conduct a sensitive search for $\nu_\mu \rightarrow \nu_e$ oscillation leading to a measurement of θ_{13}. The task of the ν_e identification algorithm is to look for the presence of an electron in the final state of neutrino interaction. In MINOS, this distinction is achieved using the shower topology, the transverse and the longitudinal shapes of the pulse heights associated with the shower. The hadronic showers are transversely more diffuse and longitudinally penetrate deeper. The electromagnetic (EM) showers are transversely more collimated and longitudinally shorter. However, the ν_e identification is more difficult than the separation of electrons and charged mesons. The electron neutrino can interact with target nucleon by exchanging a W boson and create hadrons and an electron. It will be almost impossible to identify the electron when the energy of the hadrons is much larger than the energy of the electron. Moreover, because of the limited granularity of the MINOS calorimeter, it is difficult to separate π^0's and electrons. The dominant background in this analysis is the NC π^0s. Other background sources consist of ν_μ CC interactions with a short muon track and the intrinsic beam ν_e component. In the Far Detector, τ, which come from ν_τ CC interaction, will add another background.

The ANN PID was chosen as the primary PID for the first ν_e appearance analysis. We have retuned the ANN PID for the second ν_e analysis:

- **New MC simulation:** The second ν_e analysis will use *Daikon04* MC, which has an improved intranuke modeling than the previous *Daikon00* MC.
- **New Reconstruction:** In the *dogwood* reconstruction, 2-PE cut is applied at the reconstruction level and an improved cross-talk model is also used.
- **Sensitivity:** We need to improve the old ANN PID to reach a higher ν_e sensitivity.

A.2. Tuning samples

We only expect to see potential $\nu_\mu \rightarrow \nu_e$ oscillation signals in the Far Detector, thus we need to tune the neural network based on the Far Detector MC.

The Far Detector MC samples are generated using the *daikon04* simulation and reconstructed with *dogwood* reconstruction release. Three types of MC samples, including unoscillated and maximal oscillated ν_e and ν_τ MC, are used.

We need to applying the proper oscillation probability to the MC samples. By assuming the following oscillation parameters:

$$\sin^2(2\theta_{13}) = 0.15, \quad |\Delta m^2_{31}| = 2.43 \times 10^{-3} eV^2, \quad \sin^2(2\theta_{23}) = 1,$$
$$|\Delta m^2_{12}| = 8.0 \times 10^{-5} eV^2, \quad \sin^2(2\theta_{12}) = 0.86.$$

The CP violating phases and the matter effects are neglected in calculating the oscillation probabilities.

We assume an exposure of 7.0×10^{20} proton on target (POTs) which corresponds to roughly 4 years of MINOS running.

A.3. ν_e Selection Strategy

The strategy of the selecting ν_e events can be summarized as follows: Firstly, We can remove some obvious background events, such as long-track ν_μ CC events,

by applying the pre-selection cuts; Secondly, we compute several variables that describe the event topology and feed them into the neural network to enhance the signal/background separation. At last, we can select the ν_e candidates by applying the ANN PID cut.

A.3.1. Fiducial Volume Cuts. We are only interested in the neutrino interactions that occur inside the detector and away from the magnet coil hole. Thus we apply the fiducial volume cuts to remover events that occur in the periphery of the detector or close to the coil hole. The Far Detector fiducial Volume cuts we use in the ν_e analysis are:

$$0.5 \leq \sqrt{x^2 + y^2} \leq \sqrt{14}, \quad 0.48 \leq z \leq 14.28 \text{ or } 16.26 \leq z \leq 27.97 \tag{A.1}$$

where (x,y,z) are the coordinates of the reconstructed event vertex, and z axis is along the beam direction. The lower radial cut is to exclude the coil hole. The two intervals of z cut correspond to the two super-modules.

A.3.2. Pre-selection Cuts. Through the pre-selection study done by Minerba and Joao, we decide to use the same pre-selection cut as the first ν_e appearance analysis:

- Track planes<25, Track-like planes<16 : reject events with a long track (predominantly ν_μ CC backgrounds);
- $1 < E_{reco} < 8$GeV : reject events in which the visible energy does not fall with our interested range.

There are several other cuts we apply in addition to the cuts described above. One cut requires that there should be at lease one hit on each of 5 contagious planes in order to remove poorly reconstructed events. Furthermore, the pre-selection rejects events without showers. In Far Detector, additional cuts are applied to remove cosmic ray background.

The next step is to compute some topological variables and feed them into a neural network to further enhance the signal and background separation.

A.4. PID variables

The retuned ANN PID uses the same 11 input variables as the old ANN PID [Yang].

- **shwfit.par.a:** fit the longitudinal profile of the event energy to a Γ function. Parameter a describes the rise of the longitudinal shower profile.
- **shwfit.par.b:** Parameter b describes the fall of the longitudinal shower profile. A small b value means the shower profile has a long tail.
- **shwfit.uv_molrad_peak_9s_2ps_dw:** the radius of an imaginary cylinder around the shower axis which contain 90% of the visible event energy (Moliere radius).
- **shwfit.uv_rms_9s_2pe_dw:** RMS of the transverse energy loss profile of a shower.
- **shwfit.longE:** the sum of the magnitude of longitudinal projections of the vectors defined by each hit and the vertex. Each vector is multiplied by the hit pulse height.
- **mstvars.e4w + mstvars.o4w:** We form a Minimal Spanning Tree from hits whose pulse height is larger than the average pulse height. This variable is the sum of distances between hits in the Minimal Spanning Tree.
- **fracvars.fract_2_planes:** the fraction of the maximum energy loss in a 2 planes window.
- **fracvars.fract_4_planes:** the fraction of the maximum energy loss in a 4 plane window.
- **fracvars.fract_6_planes:** the fraction of the maximum energy loss in a 6 planes window.

- **fracvars.fract_8_counters:** the fraction of the maximum energy loss in the 8 strips.
- **fracvars.fract_road:** We find the shower axis by doing a energy weighted least squares fit to the position of the shower strips. This variable is defined as the ratio of the total energy of the strips which is located within 1.5 strip with respect to the shower axis over the total event energy.

A.5. Constructing ANN

Multivariate classification methods based on machine learning techniques have become a fundamental ingredient to HEP analysis. Artificial neural network (ANN) is one of the best multivariate classification methods based on machine learning techniques. An ANN consists a pool of simple processing units (neurons) which communicate by sending signals to each other over a large number of weighted connections. A neural network has to be 'tuned' such that the application of a set of inputs produces the desired set of outputs. This ANN 'learning' process involves adjustments to the connection weights.

A typical structure of this ANN is composed of an input layer, a hidden layer and an output layer. TMultiLayerPerceptron is a ROOT implementation of ANN based on MLPfit package. We employ this ROOT class to build the electron identification ANN. We compute 11 variables as described in the previous section and use them as the input to ANN.After the pre-selection cuts, the ν_e CC events are used for the signal sample while the NC and ν_μ CC events are used for background sample. Both signal and the background events are weighted based on the neutrino oscillation probabilities. The training sample is split into two samples, one for tuning the network weights, the other one for monitoring to avoid overtraining. We have used 46132 events for our training sample. The events are properly reweighted so that we have roughly the same number of signal and background in the training sample. All the

input variables need to be normalized. The training process is iterated many times and the best neural network is chosen.

The architecture of the final ANN is 11:14:9:1, as illustrated in Figure A.1. It has one input layer, two hidden layers and one output layer. The input layer has 11 nodes which corresponding to the 11 input variables. The output PID node is on the final output layer.

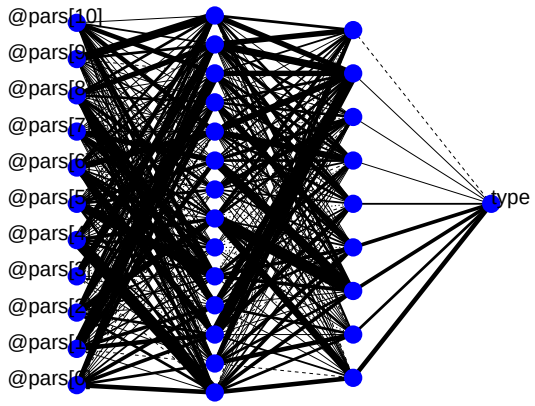

FIGURE A.1. Structure of the ANN11 Pid. 11:14:9:1

Figure A.2 shows the ANN output for ν_e signal events and various background components. The signal distribution is scaled up by a factor of 10 for clarity. Compared with the old ANN PID, the new ANN PID has a slightly better separation between signal and background events. However, due to the granularity of the MINOS detectors, there is a large overlapping between signal and background events.

Figure A.3 shows the ν_e signal events PID distributions. The ANN PID prefers to select the clean quasi-elastic (QE) events than the ν_e deep inelastic (DIS) events, which has hadronic showers as well.

In order to optimize the cut on ANN output, we choose the following equation as the figure of merit (FOM):

$$FOM = N^{sig}/\sqrt{(\sigma^{bg}_{stat})^2 + (\sigma^{bg}_{syst})^2} = N^{sig}/\sqrt{N^{bg} + (7\% \times N^{bg})^2} \qquad (A.2)$$

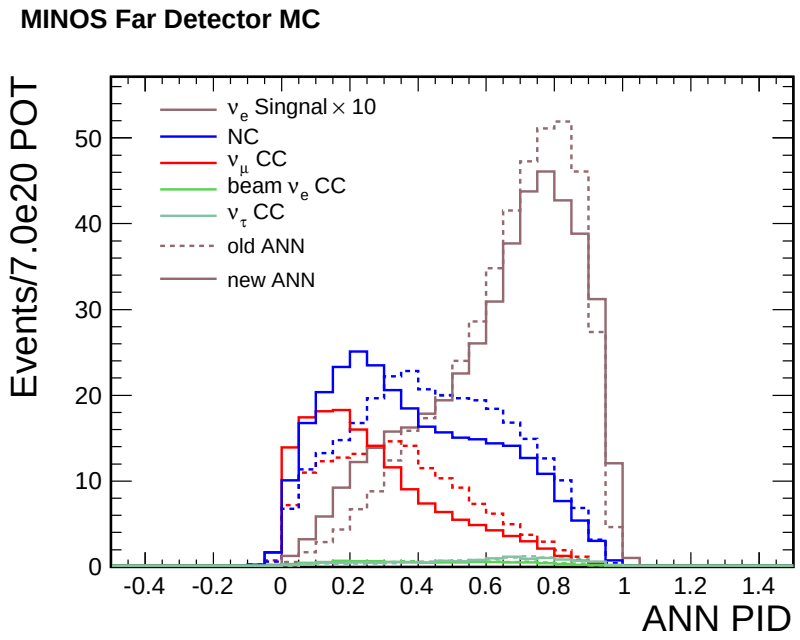

FIGURE A.2. Distributions of the ANN11 Pid in far detector for signal and various backgrounds. The signal is scaled by a factor of 10 for clarify. The dot lines represent the old ANN pid distributions and the solid lines represent the new ANN pid distributions.

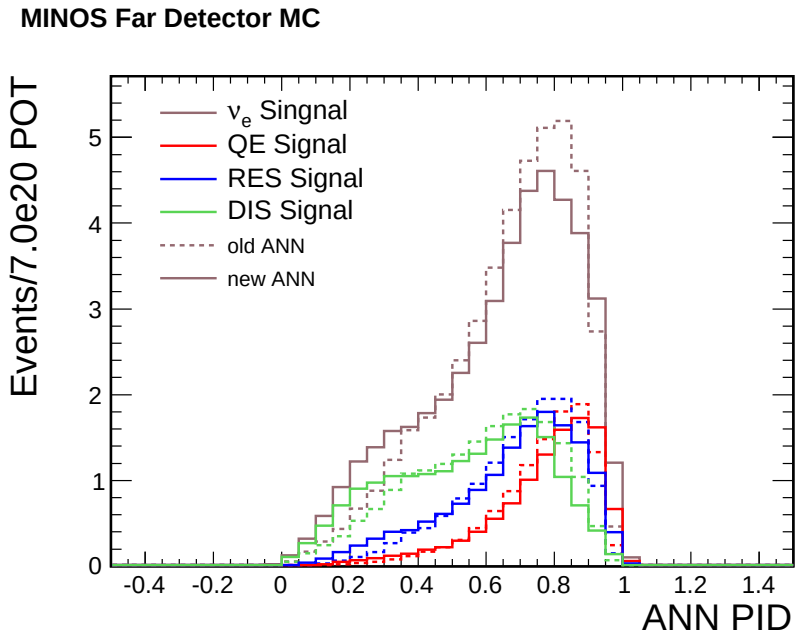

FIGURE A.3. Distributions of the ANN11 Pid in far detector for various signals. The dot lines represent the old ANN pid distributions and the solid lines represent the new ANN pid distributions.

where N^{sig} and N^{bg} denote the number of signal events and background events, respectively. Here we use 7% systematic error on the number of predicted background events. This FOM was chosen because it represents the statistical significance of observed signal events with a given number of background events. It is directly relative to the limit we can impose on the neutrino oscillation parameter θ_{13} if we don't observe any signal events in the Far Detector.

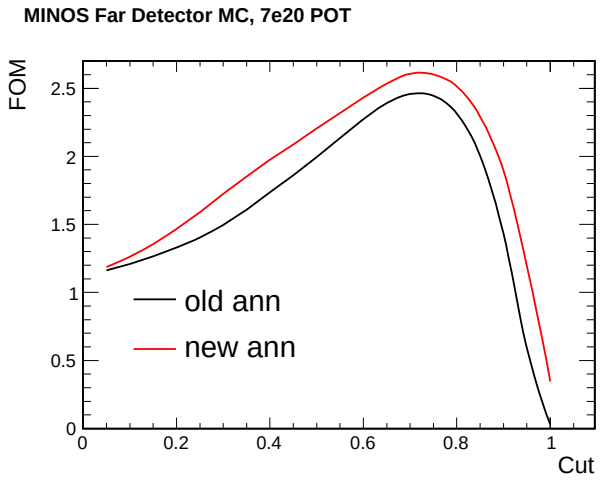

FIGURE A.4. Figure of Merit (FOM) as a function of the cut on ANN11 pid in far detector. The dot lines represent the old ANN pid and the solid lines represent the new ANN pid.

Figure A.4 shows the FOM as function of the cut on the ANN output. The new ANN PID has a better performance than the old ANN PID. The maximal FOM, 2.61, is achieved at the cut position on 0.7.

A.6. FAR DETECTOR ν_e SELECTION EFFICIENCY AND PURITY

TABLE A.4. Summary of Far Detector data reduction for $7.0 \times 10^{20} POTs$.

	sig	bg	NC	ν_μ CC	ν_e^{beam} CC	ν_τ CC	FOM
Fid. Vol.	57.51	2715.44	753.99	1906.84	36.83	17.77	
Pre-selection	44.89	475.59	292.73	160.61	12.73	9.52	
old ANN11>0.7	22.84	65.41	48.10	10.29	4.92	2.10	2.46
new ANN11>0.7	21.58	54.12	40.47	7.52	4.36	1.77	2.61
old eff/rej	39.7%	97.6%	93.6%	99.5%	86.6%	88.2%	
new eff/rej	37.5%	98.0%	94.6%	99.6%	88.2%	90.0%	

Table A.4 summarizes the data reduction at different cut levels. The new ANN PID is able to accept roughly 37.5% of the signal events while rejecting 94.6% of the NC and 99.6% of the ν_μ CC background events. The new PID has a better background rejection than the old PID with the sacrifice of a slightly lower signal efficiency.

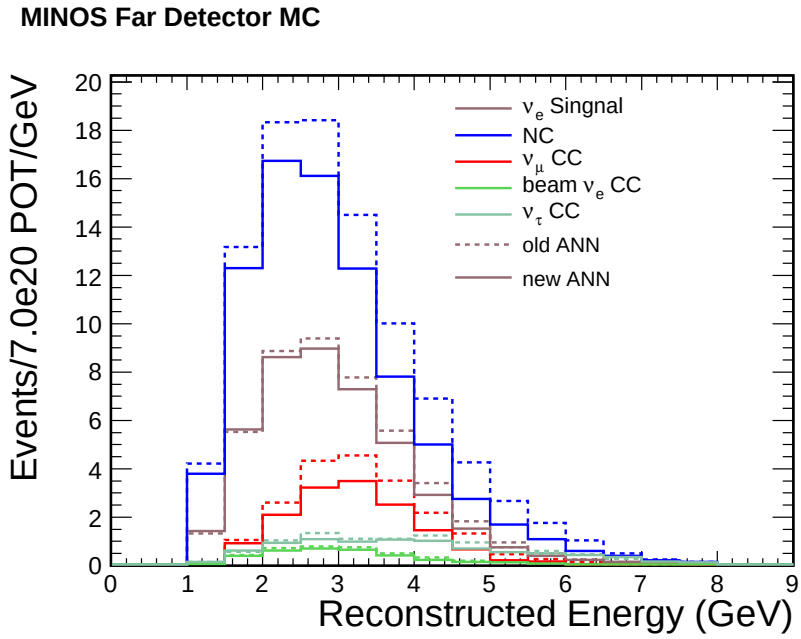

FIGURE A.5. Distributions of reconstructed energy after the ANN11 pid cut in far detector. The dot lines represent the old ANN pid and the solid lines represent the new ANN pid.

Figure A.5 shows the reconstructed energy distribution of events after applying all the ν_e selection cuts. Figure A.6 shows the ν_e selection efficiency and purity as a function of the reconstructed event energy. The ν_e selection efficiency peaks between $2-4$GeV and drops at high energy. This might be contrary to what one would expect since it is usually easy to identify high energy electrons. The reason may be that the signal events are weighted by the oscillation probabilities, thus high energy ν_e events are highly suppressed.

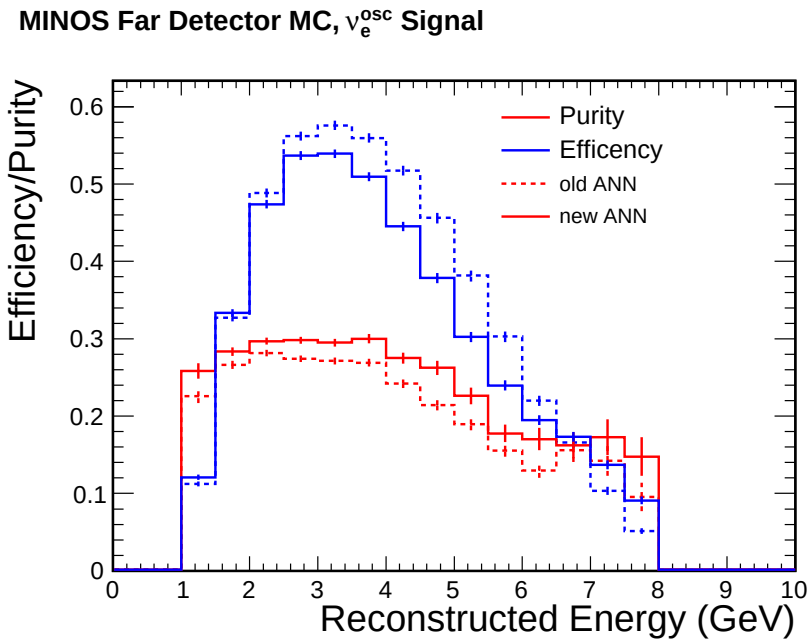

FIGURE A.6. Efficiency and purity of the ν_e signal as a function of recontructed energy after the ANN11 pid cut in far detector. The dot lines represent the old ANN pid and the solid lines represent the new ANN pid.

A.7. MINOS NEAR DETECTOR DATA AND MC COMPARISON

We have described the ANN we constructed based on the Far Detector Monte Carlo. It is very important to understand the Near Detector data in terms of the detector performance and the event reconstruction. The purpose of the MINOS Near Detector for the ν_e analysis is to measure and study the background rate. Near Detector measurements will verify and check the accuracy of the neutrino beam simulation, cross-section modelling and the detector response simulation. In this section, we will show the Near Detector data and MC comparison for the PID input variables, ANN PID, and the energy spectra.

A.7.1. Data and MC samples. The Near Detector MC samples are generated using the *daikon04* simulation. Both the data and MC are reconstructed with *dogwood* reconstruction release.

We have sampled some portion of ND data taken between May 2005 and February 2007 as our data sample. The total number of proton on target (POTs) for the selected ND data sample is 2.22×10^{19}. The total number of POTs for the ND MC sample is 0.96×10^{19}. Both the data and MC distributions are normalized to 1×10^{19} POTs.

A.7.2. Selection Cuts. Firstly, we applied data qualities cuts to remove data taken under bad beam conditions or unhealthy detector conditions.

Secondly, as we did for the Far Detector, we applied the Near Detector fiducial volumes cuts first:

$$\sqrt{(x - 1.4885)^2 + (y - 0.1397)^2} \leq 0.8, \quad 1 \leq z \leq 5 \tag{A.3}$$

where (x,y,z) are the coordinates of the reconstructed event vertex, and z axis is along the beam direction. Coordinates (1.4885m, 0.1397m) represent the beam center position.

After the pre-selection cuts, we calculate the ANN PID, which is constructed by the Far Detector MC. Figure A.7 shows the ANN output for ND data and MC events that pass the ν_e pre-selection cuts. The breakdown of MC distribution is also shown.

Finally, we can compare the MC events passing the ANN PID cut with those for data. This gives us a background estimate.

Figure A.8 shows the reconstructed energy spectra of the data and MC events accepted by the ANN PID as ν_e candidates. Just a reminder, if we compare the data and MC comparison with what we once had in the first ν_e analysis, we can clearly see that the Daikon04 MC agrees with the data much better. The improved intranuclear and cross-talk modelling did a very nice job.

A.7.3. Near Detector Cut Table. Table A.8 shows the data reduction of data and MC. After all the ν_e selection cuts, the data and MC agree within 10%.

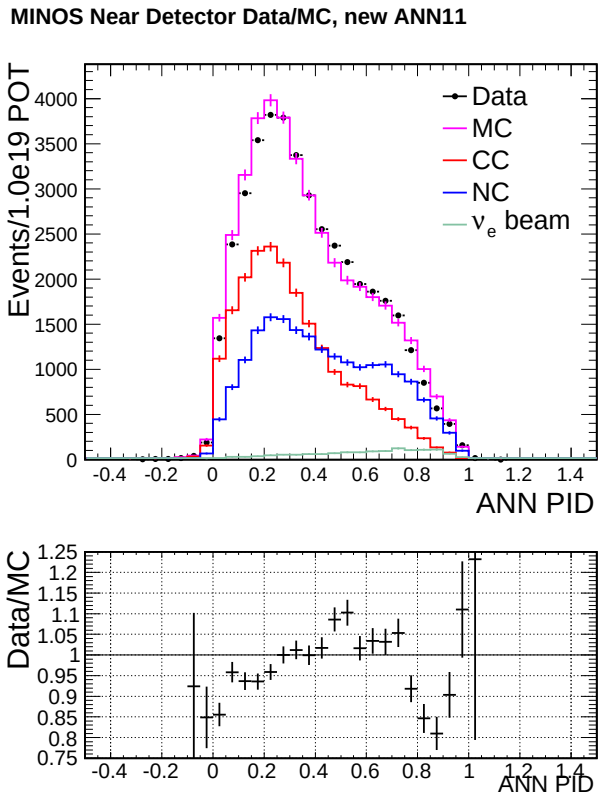

FIGURE A.7. **Top:** Distributions of the ANN11 Pid in the Near Detector for data (black) and MC (pink). Each MC component, including ν_μ CC (red), NC (blue) and beam ν_e (cyan), is showed respectively. **Bottom:** data/MC ratio distribution.

TABLE A.8. Summary of Near Detector data reduction for 1.0×10^{19} POTs.

	data	MC	NC	ν_μ CC	ν_e^{beam} CC	data/MC
Fid. Vol. Cuts	261990	261820	56941	201433	3454	1.001
Pre-selection Cuts	42188.4	42861.3	19783.1	21749.7	1328.8	0.984
old ANN11>0.7	5789.54	5988.20	3775.01	1653.61	559.59	0.967
new ANN11>0.7	4789.66	5128.98	3328.27	1262.81	537.90	0.934

A.8. SENSITIVITY

After we did the Near Detector data and MC comparison, we can estimate how many background events in our Far Detector data sample.

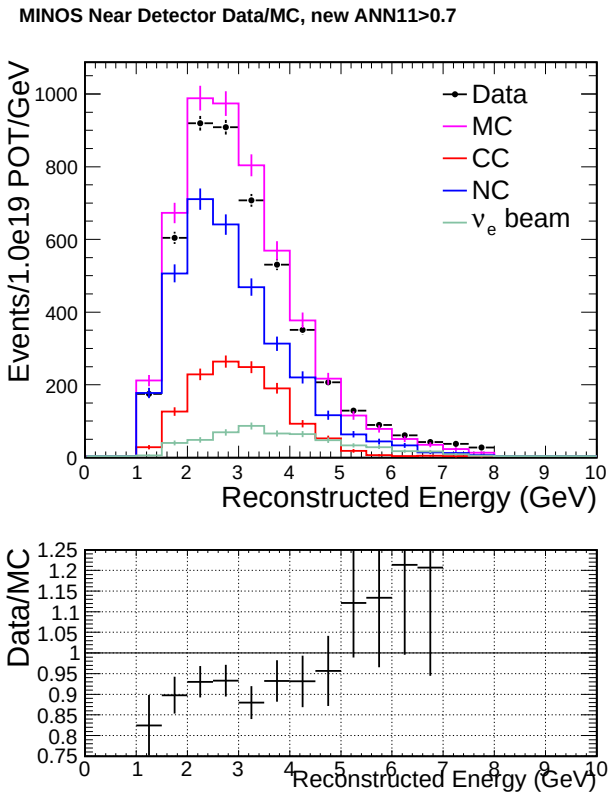

FIGURE A.8. **Top:** Distributions of the reconstructed energy after ANN11 Pid cut in Near Detector for data (black) and MC (pink). Each MC component, including ν_μ CC (red), NC (blue) and beam ν_e (cyan), is showed respectively. **Bottom:** data/MC ratio distribution.

For simplicity, we didn't do the official Horn On and Horn Off (HOO) or MRCC (muon removal Charged Current) analysis. We can roughly estimate the Far Detector background by correcting the Far Detector MC NC and ν_μ CC components simultaneously with the ND data.

After the F/N extrapolation and background correction, we can get totally 63.30 background events after the old ANN PID cut and 50.61 background events after the new ANN PID cut. Thus, we can roughly estimate the effective FOM for the old ANN PID:

$$FOM^{old}_{eff} = N^{sig}/\sqrt{N^{bg} + (7\% \times N^{bg})^2} = 22.84/\sqrt{63.30 + (7\% \times 63.30)^2} = 2.508 \tag{A.4}$$

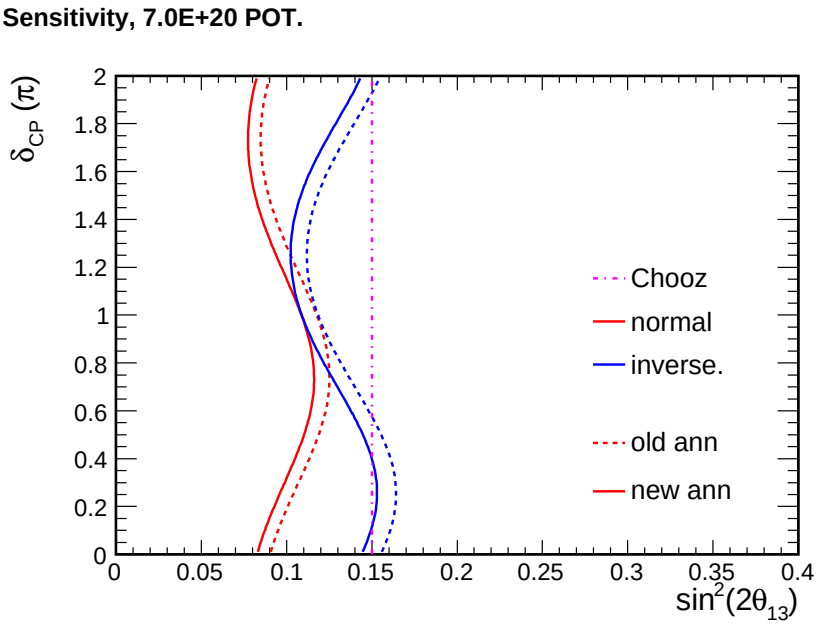

FIGURE A.9. Sensitivity of MINOS $\nu_\mu \to \nu_e$ oscillation for 7.0×10^{20} POT. The solid line represents new ANN11 pid and the dot line represents old ANN11 pid. The pink dash line shows the Chooz limit.

And the effective FOM for the new ANN PID is :

$$FOM_{eff}^{new} = N^{sig}/\sqrt{N^{bg} + (7\% \times N^{bg})^2} = 21.58/\sqrt{50.61 + (7\% \times 50.61)^2} = 2.715 \tag{A.5}$$

The effective FOM of the new PID is about 8% higher than the old PID.

Similarly, based on the background we estimated for the Far Detector, we can calculate the sensitivity to θ_{13}. Figure A.9 shows the ν_e sensitivity plots for the old and new ANN PID with 7.0×10^{20} POTs.

Appendix B

A Study of Cosmic-Ray Muon Induced EM Shower in MINOS Detectors

B.1. Introduction

It is important to accurately distinguish the electromagnetic (EM) shower from the hadronic shower to conduct a sensitive search for $\nu_\mu \to \nu_e$ oscillation leading to a measurement of θ_{13}. In MINOS, this distinction is achieved using the shower topology, the transverse and the longitudinal shapes of the pulse heights associated with the shower at a given energy. The hadronic showers are transversely more diffused and longitudinally penetrate deeper. The EM showers are transversely more collimated and longitudinally shorter. The CalDet measurements provide test samples of hadronic showers by single hadrons ($\pi^\pm/p$). Importantly, the hadronic showers is further constrained, and checked *insitu*, by using the shower associated with a ν_μ charged current (CC) events. From a CC events, the fitted muon is removed, leaving an approximately pure neutrino-induced hadronic shower —the MRCC sample. The identical analysis is repeated with the ν_μ-CC Monte Carlo (MC) sample. The comparison of the MRCC data and MC, thus, removes any bias due to the muon-removal.

The CalDet measurements also provide test samples of EM showers by single $e^\pm$. Since an EM shower is a QED process, the simulation of ν_e-induced electron, checked against the CalDet data, should be well modeled, i.e. the efficiency of identifying a ν_e-induced electron can be trusted to a good precision. However, having an *Insitu* and redundant check of EM shower reconstruction in MINOS will have two benefits:

first, it will provide an important check on the signal ν_e efficiency; second, it will provide a means to ascertain an error the efficiency.

It was suggested at the MINOS collaboration meeting in Austin that we can check *in situ* the EM shower reconstruction efficiency using the cosmic-μ data accumulated at the MINOS Near and Far Detector. Muons undergo catastrophic energy loss while traversing through steel. These showers are mostly EM induced by a hard photon. The idea is to isolate the cosmic-μ showers, in data and MC, use the MRCC technique to 'remove' the muon, and apply the EM-shower algorithm developed by the ν_e-group. The analysis is conducted as a function of shower energy. The efficiency as measured in the data can then be directly compared with that in the MC as a function of shower energy. Finally, MINOS detectors — especially the FD — provide one the most precise determination of the rate of μ^- and μ^+ energy loss while traversing steel and the EM nature of the shower. This can be done in bins of muon energy.

B.2. Procedures

Since the goal of this analysis is to check EM-shower modeling in data and MC, we can remove muon hits at the strip level. A more accurate approach, however, is to implement a complete muon removal at the digitized hit level and, then, reconstruct the event on the remaining digitized hits in data and MC. Unfortunately most of the cosmic ray candidate files were corrupted during the production. As a result, we had to run the standard reconstruction even before the muon removal. We undertook the following analyses:

(1) Run the standard cosmic cedar_phy reconstruction on cosmic samples

(2) Remove the μ-track hits by using MRCC techniques

(3) Run the standard spill cedar_phy reconstruction on the remaining hits

B.3. Muon Removal Algorithm

Unlike the ν-beam data, most of the cosmic ray data have a single clean μ-track. We use reconstructed cosmic-μ track to remove hits associated with the track. Since the cosmic ray data are different from the neutrino data, we wrote a new algorithm *AlgCosmicMuonRemoval* based on Caius's original muon removal code. The steps taken are:

(1) We define a shower region and remove all the hits outside this region including track hits and crosstalk hits. Figure B.1 and Figure B.2 show a cosmic muon event composed of a fitted μ-track (shown in red-symbol) accompanied by a shower (shown in black-symbol) in Near and Far Detector.

(2) We calculate the average *mip* using the track hits near the shower region.

(3) The average *mip* is subtracted from the pulse heights (PH) within the shower region; if the PH is below 0.3 *mip*, it is retained.

(4) We write out the new CandDigitList and rerun the spill reconstruction.

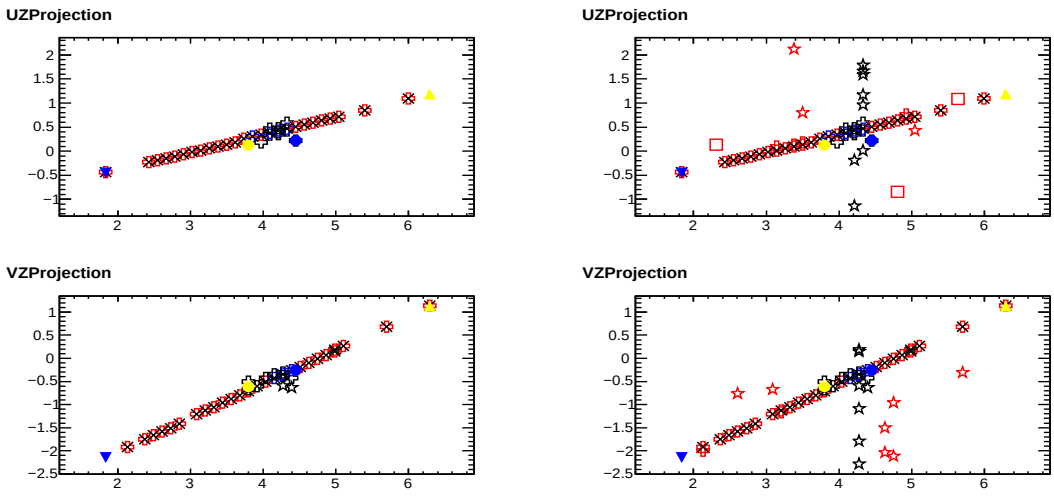

Figure B.1. Illustration of Muon Removal in the Near Detector: Left columns show UZ view and VZ view of an event which is extracted from the UZ view and VZ view of the slice as the right columns show. Red markers represent the removed track hits; blue markers represent scaled track and shower hits; and black markers represent retained shower hits.Stars represent cross-talk.

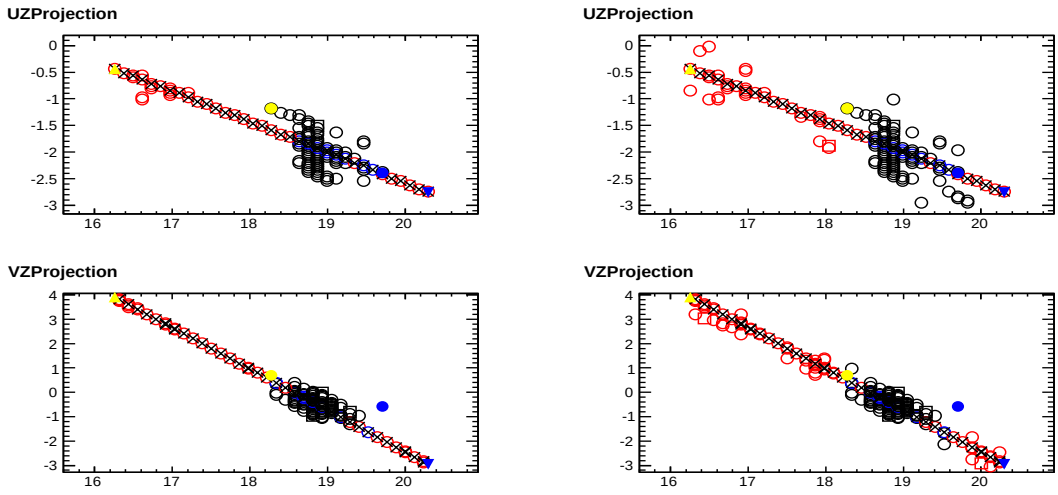

FIGURE B.2. Illustration of Muon Removal in the Far Detector: Left columns show UZ view and VZ view of an event which is extracted from the UZ view and VZ view of the slice as the right columns show. Red markers represent the removed track and crosstalk hits; blue markers represent scaled track and shower hits; and black markers represent retained shower hits.

B.4. SELECTION OF COSMIC RAY MUONS

A cosmic ray muon must satisfy the cuts enumerated below.

- Each event must have at least one track
- The azimuthal angle distributions, for the Near and Far Detectors, are shown in Figure B.3. The data (symbol) are compared to the MC (histogram). The azimuth angle must satisfy the following cuts: $(\phi \leq 10\,^\circ)$, or $(120\,^\circ \leq \phi \leq 180\,^\circ)$, or $(\phi \geq 300\,^\circ)$
- The zenith angle distributions, for the Near and Far Detectors, are shown in Figure B.4. The data (symbol) are compared to the MC (histogram). The zenith angle must satisfy the following cuts: $40\,^\circ \leq \theta \leq 90\,^\circ$
- For through-going muons, the distance from the track-vertex and track-end to the detector-edge are shown in Figure B.5 and Figure B.6 respectively. These distances must satisfy: $dist \leq 0.2m$
- Each event must have at least one shower.

- To avoid side entrant hadrons and remove edge-effects, a cut is imposed that the shower hits must be at least 5 planes away from the track-vertex plane and the track-end plane. The longitudinal distance distributions of the shower from the track-vertex and the track-end are shown in Figure B.7 and Figure B.8 respectively. These cuts are particularly relevant to measure the shape and, thereby, to isolate the EM shower.

The data and MC samples used in this analysis are:

- Cosmic-ray muon data in June 2005, December 2005, October 2006 and March 2007
- comparable daikon_03 cedar_phy_bhcurve MC files

Table B.2 showes the events selection cut table for both data and MC in the Near and Far Detectors, respectively.

TABLE B.2. Cosmic Events Cut Table

Event selection cuts	ND		FD	
	Data	MC	Data	MC
Total cosmic events	9.50×10^6	7.13×10^6	4.41×10^6	2.43×10^6
Zenith and azimuth angle cut	340376	239973	283170	153467
Through-going muon quality cut	212177	143444	116869	68089
Fiducial volume cut	46429	30905	106073	61427
Nue pre-selection cut	14944	9924	53801	32464
ANN11 PID cut	6402	4116	18139	11086
MCNN PID cut	1185	703	1843	1223

B.5. Comparison of the Variables in the Data and MC Cosmic Samples

We show a set of plots comparing the shapes of relevant variables in data versus MC. (The MC is normalized to the data.) Comparisons are shown for the the Near and Far Detectors. The ratio of Data/MC accompanies each plot. A variable is plotted in the Near and Far Detectors; the imposed cut is specified; the next variable follows.

Azimuthal Angle: Figure B.3 presents a comparison between data and MC of the azimuthal angle distributions in the Near and Far Detectors.

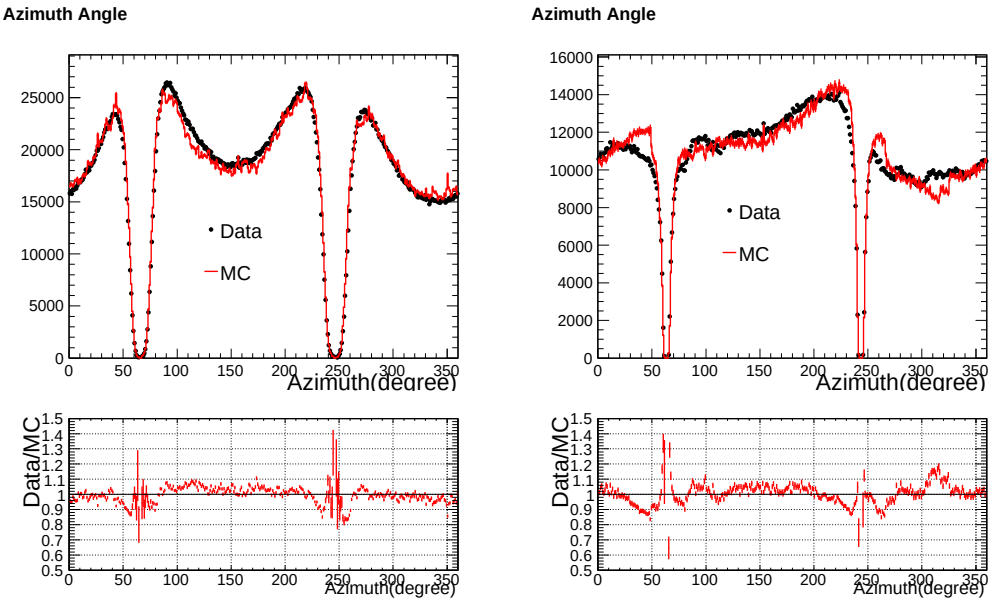

FIGURE B.3. Azimuth angle distributions for the Near Detector(left) and the Far Detector(right)

- Azimuth angle cut: $(\phi \leq 10\,^\circ)$ or $(120\,^\circ \leq \phi \leq 180\,^\circ)$, or $(\phi \geq 300\,^\circ)$

Zenith Angle: Figure B.4 presents a comparison between data and MC of the zenith angle distributions in the Near and Far Detectors.

- Zenith angle cut: $40\,^\circ \leq \theta \leq 90\,^\circ$

Distance from the Detector Edge: Figure B.5 and Figure B.6 show a comparison of the distance of the track-vertex and track-end from the detector edge between data and MC in the Near and Far Detectors.

- The cut on distance from track-vertex and track-end to the detector edge: $dist \leq 0.2m$. The spike in Figure B.5 and Figure B.6 for the Near Detector is caused due to partially versus fully instrumented planes. The data and MC disagreement for the Far Detector suggests possible problems with the Far Detector geometry simulation.

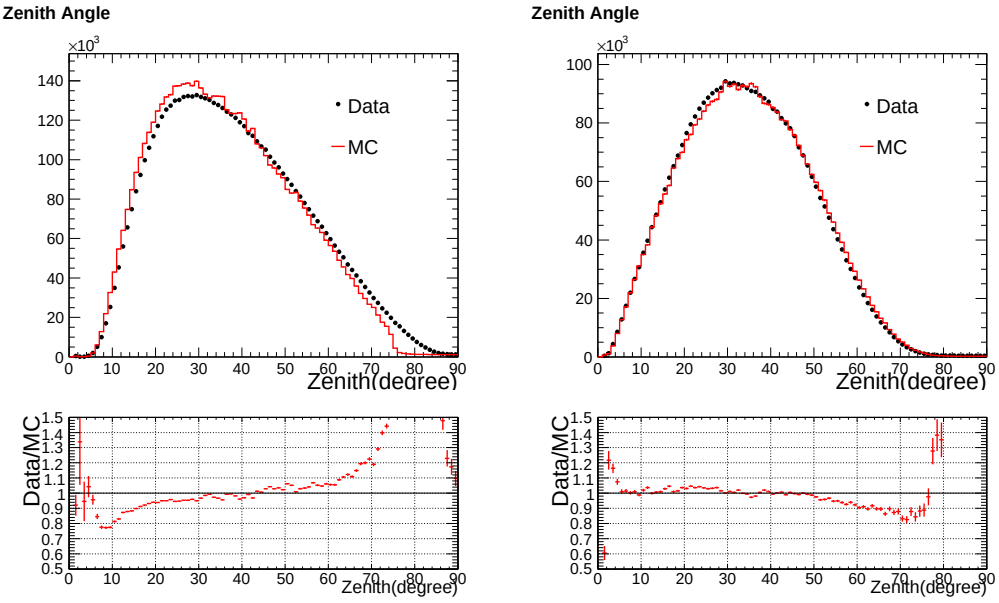

FIGURE B.4. Zenith angle distributions for the Near Detector(left) and the Far Detector(right)

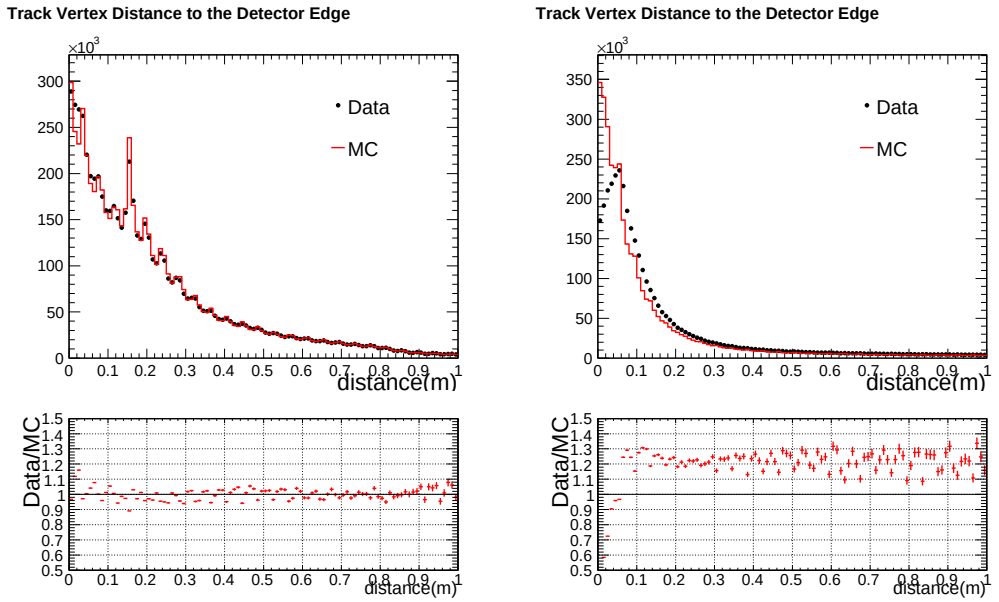

FIGURE B.5. Distribution of distance between the track-vertex and the detector edge for the Near Detector(left) and the Far Detector(right)

Distance of the Shower from Track-Vertex/End: Figure B.7 and Figure B.8 show a comparison of the distance of the shower from the track-vertex and track-end between data and MC in the Near and Far Detector. The distance cut is: $dist\_pln \geq 5$

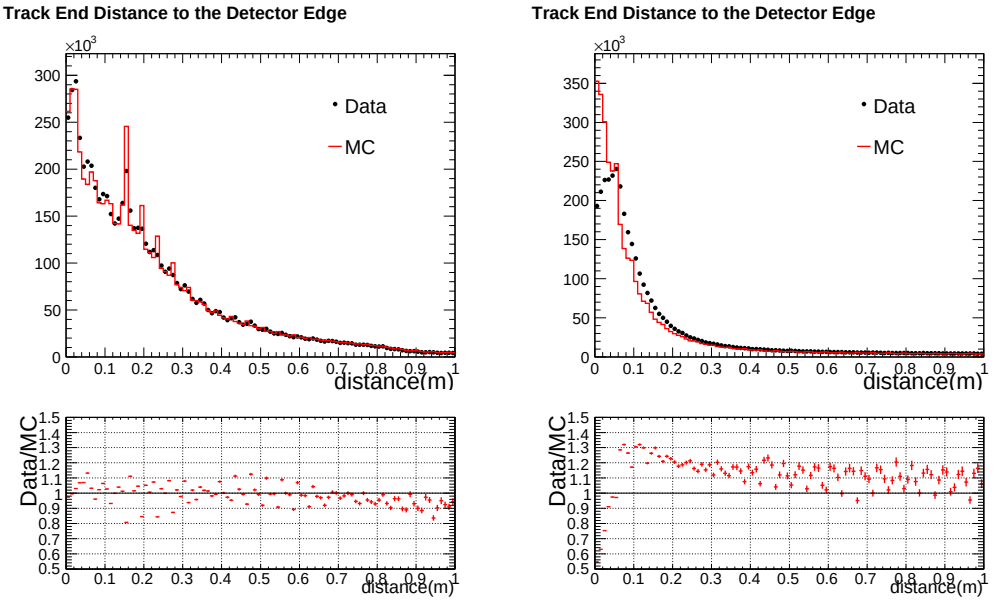

FIGURE B.6. Distribution of distance between the track-end and the detector edge for the Near Detector(left) and the Far Detector(right)

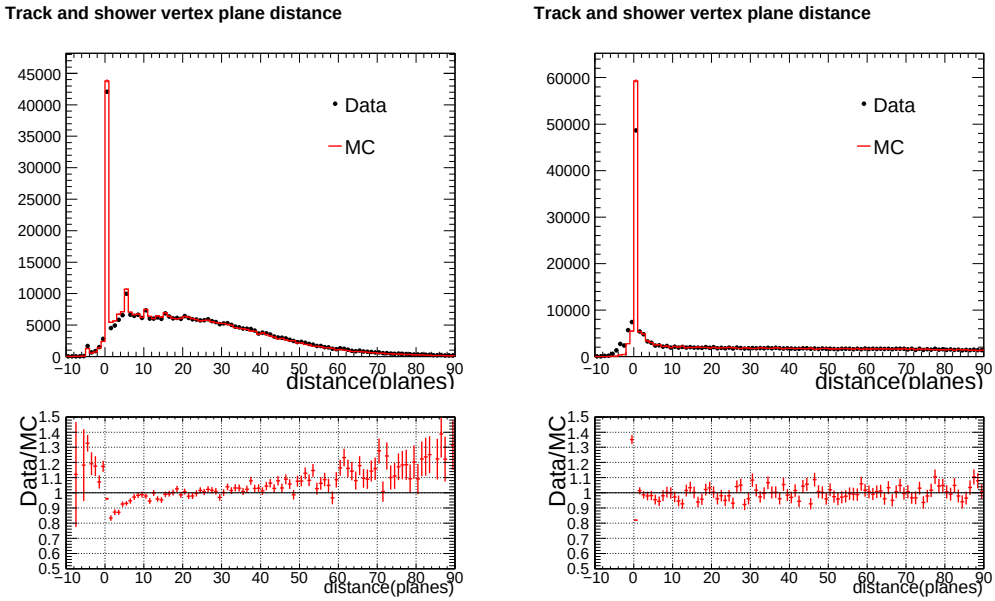

FIGURE B.7. Histogram of distance between track-vertex and shower, in number of planes, for the Near Detector(left) and the Far Detector(right)

Shower-Energy Comparison: After the aforementioned cuts, we show a comparison of the shower energy, in units of *mip*, associated with the cosmic-μ track. (Note:

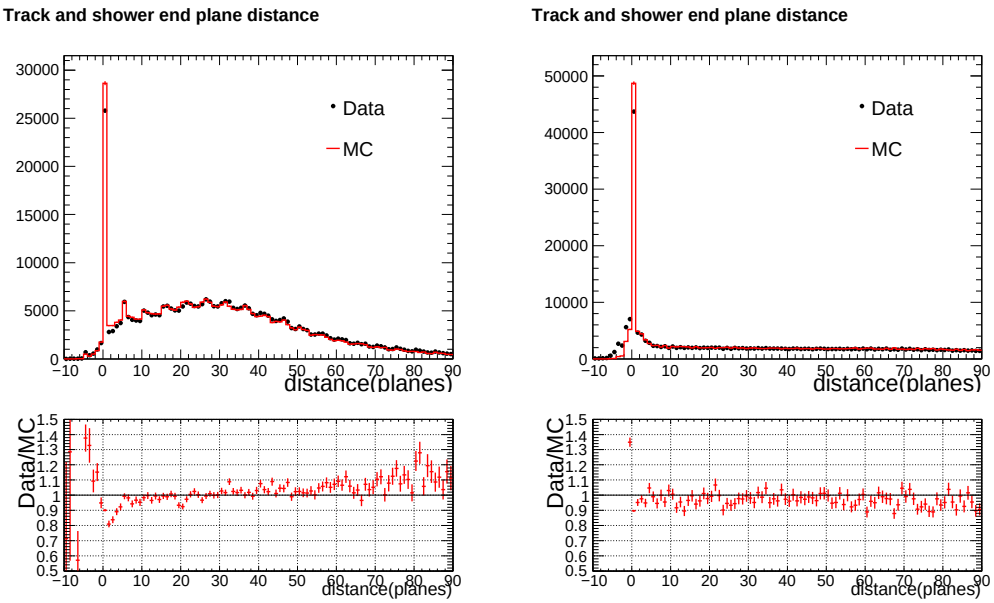

FIGURE B.8. Distribution of distance between track-end and shower, in number of planes, for the Near Detector(left) and the Far Detector(right)

$1mip \simeq 0.2$ GeV.) Figure B.9 presents the data versus MC comparison. The discontinuity in the shower energy near 32 *mip*, present in the Near and Far Detectors data *and* MC, is not fully understood.

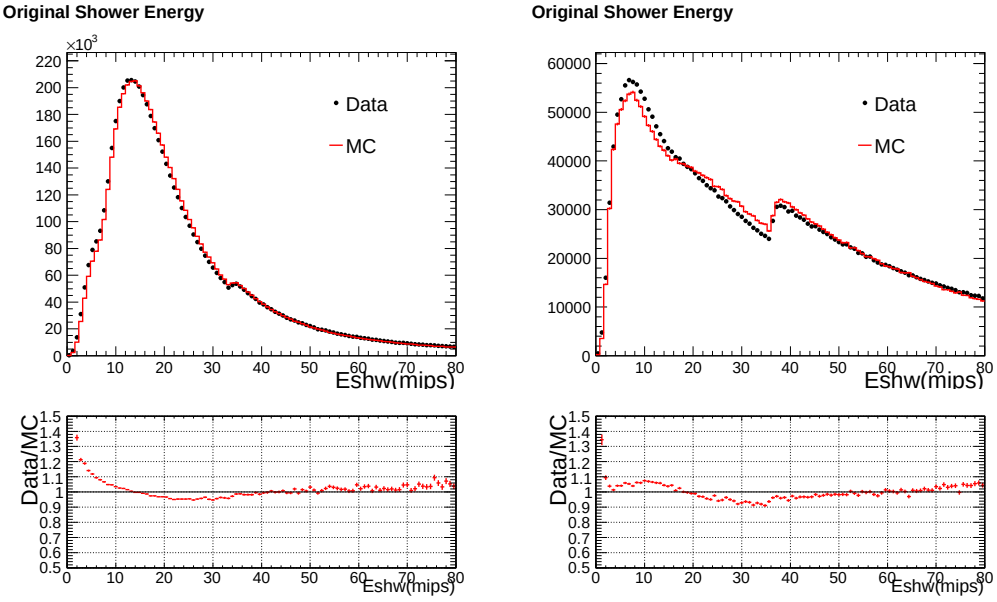

FIGURE B.9. Cosmic-ray shower energy (*mip*) distribution for the Near Detector(left) and the Far Detector(right)

B.6. Electron-Neutrino, ν_e, Pre-selection Variables

We finally present the variables, related to a shower, that are used to build multi-variate algorithm that distinguishes an EM from a hadronic shower. As before, MC (histogram) are normalized to the data (symbols); the left column compares the Near Detector and the right column compares the Far Detector.

Track Like Planes in the Shower: Figure B.10 compares the distribution of track-like planes in the shower in data and MC.

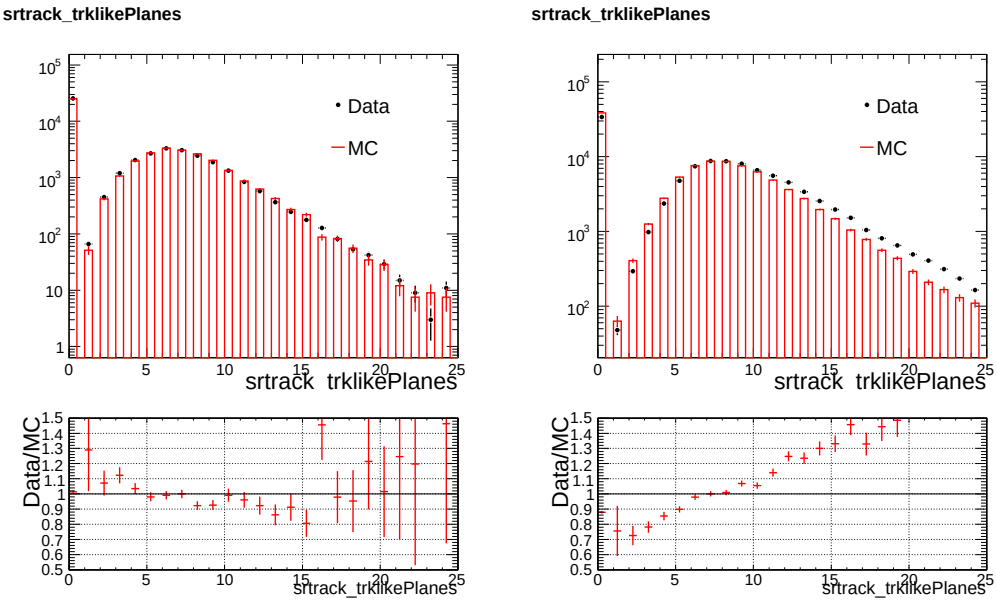

Figure B.10. Track like planes distributions for Near(left) and Far(right) Detectors after muon removal, area normalized

- Nue preselection cut: $srtrack\_trklikePlanes < 16$

Longitudinal Separation of Start and End Planes in the Shower: Figure B.11 compares the distribution of the longitudinal spread of the shower in data and MC.

- Nue preselection cut: $srtrack\_endPlane - srtrackbegPlane < 25$

Shower Energy: Figure B.12 compares the distribution of the shower energy (GeV) between data and MC.

- Nue preselection cut: $1GeV < srevent\_phNueGeV < 8GeV$

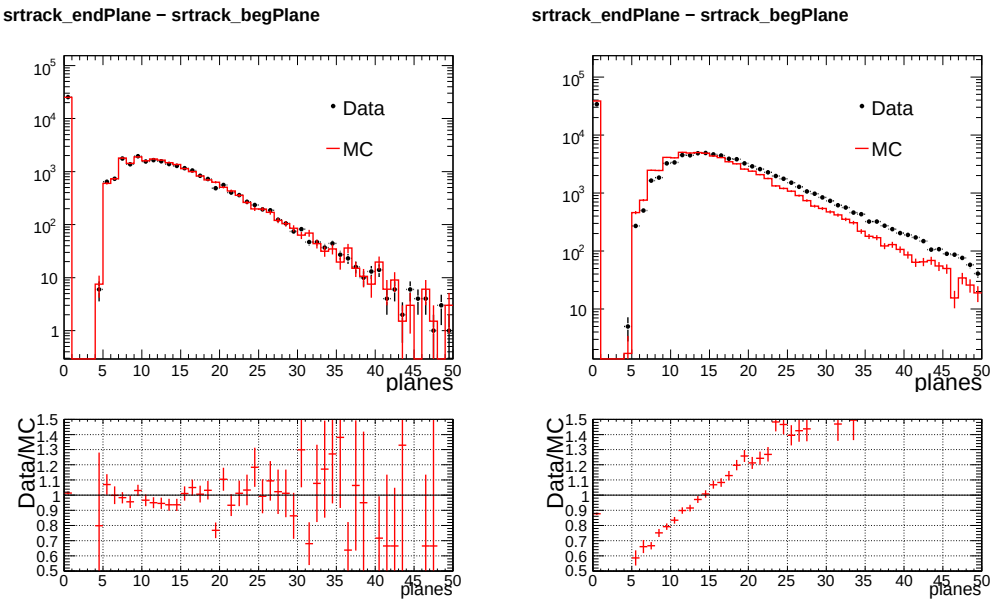

FIGURE B.11. Track length (planes) distributions for near(left) and far(right) detectors after muon removal, area normalized

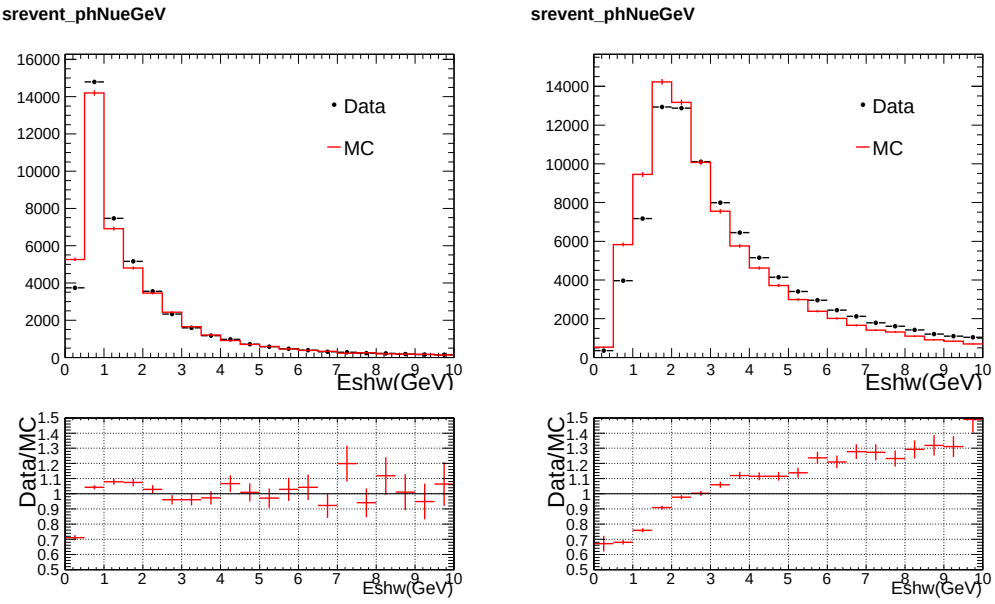

FIGURE B.12. Distributions of shower energy for the Near Detector(left) and the Far Detector(right)

- We note that the trend in Data/MC in the Far Detector as shown in Figure B.10, Figure B.11, and Figure B.12 are similar. The Near Detector

comparisons are much flatter. We are inspecting whether the muon removal affects data and MC differently in the two detectors.

B.7. Data and MC Comparison of the ν_e Shower Variables after Preselection Cuts

After the preselection cuts, we present data and MC comparison of the variables that are used to isolate the EM (ν_e-induced) shower.

Shower Fit Parameter a: Figure B.13 compares the data and MC distributions of the shower-fit parameter, a which quantifies the rise of the longitudinal EM shower profile.

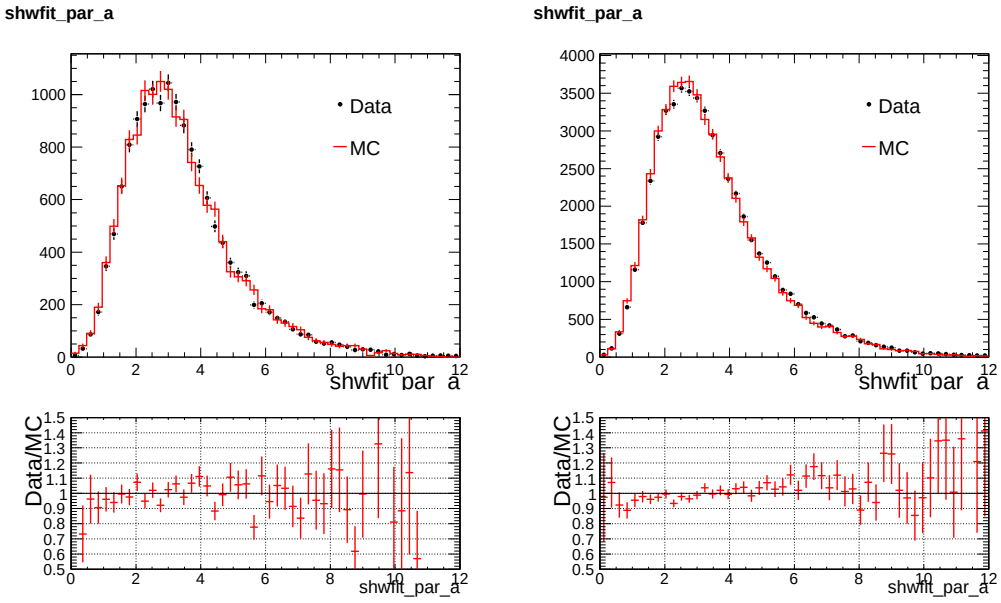

Figure B.13. Shower fit variable, parameter_a, distribution for the Near Detector(left) and the Far Detector(right)

Shower Fit Parameter b: Figure B.14 compares the data and MC distributions of the shower-fit parameter, b which quantifies the fall of the longitudinal EM shower profile.

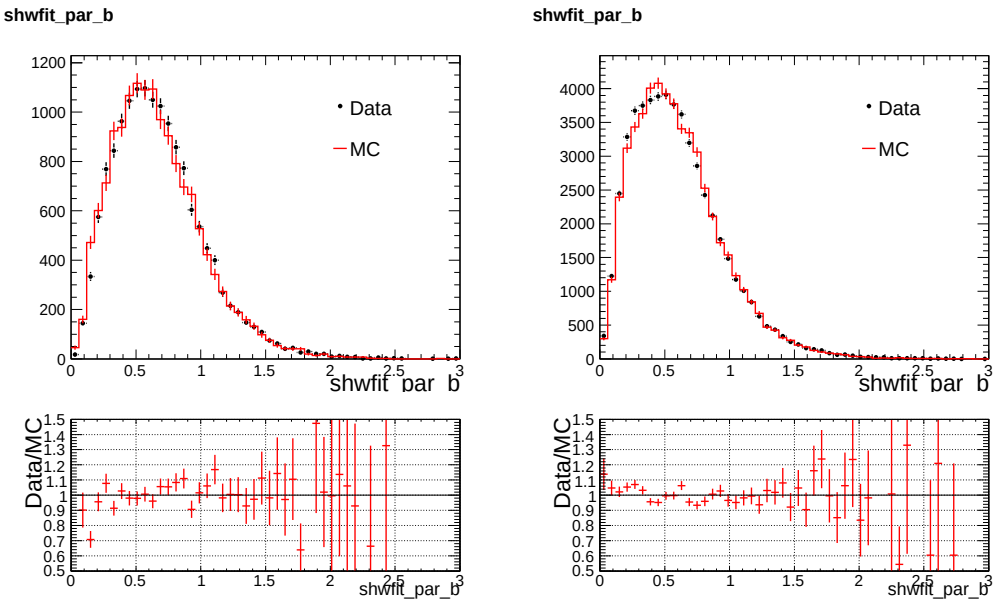

FIGURE B.14. Shower fit variable, parameter_b, distributions for the Near Detector(left) and the Far Detector(right)

The RMS of the Pulse-Heights Associated with the Shower: The transverse RMS spread of the shower is shown in Figure B.15.

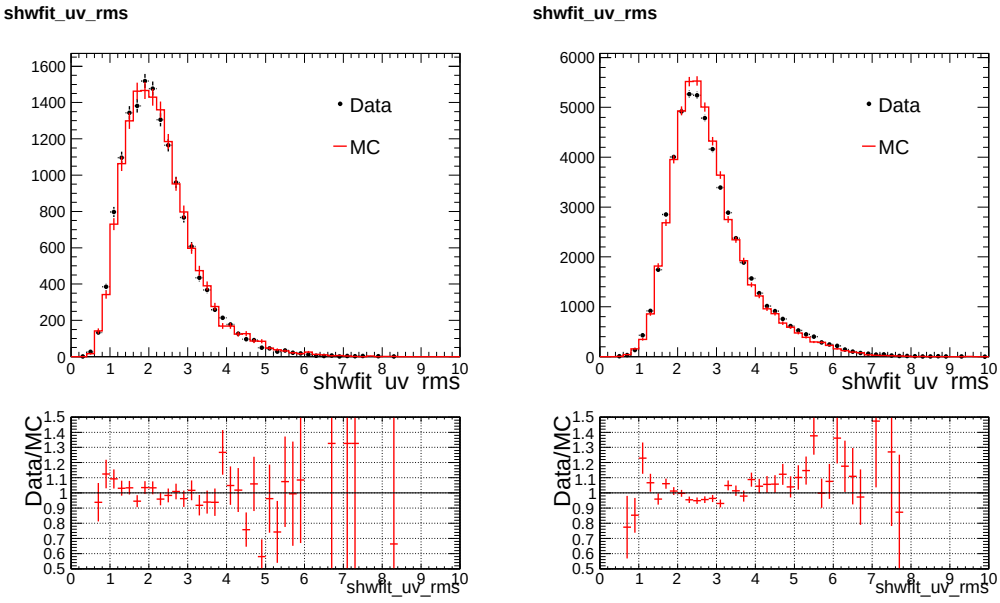

FIGURE B.15. Shower fit variable, UV_RMS distributions for the Near Detector(left) and the Far Detector(right)

The Moliere radius fit Associated with the Shower: The Moliere radius fit of the shower is shown in Figure B.16.

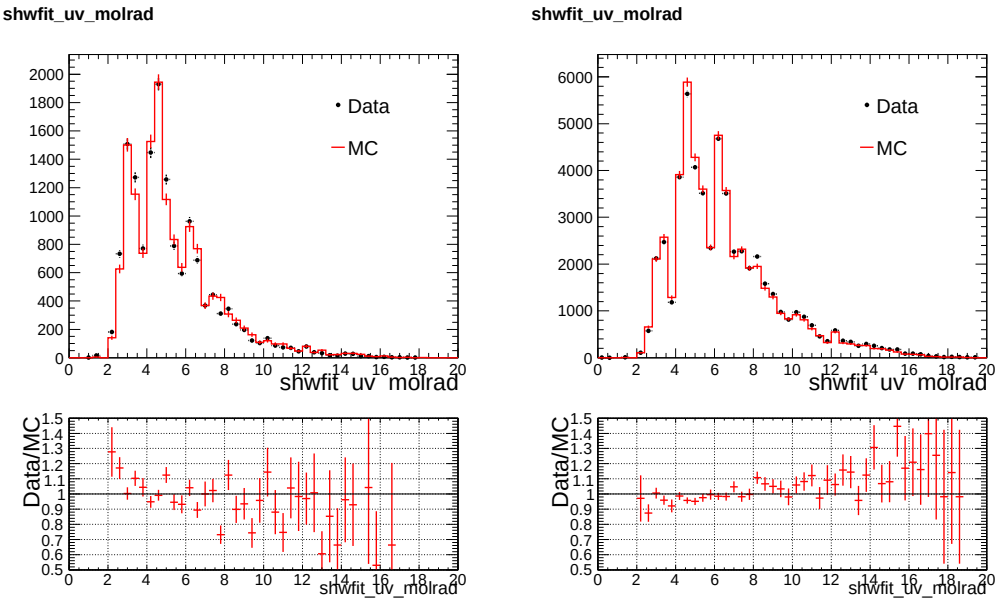

FIGURE B.16. Shower fit variable, UV_Molrad distributions for the Near Detector(left) and the Far Detector(right)

- After applying 2pe cut on the shower sample, the longitudinal and transverse profiles comparison are quite good.

The LongE variable with the Shower: The longE variable of the shower is shown in Figure B.17.

The Fractional Energy Deposited in the First Two Planes: Figure B.18 presents a data .vs. MC comparison of the fractional energy deposited in the first two planes of the shower. In an EM shower, much of the shower energy will be localized in the initial planes. The muon-removal does introduce tail. However, this is well reproduced by the MC.

The Fractional Energy Deposited in the First Four Planes: Figure B.19 presents a data .vs. MC comparison of the fractional energy deposited in the first four planes of the shower.

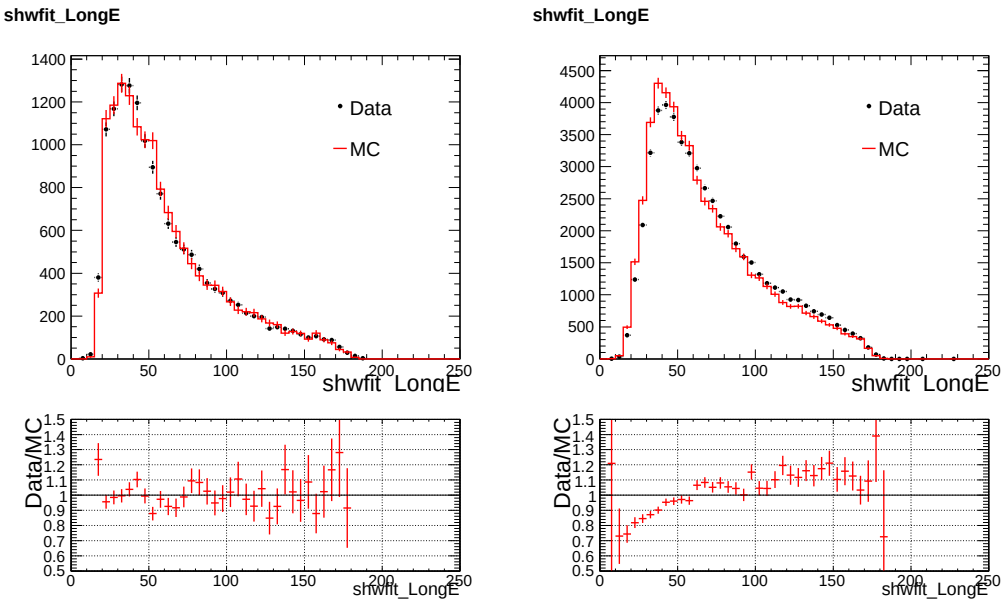

FIGURE B.17. Shower fit variable, longE distributions for the Near Detector(left) and the Far Detector(right)

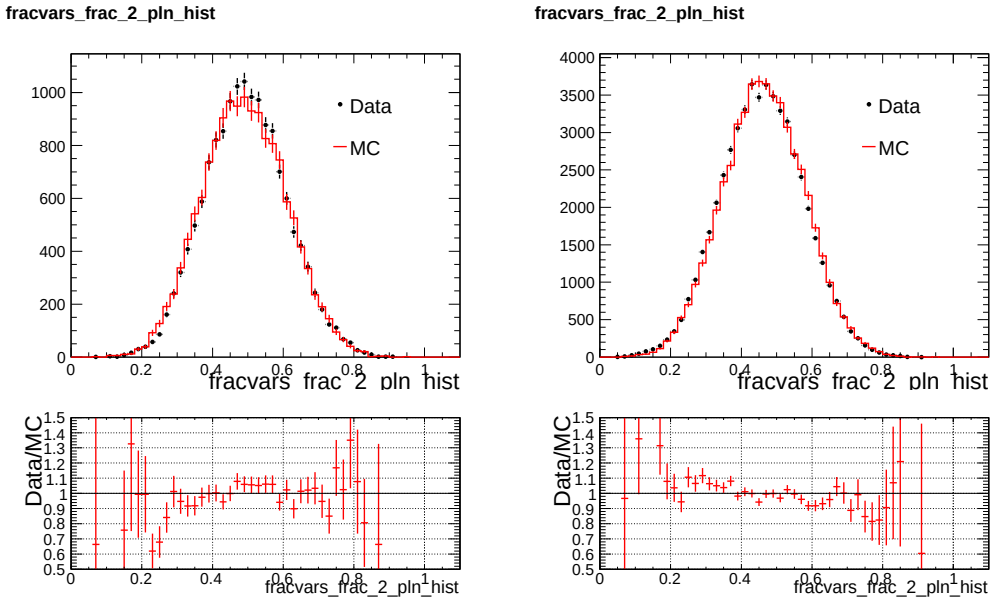

FIGURE B.18. Fraction variable, frac_2_pln, distributions for the Near Detector(left) and the Far Detector(right)

The Fractional Energy Deposited in the First Six Planes: Figure B.20 presents a data .vs. MC comparison of the fractional energy deposited in the first six planes of the shower.

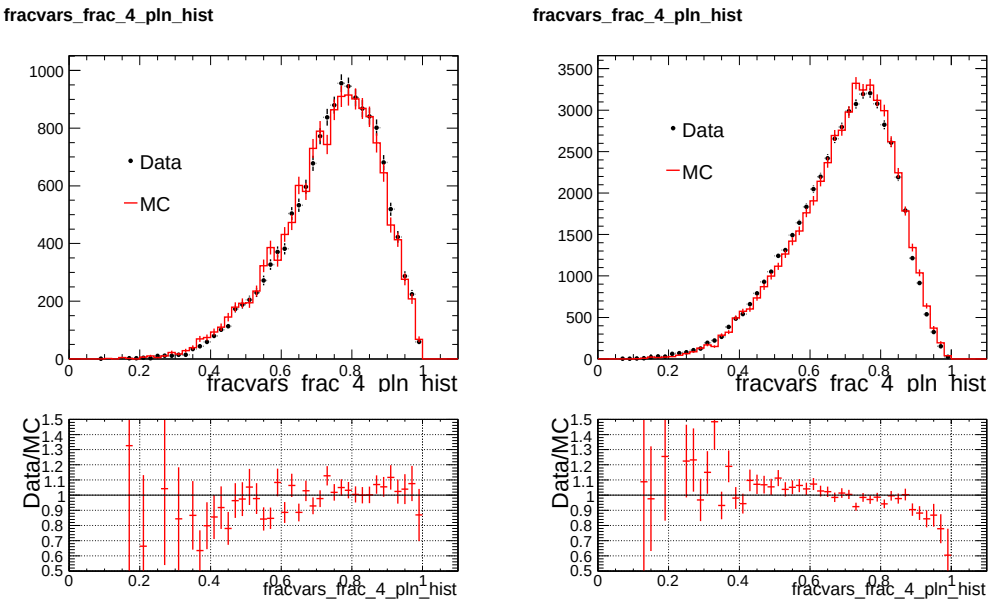

FIGURE B.19. Fraction variable, frac_4_pln distributions for the Near Detector(left) and the Far Detector(right)

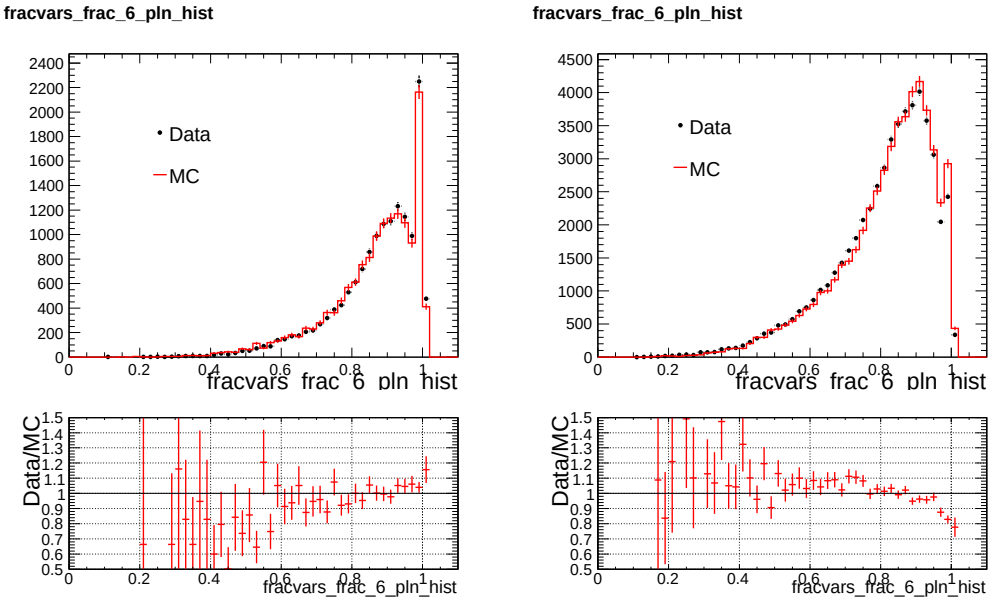

FIGURE B.20. Fraction variable, frac_6_pln, distributions for the Near Detector(left) and the Far Detector(right)

The Fractional Energy Deposited in the Highest Eight Counters: Figure B.21 presents a data .vs. MC comparison of the fractional energy deposited in the eight strips with the highest pulse height of the shower.

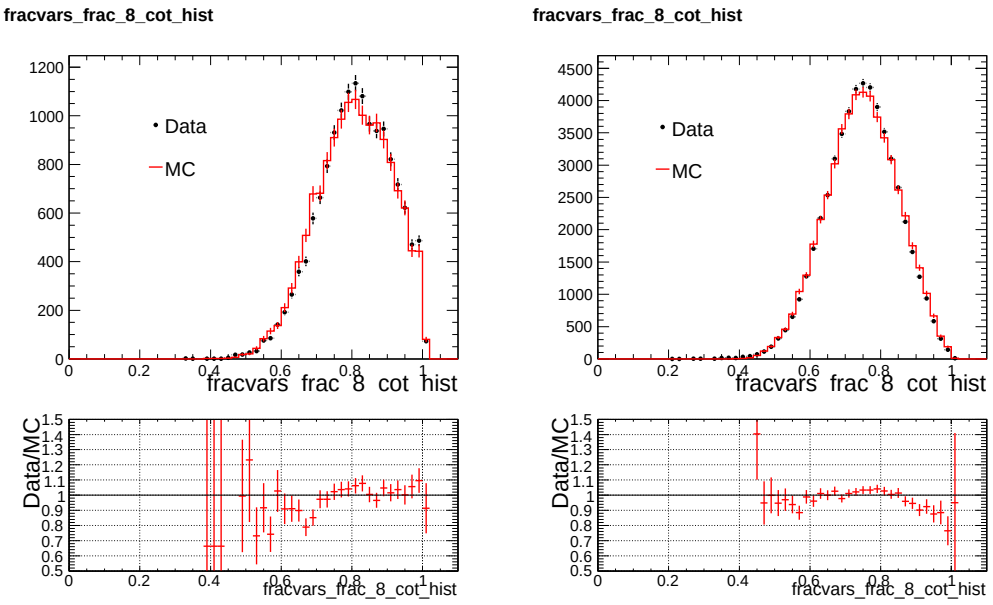

FIGURE B.21. Fraction variable, frac_8_cot, distributions for the Near Detector(left) and the Far Detector(right)

The Fractional Energy Deposited in the 'Core' of the Shower: Figure B.22 presents a data .vs. MC comparison of the fractional energy deposited in a 3-strip wide road along the shower development. The agreement between data and MC are satisfactory.

- We conclude that data and MC agree well for 'fraction-variables' used to build the multivariate function which isolates the EM shower.

The MST Variables: Comparison of mst(Minimum Spanning Tree) variable mstvars.e4w+o4w are shown in Figure B.23. The figures show that data and MC agree reasonably well.

MCNN FracCC Variable: Figure B.24 presents a data .vs. MC comparison of the fraction of the best 50 matches that are ν_e with $y < 0.9$. The agreement between data and MC is very well.

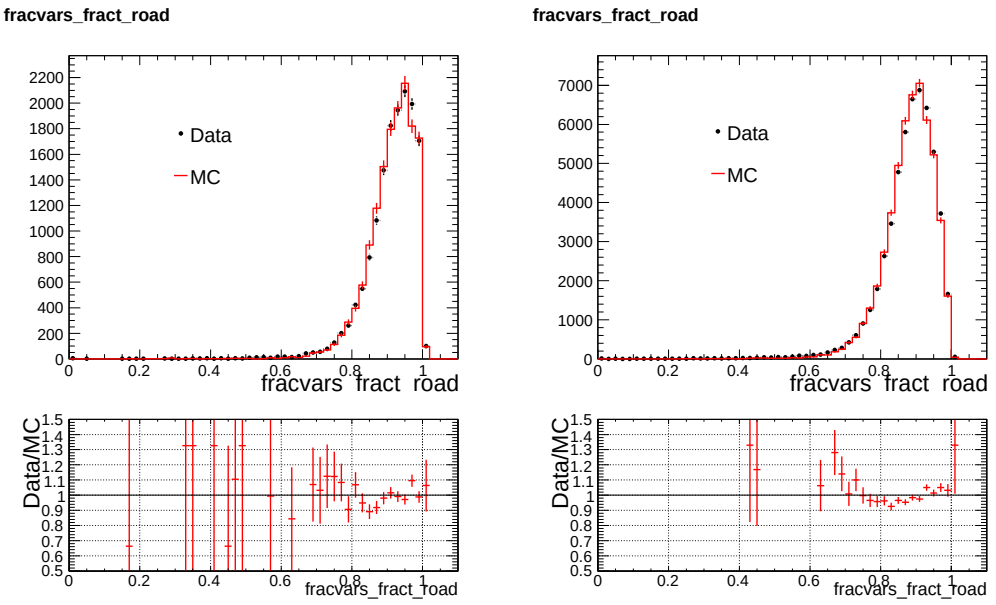

FIGURE B.22. Fraction variable, frac_road distributions for the Near Detector(left) and the Far Detector(right)

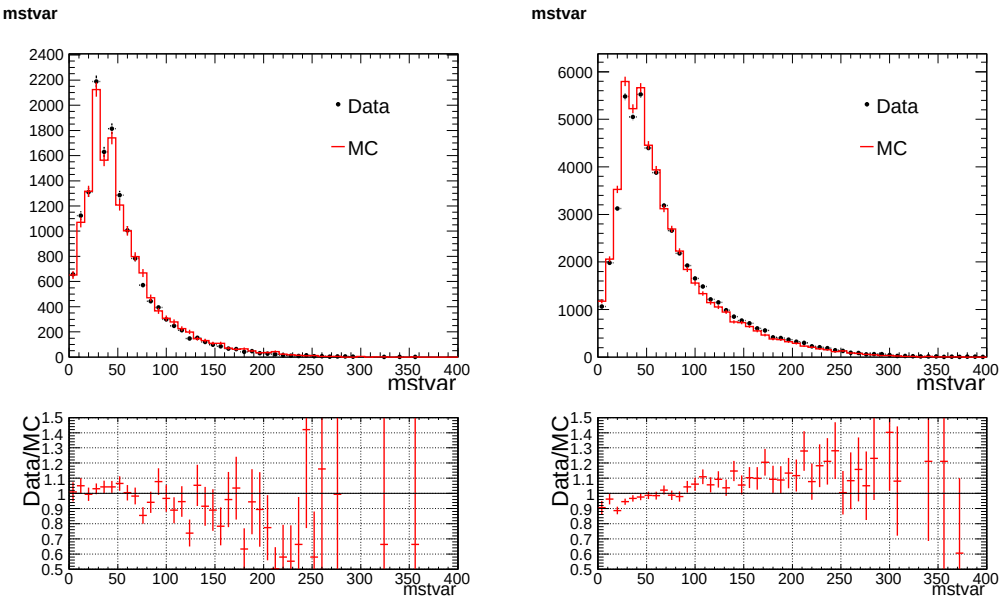

FIGURE B.23. MST variable distributions for the Near Detector(left) and the Far Detector(right)

MCNN ymean Variable: Figure B.25 presents a data .vs. MC comparison of the average y of the matches that are ν_e with $y < 0.9$ (among best 50). The agreement between data and MC is fairly well.

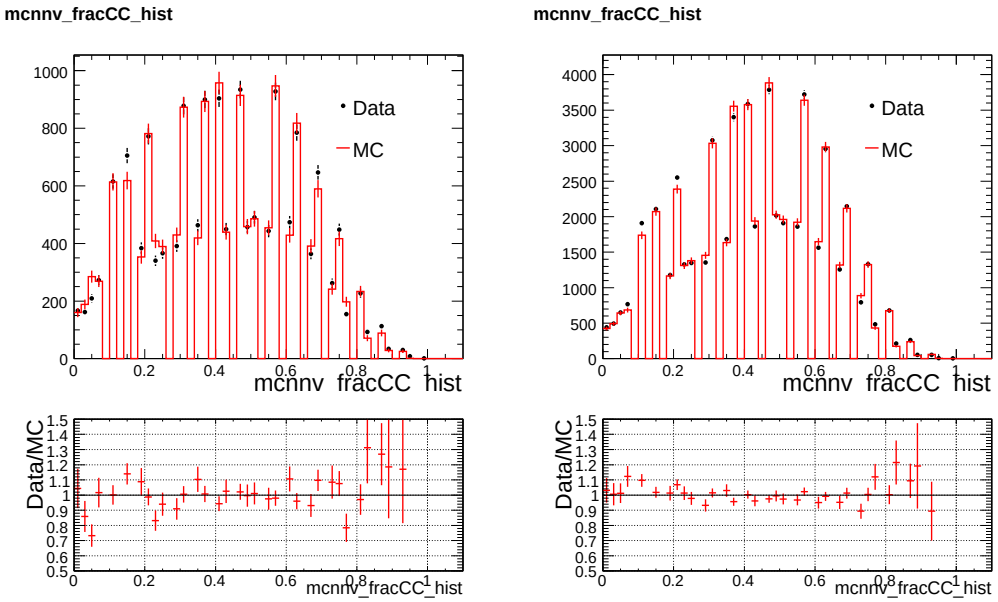

FIGURE B.24. MCNN FracCC variable distributions for the Near Detector(left) and the Far Detector(right)

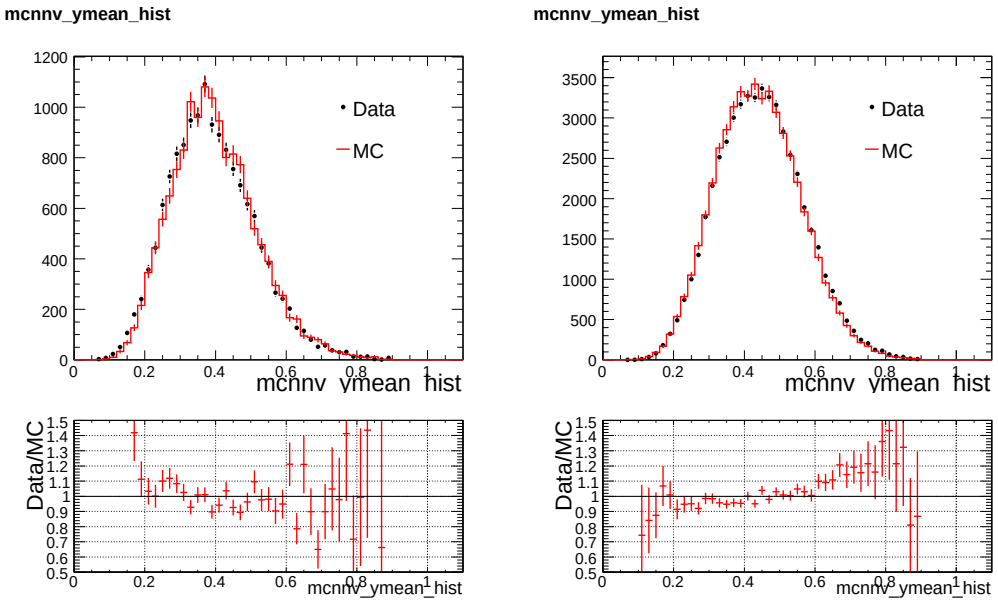

FIGURE B.25. MCNN ymean variable distributions for the Near Detector(left) and the Far Detector(right)

MCNN mean frac. Q matched Variable: Figure B.26 presents a data .vs. MC comparison of the mean fractional charged matched of matches that are ν_e with $y < 0.9$ (among best 50). The agreement between data and MC is fairly well.

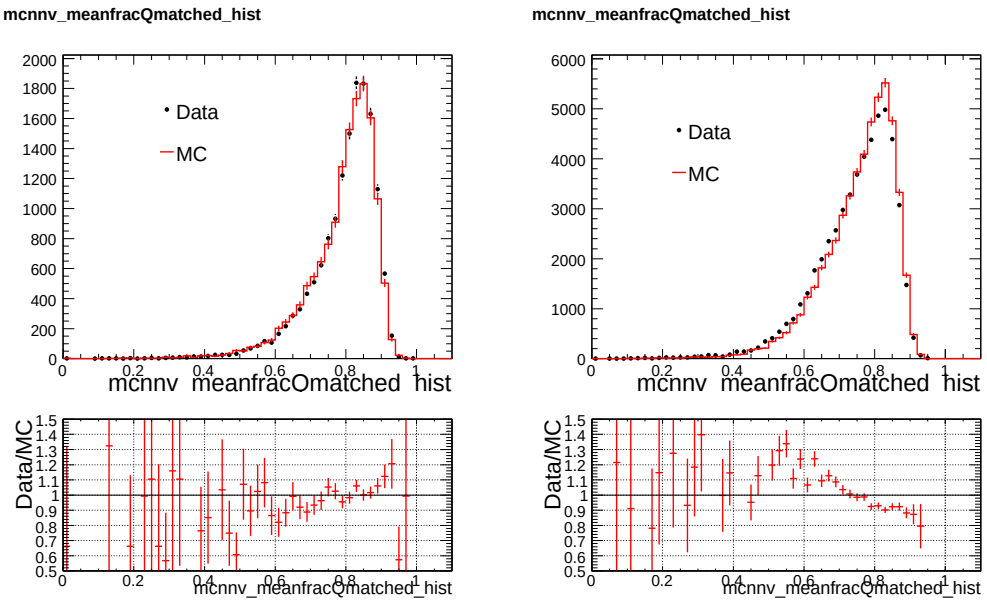

FIGURE B.26. MCNN *mean_frac_Q_matched* variable distributions for the Near Detector(left) and the Far Detector(right)

B.8. EM SHOWER PID SELECTION

Angular dependence of the EM shower selection In order to better cross check the EM shower selection efficiency, we need to have a reasonable angle cut on the cosmic-ray shower sample. Before we put any angular cut, we need to analyze the dependence of the EM shower selection PID with the cosmic-ray angles.

- For ANN11PID, data/MC agrees very well. Zenith angle between 40 and 90 degree is a reasonable cut.
- For MCNN PID, data/MC agreement is about 10% and it is quite sensitive to the cosmic-ray zenith angle. In order to have a reasonable cut, we put a harsh cut on the zenith angle between 60 and 90 degree.

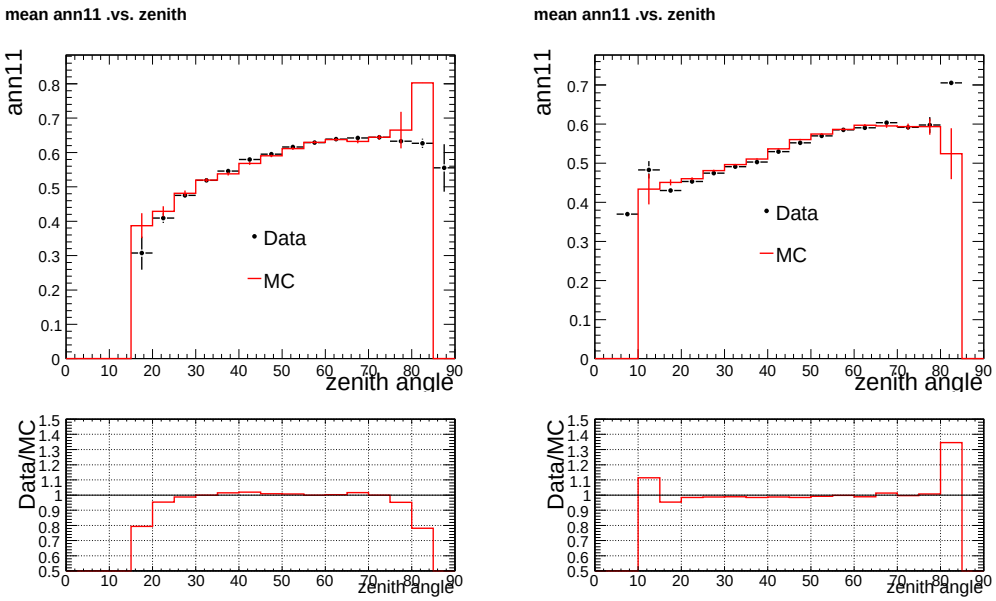

FIGURE B.27. Mean ANN11 pid value as a function of cosmic-ray zenith angle profile for the Near Detector(left) and the Far Detector(right)

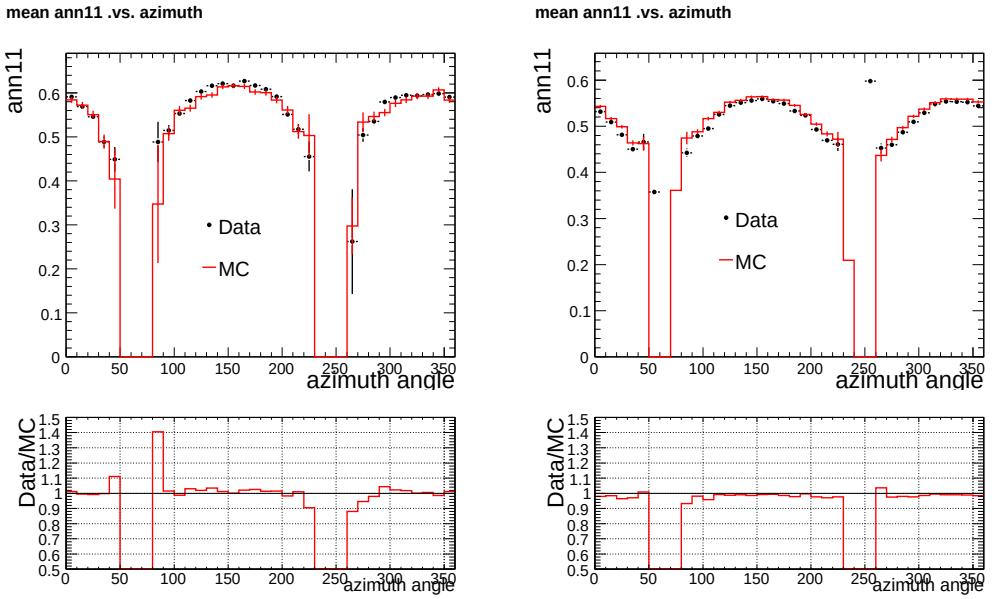

FIGURE B.28. Mean ANN11 pid value as a function of cosmic-ray azimuth angle profile for the Near Detector(left) and the Far Detector(right)

The Multivariate ANN_Pid_11inp Algorithm: Comparison of the 'ANN_pid_11inp' variable is shown in Figure B.31. The Data/MC ratio as a function of ann_pid_11inp are on the average within ±5% of unity in both the Near and Far Detectors.

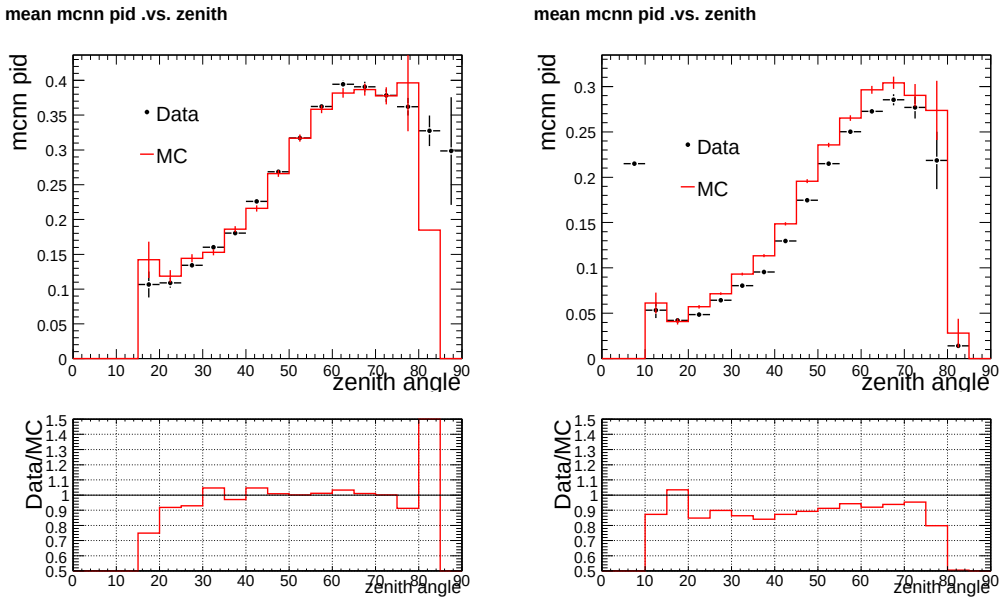

FIGURE B.29. Mean MCNN pid value as a function of cosmic-ray zenith angle profile for the Near Detector(left) and the Far Detector(right)

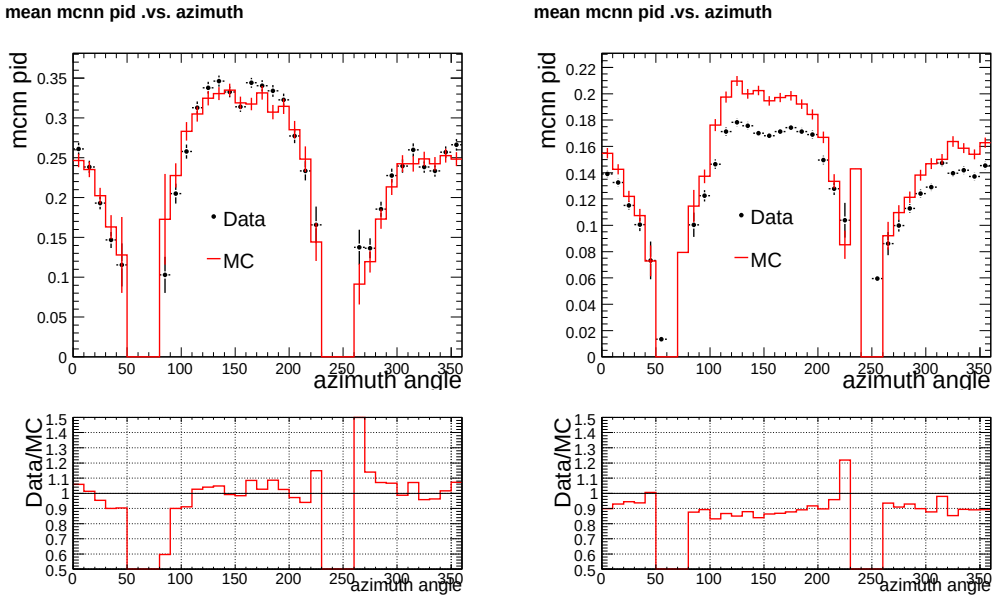

FIGURE B.30. Mean MCNN pid value as a function of cosmic-ray azimuth angle profile for the Near Detector(left) and the Far Detector(right)

The MCNN Pid Algorithm: Comparison of the MCNN pid variable is shown in Figure B.32. The Data/MC ratio as a function of mcnn pid are on the average within $\pm 10\%$ of unity in both the Near and Far Detectors.

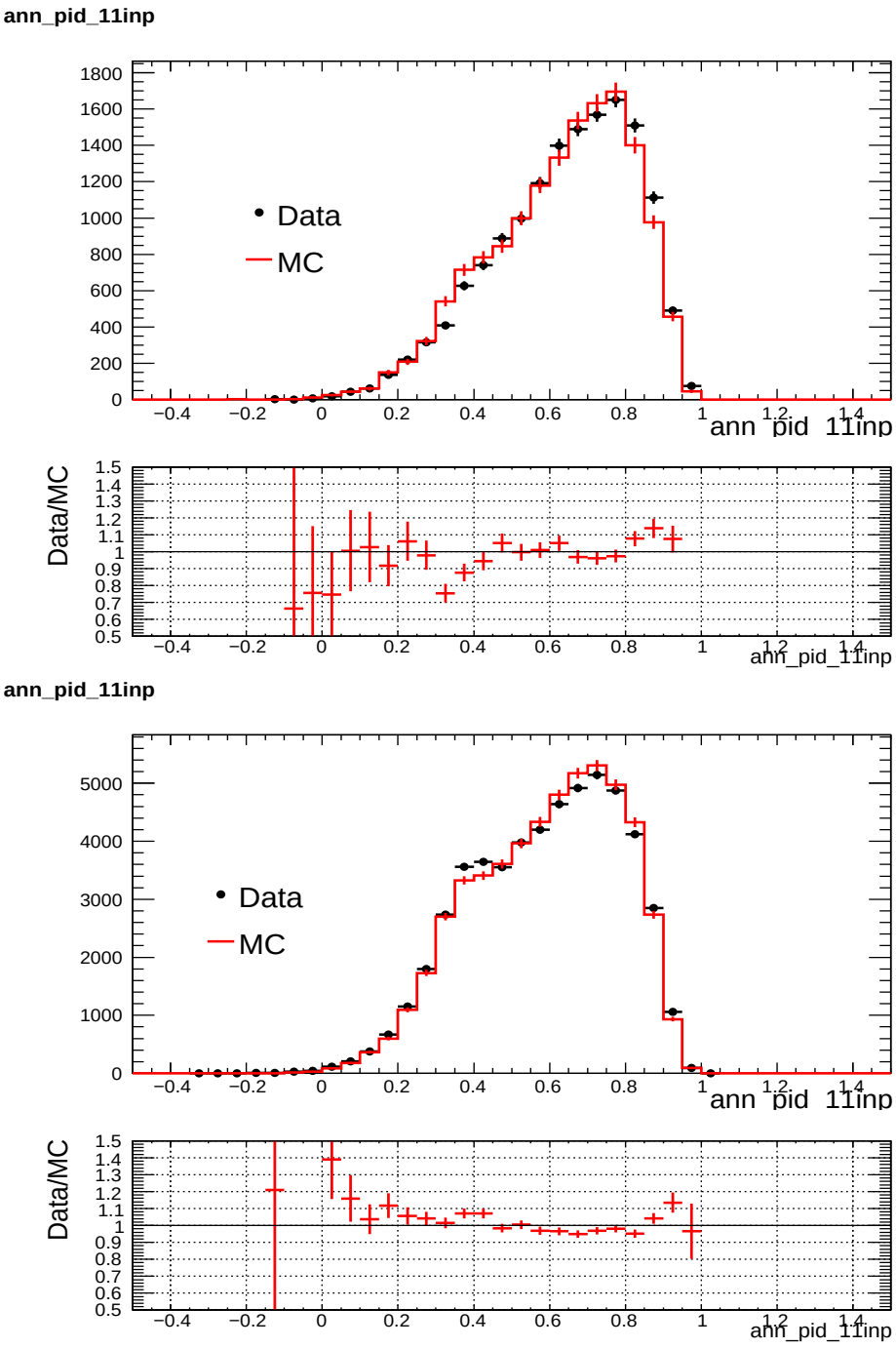

FIGURE B.31. The EM-ID variable ann_pid_11inp distributions for the Near Detector(top) and the Far Detector(bottom)

- For ANNPID11 and MCNN PID, data/MC agreement is quite good and is consistent with EM shower.

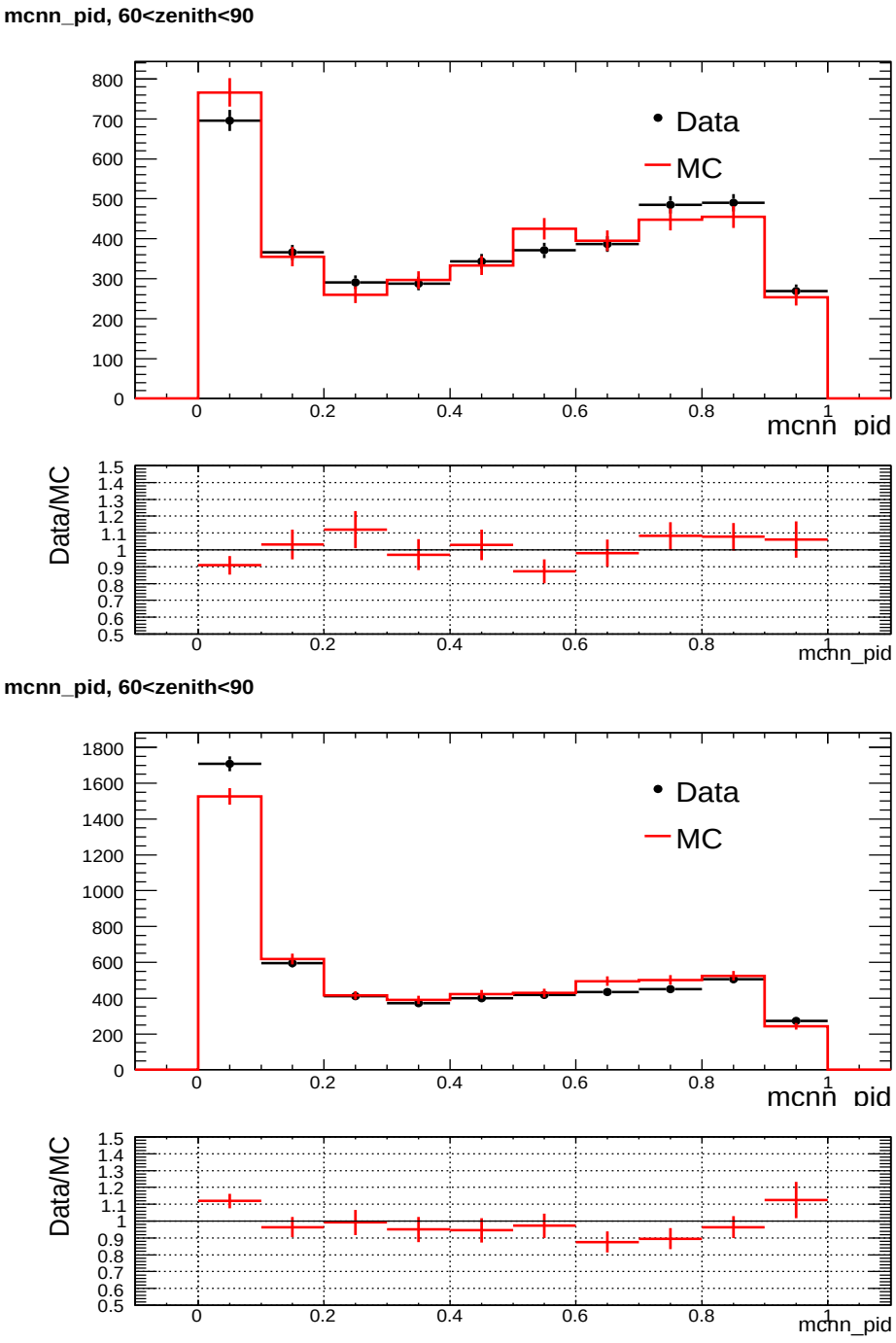

FIGURE B.32. The EM-ID variable mcnn_pid distributions for the Near Detector(top) and the Far Detector(bottom)

B.9. THE EM SHOWER SELECTION EFFICIENCY IN DATA AND MC

The *bottom line* of this analysis — a comparison of the EM shower selection efficiency, as a function of shower-energy, in data versus MC —is presented in this

section. The efficiency comparison is presented for the two EM shower algorithm alluded to in the preceding sections.

The Ann_Pid_11inp Algorithm: Figure B.33 shows the EM shower efficiency as measured, using the shower associated with the cosmic muons, in data and in MC as a function of shower energy. The Data/MC ratio is flat to better than ±5% (within 1σ) in shower energy range of 1 to 8 GeV.

The MCNN PID Algorithm: Figure B.34 shows the EM shower efficiency as measured, using the shower associated with the cosmic muons, in data and in MC as a function of shower energy. The Data/MC ratio is flat to better than ±10% in shower energy range of 1 to 8 GeV.

- Data and MC agree very well in EM shower efficiency using either of the two algorithm: the ANNPID11 or MCNNPID.
- Compared with ANN11 PID, MCNN PID has a lower EM shower selection efficiency, which is consistent with what we found in the beam sample.

B.10. Summary

By using the cosmic-ray shower (EM Shower) sample, We have demonstrated that cosmic shower is very consistent with EM shower and well modeled within 5% level for the Near and Far Detectors in the shower energy region 1 to 8 GeV.

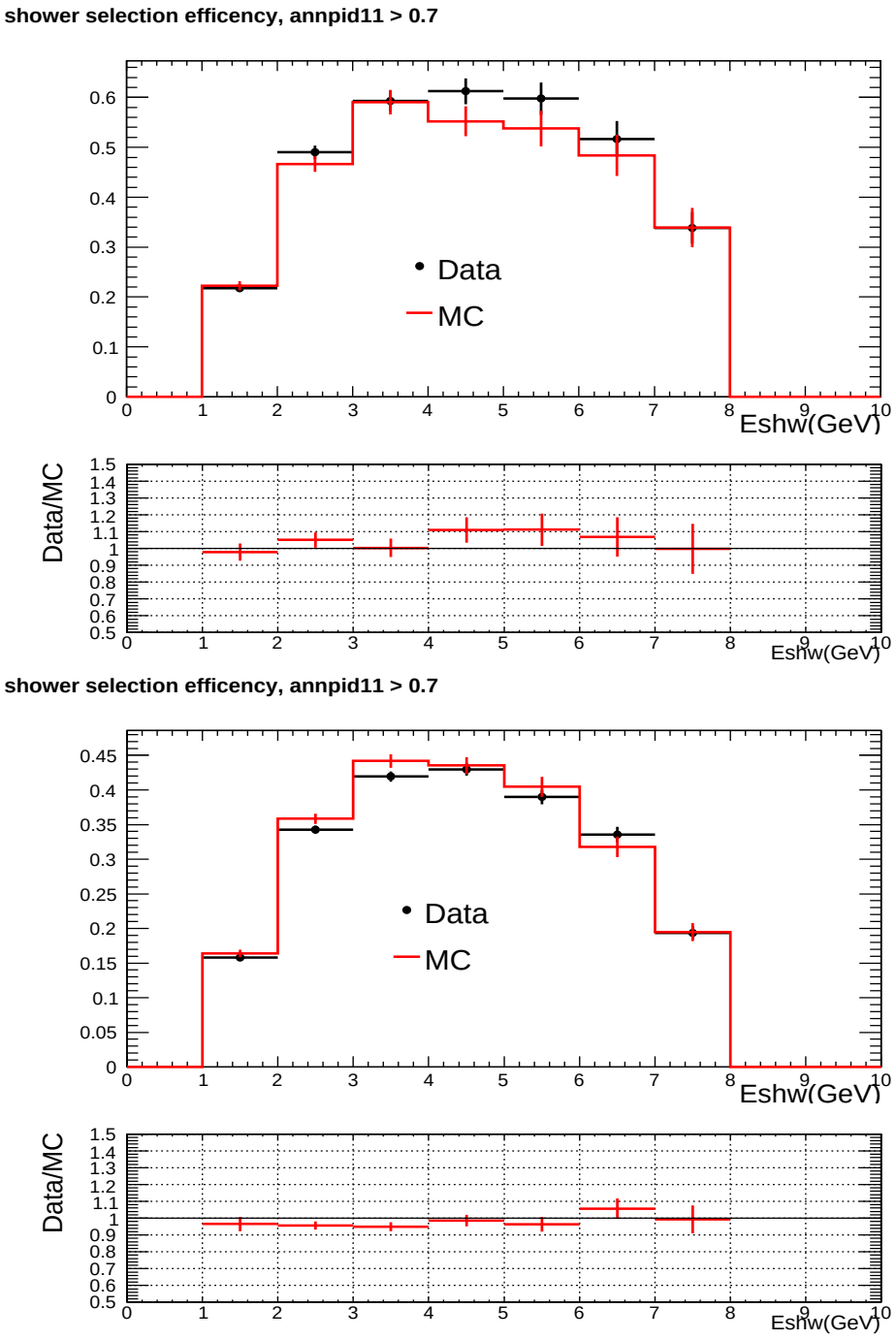

FIGURE B.33. The EM shower efficiency, using ann_pid_11inp in the Near Detector(top) and the Far Detector(bottom)

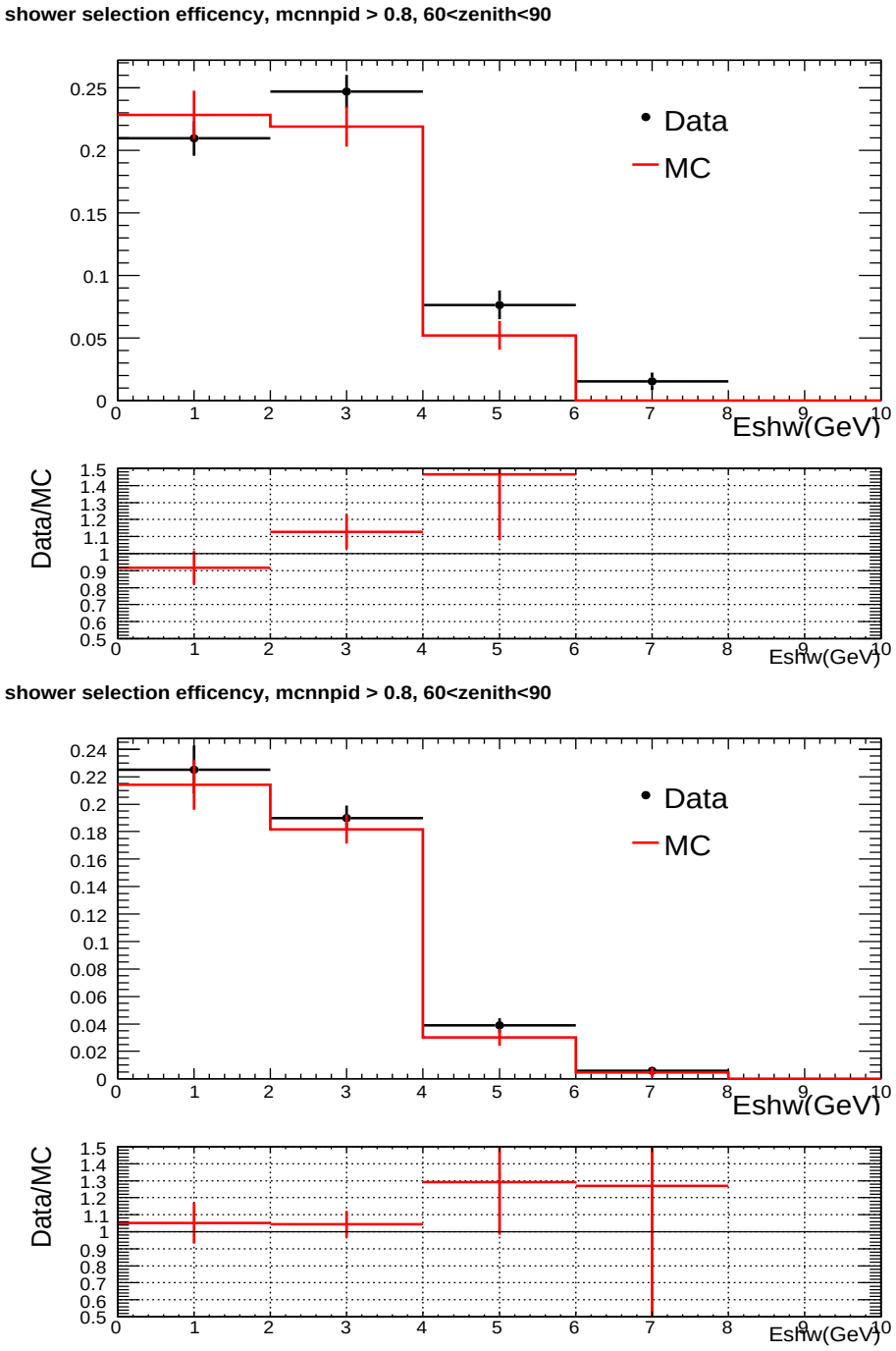

FIGURE B.34. The EM shower efficiency, using MCNN PID in the Near Detector(top) and the Far Detector(bottom)